Hydrodynamic and Sediment Transport Evaluation: Capping/Armoring Analyses for the Focused Feasibility Study Area

LOWER EIGHT MILES OF THE LOWER PASSAIC RIVER HYDRODYNAMIC AND SEDIMENT TRANSPORT EVALUATION: CAPPING/ARMORING ANALYSES FOR THE FOCUSED FEASIBILITY STUDY AREA

TABLE OF CONTENTS

LOWER EIGHT MILES OF THE LOWER PASSAIC RIVER
HYDRODYNAMIC AND SEDIMENT TRANSPORT EVALUATION:
CAPPING/ARMORING ANALYSES
FOR THE FOCUSED FEASIBILITY STUDY AREA

LIST OF TABLES

LOWER EIGHT MILES OF THE LOWER PASSAIC RIVER
HYDRODYNAMIC AND SEDIMENT TRANSPORT EVALUATION:
CAPPING/ARMORING ANALYSES
FOR THE FOCUSED FEASIBILITY STUDY AREA

LIST OF FIGURES

LOWER EIGHT MILES OF THE LOWER PASSAIC RIVER
HYDRODYNAMIC AND SEDIMENT TRANSPORT EVALUATION:
CAPPING/ARMORING ANALYSES
FOR THE FOCUSED FEASIBILITY STUDY AREA

LIST OF ATTACHMENTS

1 INTRODUCTION

The sediments of the lower 8-mile reach of the Lower Passaic River (LPR) have been identified as the major source of contamination to the rest of the river and Newark Bay. Through a Focused Feasibility Study (FFS), the U.S. Environmental Protection Agency (USEPA) is evaluating taking an action on the sediments of the lower 8.3 miles (FFS Study Area), while a larger remedial investigation and feasibility study (RI/FS) of the 17-mile LPR Study Area (LPRSA) is on-going. The FFS evaluates three active remedial alternatives (i.e., alternatives other than No Action) that include various combinations of dredging and capping or backfilling of the FFS Study Area. The engineered cap included in the alternatives with capping consists of two feet of sand, with armor stone on top where necessary to prevent the sand from eroding. The study in this report has two main objectives:

- To provide an evaluation of the stability of the proposed sand cap and to identify those areas where erosion of the sand cap is likely to occur, so that the sand cap can be stabilized with a layer of armor stone; and
- To determine changes in water elevation along the length of the LPR that would occur under high flow and/or storm surge events that, in conjunction with the capping and armoring, may result in additional flooding of the low lying areas along the LPR.

Several extreme flow conditions were considered, including 100- and 500-year flows. Flooding due to 100- and 500-year storm surges was also considered in the study. The hydrodynamic model (ECOM) used in this study is an extension of the model developed for the 17-mile LPRSA RI/FS and NBSA RI/FS. The details of the model setup and calibration have been reported previously (HydroQual, 2008). The major extension of the LPR and Newark Bay hydrodynamic model used in this analysis was to expand the model domain to include the 500-year flood plain as determined by the Federal Emergency Management Administration (FEMA) and to truncate the model

domain at the confluence of the Kill van Kull and Upper New York Bay at the south-eastern boundary and at the southern portion of the Arthur Kill as it enters Raritan Bay on the south-western boundary. Therefore, the grid designed for this study is not the same model grid used for LPR/NB model.

For the purposes of this study, SEDZLJ (Jones and Lick, 2001), a state-of-the-science sediment transport bed model, was incorporated into HydroQual's hydrodynamic and sediment transport modeling code, ECOMSED, and the resulting model code is known as ECOM-SEDZLJS.

As mentioned above, the LPR/NB hydrodynamic model was extended to include the 500-year flood plain. After extending the model grid, the applicability of the model was demonstrated by calibrating the model against available field data. The model was also validated by application of the model to Hurricane Donna, which occurred in 1960, and reproducing the observed maximum water elevation rise along the LPR. In addition, model estimates of the spatial extent of flooding, as forced by FEMA estimates of the 500-year flow and storm surge, were compared against the FEMA 500-year flood plain.

The resulting hydrodynamic and sediment transport model was applied to evaluate cap stability of two different classes of sand; one from the Ambrose Channel of New York/New Jersey Harbor and one available from upland sources. The results of the sediment transport model were used to identify areas with an excessive rate of sand cap erosion (i.e., higher than 3 inches). These areas would then be armored with 2-ft of armor stone.

After the sand cap/armor stone analysis was completed, the hydrodynamic model was utilized again to investigate the impact that the cap/armor would have on flooding of low lying areas in the LPR under different conditions of high river flow from the LPR and storm surge from New York/New Jersey Harbor and the New York Bight Apex. A key finding of this study was that it would be necessary to pre-dredge areas of the river to be

capped and armored in order to mitigate increases in flooding acreage projected to occur as a result of the capping/armoring of contaminated sediments in the river. It should also be noted that the effects of future sea-level rise on potential flooding have not been considered in this analysis.

2 HYDRODYNAMIC MODEL CONFIGURATION

In order to configure the hydrodynamic model to evaluate potential flooding issues in the LPR basin resulting from placement of a cap, FEMA's 100-year and 500-year flood area maps were obtained (Figure 2-1). The source of the data set is Q3 Flood Data derived from the Flood Insurance Rate Maps published by FEMA (1996). Figure 2-1 indicates that the 100- and 500-year flood plain areas in the LPR basin are confined to a fairly narrow area along both sides of the river for most of the length of the LPR; however, near the mouth of the LPR and in the Hackensack River basin, the flood-area is wide and in the Hackensack River covers much of the low lying marshes and tidal creeks in the Meadowlands.

The full model grid developed for the study is shown in Figures 2-1 and 2-2. During the model grid design, the lateral and longitudinal sizes of the model grid cells in the river proper (i.e. those areas that remain flooded during typical tidal conditions in the river) were kept comparable to those grid cells used for the LPR/NB hydrodynamic modeling study (HydroQual, 2008). Land surface elevations relative to the National Geodetic Vertical Datum (NGVD) 1929 in the model grid cells are shown in Figure 2-3. These elevations were deduced from land survey data compiled by the US Army Corps of Engineers (USACE) in 1990 as a part of the USACE's Passaic River Flood Control Project (Figure 2-4). The survey maps consist of 2 ft interval contours of the land elevations in the study area. The survey data in the lower sections of the river, up to RM5, were available in electronic data format. However, in the upstream sections of the river, only paper copies of the survey maps were available. Land elevation contours from these paper copies were digitized for this study so as to capture those sections within the FEMA 500-year flood areas. These detailed land survey maps helped configure the hydrodynamic model used in the flood analysis portion of this study. Figure 2-5 shows an example of the USACE survey map at the Riverside County Park of Lyndhurst near RM11. The figure shows both the aerial photography of the area as well as the digitized land elevation contours. The lower panel of Figure 2-5 depicts the vertical profile on

both sides of the river following the transect (A-A') shown in the upper panel of Figure 2-5.

Model depths of the river proper were estimated from bathymetric surveys compiled by the USACE. The Lower Passaic River surveys were conducted in 2004, and Hackensack River data were collected in the mid-1990s. The model also accounts for wetting and drying of appropriate grid cells based on bathymetric and tidal conditions, so there are a few grid cells in the Lower Passaic River where grid cells can become exposed during low tides. For locations in the Newark Bay, Kill van Kull, and Arthur Kill, USACE bathymetric survey data collected in 2003-2004 periods were used for the configuration of model depths.

Bottom sediment texture data collected in the LPR were reviewed (Aqua Survey, 2006) during the grid design effort in order to reflect proper representation of the bottom sediment properties. Bottom texture data show that, in upper section of the LPR, below the Dundee Dam and upstream of RM8.3, there are significant portions of the river that consist of coarse gravel and rock material. Figure 2-6 shows the extent of the coarse bottom in the LPR. The unshaded areas in the figure indicate fine grained material such as silt and fine sands. Bottom drag coefficients in the upstream sections containing rock and gravel were scaled up to 0.1 (unitless) (Dyer, 1986), and the rest of the silt and fine grained sand bottom areas were specified with a baseline coefficient of 0.0025. The baseline coefficient of 0.0025 was selected after extensive sensitivity analyses performed during LPR/NB hydrodynamic modeling study (HydroQual, 2008).

The computational grid consists of 68×170 cells in the horizontal plane and 11 equally spaced σ-levels in the vertical plane (i.e., 10 vertical segments). The transformed σ-coordinate system in the vertical plane allows the model to have an equal number of vertical segments in all of the computational grid cells. The computational grid for the river proper utilized four lateral grid cells with about 40 m (131 ft.) (across river) x 150 m (492 ft.) (along river) resolution from RM0 to about RM5 and then the gird was reduced

to three to two cells in the narrower sections in the upstream portion of the river. Up to ten computational cells were utilized to represent the flood plain on either side of the LPR as appropriate. The model open boundaries are located at the entrance to the Kill van Kull from New York Harbor and the entrance to Arthur Kill from Raritan Bay at South Amboy. The selection of model parameters and the grid resolutions were confirmed with extensive sensitivity and grid convergence tests performed on the LPR/NB hydrodynamic model grid, which employed comparable grid resolution (HydroQual, 2008).

3 HYDRODYNAMIC MODEL CALIBRATION

The hydrodynamic model was calibrated for a 30-day simulation using field data collected in the summer of 2004. A high quality data set, collected by the Rutgers University Institute of Marine & Coastal Sciences (IMCS), between mid-August and September 2004, was used for the calibration. These data were collected using three bottom-mounted pressure sensors, three temperature and conductivity sensors and two bottom-mounted acoustic-doppler current profilers (ADCPs) (Figure 3-1).

3.1 BOUNDARY CONDITIONS AND MODEL FORCINGS

Hourly water surface elevations and temperature and salinity (Figure 3-2) along the two open-water boundaries at the Kill van Kull and South Amboy were extracted from the Water Year 2004 archives of HydroQual's LPR/NB hydrodynamic model results (HydroQual, 2008). The LPR/NB hydrodynamic model was extensively calibrated and validated with multiple data sets that were available for the LPR, Newark Bay, and the Kills (HydroQual, 2008).

Freshwater inflows, both from riverine and non-point sources, were extracted from the input data used for the LPR/NB hydrodynamic model. The bottom panel of Figure 3-2 shows the total boundary inflows from the Upper Passaic River and the Hackensack River and the total flow from combined sewer outfalls (CSO) and stormwater outfalls (SWO) for the Lower Passaic and Hackensack River basins. Lacking observed river inflow temperatures, a three-day moving average of air temperature observed at Newark International Airport was specified as inflow water temperatures (Figure 3-3).

Hourly meteorological parameters from Newark International Airport were used to compute air-sea heat exchanges as well as surface forcing functions. The measured meteorological parameters used in this analysis included wind speed and direction, air temperature, relative humidity, barometric air pressure, and cloud cover (Figure 3-3).

Detailed discussions on the boundary forcing data can be found in HydroQual's hydrodynamic report for the LPR study (HydroQual, 2008).

3.2 CALIBRATION RESULTS

3.2.1 Tidal Elevations

Water surface elevations were collected using the three pressure sensors M1, M3, and M5 in the LPR (Figure 3-1). Figure 3-4 illustrates the computed and measured surface elevations over a 30-day calibration period, September 1st to 30th, 2004. In the figure, blue lines represent the model results while the red lines represent observations. The mean range of tide in the LPR and the Newark Bay areas is between 1.5 (4.9 ft.) and 1.8 m (5.9 ft.). The water surface elevation during spring tides can be more than 1.0 m (0.3 ft.) above mean sea level (MSL). The model-data comparisons, shown in Figure 3-4, also indicate that the amplitudes of the tide, the ranges between spring and neap tidal cycles, and times of high and low water are very well reproduced at those three locations in the river. A few exceptions can be noted around days 26-30 at M3 and days 28-29 at M5 when observed data at those stations show an increase in water elevations not reproduced by the model. Careful review of the observed elevations and corresponding river inflow and boundary forcing suggest that the pressure sensors deployed at M3 and M5 may have shifted their positions slightly during the survey. The upstream freshwater flows shown in Figure 3-2 indicate three high-flow events during the calibration period, with peak flows occurring approximately on days 8, 18, and 28 September. While the increase in the observed water elevations at M3 and M5 around day 28 might coincide with the flow peak on day 28, corresponding increases in observed water elevations do not occur for the other two high-flow peaks on days 8 and 18. Moreover, the sudden increase in water elevations recorded (about 0.5 m) at M3 around day 26 occurred one day earlier than the corresponding increase in the Passaic River flow measured at Little Falls (USGS Station #01389500). The results of flooding analysis presented in Section 6 of this report suggest that a rise of 0.5-m (1.6 ft.) water elevation at this location in the LPR would require high

inflow rates from upstream of more than 30,000 cfs. Because of these inconsistencies between the river flow rate and the abrupt changes recorded in water depth, it is believed that these elevation changes were caused by problems with the data-collection equipment and do not reflect actual changes in water depth. Although it can't be proved conclusively, these observations suggest the possibility that the M3 and M5 pressure sensors may have shifted slightly during the survey.

3.2.2 Current Velocities

Current velocity data at two locations in the LPR were available for calibration of the hydrodynamic model. The data collection instruments were two bottom moored acoustic current meters and were deployed during September 2004. The locations of the current meters are shown in Figure 3-1 (M2 and M3).

Time-series of hourly current velocities were measured at the surface, mid-depth and bottom layers, 4.1 m (13.5 ft.), 2.6 m (8.5 ft.) and 0.9 m (~3 ft.) from the bottom, respectively, at Station M2. The computed results and the observed data are shown in Figure 3-5a, where positive values indicate a downstream current and negative values indicate an upstream current. In Figures 3-5a and 3-5b, the blue lines are the model results and the red lines are the observations. Figure 3-5a indicates that there were strong tidal currents in the LPR during the calibration period. Due to fresh water inflows around day 28 (see Figure 3-2), the maximum ebb tidal velocities at the surface were about 1.25 m/s (4.1 fps) and the maximum flood tidal velocities were about 0.85 m/s (2.8 fps). In the vertical, it can be noted that velocities decrease with increasing depth. At the bottom layer, the maximum ebb tidal velocities were about 0.8 m/s (2.6 fps) and the maximum flood tidal velocities decreased to about 0.65 m/s (2.1 fps). At Station M2, the model slightly overestimates ebb tide velocities near the surface and bottom layers around days 2, 14, and 28 during spring tidal periods. In general, however, the model performance, with respect to reproducing tidal currents, their time of occurrence, and the variations between spring and neap tidal cycles, is good. Three sub-tidal events were recorded at

days 7, 18 and around 28. At M2, the model computed slightly higher bottom velocities than those observed at 0.9 m (~ 3ft.) above bottom.

Shown in Figure 3-5b are the time-series of hourly current velocities at surface, mid-depth and bottom layers, 6.0 m (19.7 ft.), 3.0 m (9.8 ft.) and 1.0 m (3.3 ft.) from the bottom, respectively, for Station M3. At this upstream location, surface tidal currents are not as strong as those observed at the downstream current meter, M2. The maximum ebb tidal velocities at the surface are about 1.0 m/s (3.3 fps) and the maximum flood tidal velocities are about 0.70 m/s (2.3 fps). As depth increases, current velocities decrease. However, at the bottom layer, the maximum ebb and flood tidal velocities, 1.0 m/s (3.3 fps) and 0.75 m/s (2.5 fps), respectively, are larger than those computed at M2.

Only 14 days of mooring data were collected at M3 in September 2004. Figure 3-5b shows that the model reproduces the amplitudes and phases of velocity observed near the bottom quite well. At surface and mid-depth layers, the phase of current is well simulated, but the amplitude is over-estimated. Both the computed and observed current velocities show a sub-tidal event around day 28.

3.2.3 Temperature and Salinity

Continuous observations of surface and bottom water temperature and salinity were made at six locations in the LPR from August through October 2004. The locations of these stations are shown in Figure 3-1 and are denoted as M1, M2, M3, M4, Bridge Street Bridge (BSB), and M5 from downstream to upstream. The data collected at these stations in September 2004 were used to calibrate the hydrodynamic model for temperature and salinity.

The model-data comparisons of hourly temperature and salinity at these locations are shown in Figures 3-6 and 3-7, respectively. The blue lines represent the computed values and the red lines the observations at surface and bottom layers. In order to correlate

changes in temperature and salinity with the model forcing terms, the upstream river inflow data are also shown with the temperature and salinity plots.

During the simulation period, temperatures were basically maintained above 20ºC in the LPR except for a decrease around day 19 due to a high flow event. The model and data indicate small differences in surface and bottom temperatures showing relatively weak thermal stratification in the river. Figure 3-6 indicates that the model computed surface and bottom temperatures follow closely the observed temperature for most of the simulation period. However, the model does not quite capture the temperature variations following the high flow event. The discrepancy in the computed and the measured temperatures around the day 19 flow event may be attributed to a lack of information concerning the actual water temperature to be assigned to freshwater inflows (see the previous section). The model-data differences are relatively small at downstream locations (M1, M2 and M3) but become more apparent at upstream locations (M4, Bridge St. Bridge and M5) closer to the source of the inflow, i.e., water over the Dundee Dam.

Figure 3-7 indicates that freshwater flow and estuarine circulation have a significant influence on the salinity variations. Strong salinity stratification is shown at the downstream station during the high flow event. At M1, the surface salinity can decrease to near 0 practical salinity units (psu) while the corresponding bottom salinity has a value of about 13.5 psu around day 18. The observed tidal variation in the surface salinity at M1 can be as much as 12 psu most of the time. This variation in salinity represents the tidal excursion of high salinity water entering the river from Newark Bay during flood tide and low salinity water moving downstream from the upstream LPR during ebb tide. Moving upstream, salt intrusion and vertical stratification become weaker and freshwater flow influence becomes more dominant. At M5 and Bridge St. Bridge, the surface-to-bottom salinity differences are only about 1-2 psu during the low flow period, and salinities at surface and bottom approach 0 psu during the high flow period. Corresponding to each high flow event, model computations (Figure 3-7) also show corresponding decreases in observed and computed salinity. The surface salinity can

decrease from 17 psu to close to 0 psu at the downstream stations and from 7 psu to 0 psu at the upstream stations.

In general, the model was able to reproduce both the surface and bottom salinity at all stations very well in the LPR except for a few occasions at M1, M2 and M3 at the bottom. At times, the observed salinity at the bottom at those stations shows little or no tidal fluctuations. For example, at M2, the observed salinity between days 4 and 14, and between days 22 and 26 shows not as much tidal fluctuations as observed at other period. Similar pattern is visible at M3 between days 4 and 7. Field crew noted that, during the field survey, many bottom sensors were retrieved with being covered with mud or foreign objects such as plastic bags (Bob Chant, personal communication). The computed temporal variations in surface salinity, as well as vertical stratification due to tidal movement of water, are in good agreement with the observations. In particular, the model reproduced changes in salinity associated with the high freshwater inflow events that occurred on days 8, 18 and 28. In response to freshwater flow, both the timing and magnitude of salinity fluctuations were accurately represented by the model. At station M5 and Bridge St. Bridge, the most upstream locations of the survey where not many data were available, the computed salinities agree reasonably well with the observed data. The extent of the salt intrusion into the LPR was well represented by the model. This suggests that the physical configuration (geometry) of the LPR is adequately addressed, and hydrodynamic transport and mixing characteristics are well resolved in the model.

3.3 STATISICAL ANALYSIS

Statistical analyses were performed in order to assess the model performance in terms of model/data comparisons. The model computed values of temperature, salinity, velocity and elevation were compared against the observations at several locations.

The statistical parameters considered included the root mean square error (RMSE), the relative RMSE, and the correlation coefficient. The RMSE, a measure of the error between the model and observed data, can be expressed mathematically as:

$$RMSE = \sqrt{\frac{\sum (C_{OBS_i} - C_{MODEL_i})^2}{n}}$$

where C_{OBS} is the observed variable, C_{MODEL} is model calculated variable, and n is number of paired variables. The relative RMSE (percent) is defined as the RMSE divided by the data range and measures the model performance in terms of reproducing the observations accounting for the variability in the observations. The correlation coefficient measures the strength of the linear association between the predicted and actual values.

3.3.1 Tidal Elevations

Table 3-1 highlights the results of the statistical analysis for tidal elevations at three tidal gauge stations (M5, M3 and M1) in terms of the above mentioned parameters. The tidal elevation data were compared with the model results for the period of one month, starting September 2004. The number of data points used in the statistical analysis, based on the data, along with the statistical parameters are presented in the table.

For the three stations, the mean RMSE and the mean correlation coefficient are 0.22 m (0.72 ft.) and 0.93, respectively. It is to be noted that the model performance, in terms of reproducing the tidal elevations, is better at M5 and M1 as compared to M3. The average relative RMSE is 8.3 percent.

The results of the statistical correlation analysis in the form of scatter plots are presented in Figure 3-8. As can be observed, the model and data values seem to be closely correlated. Most of the point comparisons lie within close proximity to the one-to-one line in the plot, emphasizing the fact that the model predicted values are in close agreement with the data measurements.

Table 3-1. Statistical Evaluation of Model Performance for Water Elevation

Station	No. Data Pairs	Data Range (m)	RMSE (m)	Relative RMSE (percent)	Correlation Coefficient (R^2)
Upper Tidal Gauge (M5)	3887	2.66	0.22	8.2	0.94
Middle Tidal Gauge (M3)	1296	2.69	0.26	9.7	0.84
Lower Tidal Gauge (M1)	3456	2.55	0.18	7.1	0.96

Table 3-2 compares results of harmonic analyses of computed and observed water surface elevations at the tidal gauge stations. The amplitudes and phases of four major tidal constituents, the principle lunar (M_2) and solar (S_2) semi-diurnal components and luni-solar (K_1) and principle lunar(O_1) diurnal components, are presented in the table. The dominant tidal constituent is M_2, with observed amplitude varying from 0.80 m (2.62 ft.) at the M5 tide gauge to 0.72 m (2.36 ft.) at the M1 gauge. For the M_2 tide, the maximum error in amplitude is about 0.06 m (0.2 ft.), and the maximum phase error is about 2º (4 minutes). Among all four tidal constituents, amplitude errors never exceed 0.06 m (0.2 ft.), while phase errors are always less than 1 hour.

For the semi-diurnal components M_2 and S_2, the comparison between observed and calculated phase shows the maximum phase error not exceeding 7° (or 15 minutes). In several instances, the calculated phase error is less than 2° (or 5 minutes) for M_2, signifying the robustness of the model in capturing the dominant tidal components. In general, the harmonic analysis shows that the model reproduces the observed water surface elevations at the M5 and M1 tide gauges better than it does at the M3 tide gauge, which is consistent with the results from the previous statistical analysis.

The results of harmonic analysis obtained in this study compare well with the results of the earlier NY Harbor Study (Blumberg et. al., 1999), where the M2 amplitude differences are less than 10 cm (3.9 inch) and phase differences are less than 15° (or 30 minutes).

Table 3-2. Comparison of Harmonic Constants for Water Elevation

M_2 Component

Station	Observed		Calculated	
	Amp (m)	**Phase (deg)**	**Amp (m)**	**Phase (deg)**
Upper Tide Gauge (M5)	0.80	243	0.76	242
Middle Tide Gauge (M3)	0.80	241	0.74	239
Lower Tide Gauge (M1)	0.72	236	0.66	234

S_2 Component

Station	Observed		Calculated	
	Amp (m)	**Phase (deg)**	**Amp (m)**	**Phase (deg)**
Upper Tide Gauge (M5)	0.20	264	0.18	271
Middle Tide Gauge (M3)	0.20	261	0.18	268
Lower Tide Gauge (M1)	0.17	257	0.16	257

K_1 Component

Station	Observed		Calculated	
	Amp (m)	Phase (deg)	Amp (m)	Phase (deg)
Upper Tide Gauge (M5)	0.09	120	0.05	101
Middle Tide Gauge (M3)	0.08	116	0.05	99
Lower Tide Gauge (M1)	0.09	113	0.05	98

O_1 Component

Station	Observed		Calculated	
	Amp (m)	Phase (deg)	Amp (m)	Phase (deg)
Upper Tide Gauge (M5)	0.05	105	0.05	97
Middle Tide Gauge (M3)	0.06	97	0.05	96
Lower Tide Gauge (M1)	0.05	94	0.04	88

3.3.2 Current Velocities

The model predicted velocity values were compared with the current velocity measurements to provide another measure of model performance. The velocity data were available at two different locations at several depths.

The statistical analyses for current velocities are illustrated in Table 3-3. The model output was extracted at three depth levels, and a comparison between the model and data values was performed. The resulting RMSEs, relative RMSEs, and correlation coefficients are presented in Table 3-3. As can be seen in the table, the RMSEs vary from 0.15 m/s (0.49 fps) to 0.23 m/s (0.75 fps), with a mean of 0.19 m/s (0.62 fps), and relative RMSEs vary from 8.5 percent to 13.1 percent, with a mean of 11.3 percent. The correlation coefficient ranges from 0.74 to 0.87. The table indicates that the downstream station (M2) has relatively smaller RMSEs and relative RMSEs, and higher correlation coefficients as compared to the upstream station (M3). The RMSE values also demonstrate that the model performs better in simulating the current velocities at the bottom as compared to mid-depth or surface; however, the model and data values seem to be better correlated at the surface than at the bottom or mid-depth. The statistical analysis of currents obtained in this study compare well with the results of the earlier New York Harbor (NYH) study (Blumberg et. al., 1999), where the RMSE on the current meters deployed in the East River varied between 0.15 m/s (0.49 fps) and 0.43 m/s (1.41 fps). The correlation coefficients of current velocities in the NYH study were above 0.95.

Table 3-3. Statistical Evaluation of Model Performance for Current Velocity

Station	No	Data Range (m/s)	RMSE (m/s)	Relative RMSE (percent)	Correlation Coefficient (R^2)
M3					
Surface(5.5m)	648	1.68	0.22	13.1	0.86
Mid-depth(2.5m)	648	1.69	0.22	13.0	0.81
Bottom(0.5m)	648	1.63	0.18	11.0	0.74
M2					
Surface(3.62m)	1436	2.06	0.23	11.2	0.87
Mid-depth(2.12m)	2141	1.99	0.17	8.5	0.86
Bottom(0.37m)	2112	1.39	0.15	10.8	0.81

The results of the statistical correlation analysis at different depth levels for both the stations have been presented in the form of scatter plots in Figure 3-9. As can be observed, the model and data values are fairly well correlated. Most of the points are well distributed around the one-to-one line in the plot, emphasizing the fact that the model predicted values are in good correspondence with the data measurements.

3.3.3 Temperature and Salinity

The model was calibrated by comparing model results to temperature measured by sensors collected at six locations in the region during the month of September 2004. Table 3-4 presents the statistical evaluation of model performance in terms of RMSE, relative RSME and correlation coefficient between computed and observed water temperature at surface and bottom. The RMSE in water temperature predictions varies from 1.6 ºC to 5.0 ºC, with relative RMSE varying from 9.3 percent to 31.3 percent. In general, the model does a better job simulating the surface temperatures, and the model predictions at the downstream stations are better than the upstream stations. Figure 3-10 shows the statistical correlation between the model and data values. The model and data values seem to be relatively well correlated to each other at the downstream stations (M1, M2, and M3) but at some times significantly deviate from the one-to-one correlation line at the upstream stations (Bridge St. Bridge and M4). This is likely due to uncertainties in the freshwater temperature specified in the model, which has been discussed in the previous section.

Table 3-4. Statistical Evaluation of Model Performance for Temperature

Station	No. of Data	Data Range (°C)	RMSE (°C)	Relative RMSE (percent)	Correlation Coefficient (R^2)
BSB					
Surface	335	5.1	1.6	31.3	0.50
Bottom	338	7.8	1.6	20.7	0.39

Station	No. of Data	Data Range (°C)	RMSE (°C)	Relative RMSE (percent)	Correlation Coefficient (R^2)
M5					
Surface	No data				
Bottom	35	3	0.5	15.0	0.85
M4					
Surface	623	8.1	1.2	14.5	0.73
Bottom	338	7.8	1.4	18.1	0.53
M3					
Surface	359	3.6	0.7	18.5	0.62
Bottom	359	3.8	0.7	19.1	0.64
M2					
Surface	695	7.8	1.0	12.3	0.81
Bottom	695	7.8	1.0	13.1	0.81
M1					
Surface	695	7.9	0.7	9.3	0.87
Bottom	198	5.3	0.7	12.7	0.87

Comparisons between the model predicted and measured salinity values were made at six locations in the study area for the month of September, 2004. Table 3-5 presents the statistical evaluation of model performance in terms of RMSE, relative RSME and correlation coefficient between computed and observed salinity at surface and bottom. The RMSE in salinity predictions varies from 1.1 psu to 4.6 psu, while the relative RMSE varies from 13.1 percent to 38.4 percent. Similar to the behavior of model predicted temperature, it can be noticed that the model does a better job simulating the surface salinity as compared to the bottom salinity due to reasons as noted in Section 3.2.3. Figure 3-11 shows the statistical correlation between the model and data values. The figure indicates that model-data correlation is better at surface than at bottom where the observed salinity is generally higher than computed (see Figure 3-7). Bridge St. Station

is located in the low salinity regime in the river. Therefore, small differences in the computed versus observed salinities, which are small themselves, can contribute to low correlations. In addition, it can be observed that there are small phase shifts in the computed and observed peaks in salinity, which also contributes to the low correlation coefficients.

Table 3-5. Statistical Evaluation of Model Performance for Salinity

No	Station	No. of Data	Data Range (psu)	RMSE (psu)	Rel. RMSE (percent)	Correlation Coefficient (R^2)
1	BS					
	Surface	318	6.4	1.1	17.1	0.46
	Bottom	36	9.7	3.0	30.7	0.30
2	M5					
	Surface	No data	-	-	-	-
	Bottom	35	4.5	1.6	34.8	0.53
3	M4					
	Surface	605	12.1	1.6	13.5	0.73
	Bottom	36	9.7	3.7	38.4	0.40
4	M3					
	Surface	366	12.5	2.2	17.3	0.68
	Bottom	360	16.0	5.3	33.1	0.51
5	M2					
	Surface	677	16.5	2.5	15.2	0.77
	Bottom	695	16.2	4.6	28.5	0.47
6	M1					
	Surface	677	17.1	2.2	13.1	0.77
	Bottom	198	18.7	3.1	16.7	0.45

4 HYDRODYNAMIC MODEL VALIDATION: HURRICANE DONNA

Hurricane Donna, which passed over the NY/NJ-area on September 12, 1960, is one of the largest storms ever to hit the region[1]. The hurricane produced extensive coastal flooding in Florida, North Carolina, and many states along the eastern Atlantic seaboard before the eye of the hurricane passed over the eastern end of Long Island. Harris (1963) described the characteristics of hurricane storm surges from 1928 through 1961 and included discussion on storm surge elevations in the NY/NJ region that were recorded during Hurricane Donna. In many parts of NY/NJ Harbor, the arrival of the peak surge coincided with the normal high tide for the day (Harris, 1963). NOAA tidal stations in the NY/NJ region report the historical maximum water elevation as being attributable to Hurricane Donna. Both the NOAA Battery and Sandy Hook stations recorded a storm surge of 2.56 m (8.40 ft.) (NGVD29) during the hurricane.

To validate the hydrodynamic model using the passage of Hurricane Donna, a model simulation was performed using the water surface elevations observed at the NOAA Battery station at both open boundaries in the Kills and the USGS stream gauge data measured at Little Falls (Figure 4-1). Physical conditions of the Lower Passaic River and land elevations were assumed the same as the calibration runs. While the surge elevation was one of the highest on record, the river inflow rates during the Hurricane were about 5,000 cfs, which is approximately the 1.25 year return flow rate for the station. This suggests that no significant rainfall events in the upland portion of the LPR drainage basin were associated with the passage of the Hurricane.

The model results show that the maximum surge elevations during Hurricane Donna are in good agreement with the observed data within the LPR (Figure 4-2). The maximum

[1] The modeling analyses presented in this appendix were performed before the occurrence of Superstorm Sandy in August 2011.

water elevation rises to 2.6 m (8.53 ft.) up to RM7 and then increases further upstream. The computed water elevation, 2.93 m (9.61 ft.), at RM12 matches very well with the observed elevation. As shown in Figure 4-3, the model computed flooded areas in the LPR basin during Hurricane Donna are estimated to be approximately about 1,018 acres. However, there are no data available to compare to the modeled flooding areas.

5 SEDIMENT TRANSPORT ANALYSIS OF CAP STABILITY AND EROSION FOR THE LOWER PASSAIC RIVER

5.1 INTRODUCTION

As part of the FFS, USEPA is evaluating (among other options) the placement of a sand cap as part of two remedial alternatives to address the contaminated sediments of the FFS Study Area. The stability and erosion of the proposed sand cap in the remedial alternatives were examined using a hydrodynamic and sediment transport model and sediment grain size analyses. Descriptions of the physical setting of the river, elements of cap design, and other aspects of the overall study are presented in the FFS.

5.2 SEDIMENT MODEL FRAMEWORK

Descriptions of the model framework, the grid, and model set-up and parameterization for cap stability and erosion analyses follow.

5.2.1 Model Description and Governing Equations

For the LPR cap stability and erosion analysis, an existing, peer-reviewed sediment transport bed model (SEDZLJ) (Jones and Lick, 2001) was incorporated into HydroQual's hydrodynamic and sediment transport model framework, ECOMSED (HydroQual, 2004). SEDZLJ uses measured erosion rates for sands obtained from the literature (Roberts et al., 1998) as the basis for computing sediment transport. The incorporation of SEDZLJ into ECOMSED was performed by Dr. Craig Jones (developer of the SEDZLJ computer code) of Sea Engineering, Inc. (SEI). The resulting computer code is called ECOM-SEDZLJS and was peer-reviewed by Dr. Earl Hayter of the USEPA (at the time of the review, now with USACE-ERDC). In the application of the model to the capping evaluation, transport of only sand-sized particles were simulated. Transport of fine-grained cohesive sediments was not included in the analysis.

The integration of SEDZLJ sediment transport routines into ECOMSED and other related code modifications provided four primary benefits needed to fulfill project goals:

1. Computation of erosion fluxes as a function of measured erosion rates,
2. Division of total erosion fluxes into bedload and suspended load components,
3. Simulation of bedload transport, and
4. Simulation of a user-defined number of particle size classes.

ECOM-SEDZLJS provides the ability to simulate the expected differential transport of sediments and cap materials comprised of particles with a continuum of grain sizes and subject to significant bedload transport.

The governing equations for hydrodynamics, following a system of orthogonal cartesian coordinates (*X*, *Y*, *Z*) and using the hydrostatic pressure assumption (*i.e.*, the weight of the fluid identically balances the pressure) and the Boussinesq approximation (*i.e.*, density differences are negligible unless the differences are multiplied by gravity), are:

Conservation of Mass (Continuity Equation)

$$\nabla \cdot \vec{V} + \frac{\partial W}{\partial Z} = 0 \tag{5-1}$$

Conservation of Momentum (Reynolds Momentum Equations)

$$\frac{\partial U}{\partial t} + \vec{V} \cdot \nabla U + W \frac{\partial U}{\partial Z} - fV = -\frac{1}{\rho_0}\frac{\partial P}{\partial X} + \frac{\partial}{\partial Z}\left(K_M \frac{\partial U}{\partial Z}\right) + F_X \tag{5-2}$$

$$\frac{\partial V}{\partial t} + \vec{U} \cdot \nabla V + W \frac{\partial V}{\partial Z} + fU = -\frac{1}{\rho_0}\frac{\partial P}{\partial Y} + \frac{\partial}{\partial Z}\left(K_M \frac{\partial V}{\partial Z}\right) + F_Y \tag{5-3}$$

$$\rho g = -\frac{\partial P}{\partial Z} \tag{5-4}$$

where: t = time, $\vec{V}$ = horizontal vector operator with velocity components U and V; ∇ = horizontal gradient operator; U, V, W = velocities in the X-, Y-, and Z-direction,

respectively; f = Coriolis parameter; ρ, ρ_0 = potential and reference density of the fluid; P = pressure; g = gravitational acceleration; K_M = vertical eddy diffusivity of turbulent momentum mixing; and F_X, F_Y = horizontal diffusion in the X- and Y-direction, respectively.

The horizontal diffusion terms represent small (sub-grid) scale processes not directly resolved by the model grid and are expressed in a form analogous to molecular diffusion:

$$F_X = \frac{\partial}{\partial X}\left(2A_M \frac{\partial U}{\partial X}\right) + \frac{\partial}{\partial Y}\left[A_M\left(\frac{\partial U}{\partial Y} + \frac{\partial V}{\partial X}\right)\right] \quad (5\text{-}5)$$

$$F_Y = \frac{\partial}{\partial Y}\left(2A_M \frac{\partial V}{\partial Y}\right) + \frac{\partial}{\partial X}\left[A_M\left(\frac{\partial U}{\partial Y} + \frac{\partial V}{\partial X}\right)\right] \quad (5\text{-}6)$$

where: AM = horizontal diffusivity.

These equations are transformed for use in a curvilinear, orthogonal, sigma (σ)-level coordinate system as described by HydroQual (2004).

The governing equations for erosion in SEDZLJ (Jones and Lick, 2001) are:

Erosion Rate

$$E\left(\tau^b\right) = \left(\frac{\tau_{m+1} - \tau^b}{\tau_{m+1} - \tau_m}\right)E_m + \left(\frac{\tau^b - \tau_m}{\tau_{m+1} - \tau_m}\right)E_{m+1} \quad (5\text{-}7)$$

$$\ln E(T) = \left(\frac{T_0 - T}{T_0}\right)\ln E^{L+1} + \left(\frac{T}{T_0}\right)\ln E^{L} \quad (5\text{-}8)$$

where: $E(\tau^b)$ = erosion rate as a function of shear stress (τ); τ^b = bottom shear stress; τ_m = shear stress less than τ^b; τ_{m+1} = shear stress greater than τ^b; E_m and E_{m+1} denote erosion rates at τ_m and at τ_{m+1}, respectively ; $E(T)$ = erosion rate as a function of depth in the sediment bed; T = sediment layer thickness; T_0 = initial sediment layer thickness; and the superscript L and $L+1$ denote depths in the sediment profile at the upper and low

limits of the eroding sediment layer. Equations 5-7 and 5-8 can be combined to express the erosion rate as a function of both shear stress and depth. The onset of erosion is identified as the critical shear stress for erosion, τ_{ce}, and is defined as the shear stress at which erosion is initiated at a rate of 10^{-4} cm/s (~0.0004 inch/s).

When the shear stress acting on grains comprising the bed exceeds the critical shear stress for a given grain size, particles may be transported as bedload (in a thin layer in contact with the bed) or as suspended load (fully entrained in the water column away from the bed). The governing equations used to fractionate eroded sediments into bedload and suspended load are:

Non-Cohesive Bedload vs. Suspended Load Fractionation

$$\tau_{cs} = \begin{cases} \frac{1}{\rho_w}\left(\frac{4w_s}{d_*}\right)^2 & for\ d \le 400\,\mu m \\ \frac{1}{\rho_w}(4w_s)^2 & for\ d > 400\,\mu m \end{cases} \quad (5\text{-}9)$$

$$f_{SL} = \begin{cases} 0 & for\ \tau^b \le \tau_{ce} \\ \frac{\ln(u_*/w_s) - \ln\left(\sqrt{\tau_{cs}/\rho_w}/w_s\right)}{\ln(4) - \ln\left(\sqrt{\tau_{cs}/\rho_w}/w_s\right)} & for\ \tau^b > \tau_{cs} \\ 1 & for\ \frac{u_*}{w_s} \le \tau_{cs} \end{cases} \quad (5\text{-}10)$$

where: τ_{cs} = critical shear stress for transport as suspended load; ρ_w is density of water; w_s = particle fall velocity; d_* = particle dimensionless diameter = $d\left[(\rho_s - 1)g/\nu^2\right]$; ν = kinematic viscosity; ρ_s = particle density; f_{SL} = fraction of the total amount eroded that is transported as suspended load; and u_* = shear velocity. The fraction transported as bedload = (1-f_{SL}). Equations 5-9 and 5-10 can be used in conjunction with the particle grain size distribution and critical shear stress for erosion to express the erosion flux of

sediment by grain size that is transported by bedload and suspended load as a function of the bottom shear stress.

The bottom shear stress acting on the bed (*i.e,*. the total bed shear stress) is a function of the total hydrodynamic roughness and can be expressed in terms of two separate components: (1) form roughness; and (2) grain roughness (*i.e.*, skin friction). Individual grains on the surface of the sediment bed are subjected only to the skin friction component of the total bed shear stress. The total bed shear stress is computed from the near-bed hydrodynamic velocities according to the "log law" velocity profile:

$$u(z_b) = \frac{u_{*T}}{\kappa} \ln\left(\frac{z_b}{z_0}\right) \tag{5-11}$$

$$\tau_T = \rho u_{*T}{}^2 = \rho C_d \, u(z_b)^2 \tag{5-12}$$

$$C_d = \left(\frac{\kappa}{\ln \frac{z_b}{z_0}}\right)^2 \tag{5-13}$$

where: $u(z_b)$ = near-bed flow velocity, u_{*T} = near-bed shear (friction) velocity; κ = von Karman constant = 0.4, z_b = height of the near-bed layer above the bed surface; z_0 = bed roughness height; τ_T = total bed shear stress; ρ = density of the fluid; and C_d = coefficient of drag. In the sigma layer coordinate system of the hydrodynamic model, z_b is height above the bed at the mid-point of the bottom sigma layer.

The shear stress component associated with skin friction can be computed as a function of the total bed shear stress as follows (Grant and Madsen, 1982; Glenn and Grant, 1987):

$$u_{*S} = u_{*T}\left(\frac{\ln\frac{z_b}{z_0}}{\ln\frac{z_b}{z_{0S}}}\right) \quad (5\text{-}14)$$

$$\tau_S = \rho u_{*S}^{\ 2} \quad (5\text{-}15)$$

where: u_{*S} = the near-bed shear velocity attributable to skin friction; z_{OS}= the roughness height of particles comprising the bed surface; and τ_S = the skin friction shear stress.

As part of the model development process, SEI and HydroQual verified that the SEDZLJ code was properly implemented in ECOMSED by simulating and successfully reproducing the laboratory results of Little and Mayer (1972). The results of these numerical tests are presented in Attachment A. As an additional quality assurance measure, simulations were also conducted using a truncated curvilinear grid for the LPR from RM0 to RM12 to ensure that the enhanced transport computations within ECOM-SEDZLJS code properly conserved mass. These tests both indicated that the model code functions properly.

5.2.2 Model Set-up and Parameterization

The full model grid for the cap erosion study is shown in Figures 2-1 and 2-2. For reference, land surface elevations relative to the National Geodetic Vertical Datum (NGVD) 1929 are also shown in Figure 2-3. Although the focus of the cap erosion study is the LPR, the full grid includes the Hackensack River and Newark Bay as needed to account for tides and other flow conditions that impact the river. Model depths for the river were based on surveys compiled by the USACE as described in Section 2. The model accounts for the wetting and drying of grid cells as needed to account for changing water surface elevations that occur as a result of fluctuating tidal conditions. This is a necessary aspect of model formulation because there are several shallow locations in the

Lower Passaic River where grid cells representing portions of the river bed can become exposed (*i.e.*, dry) during low points in the tidal cycle.

The computational domain consists of 68×170 grid cells in the horizontal plane and 11 equally spaced σ-levels in the vertical plane (*i.e.*, 10 vertical segments). The model open boundaries are located at the entrance to Kill van Kull from New York Harbor and the entrance to Arthur Kill from Raritan Bay at South Amboy. Refer to Section 2 for additional details on model grid development.

It is important to note that boat wake and wind-induced waves were not considered in this analysis. With respect to boat wakes, Dr. Craig Jones (personal communication) suggested that boat wake or propeller wash effects would largely act to "mix" the capping material locally, since it would be unlikely that a boat (or boats) would follow the exact same path within the river time after time. With respect to wind-induced waves, due to the narrowness of the river and due to the meandering nature of the river it is unlikely that significant wind-waves could develop.

5.2.3 Development of Return Flows and Associated Hydrographs

Simulations were conducted to explore the stability and erosion of a sand cap in response to flow events of different magnitude. For these analyses, Passaic River flow records from the USGS Little Falls gauging station for the period 1891 through 2005 were analyzed to determine return flows, including flood conditions, of different recurrence intervals. The measured freshwater inflow rates for each flow event account only for the flow measured at Little Falls. The drainage area above Little Falls (762 square miles) accounts for 81 percent of the total Passaic River basin (935 square miles). The remaining 19 percent of the drainage area includes the area between Little Falls and Dundee Dam (43 square miles), the drainage area of the Saddle River (55 square miles at Lodi), which enters the Lower Passaic River just downstream of Dundee Dam and smaller tributaries and direct runoff to the LPR. For this study, total basin flows were specified as inputs at Dundee Dam (RM17) to simplify model set-up. The total flow rates

assigned at Dundee Dam were estimated by increasing the flows from Little Falls by the ratio of the total drainage area of the Passaic River Basin to the gauged drainage area. This is a reasonable approach since nearly all of the remaining tributary inputs to the river (Saddle River, Third River, etc.) occur near or above the upstream limit of the cap area, and direct drainage is expected to be small. This also represents a worst case for the stability analysis because the entire flow through the system occurs along the entire length of the capped area.

The return flows used for this study, based on a statistical analysis (log – normal recurrence interval) of daily flow data, are summarized in Table 5-1. Further details of the return flow analysis are provided in Section 6.1.1 of this memorandum. The one-month, six-month and one-year return flows were estimated separately. For flows with longer return periods, this was accomplished by analyzing probability of occurrence using the 107 years (1897 to 2003) of annual maximum flows at Little Falls. The one-month return flow of 5960 cfs was estimated as the 96.7^{th} percentile of the daily flows. The six-month return flow was estimated as the 41.7^{th} percentile and the one-year return flow as the 91.7^{th} percentile of the monthly maximum flows, which yielded 5,840, and 8,050 cfs, respectively, when corrected for the below Little Falls drainage area.

Table 5-1. Lower Passaic River Return Flows for Cap Stability and Erosion Analysis

Return Period	***Flow (cfs)***	
	Little Falls	*River Mouth*
1-month	3,900	5,060
6-month	4,500	5,840
1-year	6,200	8,050
2-year	6,751	8,767
5-year	9,968	12,945
10-year	12,219	15,869
25-year	15,280	19,844
50-year	17,465	22,681
100-year	19,808	25,725

Synthetic hydrographs for each of the Lower Passaic River return flows listed in Table 5-1 were developed by review of observed high flow hydrographs between 1897 and 2003 at the USGS Little Falls gauging station (Figure 6-1). These Little Falls hydrographs were reviewed to determine their shape (*i.e.*, rising and falling limbs) and duration. Most of high flow events recorded at the Little Falls station were less than five days in duration. The high flow event observed in April 1984, with a peak flow of 18,400 cfs, was selected for this study. This is the highest flow event recorded at Little Falls in recent decades and reflects the latest land use characteristics in the upper Passaic River basin, *i.e.* upstream of Dundee Dam. For model simulations, the peak of the flow event was coupled with the peak spring tide at the open boundaries, based on astronomical harmonic tidal constituents obtained from NOAA. Hydrographs for each return flow listed in Table 5-1 were constructed by scaling the April 1984 flow curve by the ratio of return flows. The constructed hydrographs for the Lower Passaic River return flows all have the same shape and consist of the following: ramp-up from a zero initial velocity condition (days 1-2), rising limb (days 3-5), peak (day 5), and falling limb (days 5-10) (Figure 5-1).

5.2.4 Description of Capping Materials

The erosion potential of two types of sands were evaluated as cap materials: (1) Ambrose Sand (AS) [median particle size (d_{50}) = 386 μm (~0.015 inch)]; and (2) Upland Borrow Sand (UBS) (d_{50} = 2,057 μm (~0.081 inch)). Grain size distributions for these materials and corresponding particle size classes used in ECOM-SEDZLJS are presented in Table 5-2. To best represent the spectrum of particles comprising the capping sands in the model, AS was simulated as four size classes and UBS was simulated as six size classes. The armor stone (*i.e.,* 6-inch angular rock) was considered to be non-erodible under the flow conditions simulated. All design aspects of cap placement, cap thickness, the types of sand evaluated, and sizing of armor stone are specified in the FFS.

Erosion characteristics (τ_{ce}) for sands were determined based on the measurements of Roberts et al. (1998). Fall velocities (w_s) for each particle type simulated were

determined from the formula of Cheng (1997). Similarly, the critical shear stress for transport as suspended load (τ_{cs}) was determined from fall velocity and particle diameter following the method of van Rijn (1984). A summary of these parameters is also presented in Table 5-2.

Table 5-2. Characteristics of Capping Materials

Property	*Size Class*					
	1	2	3	4	5	6
Ambrose Sand						
d_p (μm)	125	222	1,020	3,360	N/A	N/A
Composition By Weight (%)	10	80	6	4	N/A	N/A
τ_{ce} (dynes/cm^2)	1.2	1.7	5.4	25	N/A	N/A
w_s (cm/s)	0.9	2.3	11.3	25	N/A	N/A
τ_{cs} (dynes/cm^2)	1.2	2.4	16.8	81	N/A	N/A
Upland Borrow Sand						
d_p (μm)	150	300	1180	2360	4750	12,500
Composition By Weight (%)	4	22	32	32	5	5
τ_{ce} (dynes/cm^2)	1.4	2.0	6.4	15.6	38.4	111.2
w_s (cm/s)	1.2	3.4	12.6	20.0	30.0	50.4
τ_{cs} (dynes/cm^2)	1.4	2.9	20.1	53.4	120.3	343.5

For each size class simulated, the particle diameter given is the mean particle diameter of the grains in that class. As a rule of thumb, the largest size class is chosen as the size for which more than 2-3 percent of the mass is retained on a sieve. Similarly, the smallest size class can be chosen as the size for which 2-3 percent of the mass is retained on the smallest sand-sized sieve. For AS, the grain size distribution is comparatively narrow with 80 percent of the distribution having a mean particle diameter of 222 μm (0.009 inch), and the entire distribution could be represented with four size classes. For the UBS, the size distribution was less well sorted, with up to 5 percent of the distribution having a mean particle diameter of 12,500 μm (0.492 inch). Consequently, the UBS was

represented as six size classes. Additionally, since a wider size range occurs in the UBS, the additional size classes are needed to more accurately simulate the expected coarsening of the bed that would occur over time.

The hydrodynamic model calibration effort included a sensitivity analysis for several model parameters, including the effective bottom roughness, Z_0. Model-data comparisons were evaluated for a range of Z_0 values between 0.0001 (0.004 in.) to 0.003m (0.12 in.). For the calibration conditions, virtually identical model-data comparisons were achieved with Z_0 values ranging from the calibration value of 0.001m (0.04 in.) down to 0.0004m (0.16 in.). For the extreme flood conditions (e.g. 100- and 500-year flows) varying the value of Z_0 within this range produced differences in bottom water velocity and bottom shear stress. In order to be conservative the cap stability evaluations described below were conducted with a Z_0 value of 0.0004 m (0.16 in.), which results in more cap erosion than is computed with the Z_0 value of 0.001 m (0.04 in.). To represent the expected additional roughness and flow resistance caused by large, 6-inch angular stone, the bottom roughness height in armored areas (on a cell by cell basis in the model) was increased by a factor of 25 (Z_0 = 0.01 m (0.4 in.)). Further details of the selection of roughness length for armor stone are discussed in Section 6.4.2. Armored cells were assumed to be non-erodible.

5.2.5 Description of Modeling Scenarios and Determination of Armor Placement

The stability of AS sand as a capping material for the Lower Passaic River was evaluated for modeling scenario 1 (8-Mile Cap); however, this material was found to be unsuitable (see section 5.3.1) and was not evaluated further. Three additional scenarios were developed (model scenarios 2 through 4 below) and were evaluated using the coarser-grained UBS sand as a capping material:

1. 8-Mile Cap: This scenario included the placement of a two-foot thick AS sand cap across the entire bed of the FFS Study Area from RM0 to RM8.3. In this scenario, the placement of the cap on the bed reduces river depths (increases bed

elevations) by two feet throughout the capped area. Therefore, post-remediation depths would be two feet shallower than pre-remediation bathymetry.

2. Capping with Armor Area Pre-Dredging: This scenario included the placement of a UBS sand cap as described in the above scenario, and the placement of armor stone on selected model grid cells to protect the cap and reduce the potential for erosion. In this scenario, it was assumed that pre-dredging would be conducted in armored areas such that bed elevations in these areas would be reduced by the specified thickness of the armor layer prior to armor placement. As such, bed elevations after armoring would be no greater than for the sand cap alone, and post-remediation depths would be two feet shallower than pre-remediation bathymetry.

3. Capping with Dredging for Flooding - Exposed Armor Areas: This scenario includes the placement of the UBS sand cap and armor as described in the above scenario (2). However, in this scenario, all model grid cells from RM0 to RM8.3 were pre-dredged such that post-remediation depths were equal to pre-remediation bathymetry. In this case, two feet of pre-dredging would be incorporated for cells in which the sand cap was placed, and four feet of pre-dredging would be performed for cells where both sand and armor were placed.

4. Capping with Dredging for Flooding – Smoothing Layer: For this scenario, with the same depth condition as the above "Capping with Dredging for Flooding – Exposed Armor Areas" scenario, all armored areas were covered with a one-foot UBS sand "smoothing layer". Those areas requiring armor would be dredged a total of five feet and a one-foot "smoothing layer" sand layer would be used to cover the armor surface to reduce the higher surface friction associated with 6-inch armor stone and mitigate any additional flooding the increased surface friction of the armor stone may have caused.

Scenarios (2), (3), and (4) incorporated the placement of armor in selected model grid cells to prevent erosion of the underlying sand cap. The grid cells, in which armor stone was placed, were selected through an iterative modeling process. An initial modeling run was conducted in which no armor was included, and the predicted erosion in each grid cell was calculated. A 3 inch (7.62 cm) erosion criterion was used to determine armor placement; that is, any grid cell that experienced more than 3 inch of maximum erosion during the initial modeling run was selected to be armored in the next modeling run. For each iteration, HydroQual provided the maximum erosion values for each grid cell to Malcolm Pirnie, Inc. (MPI) (main contractor for the FFS at the time of this study, now Louis Berger Group). Then, MPI identified the grid cells to be armored based on the 3 inch (7.62 cm) erosion criterion described above, and a new simulation was conducted with the adjusted armor layout. This procedure was repeated until no sand capped cells were found to experience more than 3 inch (7.62 cm) of maximum erosion, at which time the development of the armor layout for the modeled scenario was completed. For these armoring simulations, 39 individual cells on the model grid were armored for scenario (2) ("Capping with Armor Area Pre-dredging") and 14 cells were armored for scenario (3) and (4) ("Capping with Dredging for Flooding"). The final armor layouts for the modeled capping scenarios are presented in Figure 5-2. Only two layouts are presented in the figure, as scenario 3 ("Capping with Dredging for Flooding – Exposed Armor Areas") and scenario 4 ("Capping with Dredging for Flooding – Smoothing Layer") used identical armoring layouts.

For scenario (1), 10-day simulations were conducted for the 1-year, 25-year and 100-year return flow events when modeling the AS capping material. When modeling the UBS capping material, 10-day simulations were conducted for scenarios (2)-(4) under the 100-year return flow event identified in Table 5-1.

5.3 Model Application and Results

Computer simulations of hydrodynamics and cap sand sediment transport for the LPR were performed. Simulations were conducted across a range of flow events for

combinations of sand cap materials, armor stone, and channel depth conditions. Results of the ECOM-SEDZLJS model application to the study area are described below.

5.3.1 Cap Stability and Erosion Analysis: Ambrose Channel Sand

ECOM-SEDZLJS was used to examine the response of sands taken from the Ambrose Channel, located at just outside the mouth of New York/New Jersey Harbor, and placed on the river bed. The model was set to run four non-cohesive particle size classes as defined in Table 5-2. Ten-day simulations were set up and conducted for three return flow events (1-, 25- and 100-year) with 2-feet sand cap under the "8-Mile Cap" scenario. Results for all simulations were summarized for the river bed from RM0 to RM8.3 in terms of the cross-river averaged net bed elevation change at the end of the simulation, the maximum bed erosion computed during the simulation period, and maximum bottom shear stress. The results are presented in Figure 5-3. Bottom shear stresses discussed in this section refer to the "skin friction" component of the total bottom shear stress. Results for each of the three individual events, showing net bed elevation change, the maximum bed erosion, and maximum bottom shear stress for each model cell are presented in Attachment B. (In this sequence of figures in Attachment B, blue shaded areas indicate net deposition while red shaded areas indicate net erosion.) Figures 5-4a and 5-4b display the horizontal distributions of the maximum bed erosion for the 1-year and 25-year flow events, respectively. (Maximum bed erosion plots for other flows are presented in Attachment B). It should be noted that in some locations it is possible that bed erosion could occur initially as the smaller sand particle size classes are eroded but later these areas could show a net increase in bed elevation due to the resuspension and relocation of upstream sand particles.

The model results in Figures 5-3 and 5-4 indicate that excessive net erosion and transport of an AS cap can be expected. At some locations along the river, nearly the entire 2-foot (~60 cm) thickness of the cap could be eroded during a 25-year flow event. Around RM5.5, even a 1-year event has the potential to erode approximately 1-foot (~30 cm) of the sand cap.

Bottom shear stresses vary by position along the river as well as with freshwater flow and tidal conditions. Note that the maximum cross-sectionally-averaged bottom shear stress is greater than 40 dynes/cm^2 for the 100-year flow condition (Figure 5-3). This is substantially larger than the critical shear stress for erosion of even the largest particles used in the AS grain size distribution (maximum τ_{ce} = 25 dynes/cm^2).

These results indicate that fine to medium sand capping materials such as AS will not be stable unless substantial areas of the cap are also protected with armor stone. In this case, the extent of erosion was judged to be so severe and so extensive that no further simulations using AS as a cap material were attempted.

5.3.2 Cap Stability and Erosion Analysis: Upland Borrow Sand

ECOM-SEDZLJS was also used to examine the response of UBS placed on the river bed. Ten-day simulations were set up and conducted for the 100-year return flow event with a 2-foot UBS cap under the "Capping with Armor Area Pre-Dredging" and "Capping with Dredging for Flooding – Exposed Armor Areas" scenarios. For each scenario, model simulations were conducted separately for "capping only" and "capping with armoring," providing four sets of results for evaluation. Results for all four simulations were summarized for the river bed from RM0 to RM8.3 in terms of the cross-river averaged net bed elevation change at the end of the simulation, the maximum bed erosion during the simulation, and the bottom shear stress. The summary results are presented in Figure 5-5. The figure indicates that under the "Capping with Dredging for Flooding – Exposed Armor Areas" scenario, maximum erosion at most of the areas except at around RM5.4 is less than 10 cm (4 inches) with the USB cap material, which is substantially less than the maximum erosion values under AS cap material (see Figure 5-3). Under the "Capping with Dredging for Flooding – Exposed Armor Areas" scenario, most of the areas have less than 5 cm (2 inches) of maximum erosion. A maximum erosion of 6 cm (2.4 inches) was computed at around RM3.8 under this scenario. Plan-view results showing net bed

elevation change, maximum bed erosion, and maximum bottom shear stress for each model cell for each of the four simulations are presented in Attachment C.

Because UBS contains an appreciable fraction of very coarse sand and very fine gravel, the UBS cap is subject to less erosion and generally is expected to be more stable than the AS cap. To further illustrate the erosion characteristics of the UBS, 10 representative locations along the river, as identified in Figure 5-6, were examined in more detail. Bed elevation change (BEC), bottom shear stress (BSS), and median grain size (D_{50}) over time are shown for each of these locations in Figures 5-7, 5-8, and 5-9, respectively. The results shown in these figures were obtained from the first iteration of scenarios (2) and (3) with a 2-foot UBS sand cap placed at the river bed. Results for scenario (4) ("Capping with Dredging for Flooding – Smoothing Layer") are identical to scenario (3) so that the results of this scenario will not be presented in the report. Each location was represented by a single grid cell rather than the cross-river averages presented in Figure 5-5. The cells at RM3.11, RM3.62, RM4.00, RM5.54, RM6.15, and RM6.56 are located in the channel, and the cells at RM0.25, RM1.81, RM2.57, and RM4.63 are located in the shoals of the river. The cells in the channel are exposed to higher bottom shear stress and, therefore, higher rates of erosion. The results presented in Figure 5-8 and Attachment C also indicate that in most locations bottom shear stresses typically do not exceed the critical shear stress for erosion of the largest grain size (12,500 μm, τ_{ce} = 111.2 dynes/cm^2) of the USB capping material. However, more than 3 inches (7.62 cm) of erosion can occur at some of the locations in the capped region of the river. Figure 5-9 shows the time history of median grain sizes (D_{50}) at ten locations along the river, which were computed at the active layers. The figure shows that median grain sizes alternate from original value of about 2,000 μm (0.08 in.) during flood and ebb currents to less than 200 μm (0.08 in.) during slack tides until the river inflow reaches its maximum value around day 5. With the passage of the peak flow, the median grain sizes increase to 3,000 μm (0.12 in.) or higher at many locations, which suggests that most of the fine grain size class sands have been eroded from those cells during the high flow and those cells are left with coarser size class sands.

To address areas with more severe erosion [*i.e.*, as specified by the 3-inch erosion criterion discussed in Section 5.2], a further series of simulations was conducted for scenarios (2) and (3) to examine the effectiveness of protective armor stone over the sand cap during 100-year flow condition. Based on a review of the locations subject to three inches or more erosion, areas for armor stone placement and protection were identified using the iterative procedure described in Section 5.2.

5.4 Discussion

The model results indicate that severe erosion is expected for a cap composed of AS. Even under low to moderate flows such as the 1-year return flow event, approximately 20 cm (~8 inches) of the cap could erode in areas that experience high bottom shear stresses. A sequence of smaller events could also lead to significant cap loss over time. This high potential for erosion is a reflection of the small median particle diameter (222 μm (0.009 in.)) and narrow range of grain sizes comprising this material.

In contrast, the UBS is expected to be far more stable under typical flow conditions in the FFS Study Area. Although significant bed erosion may still occur in some areas of the river, the extent of maximum erosion is expected to be much lower than for the AS. This decreased erosion potential is a reflection of the larger median particle diameter (1180 μm ~0.05 in.) and broader range of grain sizes comprising this material, including very coarse sand and very fine gravel. However, in areas with high bottom shear stress (e.g., Figure C-1b), even UBS could be subject to significant erosion (i.e., more than 3-inches), requiring placement of protective armoring at select locations (Figure 5-2).

The placement of armor stone in high shear stress areas of the bed is expected to greatly increase the stability of the cap. Such armoring is expected to improve cap stability regardless of channel depth configuration. With armor, the maximum erosion was found to be less than 3 inches (7.62 cm) for the 100-year return flow under the "Capping with

Armor Area Pre-Dredging" and the "Capping with Pre-Dredging for Flooding – Exposed Armor Areas" scenarios (Figures 5-5, C-2b, and C-4b). Flooding analyses were conducted with these two capping/armoring scenarios and the results are presented in Section 6. It should also be noted that the analysis conducted herein does not include consideration of any sands (non-cohesive) and cohesive solids that might enter the LPR system at the Dundee Dam or from rainfall related runoff from the drainage area below the Dundee Dam. Hence, the cap erosion results presented in this memorandum may be considered to be conservative in nature.

6 FLOODING ANALYSIS

6.1 FLOW AND STORM SURGE ANALYSES

The analyses described in this chapter were conducted to evaluate the potential for additional flooding adjacent to the Lower Passaic River that might occur as a result of the capping/armoring scenarios (presented in Chapter 5). Some of the scenarios result in a reduction in the cross-sectional area of the estuary while others include capping/armoring portions of the sediment bed, which can increase the frictional drag on the flowing water. Both of these changes could potentially affect the flood routing capacity of the system. Analyses intended to assess potential flooding impacts considered relatively infrequent freshwater inflow and tidal elevation conditions. Daily mean stream flow data for the Passaic River at Little Falls, NJ from USGS (Station #01389500) and historic monthly extreme values of water level from NOAA's Bergen Point (Station #8519483 NY) and Battery (Station #8518750 NY) were downloaded from the agencies' websites (USGS and NOAA). These data sets were used to perform flood and storm surge analyses.

6.1.1 Flow Analysis

Observed daily mean stream flow data at the Little Falls gauging station are available from 1897 through 2003. The long-term average (107 years) flow of the Passaic River measured at this most downstream gauging station is 1,140 cfs. During the past 107 years, the maximum peak flow measured at Little Falls was 31,700 cfs, with a corresponding daily maximum of 28,000 cfs, which was observed on October 10, 1903. The maximum peak flow during the last sixty years was 18,400 cfs, recorded on April 7, 1984. On a yearly averaged basis, water year 1902 yielded the largest flow of 2,400 cfs, while the driest year, 1965, yielded 270 cfs. Maximum mean daily flow for each year was extracted from this 107 year data record (Figure 6-1). Figure 6-2 shows the probability distribution of annual maximum mean daily flows. The figure indicates that median annual maximum mean daily flow of the Passaic River for the 107 year USGS measurement period is about 7,000 cfs. The 100-year return flow (plotted at the 99.0th

percentile) lies between 18,000 cfs and 24,000 cfs and depends on how one extrapolates the distribution curve beyond the 95th percentile. Determining the 500-year return flow (which occurs at the 99.8th percentile) from this flow probability distribution plot is more difficult to estimate due to lack of data at this extreme high flow range.

Estimation of the 100- and 500-year floods was performed using a parametric flood-frequency curve procedure described in "Methods of Stream-flow Data Analysis" by Andre Leher of Humboldt State University (2005), which is based on the methods suggested by Chow *et al*. (1988). Leher suggests two different methods for estimating flow recurrence intervals: (1) Log-Normal and (2) Type 1 Extreme-Value (Gumbel) methods. These procedures are described in general below:

- Compile a list of water-year annual maximum flows,
- Take common logs ($\log_{10}$) of the annual flows, and
- Compute the mean ($\bar{x}$) and standard deviation (s) of the original data; then compute the mean ($\bar{x}_l$), standard deviation (s_l), and coefficient of skewness (g_l) of the log-transformed data.

The general form of the equation defining the flows of different recurrence intervals (Q_{Tr}) is

$$Q_{Tr} = \bar{x} + K_T \, s \qquad (6\text{-}1)$$

where K_T is the frequency factor and depends on the probability distribution assumed for the flows (as described below).

Log-Normal distribution

For a log-normal fit, the defining equation is:

$$Q_{Tr} = 10^{\bar{x}_l + K_{TL} s_l} \qquad (6\text{-}2)$$

The values of frequency factor, K_{TL}, to use in the equation and the corresponding return-year flows for the Passaic River are listed in Table 6-1.

Type I Extreme–Value (Gumbel) distribution

For an extreme value fit, the defining equation is:

$$Q_{Tr} = \bar{x} + K_{TG}\ s \qquad (6\text{-}3)$$

where the frequency factor $K_{TG} = -\frac{\sqrt{6}}{\pi}\{0.577 + \ln[\ln T_r - \ln(T_r - 1)]\}$ Values for the frequency factor (K_{TG}) and the computed recurrence flows for the Passaic River are listed in the Table 6-2.

Table 6-1. Frequency factor K_{TL} used for log-normal recurrence interval computation and the recurrence flows for the Passaic River at Little Falls.

Recurrence interval T_r (year)	Frequency factor K_{TL}	Flow Q_{Tr} (cfs)
1.5	-0.439	5,510
2	0.000	6,751
5	0.842	9,968
10	1.282	12,219
25	1.751	15,180
50	2.054	17,465
100	2.326	19,808
200	2.576	22,237
500	2.878	25,572

Table 6-2. Frequency factor K_{TG} used for Type I Extreme-Value (Gumbel) recurrence interval computation and the recurrence flows for the Passaic River at Little Falls.

Recurrence interval T_r (year)	Frequency factor K_{TG} (unitless)	Flow Q_{Tr} (cfs)
1.5	-0.523	5,509
2	-0.164	6,890
5	0.720	10,293
10	1.305	12,544
25	2.044	15,389
50	2.592	17,498
100	3.137	19,596
200	3.679	21,682
500	4.395	24,483

Figure 6-3 shows the results of both the Log-Normal and Type I Extreme-Value (Gumbel) methods. Both analyses yield similar results for the 100-year flow, which are 19,808 and 19,596 cfs, respectively; a difference of about one percent. However, due to relatively few records exceeding 20,000 cfs in the past 107 years, the estimations of 500-year flow yield somewhat different results by each method. The Log-Normal method yields 25,572 cfs, and the Type 1 Extreme-Value (Gumbel) method yields 24,483 cfs (approximately a 4 percent difference).

During the study, HydroQual contacted the USGS Trenton Office and sought their advice concerning these estimates. The USGS Trenton Office provided their 100- and 500- year flow estimates as 20,000 and 26,000 cfs, respectively, at Little Falls which were estimated by the Pearson Type III frequency distribution method (USGS, 1982). These USGS estimates of the 100- and 500-year flows are quite similar (about 1 percent and 2

percent different, respectively) to the values obtained using the Log-Normal estimation method. To provide a slightly more conservative analysis we used the USGS estimates for the specification of 100- and 500-year flows.

6.1.2 Storm Surge Analysis

Monthly maximum water elevations are available from October 1981 through December 2004 from the NOAA Bergen Point station which is the NOAA tide observation station closest to the LPR, which is shown in Figure 6-4. These maximum water elevations represent storm surges associated with the passage of low-pressure systems through the region. Due to the orientation of the coastlines off New York Harbor, which, in general, run in southwest and northeast directions, persistent northeasterly winds with several days of duration bring coastal waters into the Harbor and can result in coastal flooding. Annual maximum elevations were extracted from the data and processed to estimate the probability distribution of extreme events. The results are shown in Figure 6-5. The plot suggests that the 100-year storm surge elevation (the 99^{th} percentile) lies between 1.84 and 1.92 m (6.0 and 6.3 ft) above MSL. Based on the Bergen Point data the 500-year storm surge (the 99.8^{th} percentile) is about 1.96 m (6.4 ft) above MSL.

Because of the relatively short time period for which records are available at the Bergen Point station, the estimated values for the 100- and 500-year storm surge elevations using the data from Bergen Point may not be reliable. An additional analysis of maximum water elevations was conducted using the data observed at the Battery, located at the southern end of Manhattan. The highest water levels recorded in the 150 years of operation of this station were caused by the storm surge related to the passage of Hurricane Donna on September 12, 1960. Hurricane Donna caused extreme water elevations, as much as 2.56 m (8.4 ft) relative to NGVD29, in many parts of the coastal areas around the New York Harbor (Harris, 1963). According to Harris (1963), the highest water level within the LPR was 2.93 m (9.6 ft) relative to NGVD29 near Rutherford, NJ during Hurricane Donna.

In order to justify the use of the Battery data for inferring surge events in the LPR area, a correlation analysis of maximum water elevations at both gauges was conducted. Monthly maximum events observed from October 1981 through December 2003 were used for this analysis. The results shown in Figure 6-6 indicate that there is a high correlation ($R^2 = 0.96$) between these stations due to proximity. The linear regression also suggests that, in general, the maximum elevations at Bergen Point are about 10 cm higher than those observed at the Battery. The probability distribution of the annual maximum water elevations at the Battery is shown in Figure 6-7. The figure shows that water elevations for the 100- and 500-year storm surges (the 99th and 99.8th percentiles, respectively) for the Battery are 2.40 m (7.9 ft) and 2.67 m (8.8 ft) above MSL, respectively. The 100- and 500-year maximum water elevations at the Battery were estimated by extrapolating a linear fit of the upper 10-percentile data, shown on Figure 6-7. Estimates of 100- and 500-year water elevations for Bergen Point can be estimated from the corresponding elevations for the Battery and then applying the regression equations developed from the monthly maximum elevations (Figure 6-6). Resulting estimates of the 100- and 500-year water elevations for Bergen Point are 2.50 m (8.2 ft) and 2.78 m (9.1 ft), respectively. The storm surge values estimated at the Battery—2.40 m (7.9 ft) and 2.67 m (8.8 ft) for 100- and 500-year storm surges, respectively—were used directly for prescribing model boundary conditions during 100- and 500-year storm surge events due to the proximity of the Battery to the open boundary cells at the mouth of the Kill Van Kull.

6.1.3 Correlation of Flow and Storm Surge Events

Further analysis of flood waters from upstream freshwater inflows resulting from heavy rainfall events and the storm surge elevations was conducted to determine whether a correlation exists between the high river inflows and storm surge events. For the years 1981 to 2003, the monthly maximum water elevations at Bergen Point were plotted against the daily flows of the Passaic River measured at the Little Falls to deduce correlation between high flows and storm surge (Figure 6-8).

The correlation results are shown in Figure 6-9 (upper panel), and the correlation coefficient (R^2) is less than 0.02. Further efforts were conducted to evaluate whether the response of river discharge to a storm lagged the timing of the storm-surge maximum. Regressions were made of monthly storm-surge maxima at Bergen Point versus mean daily river discharge lagged by 1, 2, and 3 days after the day of maximum storm surge (remaining panels in Figure 6-9). The correlation coefficients improve when comparing the flow records a few days after the storm surge events. However, the results did not result in a meaningful correlation between the high flow events and storm surge events, and it was concluded that there is no direct correlation between them. Therefore, in conducting the flood analyses presented later in this section, flooding due to high river inflow and storm surge were evaluated independently.

6.2 FEMA Flow and Storm Surge Simulations

Two model runs were constructed in order to compare the flood areas computed by ECOM-SEDZLJS with those estimated by FEMA. FEMA used 100- and 500-year flow and storm surge conditions estimated by USACE (1972 and 1973) and applied both the flow and storm surge conditions concurrently for the estimation of the flood areas in the LPR.

Following is the summary of the flow and storm surge conditions of the FEMA flood study:

- 100-year condition
  - Flow: 49,660 cfs
  - Storm surge: 3.1 m (10.2 ft) (NGVD29) at RM8
- 500-year conditions
  - Flow: 73,175 cfs
  - Storm surge: 3.9 m (12.8 ft) (NGVD29) at RM8

It is worth noting that FEMA's 500-year flow and storm surge values are about 181-percent and 40-percent higher, respectively, than those estimated by HydroQual for use in this study. It is unclear how FEMA arrived at these values. While perhaps a more conservative flooding analysis could have been conducted using the FEMA estimates, the estimates of flow and storm-surge water elevation used in this analysis were based on observed data (and the flow estimates confirmed by the USGS) and are believed to provide a more realistic, but still conservative, estimate of potential flooding in the LPR. However, as another confirmation of the hydrodynamic flood model, the hydrodynamic model was configured with the above FEMA forcing information, and 10 day events were simulated. Computed maximum water elevations along the LPR during the 100- and 500-year events are shown in Figure 6-10. The figure also shows the maximum water elevations along the river computed by FEMA. The results indicate that the ECOM-SEDZLJS computed water level during the 100 year event rises from 2.6 m (8.5 ft.) at the river mouth to 6.0 m (19.7 ft.) at the upstream end of the river. During the 500 year event, the water level rises from 3.5 m (11.5 ft.) to 7.0 m (23.0 ft.). However, the FEMA results indicate that water level rise during the 100-year event varies from 3.2 m (10.5 ft.) at RM8 to 6.9 m (22.6 ft.) at the upstream end. The FEMA 500-year event shows even more significant water level rise: 3.8 m (12.5 ft.) at RM8 to 8.4 m (27.6 ft.) at the upstream end. The two model results show comparable water level rises in the narrow sections of the LPR upstream of RM8. However, there are still a few underlying differences in the application of two models. The most probable causes of the differences could be:

1) Modes of hydraulic computation: steady-state (FEMA) vs. dynamic computation (ECOM-SEDZLJS). In a steady-state computation, it is assumed that the surge and flow conditions are constant. On the contrary, ECOM-SEDZLJS defined a flow curve which reaches the peak flow for only a short period of time (*i.e.*, less than few hours).

2) Physical configuration of the river such as hydraulic capacity (channel dimension), bottom resistance, land elevation, etc. As described in Section 2, the ECOM-SEDZLJS model was configured with recent USACE survey data for both the river (2004) and land elevations (1995). There are about 10 bridges that are partially or fully submerged during the 500-year flow. Flooding of these bridges might further impact the water surface elevation profile. These man-made structures are not considered in ECOM-SEDZLJS.

Figures 6-11 and 6-12 show the projected flood areas computed by ECOM-SEDZLJS for the 100- and 500-year events (red shading in the figures) using the FEMA-estimated values for flows and storm surge elevations. About 1,800 acres and 2,491 acres would be flooded under the 100- and 500-year events, respectively. The model results indicate that most of the downstream locations are flooded during the events, except some areas where the land elevations are higher than 6 m (19.7 ft.). The ECOM-SEDZLJS computed flood areas were compared with the FEMA-estimated 100- and 500-year flood areas in the LPR. The approximate FEMA 100- and 500-year flood areas in the LPR (green shading in the figures) are about 2,360 and 3,230 acres counting from the mouth of the river, respectively. ECOM-SEDZLJS computed 100- and 500-year flood areas that account for about 76 and 77 percent of the area estimated by FEMA, respectively. Most of the discrepancies in the flooded areas are found to occur within the first three miles of the river (see Figures 6-10 and 6-11), where the green shaded areas are FEMA estimated 100- and 500-year flood areas in upstream of RM0 and red shaded areas are the ECOM-SEDZLJS computed flood areas. In upstream locations, the ECOM-SEDZLJS computed flood areas overlap most of the FEMA estimated areas except for a few locations downstream of the Dundee Dam and the "S" shaped section of the river (between RM14 and RM16) near the City of Passaic. ECOM-SEDZLJS computed flooded areas upstream of RM3 account for about 84 percent (1,230 acres out of 1,460 acres) of the flooded area during 100-year event and about 86 percent (1,680 acres out of 1,950 acres) of the flooded area during 500-year event estimated by FEMA model. Although ECOM-SEDZLJS does not provide an exact match to the FEMA model estimates of flooding

acreage, it is reasonably close and is believed to be sufficient for use in this analysis, which is to estimate relative differences in flooding associated with various capping/armoring/pre-dredging scenarios.

6.3 Capping and Simulation Scenarios

6.3.1 Model Set-up

The boundary forcing data of the model include freshwater flows from rivers, and water surface elevation, temperature, and salinity at open boundaries. Several model forcing conditions were considered for the capping scenarios:

- 100-year flow,
- 500-year flow,
- 100-year storm surge, and
- 500-year storm surge.

The 100- and 500-year flow events, developed from the USGS data recorded at Little Falls, were scaled up to account for flow from the portion of the Passaic River basin downstream of Little Falls. As described in Chapter 5, the drainage area above Little Falls (762 square miles) accounts for 81 percent of the drainage area upstream of the mouth of the Passaic River (935 square miles). The remaining 19 percent of the drainage area downstream of Little Falls includes the area between Little Falls and Dundee Dam, tributaries (Saddle River, Third River and Second River) that enter the Passaic River downstream of Dundee Dam, and areas between Dundee Dam and the mouth of the Lower Passaic River that drain directly to the river. The hydrographs for the 100- and 500-year events, assigned at the upstream boundary of the model (at Dundee Dam) were estimated by multiplying the hydrographs developed from the Little Falls data by the ratio of the total drainage area of the Passaic River Basin to the drainage area at Little Falls. These additional flows were placed at the Dundee Dam instead of distributed along the river. As mentioned in Section 5.2.3, this is a conservative approach since the total

flow estimated at the mouth of the river passes through the cap/armor areas. The peak flow rates assigned in the input to the model for the 100- and 500-year flows are 26,000 and 33,800 cfs, respectively. Because the data do not indicate a correlation between high-flow and storm surge events, as discussed in Section 6.1.3, the joint probability of the 100-year/500-year flow and 100-year/500-year storm surge occurring together is extremely small. Therefore, the model simulations for high flow and storm surge events were conducted separately. It should also be noted that modeled estimates of storm surge are based on historical data and do not take into account potential future increases in sea level elevation.

The harmonic constituents in the New York Harbor were used to generate water surface elevations along open boundaries. A storm surge analysis of water surface elevation data at the Battery was conducted, and the 100- and 500-year surge peaks (2.40 m (7.87 ft.) and 2.67 m (8.76 ft.) above MSL) were obtained (refer to Section 6.1.2). A storm surge curve observed at the Battery during Hurricane Donna (which lasted for about two days in 1960) was used for this study. These water elevations were added to the astronomical tide for the projection simulations. In order to create the maximum possible water elevation during each simulation, the storm surge peaks were added to the peak spring tide within the simulation period. Constant temperature and salinity were applied to the open boundaries.

6.3.2 Scenario Descriptions

Several capping/armoring scenarios were considered in the study with various combinations of capping/armoring areas with different depth conditions:

1. Base Case: using existing bathymetry conditions in the LPR and no capping/armoring.

2. Capping with Armor Area Pre-Dredging: the first 8.3 miles of the LPR were capped with 2 feet of Upland Borrow Sand (UBS) and armored at selected locations with 2 feet of 6-inch angular cobble. Armored areas were to be pre-

dredged 2 ft before being capped with sand and then armored with stone. Therefore, the top of armored areas would be level with other areas that are sand capped, and post-remediation depths would be two feet shallower than pre-remediation depths.

3. Capping with Dredging for Flooding – Exposed Armor Areas: the river bottom of the LPR between RM0 and RM8.3 was dredged by 2 feet before capping and 4 feet before capping and armoring. With this configuration, current river depths would be maintained in the capped/armored areas. Bed roughness, however, is increased by the exposed armoring material (i.e. z_0 = 0.01 m (0.4 in.)), so this scenario was considered for flooding analysis. (Sensitivity to the selection of bottom roughness is discussed in Section 6.4.2.).

4. Capping with Dredging for Flooding – Smoothing Layer: This scenario has the same depth condition as the above "Capping with Dredging for Flooding – Exposed Armor Areas". The only difference is the placement of a 1-foot sand "smoothing layer" on top of the armor layer. For this scenario, an additional 1 foot of pre-dredging in the armored cells was assumed. Both scenarios (3 and 4) result in a final depth the same as the existing bathymetry. Please note that flooding simulations conducted with the sand "smoothing layer" on top of the armor stones would result in the same water elevations and flooding as the "Base Case," because the bottom roughness of the sand cap was assumed to be the same as the background sediment (i.e., z_0 = 0.0004 m ~0.015 in.). Therefore, no additional flooding simulations were conducted under the "Capping with Dredging for Flooding – Smoothing Layer" scenario.

Figure 5-2 shows the extent of different capping and armoring scenarios. Ten-day simulations were set up for the various capping/armoring scenarios and the forcing conditions (high flow and storm surge). The Base Case scenario runs were also performed, using the existing bathymetry with no capping or armoring for the 100- and

500-year flows and storm surge events in order to provide a basis or reference water elevations for determining any change in the flooding areas under the different capping/armoring and dredging scenarios.

Modification of model bathymetry resulting from capping/armoring activities could change the total water volume in the river, and, therefore, change the distributions of computed water surface elevations and current velocities. In addition, sediment grain size distributions (*i.e.*, placement of sand cap and armor) could modify model-computed fields of current velocities and water surface elevations since the bottom drag coefficient in the hydrodynamic model is directly correlated with sediment grain size. Equation (6-4) shows the formulation used to estimate the bottom drag coefficient (C_D) in ECOM-SEDZLJS (Blumberg and Mellor, 1987).

$$C_D = \left[\frac{1}{\kappa} \ln(0.5 * Z_b / Z_0) / z_0 \right]^{-2}, \qquad (6\text{-}4)$$

where z_0 is the bottom roughness, z_b is the thickness of the grid nearest the bottom and κ (= 0.40) is the von Karman constant. In the above equation, C_D is a function of hydrodynamic bottom roughness (z_0), which is related to sediment grain size (Kamphuis, 1974). Table 6-3 displays hydrodynamic bottom roughness lengths specified in the LPR model. Using Equation (6-4) and assuming a water depth of 5 m (16.4 ft.), which is a typical river channel depth between RM0 and RM5, the corresponding bottom drag coefficients are estimated in Table 6-4. These calculations assume ten equally spaced vertical model layers, which was the configuration applied for the LPR.

Table 6-3. Hydrodynamic Bottom Roughness Length (m) under Different Bottom Conditions in the Lower Passaic River

Base Case	0.0004
Capping Area	0.0004
Armoring Area	0.010

Table 6-4. Bottom Drag Coefficient for a Grid Cell with a 5-m Depth under Different Model Bottom Conditions in the Lower Passaic River

Base Case	0.004
Capping Area	0.004
Armoring Area	0.015

6.3.3 Results

6.3.3.1 Changes in Water Elevations

Maximum values of water surface elevation at each model grid cell were extracted from the model computations during each 10-day simulation period. Maximum water surface elevations along the length of the LPR, computed for the Base Case and each of the capping/armoring alternatives, are summarized on Figures 6-13a and 6-13b for the high flow and Figures 6-14a and 6-14b for the storm surge simulations, respectively. The figures summarize the maximum water elevations at different locations in the river under different flow and storm surge conditions in response to various capping and armoring scenarios.

For all simulations, the results indicate that the water surface elevations increase in an upstream direction. Under the "Base Case" scenarios, which uses the existing depth of the river, the downstream-upstream difference in the maximum water surface elevations can be as large as 3.6 m (11.8 ft.) during the 100-year flow event and 4.2 m (13.8 ft.) during the 500-year flow event (blue lines in Figure 6-13a). However, this increase is mainly limited to the narrow upper section of the river (upstream of RM8). In the downstream section below RM8, where the river becomes wider, the increase in the water level during the 100-year flow is computed to be less than 0.5 m (1.6 ft.) between RM0 and RM8 and less than 0.8 m (2.6 ft.) during the 500-year flow.

Comparing the "Capping with Armor Area Pre-Dredging" scenarios (green lines in Figure 6-13a) to the "Base Case" scenarios, the largest water elevation increase occurs immediately upstream of the armored regions, which are around RM3 and RM5.5. This increase, relative to the "Base Case", is as large as 0.3 m (~1 ft.) and 0.5 m (1.6 ft.) for the 100- and 500-year flows, respectively, at RM8. Figure 6-13b shows the differences in the maximum water elevations compared to the results of the Base Case. High bottom drag coefficients were computed for the armored areas, which were about 4-times larger than those used for the sand capped areas (Table 6-4). It appears that high bottom drag coefficients in the armored area hinder movement of water downstream and result in the increase of water elevations in upstream locations (*i.e.*, a backwater is generated). These changes in the water elevations in the upstream section of the river result in additional flooding in the low-lying areas. The spatial extent of flooding areas due to various capping and armoring scenarios are discussed in the next section.

Full pre-dredging (as shown in the "Capping with Dredging for Flooding - Exposed Armor Areas" scenario) of 2 to 4 feet in the lower 8.3 miles of the river, where capping (2 feet of pre-dredging) and armoring (an additional 2 feet of pre-dredging) are planned, results in a reduction of about 0.2 to 0.3 m (0.7 to 1.0 ft.) in water elevation rise at RM8 compared to the non-pre-dredged "Capping with Armor Area Pre-Dredging" scenario (in which the top of cap is modeled as two feet shallower than existing bathymetry) for both the 100- and 500-year flows. The results reflect the water-level change in response to the downstream water-depth change (*i.e.*, the pre-dredging). Positive values in Figure 6-13b indicate that the water elevation would rise compared to the Base Case, and vice versa.

During the 100- and 500-year storm surge events, the upstream-to-downstream difference in water surface elevation is about 0.25 m (0.82 ft.) (Figure 6-14a) under the Base Case. However, water elevations in the LPR rise about 2.7 m (8.9 ft.) and 3.0 m (9.8 ft.) above NGVD29 at the mouth of the river (RM0), respectively, for the 100- and 500-year storm surges, which would result in additional flooding in the low-lying regions near the mouth

and the upstream portions of the river. It was found that during storm surge events the maximum water elevation between RM3 and RM8 would be lowered by about 2 centimeters under the "Capping with Armor Area Pre-Dredging" and "Capping with Dredging for Flooding - Exposed Armor Areas" scenarios compared to the Base Case scenario (Figure 6-14b). It appears that those armored areas with higher bottom roughness would impede the progression of the storm surge upstream and, hence, result in less of an elevation rise compared to those computed under relatively smooth bottom conditions in the "Base Case" scenario.

6.3.3.2 Flooded Areas

The flooded areas in the LPR are determined by comparing water surface elevations in the river to nearby landside digital elevation information during the simulations. Total flooded areas for each simulation are tabulated in Table 6-5, and do not include the in-river areas inundated during normal tides (i.e., within river wetting and drying areas under normal tidal elevations).

Table 6-5. Total Areas (acres) Flooded under Different Simulation Scenarios

	Base Case (Existing Bathymetry)	Capping with Armor Area Pre-Dredging	Capping with Dredging for Flooding – Exposed Armor Areas
100-Year Flow	485	510	485
500-Year Flow	779	809	784
100-Year Storm Surge	1138	1138	1138
500-Year Storm Surge	1469	1469	1469

6.3.3.2.1 Scenarios During the 100-Year Flow

Figure 6-15 shows the grid cells flooded during the 100-year flow under the "Base Case" scenario. Under the "Base Case" scenario, the 100-year flow event would flood an area of 485 acres along the river (Table 6-5). During the 100-year flow, the "Capping with Armor Area Pre-Dredging" scenario would increase the water elevation by 0.3 (~1 ft.) m at RM8 and increase the projected flooding area by 25 acres for a total of 510 acres (Figure 6-16). The additional flooding area under the "Capping with Dredging for Flooding - Exposed Armor Areas" scenario is projected to occur between RM5 and RM12. The "Capping with Dredging for Flooding - Exposed Armor Areas" scenario would result in a projected flooded area of 485 acres as same as computed for the Base Case. The results indicate that pre-dredging of the capping/armoring areas under the

"Capping with Dredging for Flooding - Exposed Armor Areas" scenario would raise water levels less than 0.05 m (0.16 ft.) in the LPR upstream of RM8 (Figure 6-13b) compared to those computed under the "Base Case" scenario.

6.3.3.2.2 Scenarios During the 500-Year Flow

The 500-year flow would raise the upstream water levels as much as 3.5 m (11.5 ft.) above NGVD29 at RM10 under the Base Case scenario, and it would cause flooding of 779 acres, as shown in Figure 6-17. The model results indicate that additional areas downstream of the Dundee Dam, especially between RM8 and RM11, would be flooded during the 500-year flow, in comparison to the areas flooded during the 100-year flow under the "Base Case" scenario.

For the 500-year flow event, the water elevations would increase up to 0.5 m (1.6 ft.) in the area upstream of the capping/armoring region near RM8 under the "Capping with Armor Area Pre-Dredging" scenario (Figure 6-13b) compared to those under the "Base Case" scenario. This water elevation increase would affect many grid cells from RM3 to RM9. Under this "Capping with Armor Area Pre-Dredging" scenario, the flooded area is projected to be 809 acres (Figure 6-18), which adds about 30 acres to the flooded area relative to the Base Case scenario during the 500-year flow.

It is found that pre-dredging of the capping/armoring area would lower the water elevations between RM3 and RM12 under the 500-year flow compared to the "Capping with Armor Area Pre-Dredging" scenario (Figure 6-13b). On average, the water elevation would increase by 0.05 m (0.16 ft.) upstream of RM5, with a peak increase of about 0.12 m near RM8 due to the pre-dredging, compared to those computed under the "Base Case" scenario. The total flooded area under the "Capping with Dredging for Flooding – Exposed Armor Areas" scenario is 784 acres as shown in Figure 6-19, which is an increase of 5 acres compared to those under the "Base Case."

6.3.3.2.3 Scenarios During Storm Surge Events

The 100- and 500-year storm surges would cause the significant flooding (more than 50 percent of the total flooding areas) between the river mouth and RM4, where land elevations are relatively low. As indicated in Table 6-5, flooded areas during storm surge events are much greater than those under 100-and 500-year flows for all scenarios. The increase in water elevations of as much as 3.0 m (9.84 ft.) above NGVD29 under the "Base Case" would result in the flooding of 1,138 acres and 1,469 acres during 100- and 500-year storm surges, respectively (Figure 6-20 and 6-21). Although most of the flooded areas are in the lower 5 miles of the river, both the low lying areas in the County Park of Lyndhurst (RM11) and the area near RM15 downstream of the Dundee Dam would also be flooded during the extreme storm surge events. As indicated earlier, the scenarios with the "Capping with Armor Area Pre-Dredging" and "Capping with Dredging for Flooding – Exposed Armor Areas" scenarios result in less maximum water elevation rise compared to those under the "Base Case" scenario (Figure 6-13b). However, the differences in the water elevations are less than 0.02 m (0.07 ft.) at most of the locations in the LPR and do not change the flood areas as compared to the "Base Case" scenario.

6.4 SENSIVITITY ANALYSES

6.4.1 Sensitivity to Land Surface Elevation

To properly estimate potential flooding areas under different conditions in the LPR basin, the best available shoreline and land elevation information were incorporated into the hydrodynamic model (see Section 2). The initial model land elevations were configured using the 2-foot contour lines from the USACE survey maps. However, even these data resulted in shoreline and land elevation uncertainties of ± 1 foot. Therefore, a sensitivity run was performed, where the land elevations used in the model were reduced by 1 foot, to see how the uncertainty in the land elevation might affect the estimates of the flooding areas. The simulation scenario selected was the "Capping with Dredging for Flooding –

Exposed Armor Areas" scenario. The 100- and 500-year flows at Dundee Dam and predicted tides at the open boundaries of the model were used as model forcing functions.

Figure 6-22 shows the maximum water surface elevation along the LPR during the simulations. In the figure, blue lines correspond to the model results obtained with the original land surface elevation while the red lines are the sensitivity run results obtained with 1 foot lowered land elevation. The model results indicate that lowering the land surface elevations slightly decreases maximum water surface elevations (due to additional flooding of the floodplain) during flood events when compared to the original land elevation configurations. On average, the difference between using the original and the modified land surface elevations is less than 0.15m (~0.5 ft.) during the 100- and the 500-year flow events.

Table 6-6 lists the flooded areas and the percent difference under different shoreline elevations. Figures 6-23 and 6-24 display the flooded areas when the land elevations were lowered by 1 foot during 100- and 500-year flows. Clearly the decrease in land surface elevations results in a larger flooded area. When the estimated land elevations were reduced by 1 foot, the flooded areas were projected to increase by about 22.5 percent and 8.8 percent during 100- and 500-year flow events, respectively. During the 100-year flow conditions, the additional flooding areas due to a 1 foot adjustment of land elevations are generally limited from RM9 to RM10 (compare Figure 6-15to Figure 6-23). However, under the 500-year flow conditions, most of the additional flooding areas are located from RM0 to RM9 (compare Figure 6-19 to Figure 6-24).

Table 6-6. Total Areas Flooded under Different Shoreline Elevations. All simulations are based on the "Capping with Dredging for Flooding – Exposed Armor Areas" Scenario

Sensitivity	Original Land Elevations (acres)	Land Elevations Lowered by 1 foot (acres)	Difference (percent)
100-Year Flow	485	594	22.5
500-Year Flow	784	853	8.8

6.4.2 Sensitivity to Bottom Roughness Length

The Ambrose Sand (AS) originally selected as the capping material for this study was found to be easily subject to bedload transport under normal tidal conditions during the cap erosion analysis (refer to Section 5.3.1). This was also found to be true for the smaller sand particle sizes for the UBS source (refer to Section 5.3.2). Even moderate tidal currents of about 1 ft/sec would mobilize a portion of the UBS capped material as bedload transport. Under this mode of transport, sand grains would form ripples and dunes depending on the variation of the current speed. This process is not formulated within the current hydrodynamic model algorithms. During the modeling efforts, the bottom roughness (Z_0) of the UBS capping material is assumed to be 0.0004 m (0.016 in.). Literature values indicate the bottom roughness length of medium to coarse sand would vary from 0.0003 to 0.006 m (0.012 to 0.24 in.) depending on the height of sand ripples and dunes (Dyer, 1986). In order to estimate the effect of this transient nature of bottom roughness length due to non-cohesive sand capping material, a sensitivity run was conducted using a value of 0.005 m (0.19 in.) (compared to 0.0004 m (0.02 in.)), which is a half of the value used for the 6-inch cobble armor material (i.e., 0.01). A model run was performed using various bottom roughness lengths: 0.0004 for non capped/armored areas (same as previous modeling efforts; see Table 6-3), 0.005 for capped areas

(modified from the original value of 0.0004), and 0.01 for armored areas (same as previous modeling efforts; see Table 6-3). Four scenarios were modeled: "Capping with Armor Area Pre-Dredging" and "Capping with Dredging for Flooding – Exposed Armor Areas" for 100- and 500-year flow events. The maximum water level rises for these simulations are shown in Figure 6-25. The results indicate that, with the higher bottom roughness length, maximum water level rise would increase up by 20 cm (0.66 ft.) to 30 cm (~1.0 ft.) for both capping scenarios during 100- and 500-year flows, respectively. Figures 6-26 through 6-29 show the flood areas for these sensitivity runs under 100- and 500-year flow conditions.

Table 6-7 summarizes the flooded areas and the percent difference under different hydrodynamic roughness lengths. The increase in water elevation rise due to higher bottom roughness results in a larger flooded area. However, the changes in the flooded areas were projected to increase only by between 4.3 and 8.4 percent and 3.8 and 6.1 percent during 100-year and 500-year flow events, respectively, for both capping scenarios, which are relatively small changes. This computation provides a bound on the range of uncertainty in the extent of flooded area associated with transient bottom roughness due to the mobile portions of the sand cap.

Table 6-7. Total Areas Flooded under Different Hydrodynamic Roughness Lengths of Sand Capped Area

	Capping with Armor Area Pre-Dredging			Capping with Dredging for Flooding - Exposed Armor Areas		
	Original Z_0 of 0.0004 m (acres)	Higher Z_0 of 0.005 m (acres)	Difference (percent)	Original Z_0 of 0.0004 m (acres)	Higher Z_0 of 0.005 m (acres)	Difference (percent)
100-Year Flow	510	553	8.4	485	506	4.3
500-Year Flow	809	858	6.1	784	814	3.8

7 CONCLUSIONS

A three-dimensional hydrodynamic-sediment transport model was developed to evaluate the potential for erosion of cap material that might be placed to remediate sediment contamination in the lower 8.3 miles of the LPR. The FEMA 500-year flood plain was included in the model domain, and 2 ft contour USACE land survey data were used to configure the elevation of the banks of the LPR and to determine potential flooding areas.

The hydrodynamic model used in this study is an extension of the model developed by HydroQual for use in the 17-mile LPRSA RI/FS and NBSA RI/FS (HydroQual, 2008). A calibration was performed for the revised model using field survey data collected in the summer of 2004. Model computed water surface elevations, current velocities, and temperature and salinity were compared against observed data. Model validation was conducted using the storm surge data of Hurricane Donna, and the observed surge elevations were well reproduced by the model at various locations in the modeled area. The FEMA 100- and 500-year events were also used for model validation. Although the hydrodynamic model did not fully reproduce the areas of inundation within the FEMA 500-year flood plain, the model was able to reproduce comparable FEMA computed water level rises and about 86 percent of the FEMA computed flooding areas in the LPR. Given the differences in modeling approaches (time-variable vs. steady-state), it is believed that this is an acceptable level of reproduction.

As part of the cap stability/erosion analysis conducted using the sediment transport model-SEDZLJ, it was found that sands from the Ambrose Channel, which is located at the entrance to NY-NJ Harbor near Sandy Hook, were highly erodible and thus not suitable for use as a sand cap in the LPR. Instead, it would be necessary to utilize sands from an upland borrow source. These upland sands are comprised of sands with larger particle sizes, which are heavier and less subject to the forces of erosion experienced in the LPR. There are, however, areas within the river where it will be necessary to place protective armor stone over the sand cap so as to prevent erosion of the cap. This erosion

occurs in regions of the river which experience high bottom water velocities with accompanying high bottom shear stress. The additional frictional resistance of the protective armor cobble can slow river flow sufficiently to cause backup and flooding, so a 1-foot thick sand "smoothing layer" would cover the armor layer to decrease overall frictional resistance.

Analyses of extreme flow and surge events were also conducted. The 100- and 500-year flows are estimated as 26,000 and 33,800 cfs, and the 100- and 500-year storm surges as 2.40 m (7.9 ft.) and 2.67 m (8.8 ft.) above MSL, respectively, in the modeled area. The model was configured with the 100- and 500-year flow and storm surge events. Three capping/armoring scenarios were evaluated against a "Base Case" scenario: 1) "Capping with Armor Area Pre-Dredging"; 2) "Capping with Dredging for Flooding - Exposed Armor Areas"; 3) "Capping with Dredging for Flooding with 1 foot sand smoothing layer." A summary of the modeling results is as follows:

- Under the "Base Case" scenario, the 100 and 500-year flows would inundate areas of 485 and 779 acres, respectively.

- The "Capping with Armor Area Pre-Dredging" scenario would increase the water elevation by as much as 0.3 and 0.5 m (~1 and 1.6 ft.) from those in the Base Case scenario during the 100- and 500-year flows, respectively. Compared to the "Base Case" scenario, the "Capping with Armor Area Pre-Dredging" scenario would flood an additional 25 acres during the 100-year flow (total flooded area of 510 acres) and 30 acres during the 500-year flow (total flooded area of 809 acres).

- The "Capping with Dredging for Flooding - Exposed Armor Areas" scenario would increase the water elevation by 0.05 and 0.1 m (0.16 and 0.33 ft.), as compared to the Base Case scenario during the 100- and 500-year flows, respectively. The flooded areas would remain the same during the 100-year flow (total flooded area of 485 acres) and increase by 5 acres during the 500-year flow

(total flooded area of 784 acres) compared to those computed under the “Base Case” scenario.

- The "Capping with Dredging for Flooding" scenario with 1 foot sand "smoothing layer" would produce the same maximum water elevations as well as flooding areas as compared to the “Base Case” because the underlying hydrodynamic conditions are identical between the two scenarios: water depth and bottom roughness length. (Note: water depths remain the same due to 2 feet to 5 feet of pre-dredging before placement of the sand or sand/armor cap).

- Model results indicate that the 100 and 500-year storm surges would cause the maximum flooding in the study area to be 1,138 and 1,469 acres, respectively) under the “Base Case” scenario, and most of the flooding would occur in the low-lying areas near the mouth of the river. All capping/armoring scenarios would not change the flooded areas during the storm surge events, compared to those computed under the “Base Case” scenario.

- A few sensitivity runs of the model were conducted to account for the uncertainty of the land elevation by reducing the land elevation by 1 foot and for the uncertainty of the bottom roughness length of the upland borrow-source (UBS) sand cap material by increasing the bottom roughness length to 0.005. The results suggest that, by lowering the land elevation by 1 foot, the flooding area during the 100- and 500-year flow would increase as much as 22.5 and 8.8 percent during 100- and 500-year flows compared to the results using the original land elevation configuration, respectively. A higher bottom roughness length (a value of 0.005) for the sand cap material would result in about a 8.4 to 6.1 percent increase in the flooding areas under "Capping with Armor Area Pre-Dredging" scenario during 100- and 500-year flows, respectively, compared to those computed with the value (0.0004) used for the original flooding analyses. Under the "Capping with Dredging for Flooding - Exposed Armor Areas" scenario, the flooding areas

would increase by 4.3 and 3.8 percent during 100- and 500-year flows, respectively.

It is noted that subsequent to the completion of the capping-armoring and flooding analyses, which were discussed in this report, the sediment transport model was enhanced by including the friction effects of bed forms in non-cohesive sediment areas. The results of subsequent analyses with the revised sediment transport model indicate a reduction in the need for armor areas, compared to the results presented in this report. The extent of flooded areas computed with the enhanced sediment transport formulations are the same as those presented in this report for the "Capping with Dredging for Flooding – Exposed Armor Areas" case.

8 REFERENCES

Aqua Survey Inc., 2006, Technical Report, Geophysical Survey, Lower Passaic River Restoration Project, submitted to New Jersey Dept of Transportation - Office of Maritime Resources, Trenton, NJ

Blumberg, A.F. and G.L. Mellor, 1987. A description of a three-dimensional coastal ocean circulation model. In: Three-Dimensional Coastal Ocean Models, Coastal and Estuarine Sciences, 4. N. Heaps, Ed., American Geophysical Union, Washington, D.C., 1-16.

Blumberg, A.F. and L.A. Khan, and J.P. St. John, Three Dimensional Hydrodynamic Model of New York Harbor Region, J. Hydraulic Engineering, 125, 799-816, 1999
Cheng, N.S., 1997. Simplified settling velocity formula for sediment particle. Journal of Hydraulic Engineering, 123(2):149-152.

Cheng, N. S., 1997. Simplified Settling Velocity Formula for Sediment Particle, ASCE J. Hydr. Engr., 123, 149-152.

Chow, Ven T., D.R. Maidment, and L.W. Mays, 1988. Applied Hydrology, McGraw-Hill. New York.

Dyer, Keith R., 1986. Coastal and Estuarine Sediment Dynamics. John Wiley & Sons, New York.

Federal Emergency Management Agency, 1996. Q3 Flood Data (CD-ROM).

Glenn, S.M. and Grant, W.D., 1987. A Suspended Sediment Stratification Correction for Combined Waves and Current Flows, J. Geophys. Res., 92(C8):8244-8264.

Grant, W.D. and Madsen, O.S., 1982. Moveable bed roughness in oscillatory flow, J. of Geophys. Res., 87(C1):469-481.

Guidelines for Determining Flood Flow Frequency. 1982. Bulletin 17B of the Hydrology Subcommittee, Interagency Advisory Committee on Water Data, Office of Water Data Coordination, USGS.

Harris, D. Lee, 1963, Characteristics of the Hurricane Storm Surge. Technical Paper No. 48, U.S. Dept of Commerce, Weather Bureau, Washington, D.C.

HydroQual, Inc., 2004. A Primer for ECOMSED, Version 1.4: Users Manual, Mahwah, NJ. 194 p.

HydroQual, Inc., 2008, Hydrodynamic Modeling Report, Lower Passaic River Restoration Project, submitted to the US Environmental Protection Agency Region 2 and US Army Corps of Engineers, Kansas City District.

Jones, C. and W. Lick, 2001. Contaminant flux due to sediment erosion. Proceedings of the 7th International Conference: Estuarine and Coastal Modeling, 280–293.

Kamphuis, J.W., 1974, Determination of sand roughness for fixed beds. J. Hydraulics Research, 12:193-203.

Leher, Andre, 2005. Handout notes “Methods of Stream-flow Data Analysis”, Humboldt State University.

Little, W.C. and P.G. Mayer, 1972. The role of sediment gradation on channel armoring. Publication No. ERC-0672, School of Civil Engineering in Cooperation with Environmental Research Center, Georgia Institute of Technology, Atlanta, GA. 1-104.

Malcolm Pirnie, Inc., 2007. Draft Source Control Early Action Focused Feasibility Study. Lower Passaic River Restoration Project. Prepared in conjunction with Battelle and HydroQual, Inc. June 2007.

NOAA, 2000. Effects of Hurricane Floyd on Water Levels Data Report, Technical Report NOS CO-OPS 027, Silver Spring, Maryland.

NOAA. NOAA Tides & Currents Home. http://tidesandcurrents.noaa.gov Last accessed February 7, 2014.

Roberts, J., R. Jepsen, D. Gotthard, and W. Lick, 1998. Effects of particle size and bulk density on erosion of quartz particles. Journal of Hydraulic Engineering, 124(12):1261-1267.

USACE, 1972. Passaic River Survey Report, New York District.

USACE, 1973. Supplement Report: Passaic River Survey Report for Water Resource Development, New York, NY

USGS, 1982, Guidelines for determining flood flow frequency, Bulletin 17-B of the Hydrology Subcommittee: Reston, Virginia, U.S. Interagency Advisory Committee on Water Data U.S. Geological Survey, Office of Water Data Coordination.

USGS. USGS Surface-Water Data for New Jersey. http://waterdata.usgs.gov/nj/nwis/sw Last accessed February 7, 2014.

Van Rijn, L., 1984. Sediment transport, part II: Suspended Load Transport. Journal of Hydraulic Engineering, 110(11):1431-1456.

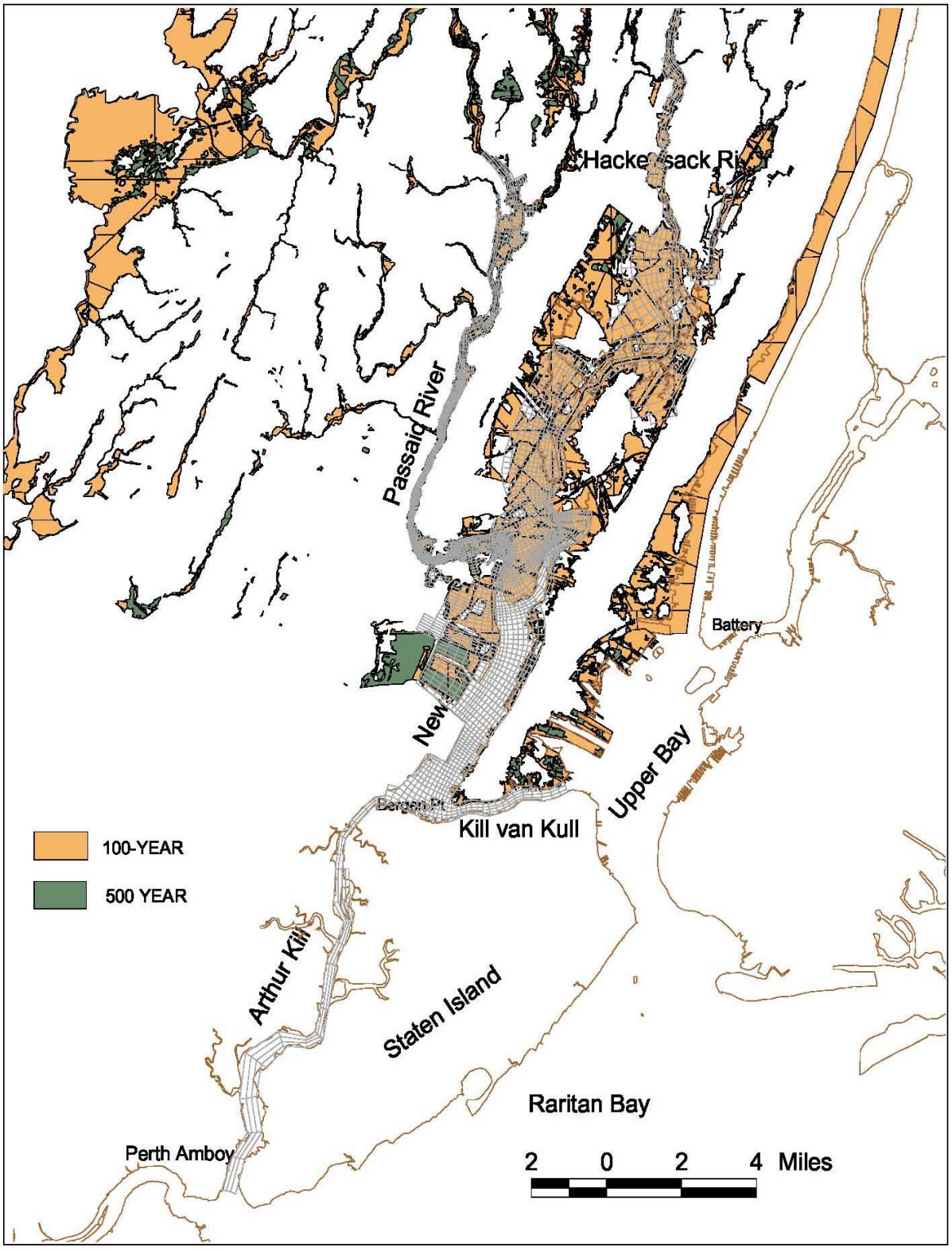

FEMA 100- and 500-year flood area with hydrodynamic model grid

Figure 2-1

Lower Eight Miles of the Lower Passaic River

2014

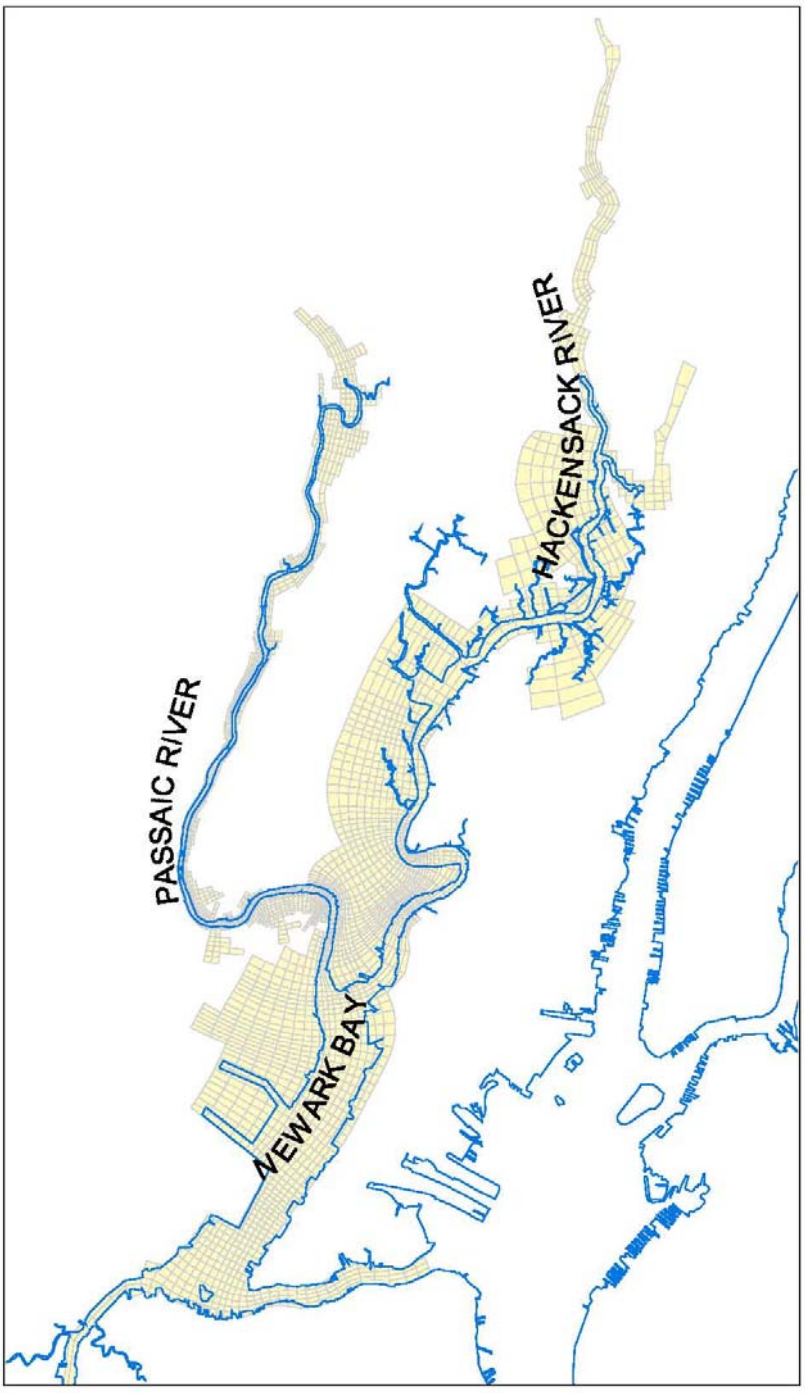

Map of the Lower Passaic River, the Hackensack River, Newark Bay, the Arthur Kill and the Kill van Kull with orthogonal curvilinear model grid *Lower Eight Miles of the Lower Passaic River*	Figure 2-2 2014

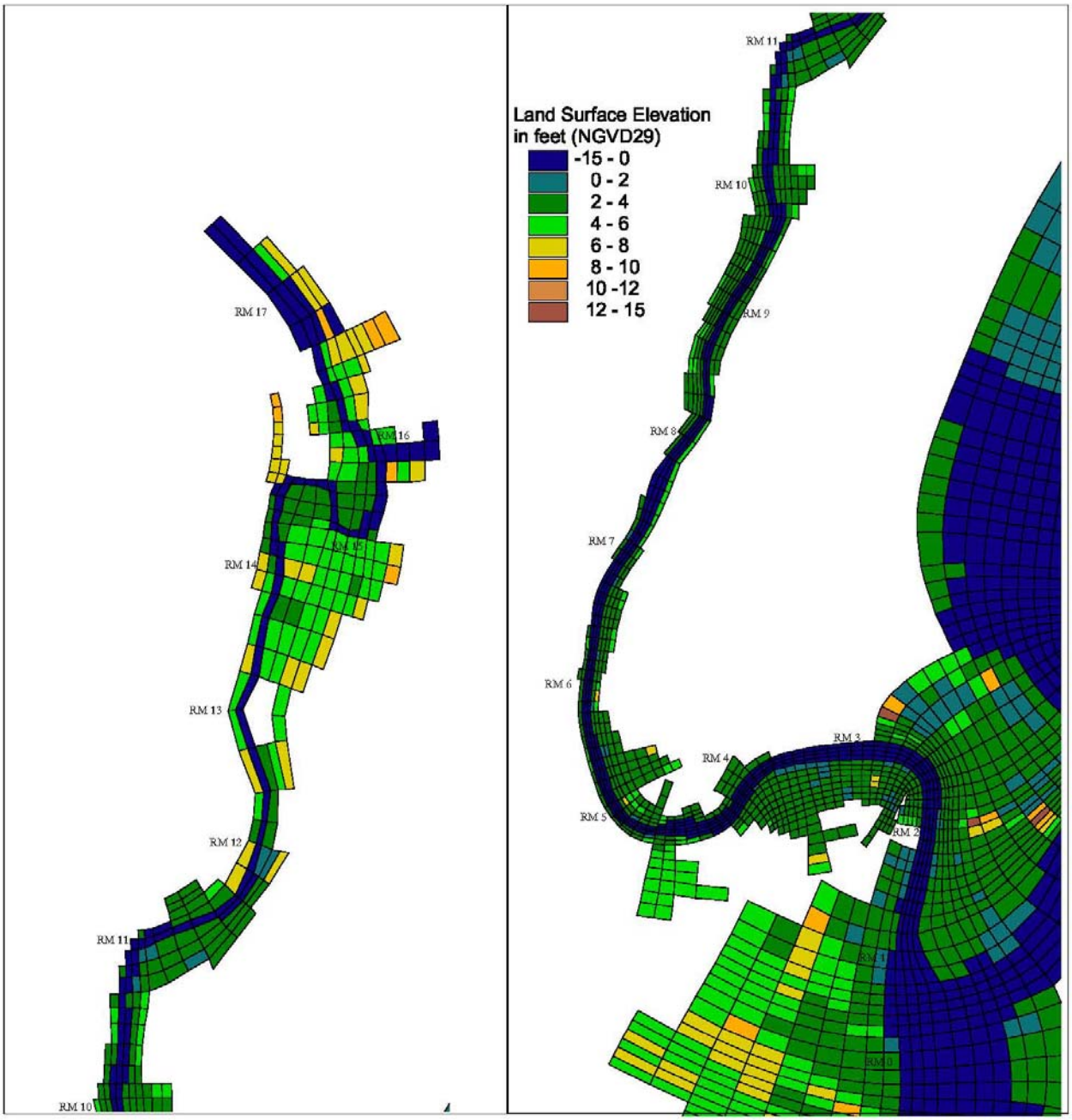

Computational grid for FFS study with depths

Figure 2-3

Lower Eight Miles of the Lower Passaic River

2014

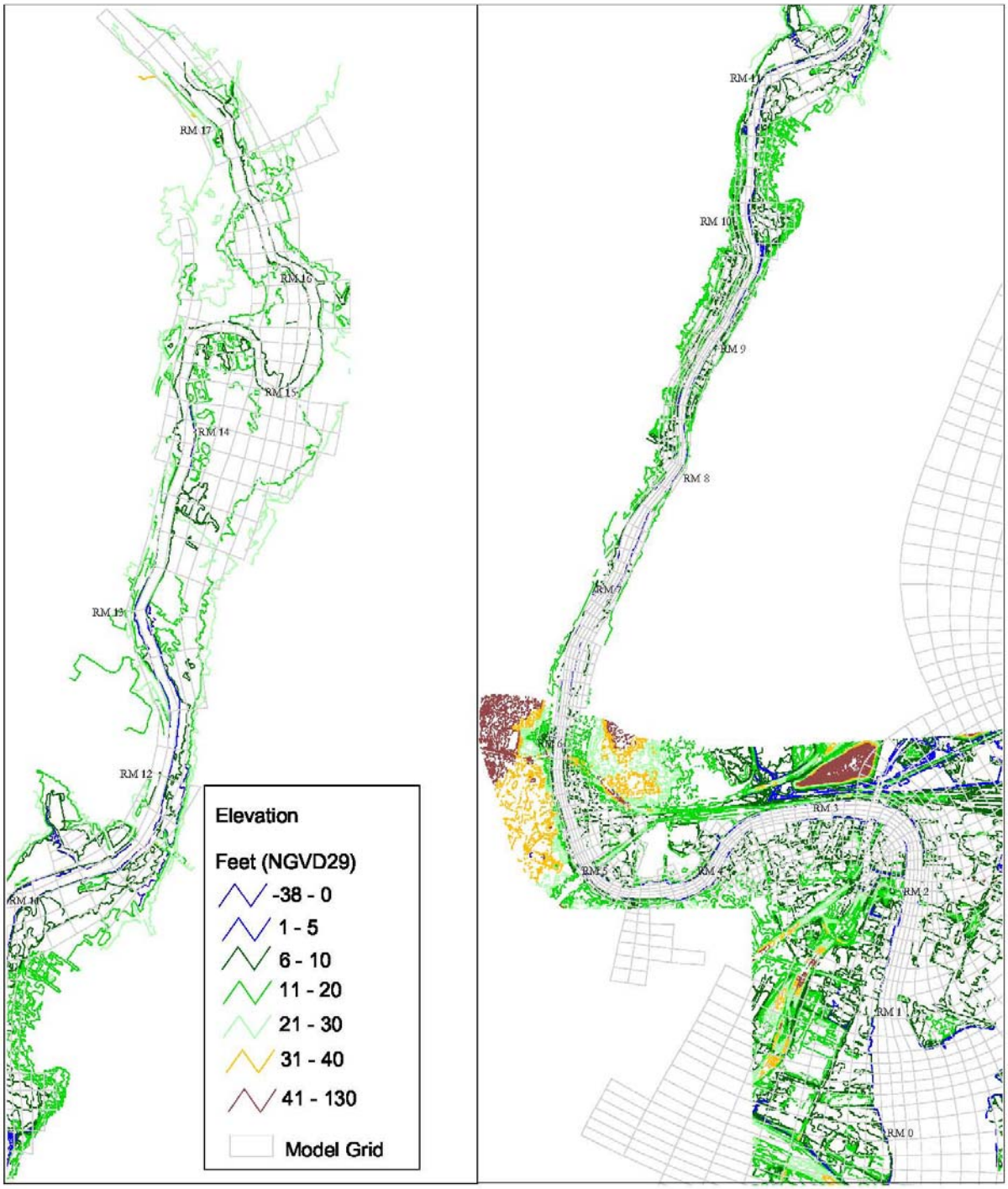

Overview of the USACE land survey data with hydrodynamic model grid	Figure 2-4
Lower Eight Miles of the Lower Passaic River	2014

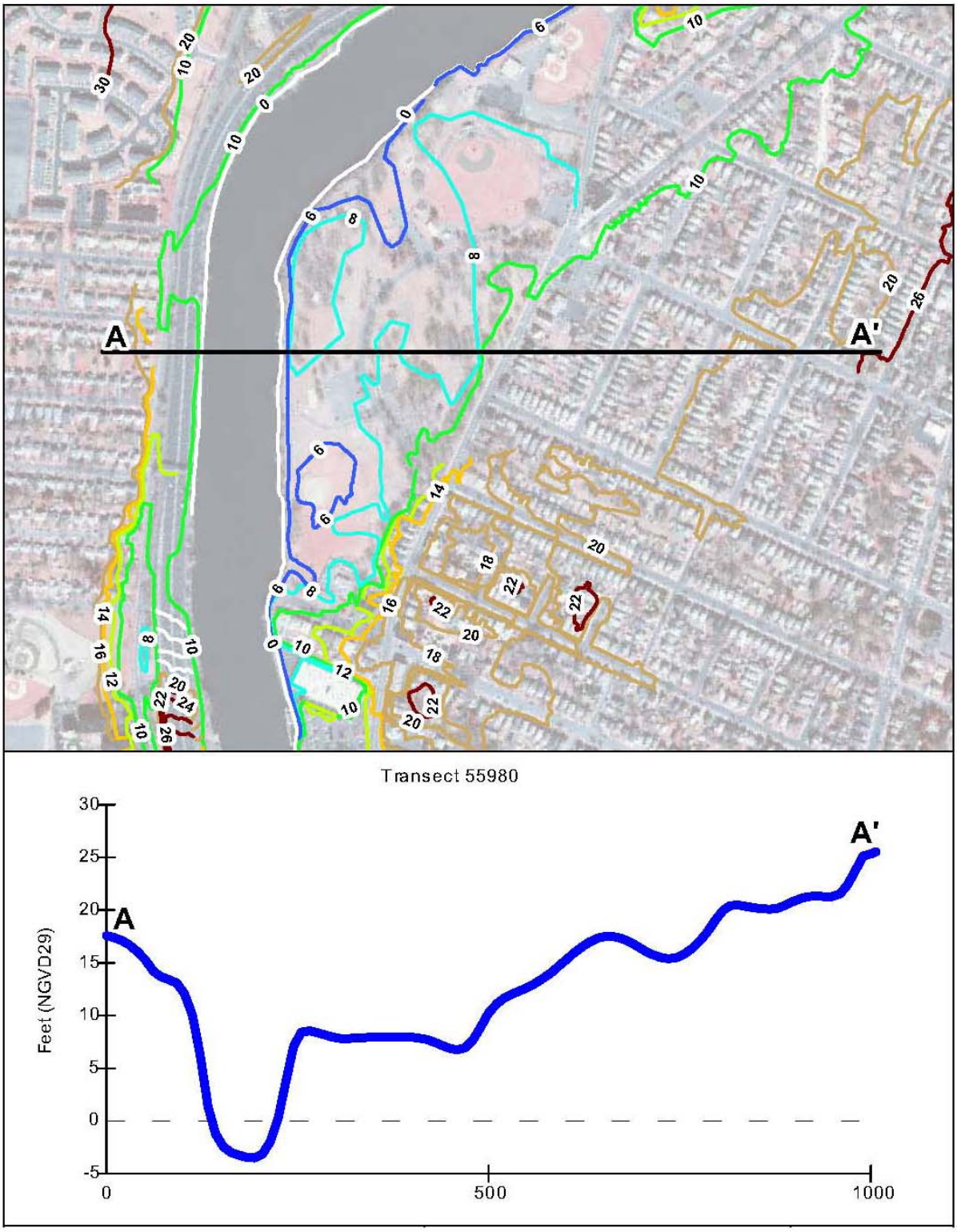

Detailed view of the USACE land survey data near RM11 and cross-section of the land elevation

Lower Eight Miles of the Lower Passaic River

Figure 2-5

2014

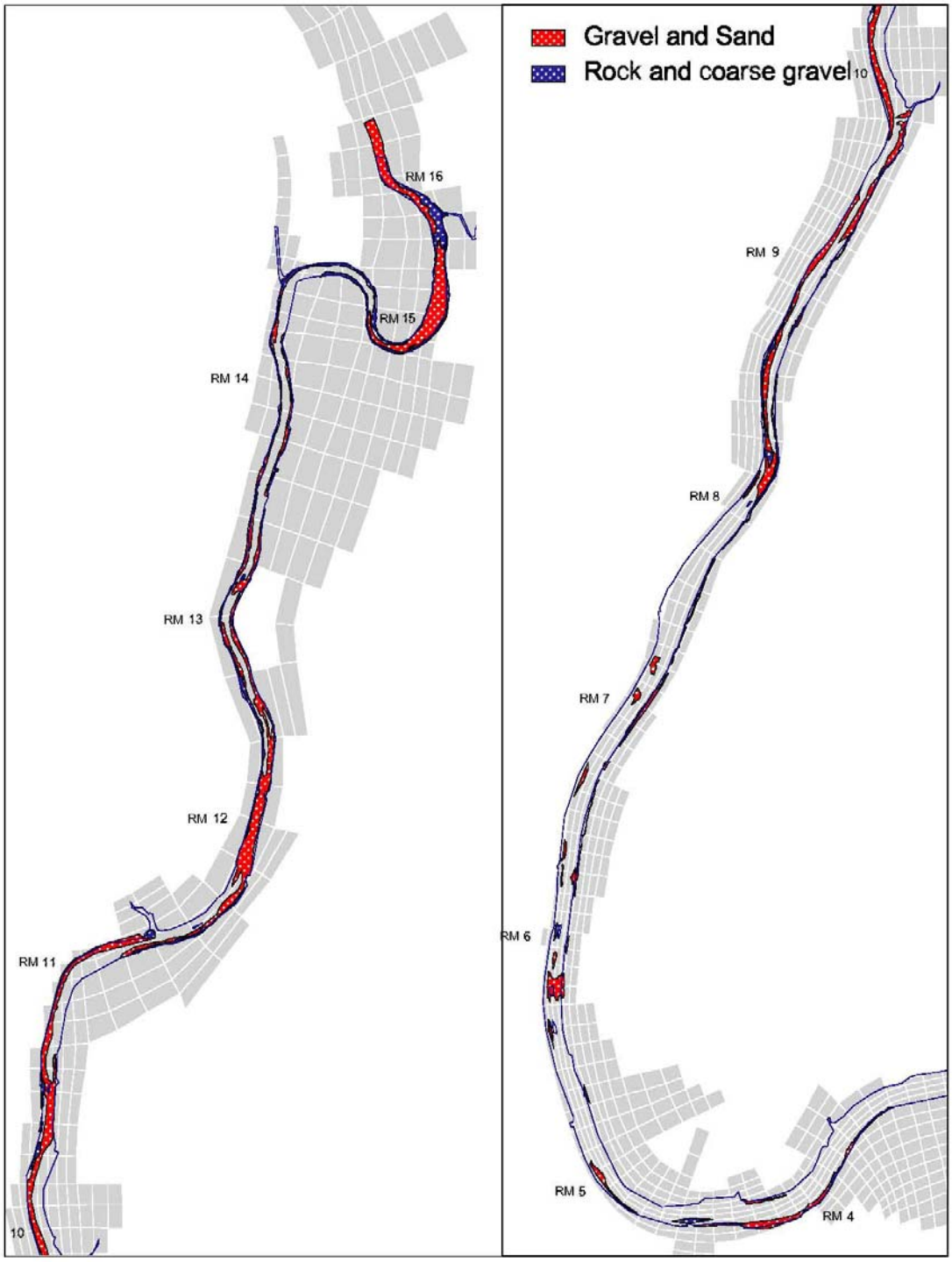

A map showing the distribution of rock, coarse gravel, gravel and sand in the Lower Passaic River

Lower Eight Miles of the Lower Passaic River

Figure 2-6

2014

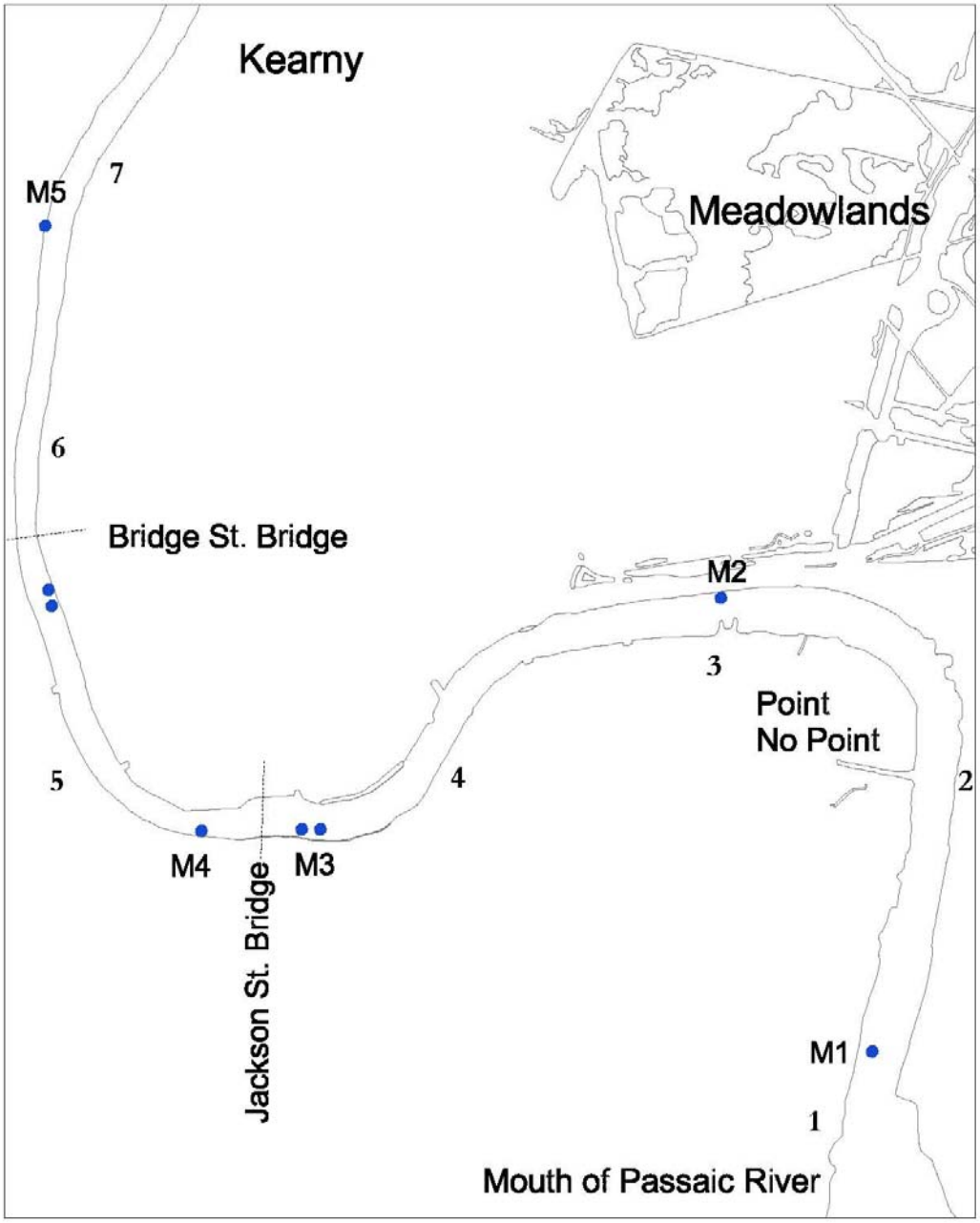

Locations of the 2004 IMCS field sampling stations in the Lower Passaic River

Figure 3-1

Lower Eight Miles of the Lower Passaic River

2014

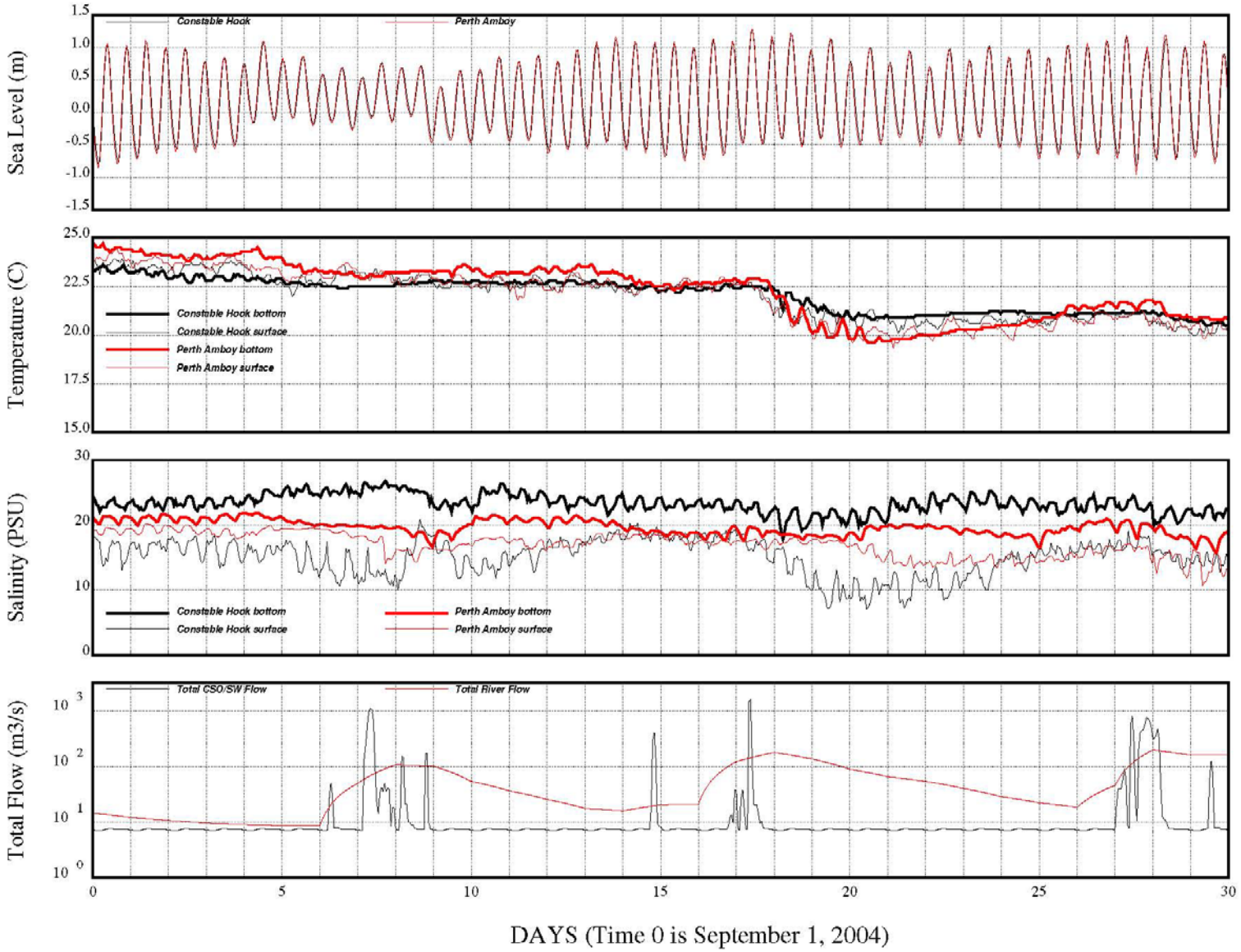

Boundary forcing data used for the model calibration

Figure 3-2

Lower Eight Miles of the Lower Passaic River

2014

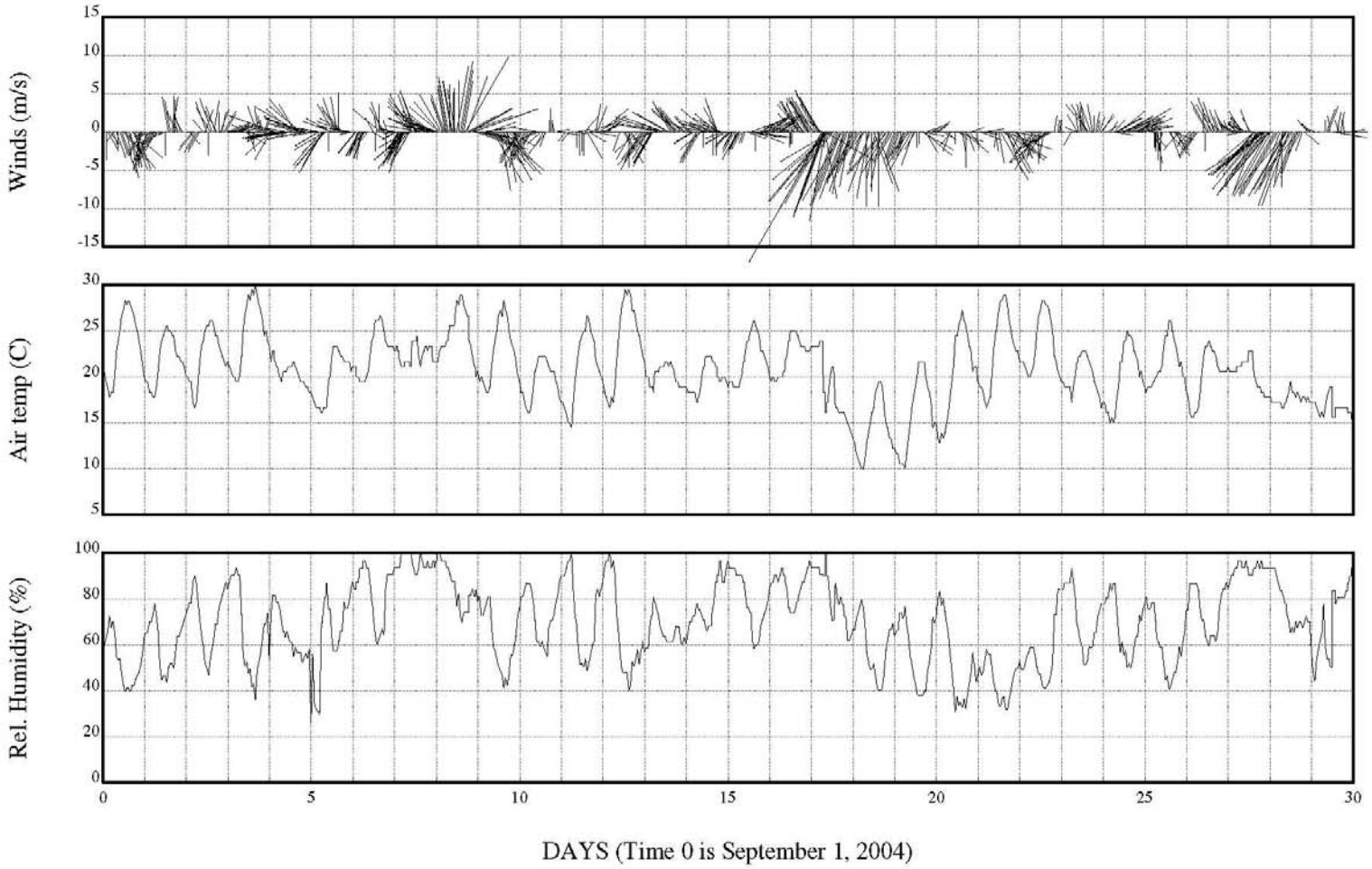

Meteorological data used for the model calibration. Data collected from Newark International Airport.

Lower Eight Miles of the Lower Passaic River

Figure 3-3

2014

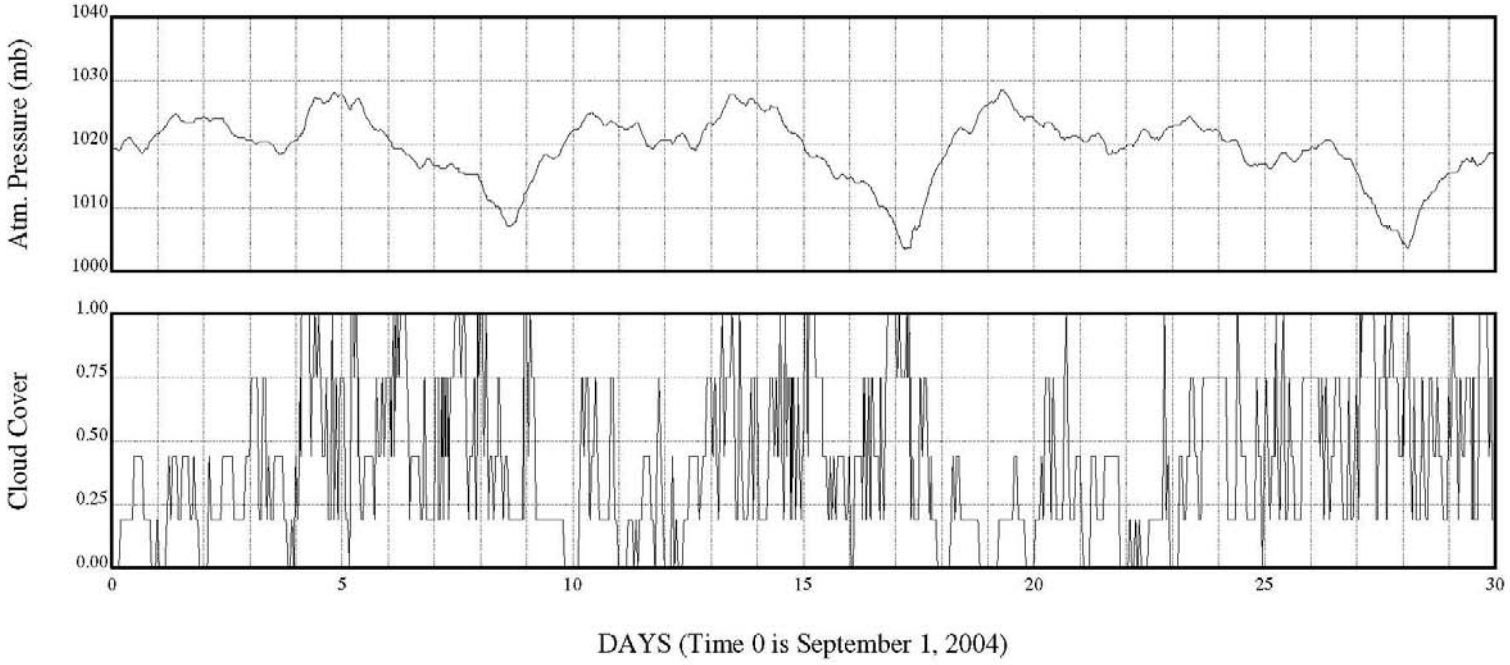

Meteorological data used for the model calibration. Data collected from Newark International Airport.

Figure 3-3 Continued

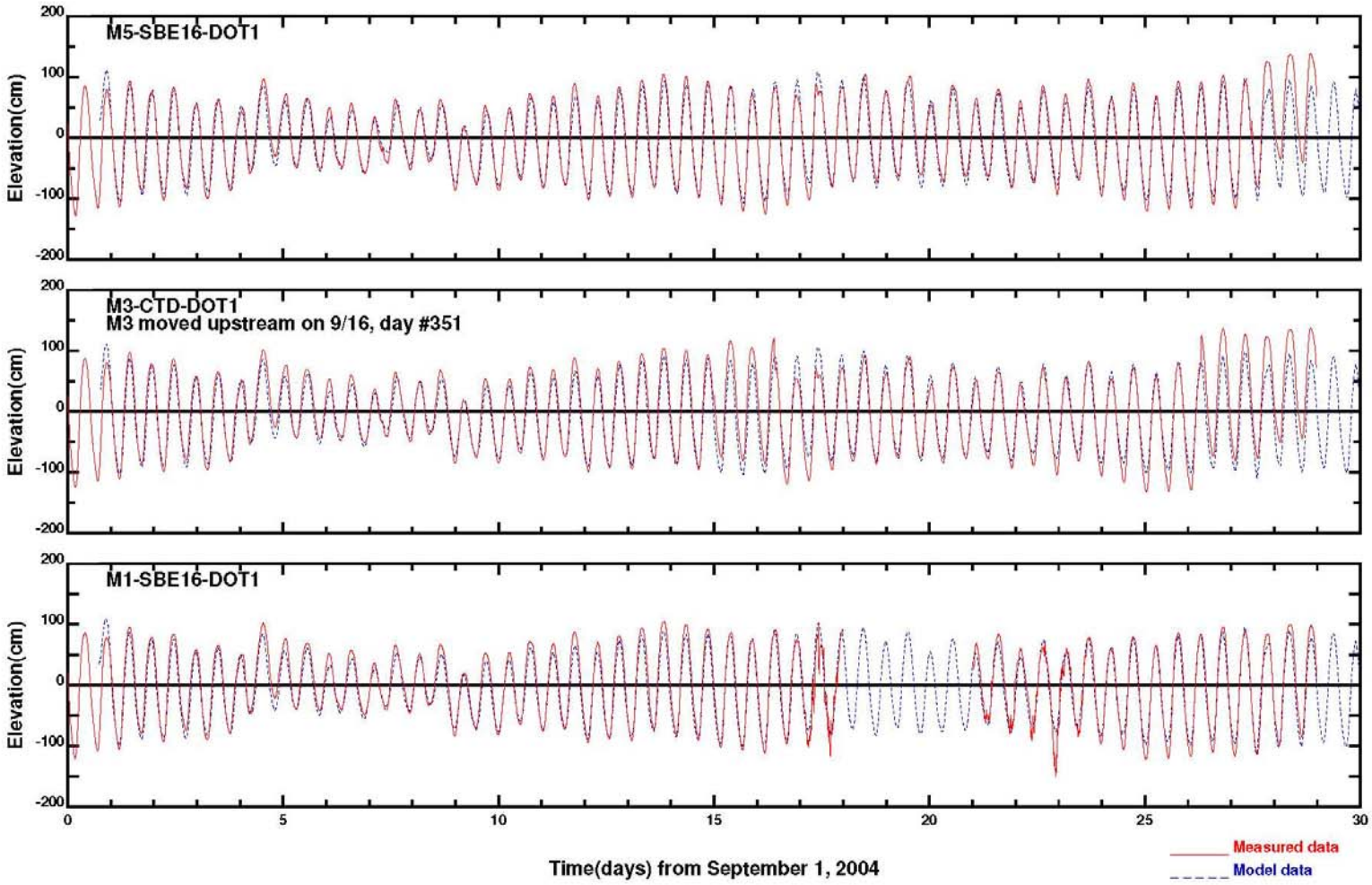

Comparison of computed water elevations with observed data

Figure 3-4

Lower Eight Miles of the Lower Passaic River

2014

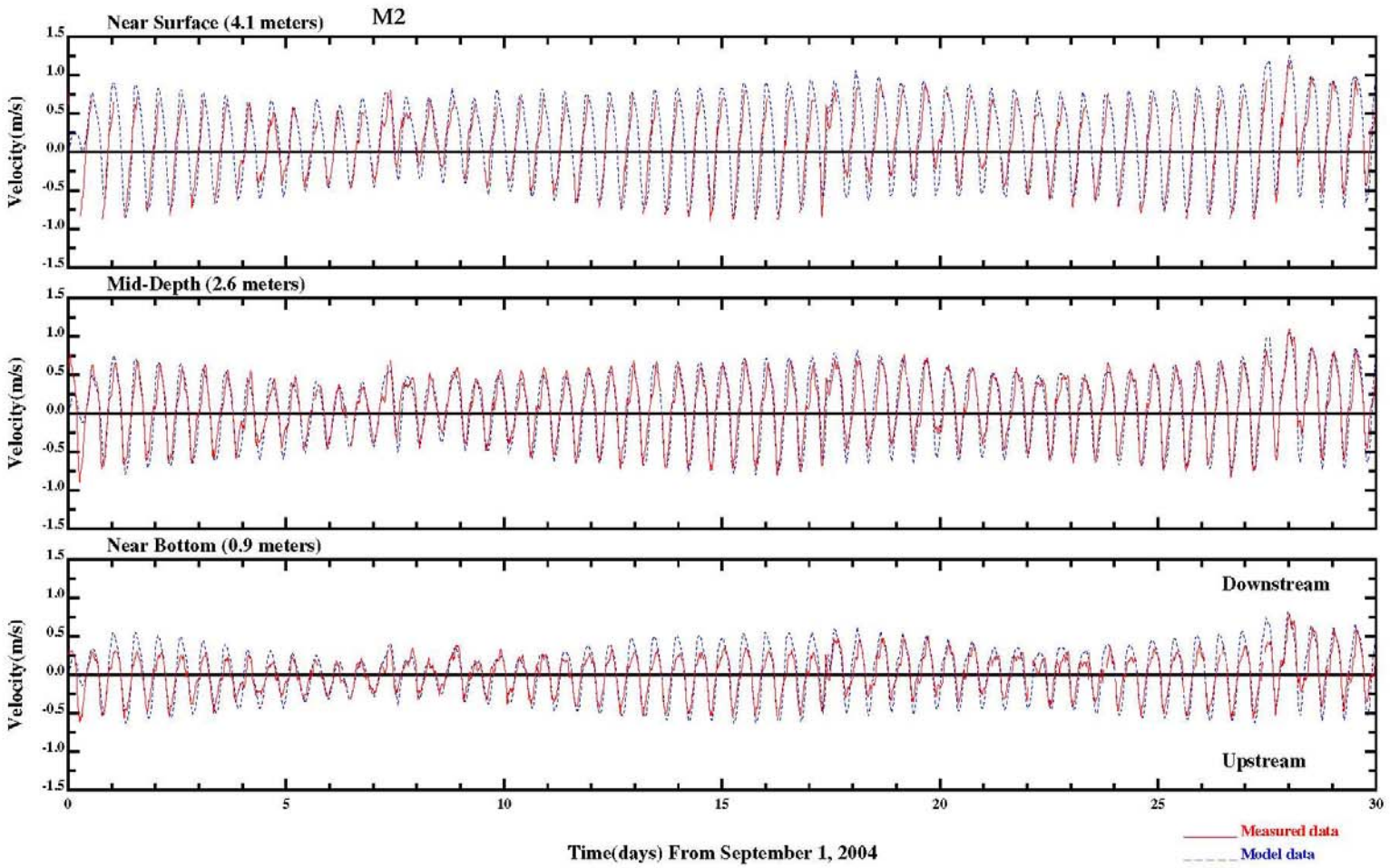

Comparison of computed current velocities at three depths with observed data at M2

Figure 3-5a

Lower Eight Miles of the Lower Passaic River

2014

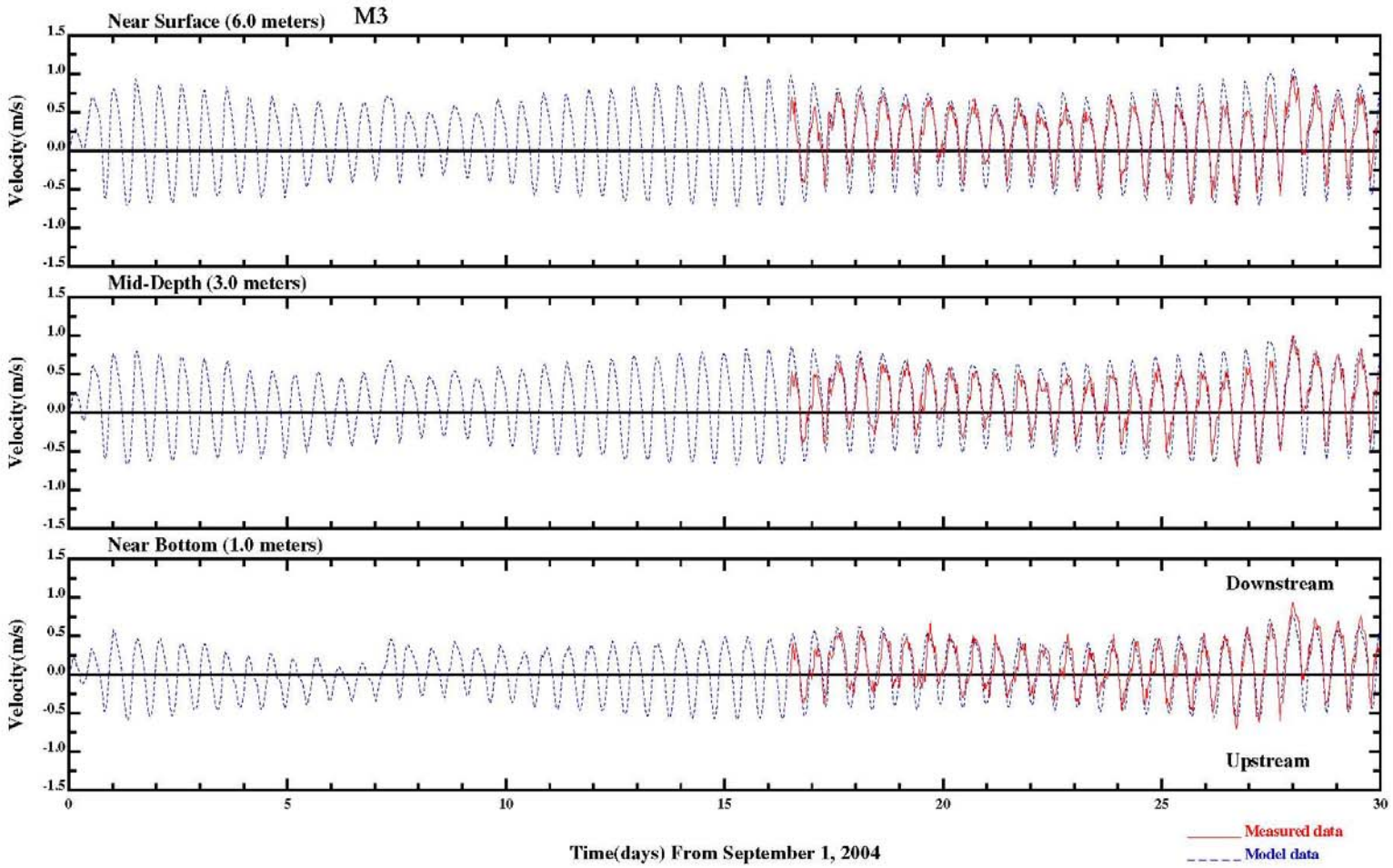

Comparison of computed current velocities at three depths with observed data at M3

Figure 3-5b

Lower Eight Miles of the Lower Passaic River

2014

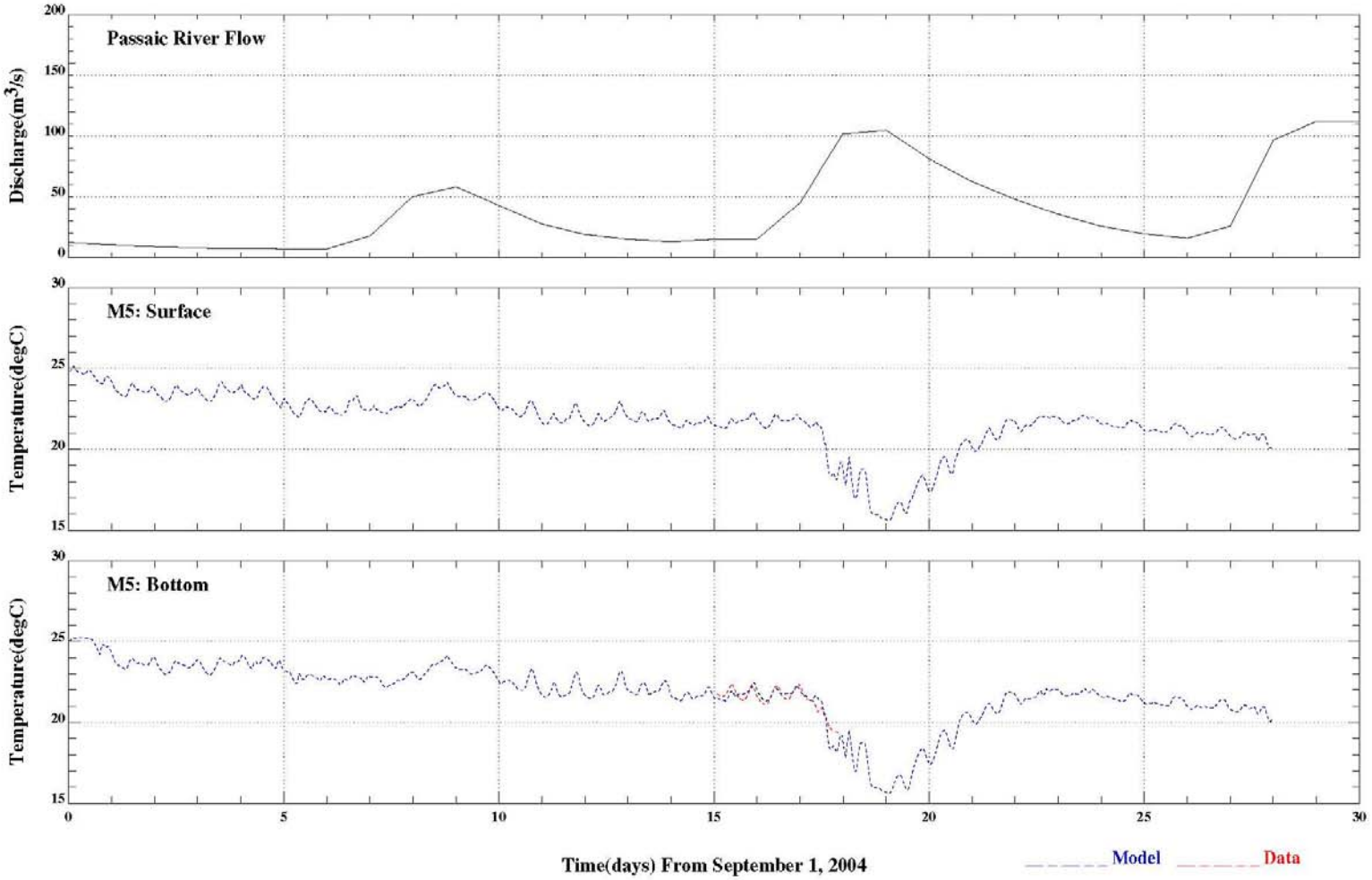

Comparison of computed water temperature with observed data

Figure 3-6

Lower Eight Miles of the Lower Passaic River

2014

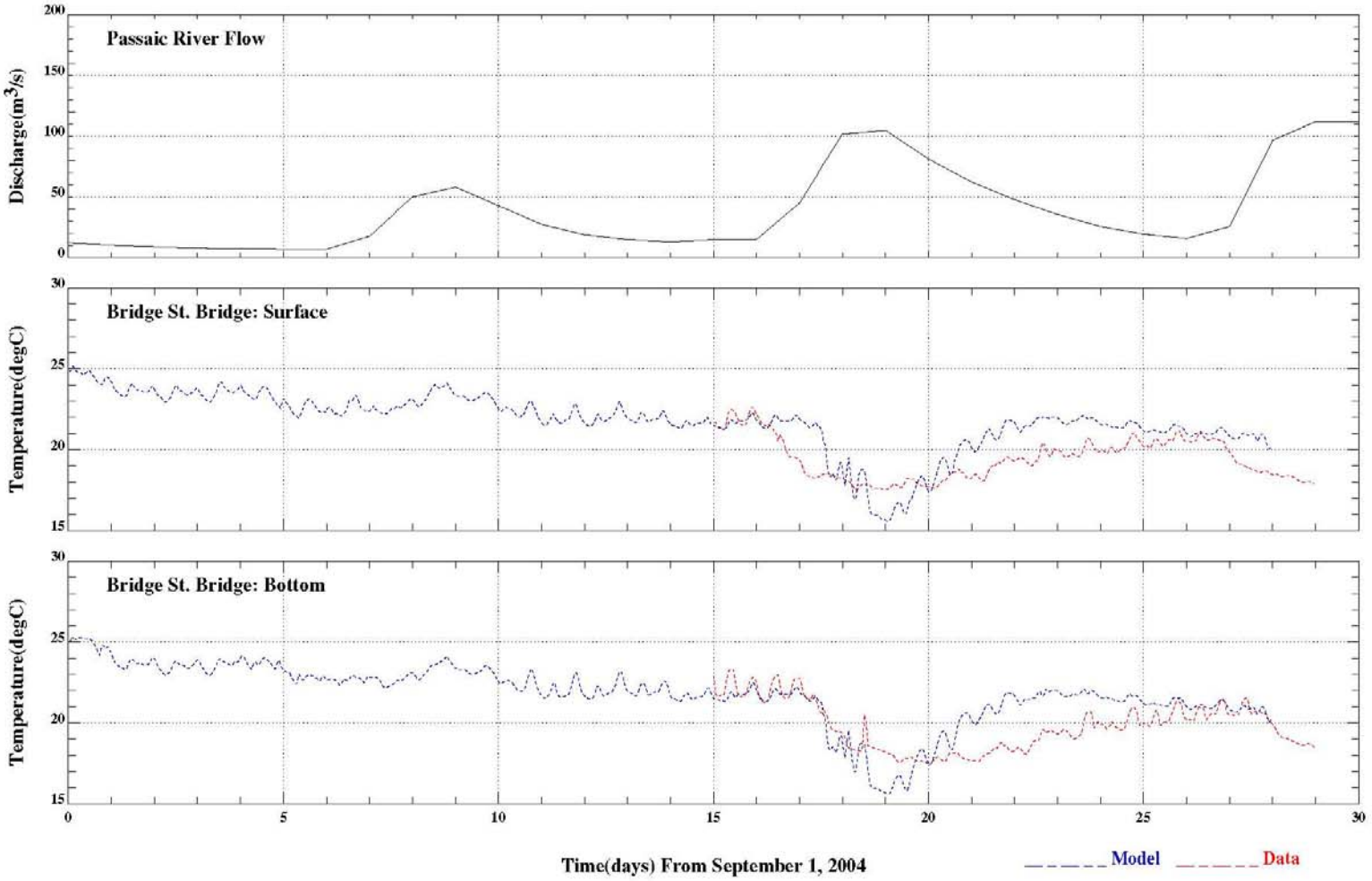

Comparison of computed water temperature with observed data

Figure 3-6 Continued

Lower Eight Miles of the Lower Passaic River

2014

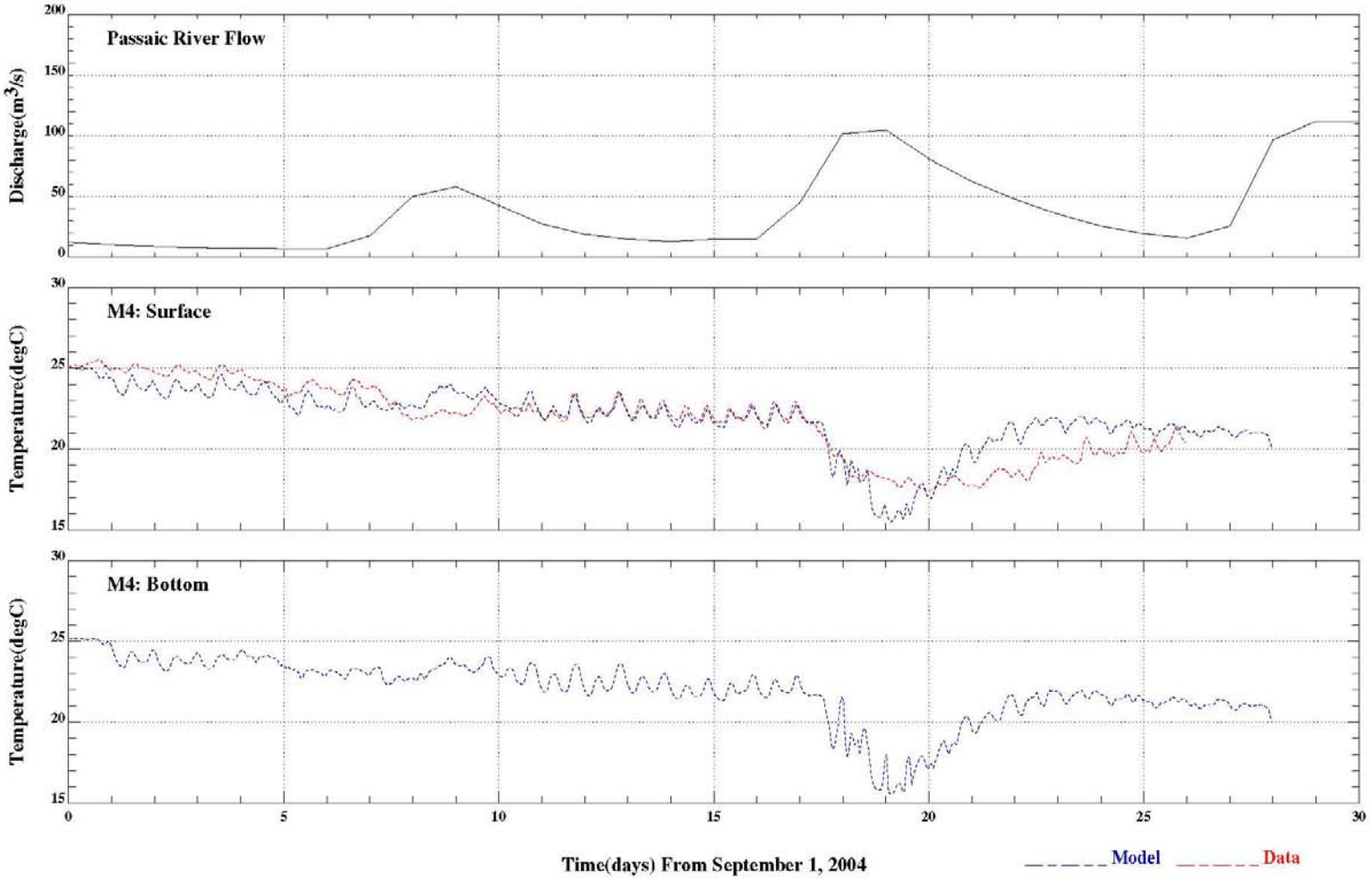

Comparison of computed water temperature with observed data

Figure 3-6 Continued

Lower Eight Miles of the Lower Passaic River

2014

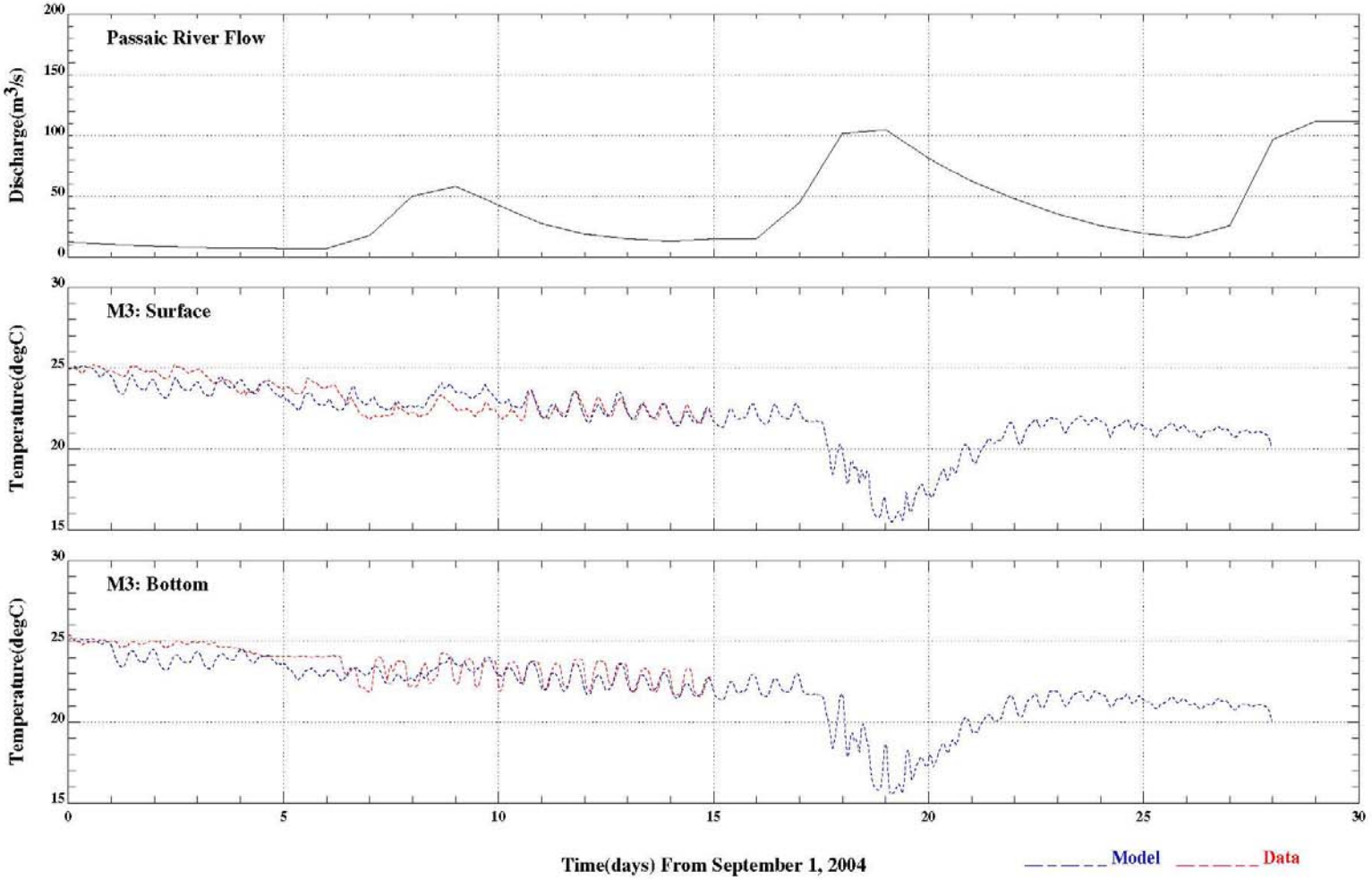

Comparison of computed water temperature with observed data

Figure 3-6 Continued

Lower Eight Miles of the Lower Passaic River

2014

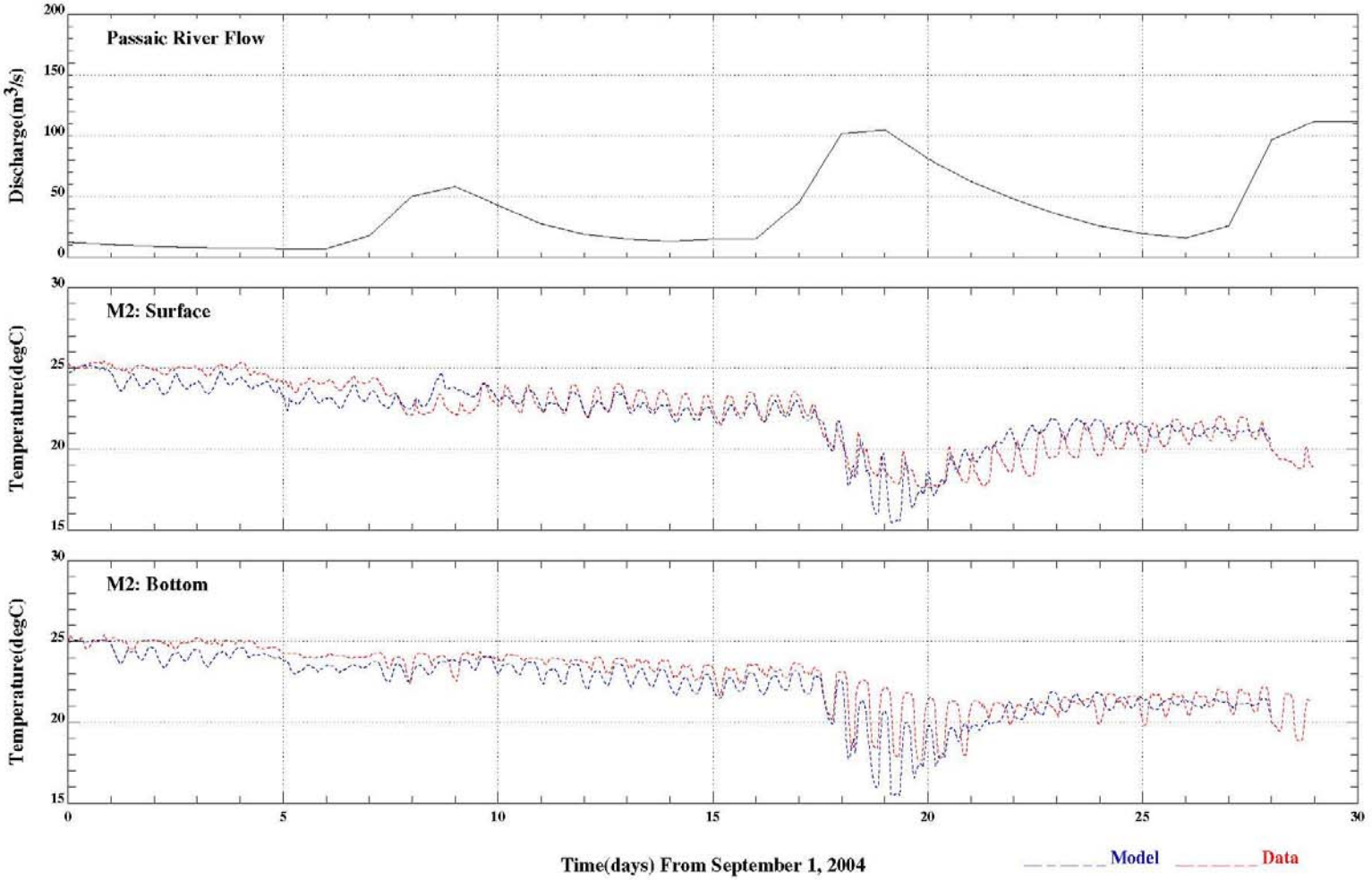

Comparison of computed water temperature with observed data

Figure 3-6 Continued

Lower Eight Miles of the Lower Passaic River

2014

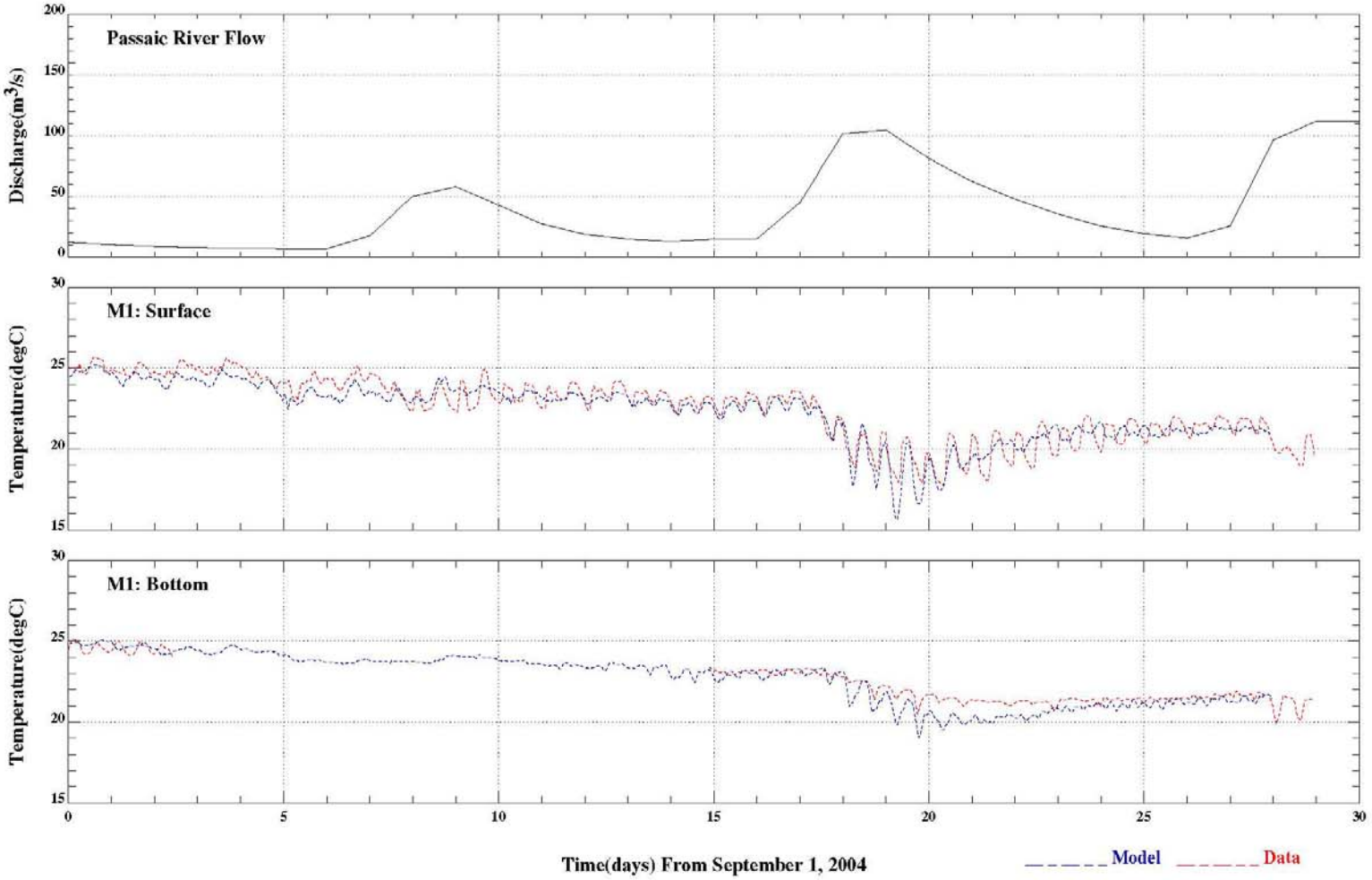

Comparison of computed water temperature with observed data

Figure 3-6 Continued

Lower Eight Miles of the Lower Passaic River

2014

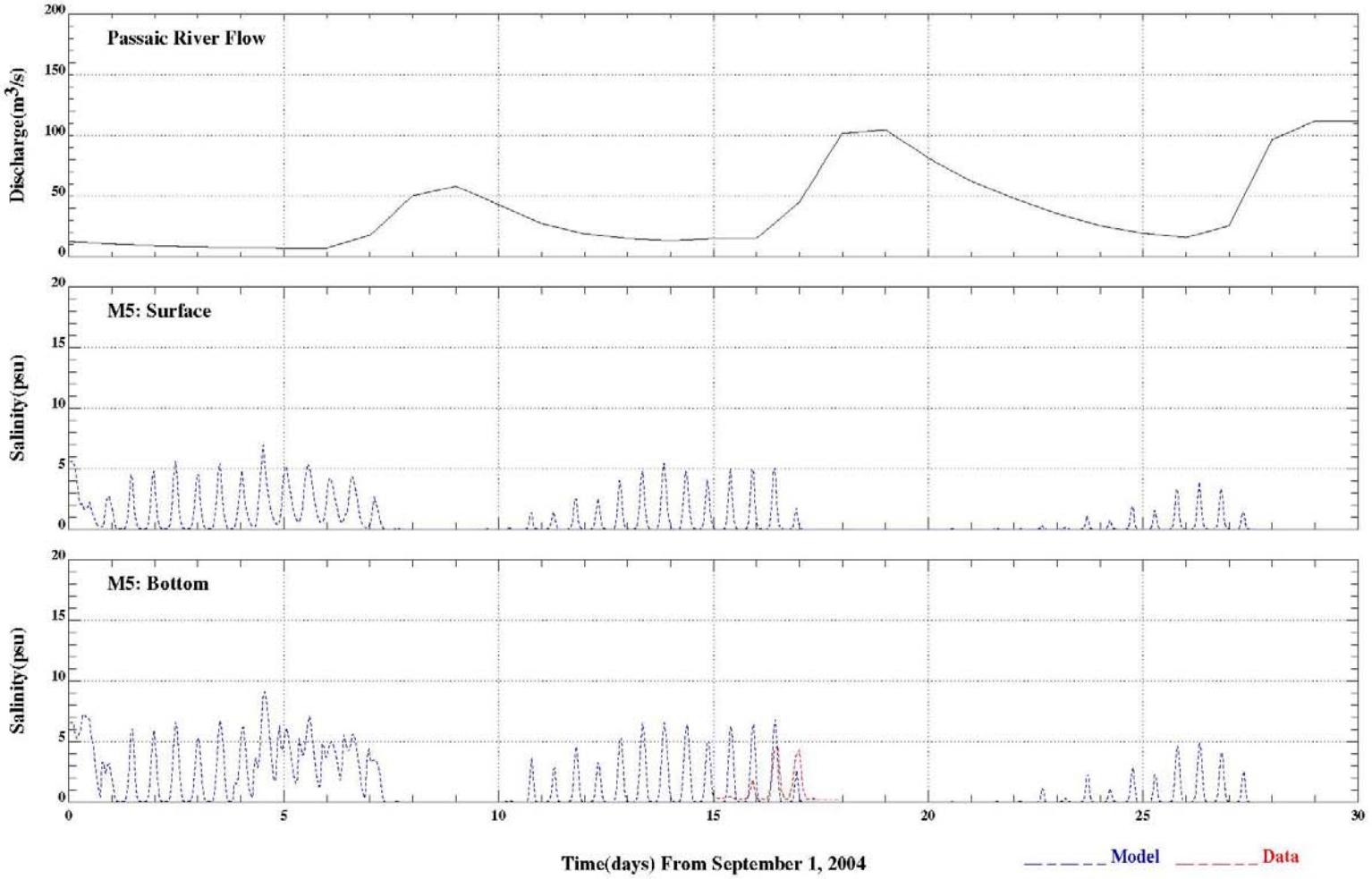

Comparison of computed salinity with observed data	Figure 3-7
Lower Eight Miles of the Lower Passaic River	2014

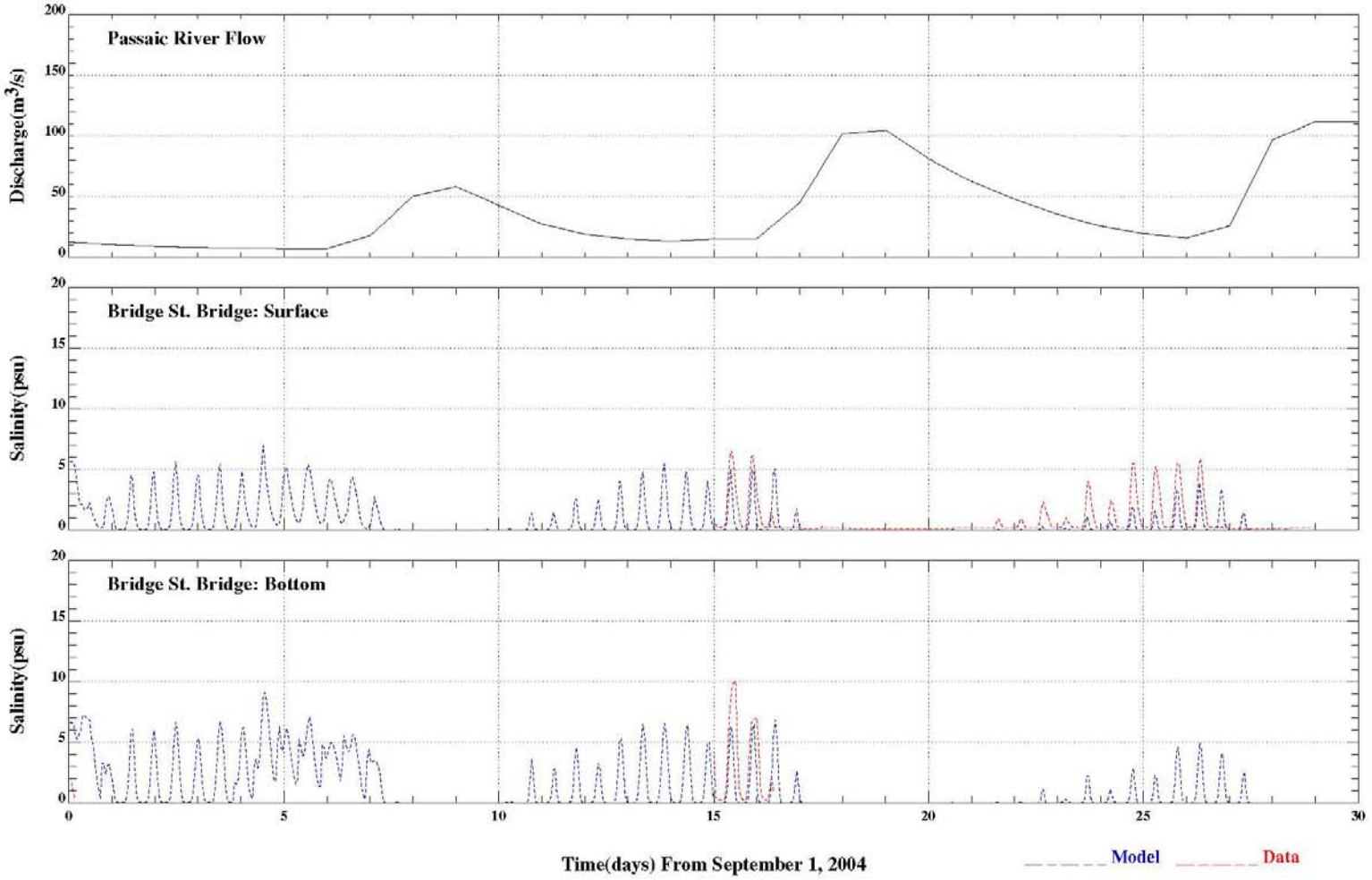

Comparison of computed salinity with observed data

Figure 3-7 Continued

Lower Eight Miles of the Lower Passaic River

2014

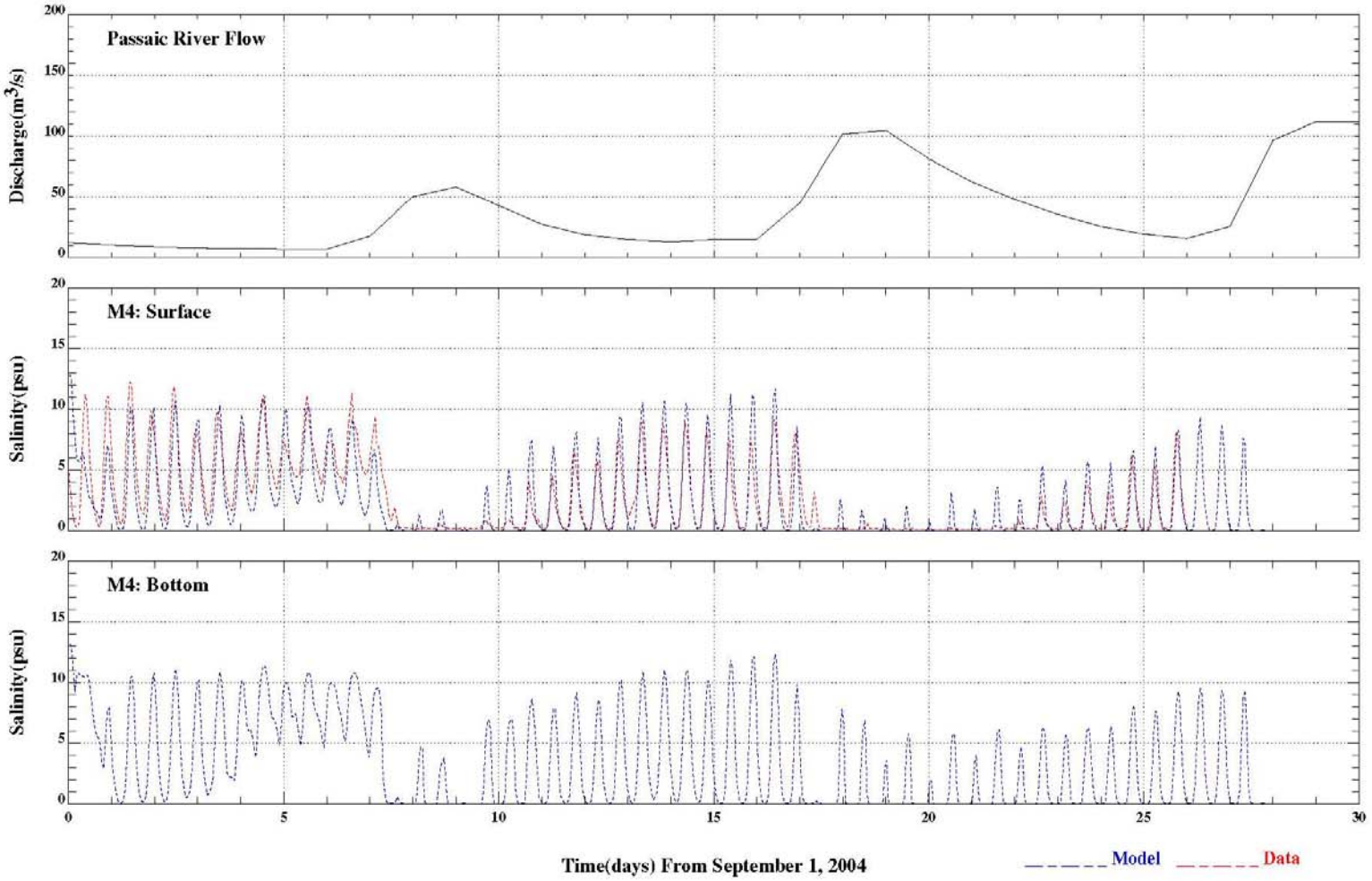

Comparison of computed salinity with observed data

Figure 3-7 Continued

Lower Eight Miles of the Lower Passaic River

2014

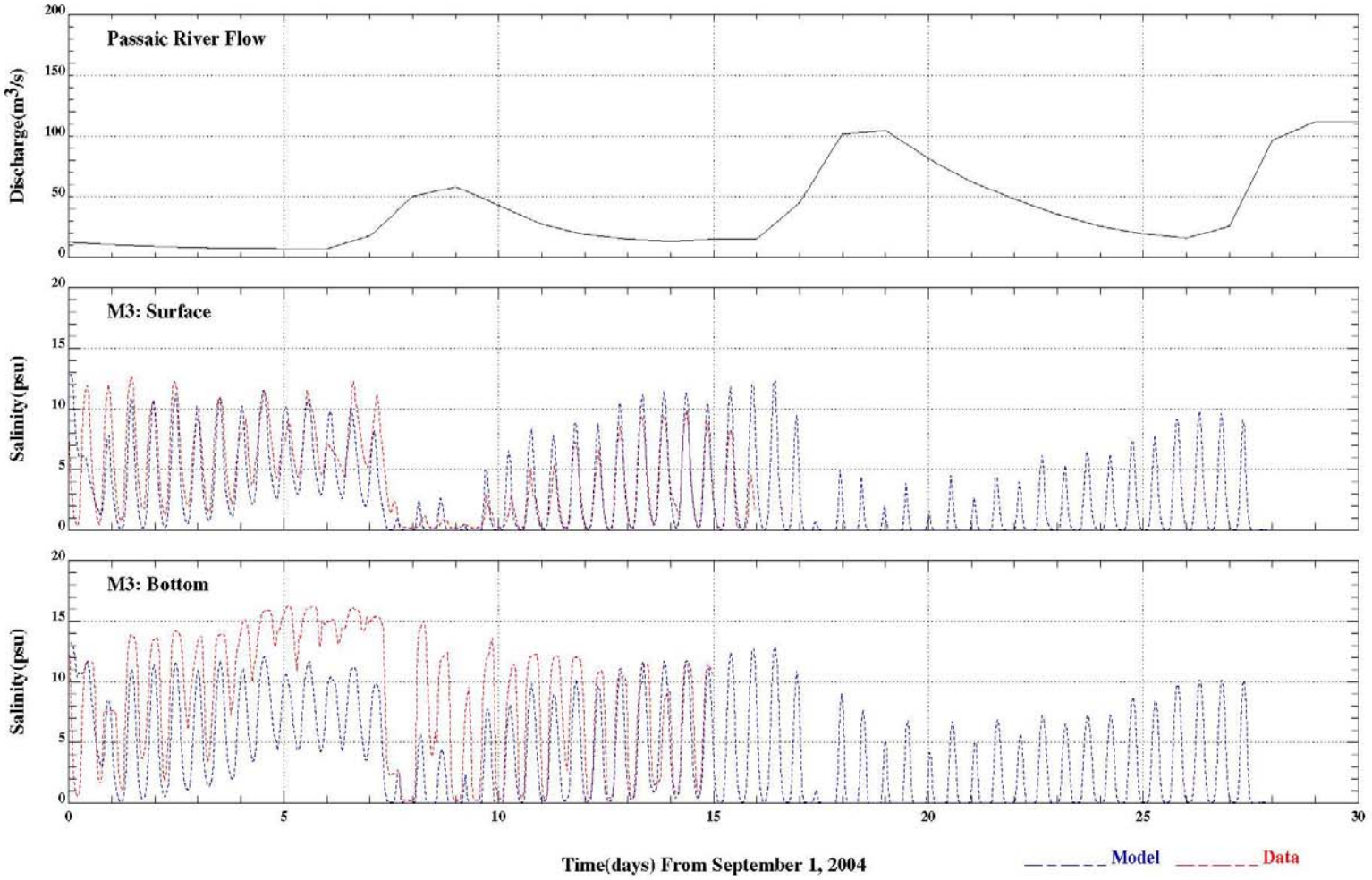

Comparison of computed salinity with observed data

Figure 3-7 Continued

Lower Eight Miles of the Lower Passaic River

2014

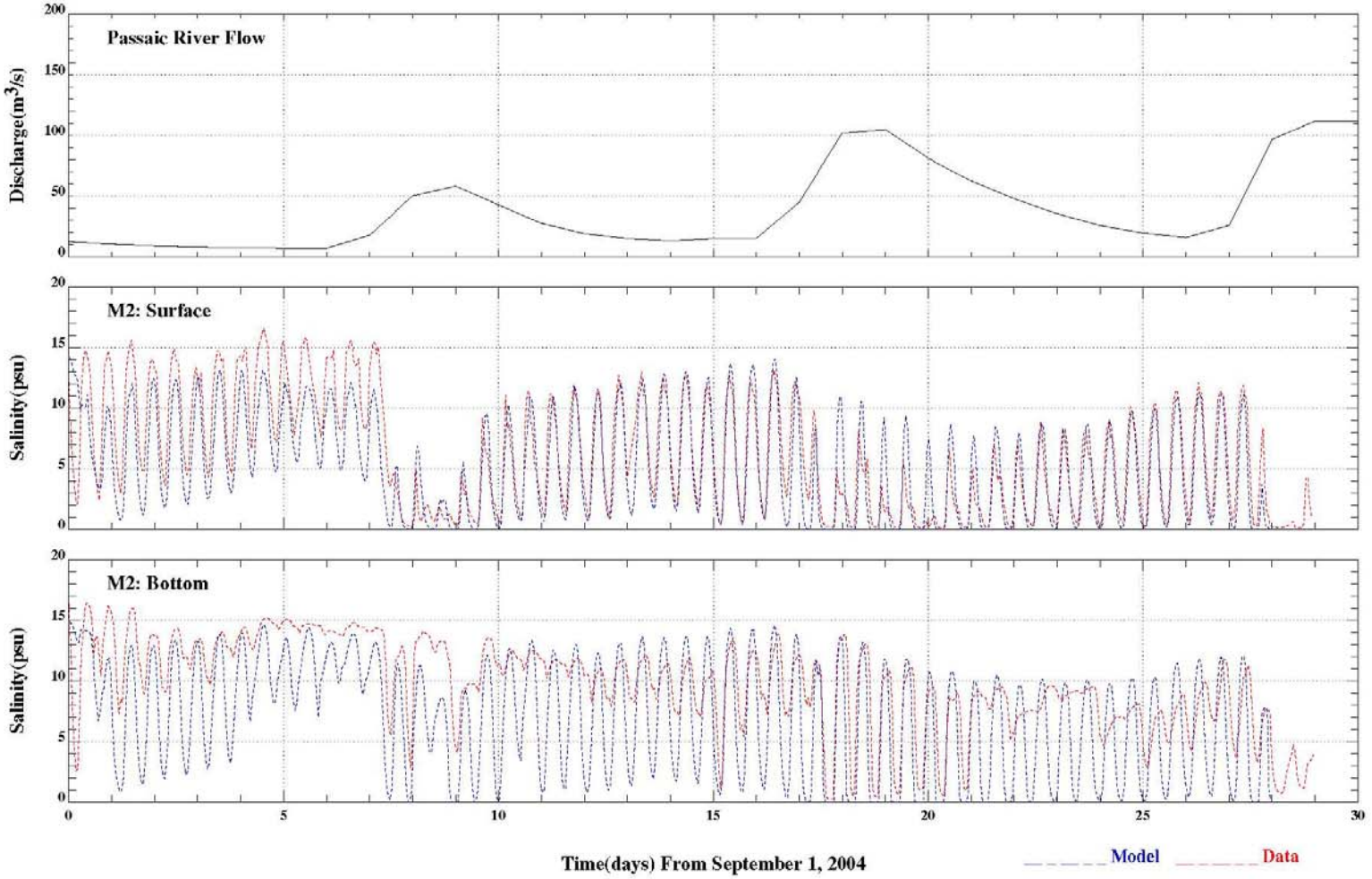

Comparison of computed salinity with observed data	Figure 3-7 Continued
Lower Eight Miles of the Lower Passaic River	2014

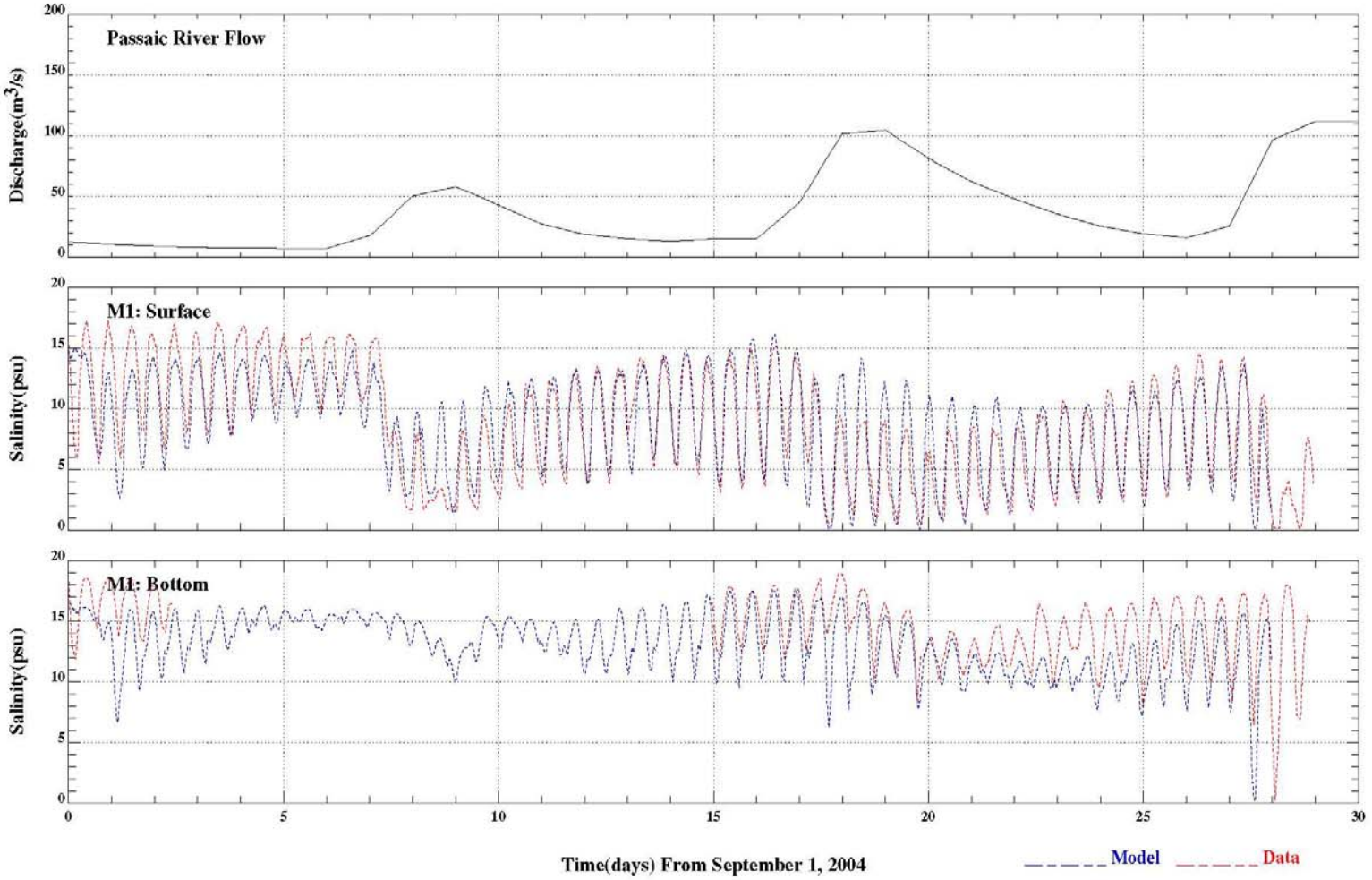

Comparison of computed salinity with observed data

Figure 3-7 Continued

Lower Eight Miles of the Lower Passaic River

2014

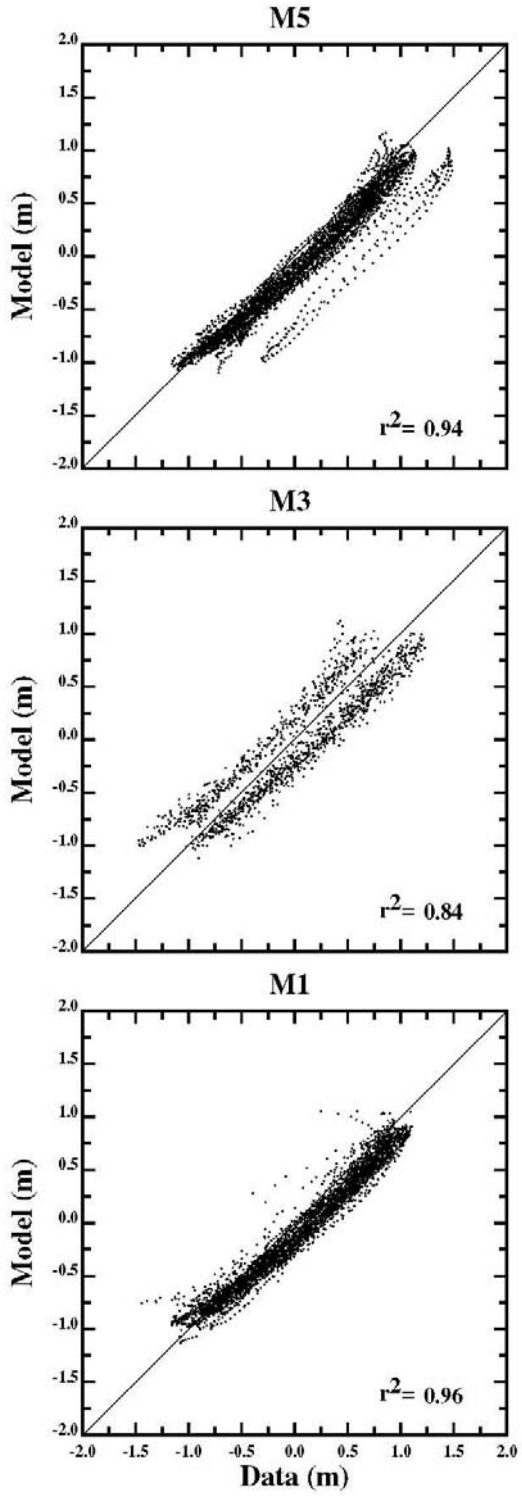

Scatter plot of computed water elevation with observed data

Figure 3-8

Lower Eight Miles of the Lower Passaic River

2014

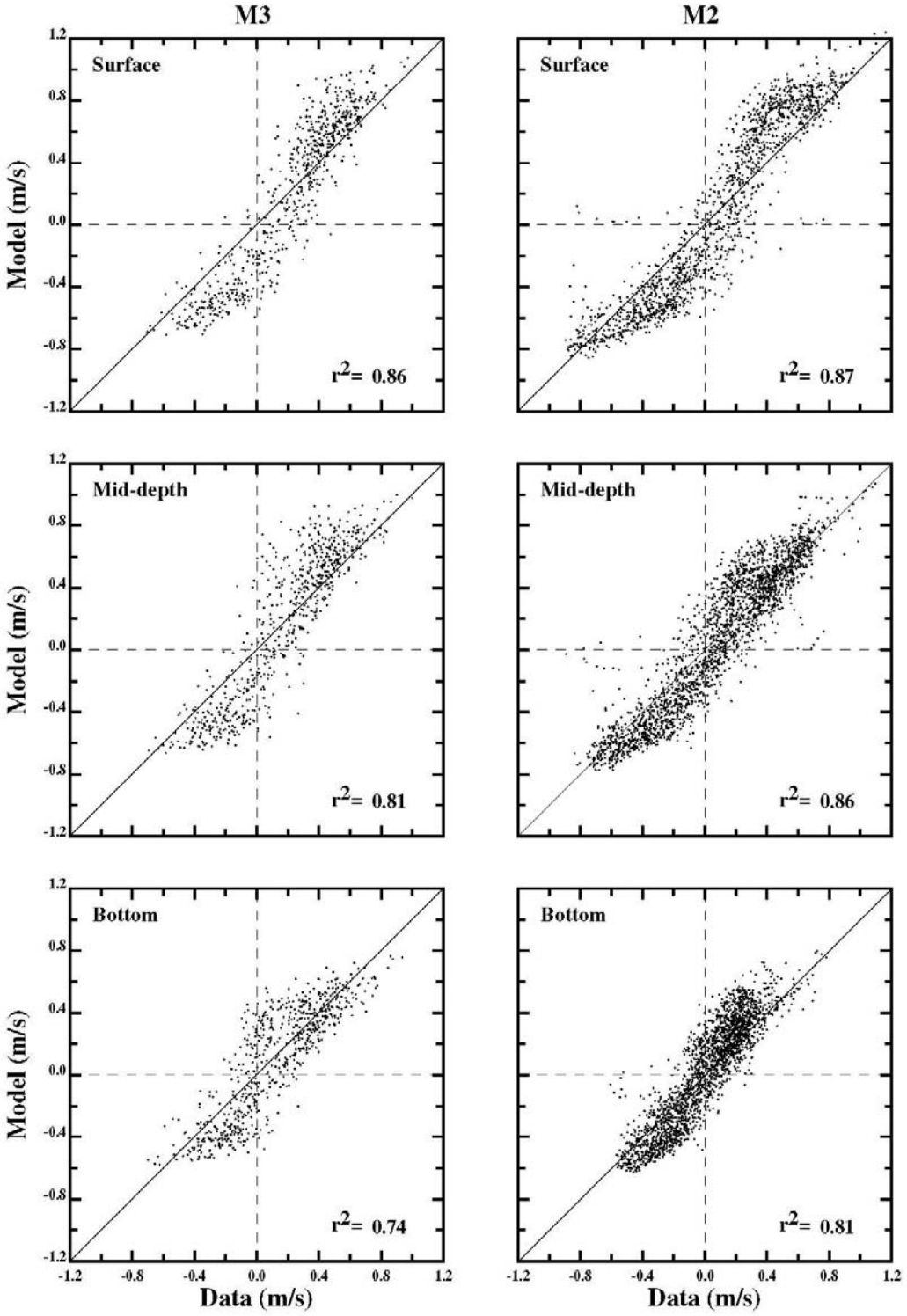

Scatter plot of computed current velocities with observed data

Figure 3-9

Lower Eight Miles of the Lower Passaic River

2014

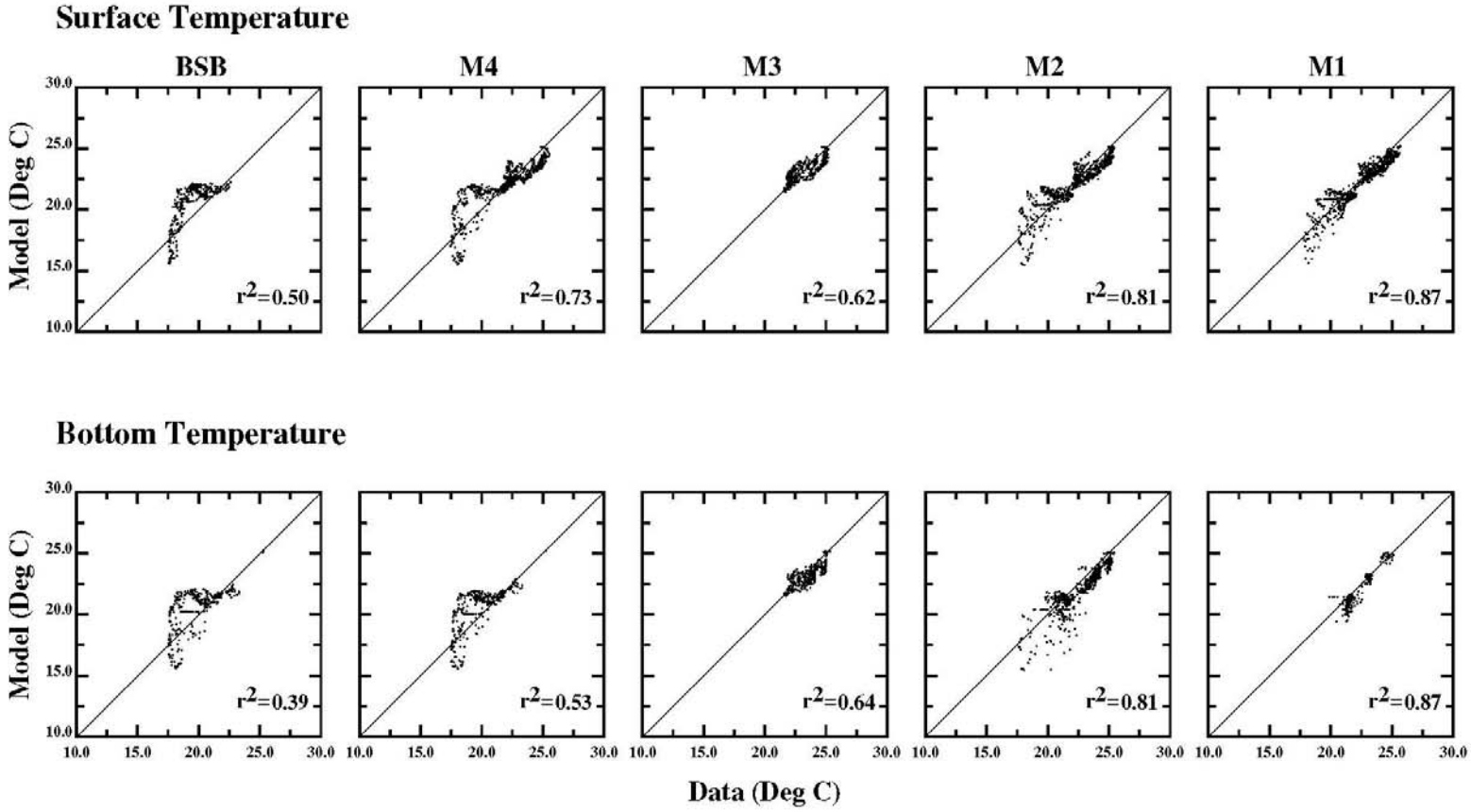

Scatter plot of computed temperature with observed data

Figure 3-10

Lower Eight Miles of the Lower Passaic River

2014

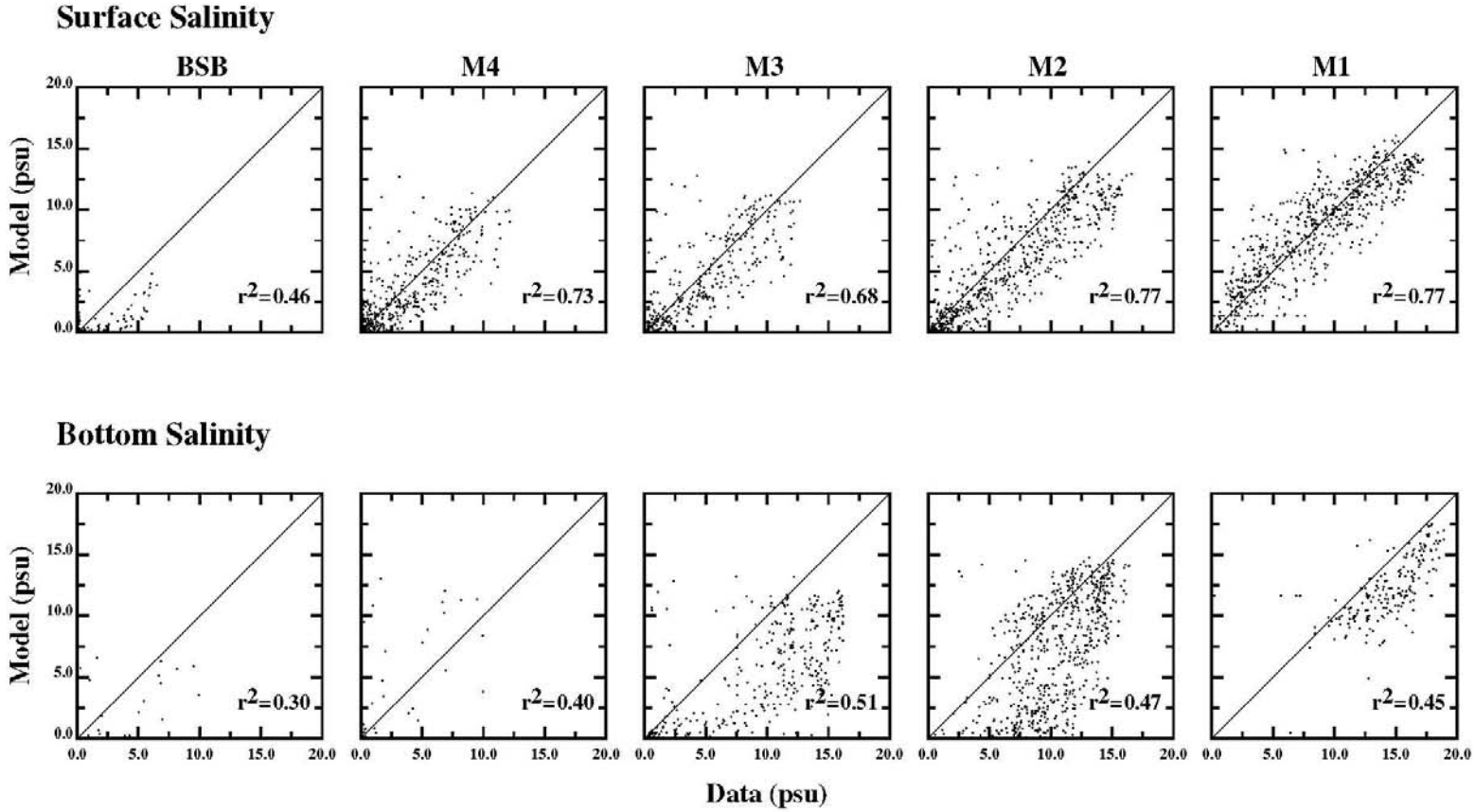

Scatter plot of computed salinity with observed data

Figure 3-11

Lower Eight Miles of the Lower Passaic River

2014

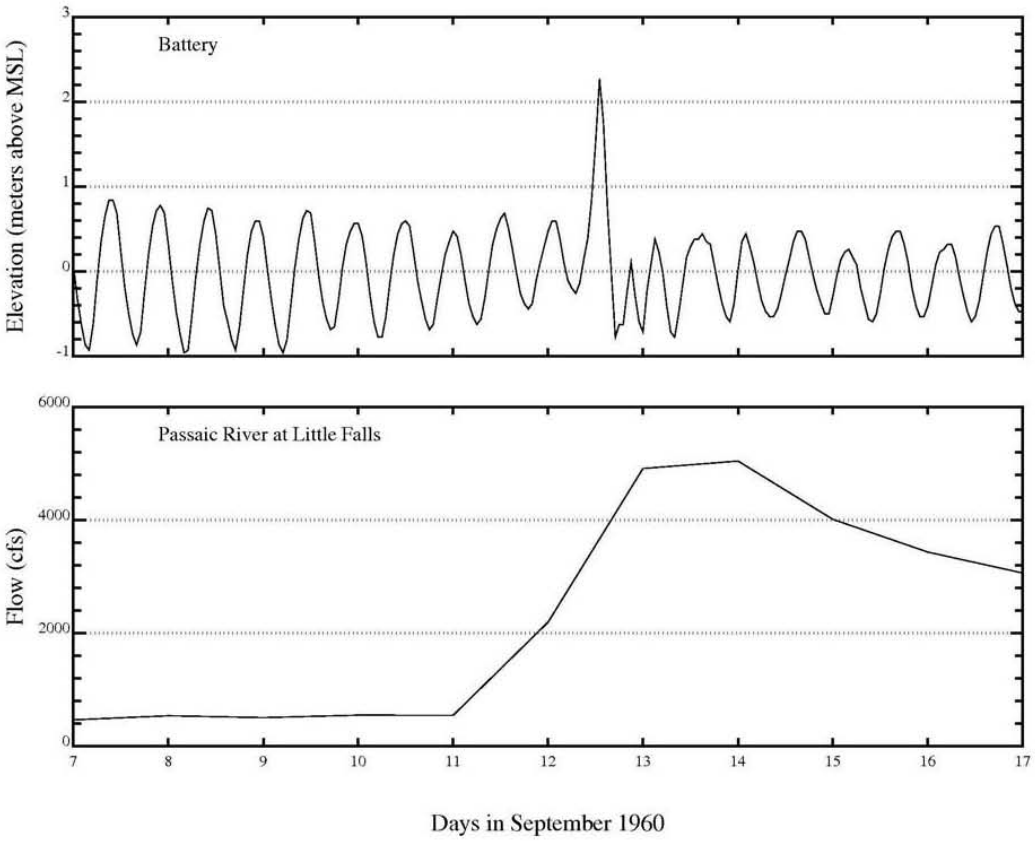

Observed water elevation at the Battery and the Passaic River flow at Little Falls during Hurricane Donna *Lower Eight Miles of the Lower Passaic River*	Figure 4-1 2014

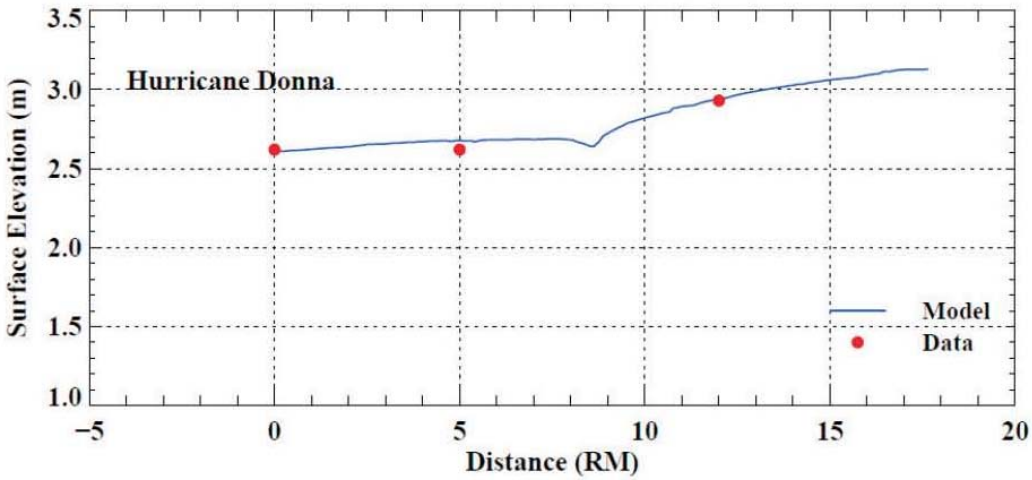

Maximum water elevations along the Lower Passaic River during Hurricane Donna *Lower Eight Miles of the Lower Passaic River*	Figure 4-2 2014

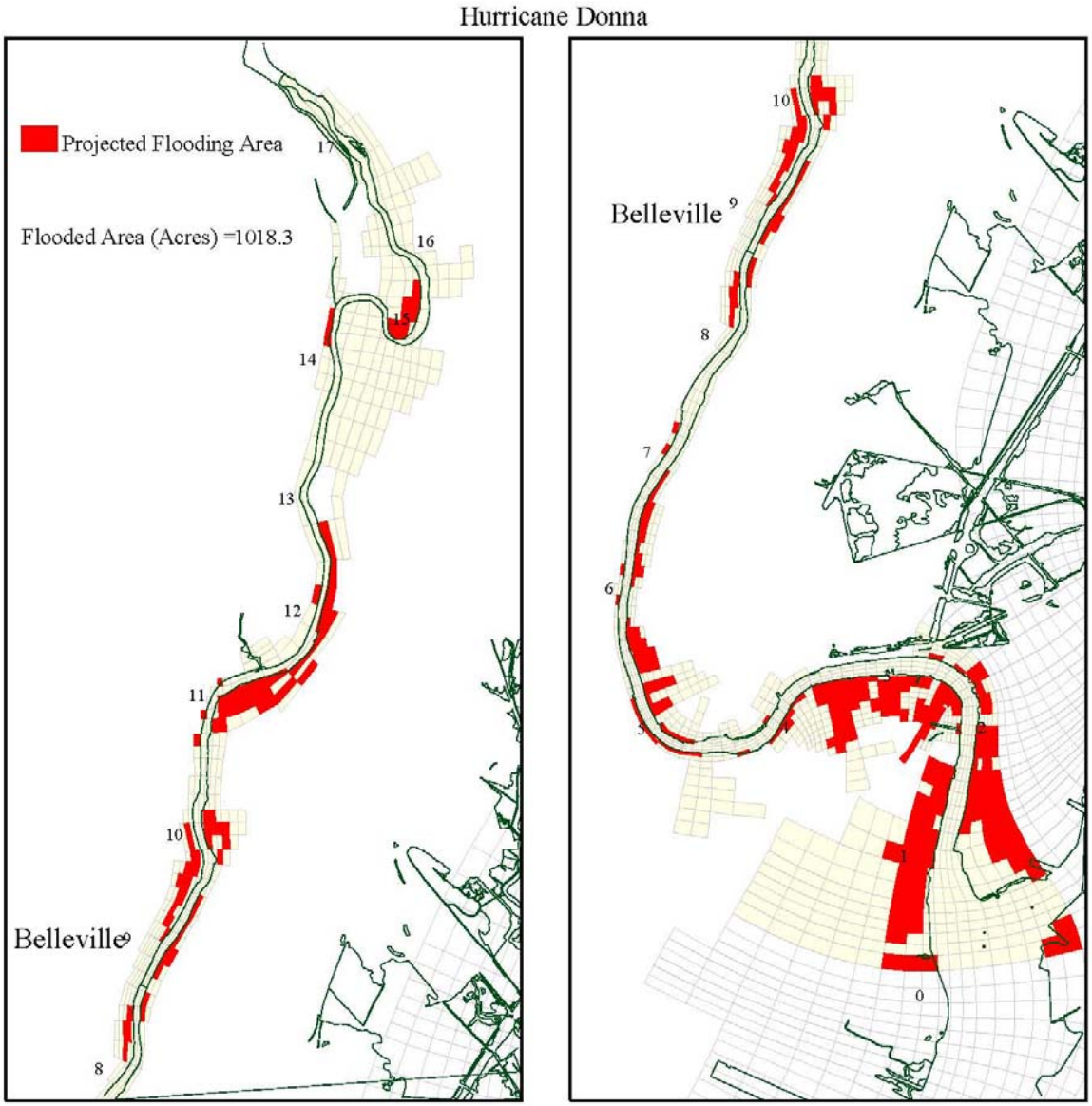

Projected flood area during Hurricane Donna	Figure 4-3
Lower Eight Miles of the Lower Passaic River	2014

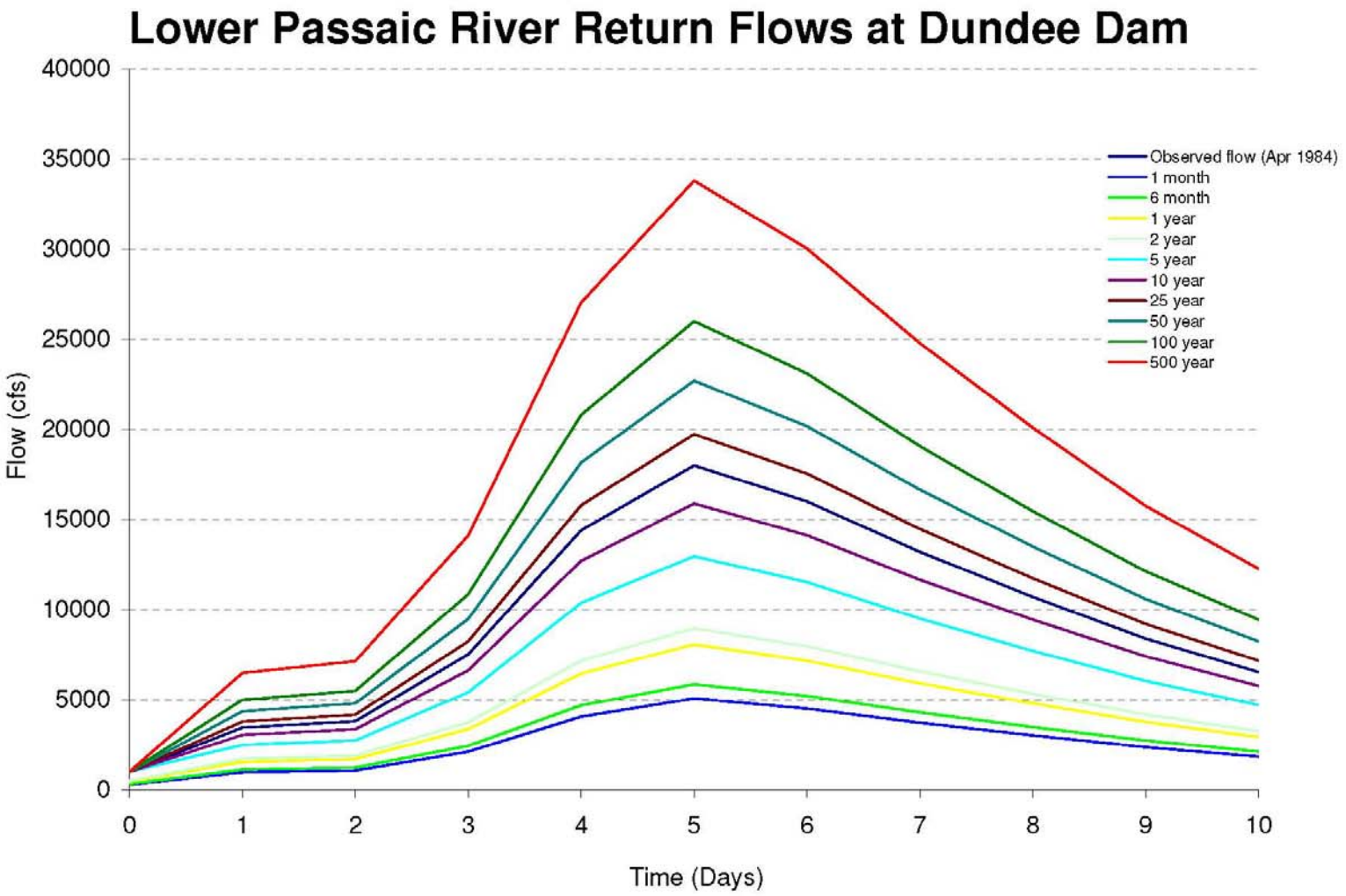

Lower Passaic River Return Flows at Dundee Dam	Figure 5-1
Lower Eight Miles of the Lower Passaic River	2014

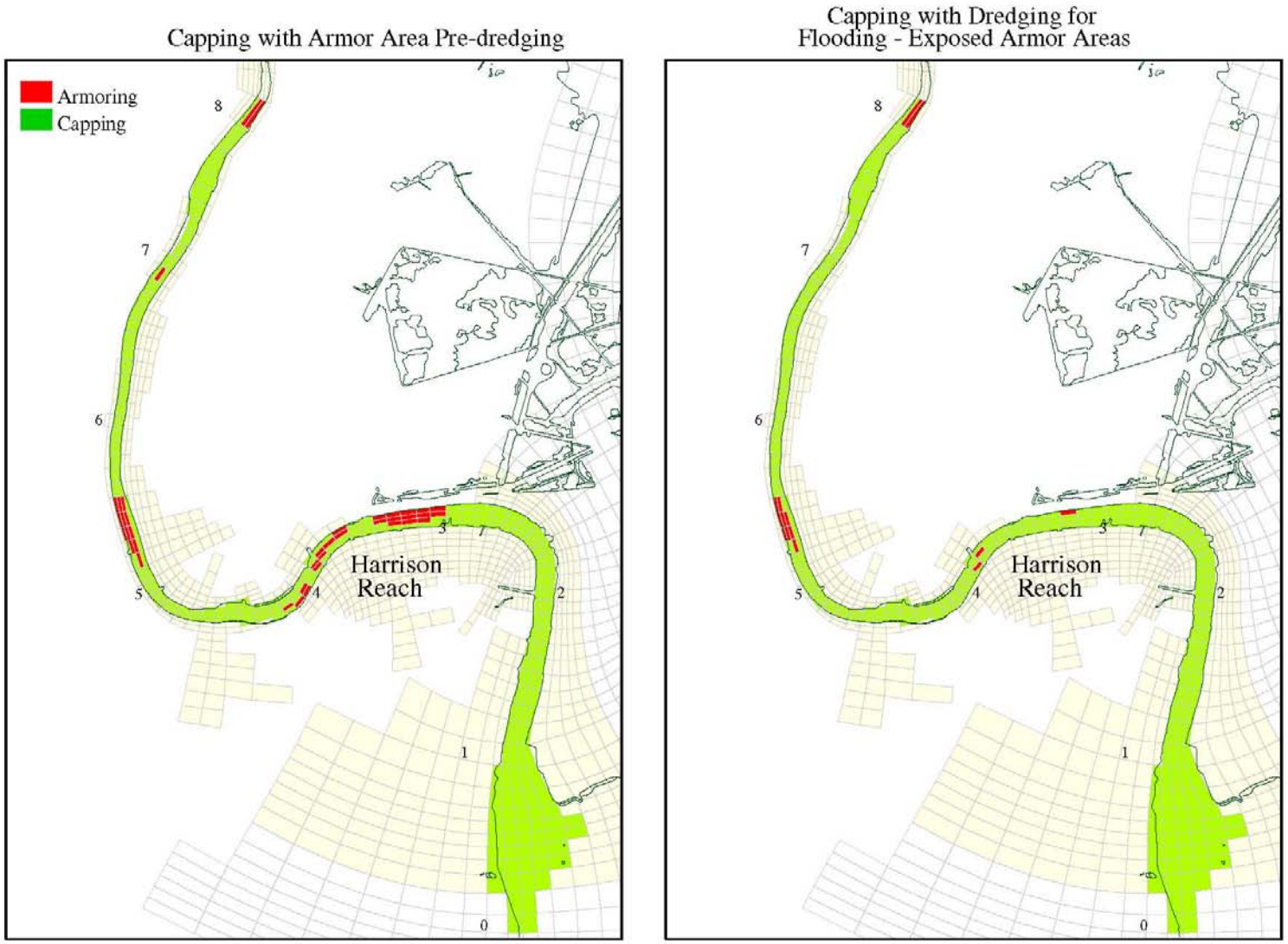

Capped and armored areas between RM0 and RM8.3 for different simulation scenarios. Only two layouts are shown because the layout for "Capping with Dredging for Flooding" is identical to "Capping with Dredging for Flooding – Exposed Armor Areas."

Lower Eight Miles of the Lower Passaic River

Figure 5-2

2014

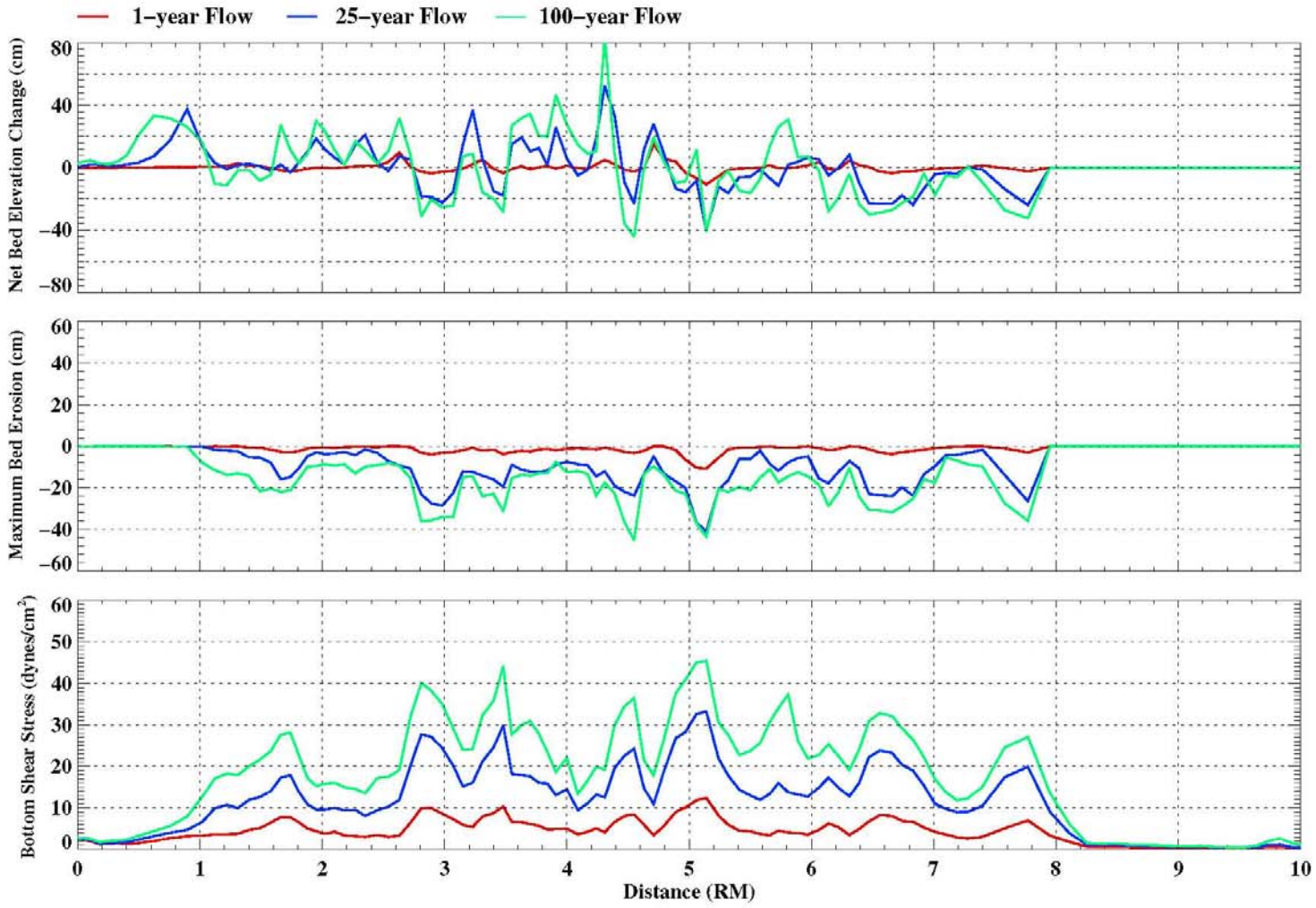

Cross-river average net bed elevation change, the maximum erosion, and bottom shear stress along the river under the 1-year, 25-year and 100-year return flow conditions at the end of each simulation (Ambrose sand used as the capping material under the "8-Mile Cap" Scenario).

Lower Eight Miles of the Lower Passaic River

Figure 5-3

2014

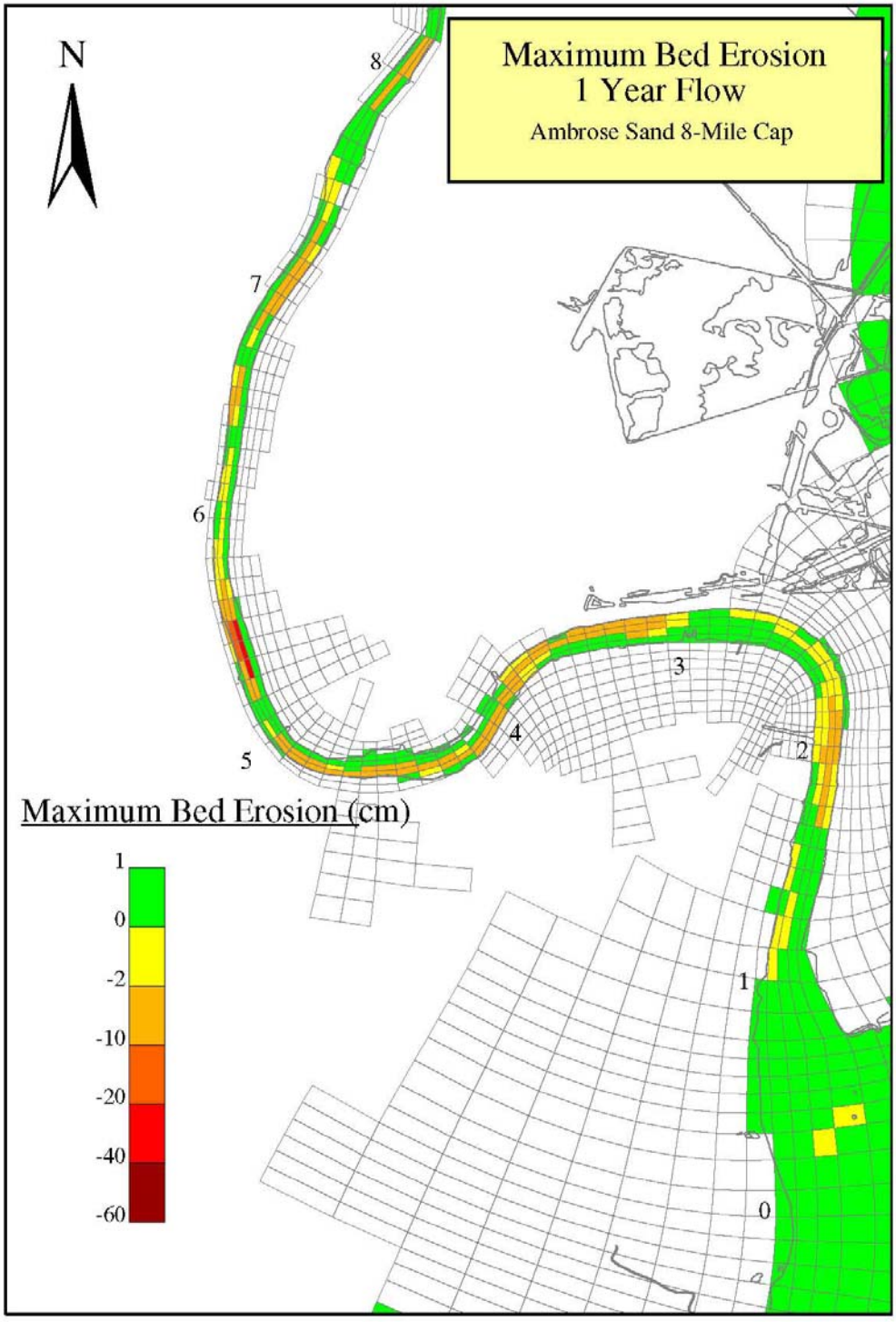

Plan view of the maximum erosion under the 1-year return flow conditions (Ambrose sand used as the capping material under the "8-Mile Cap" Scenario).

Lower Eight Miles of the Lower Passaic River

Figure 5-4a

2014

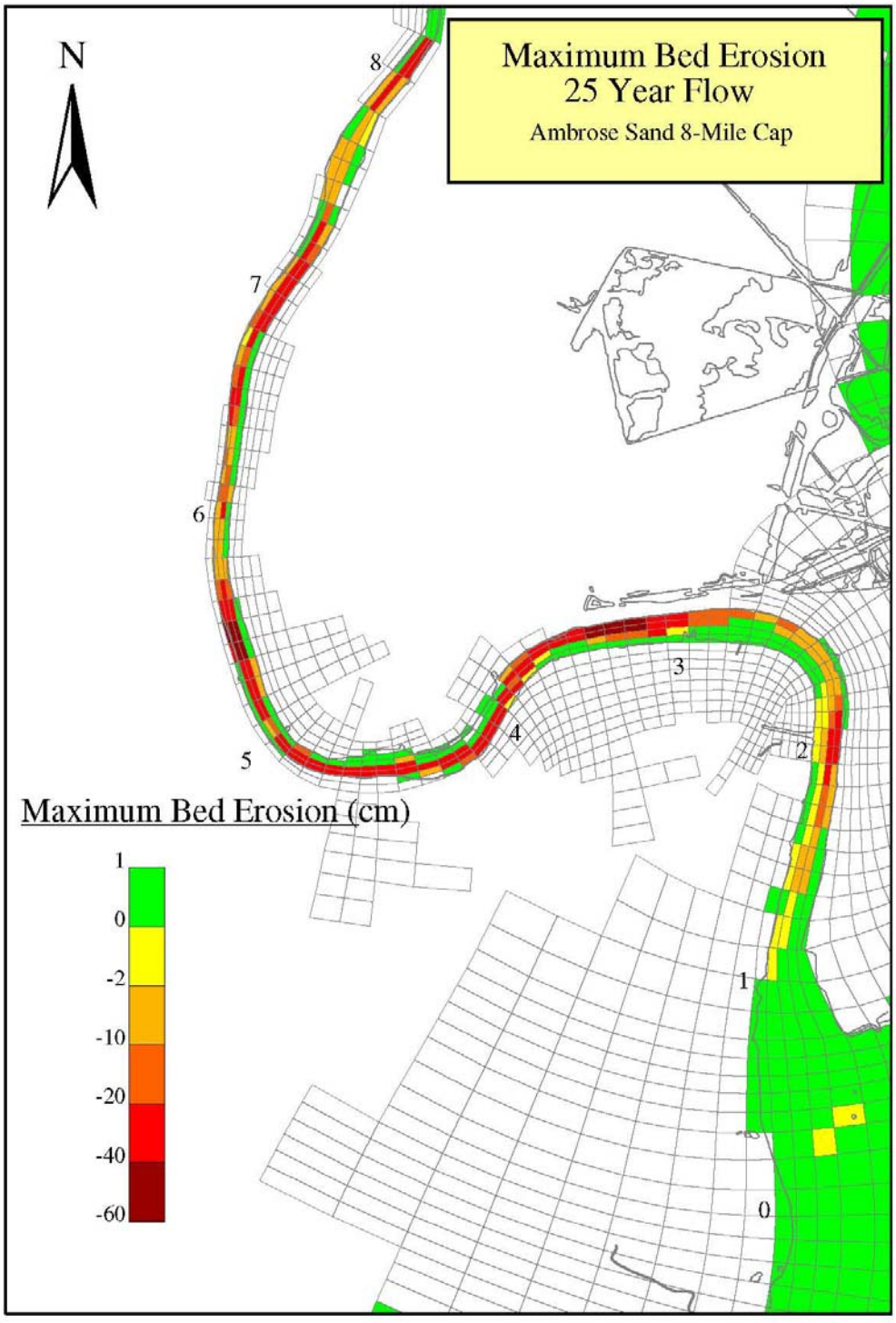

Plan view of the maximum erosion under the 25-year return flow conditions (Ambrose sand used as the capping material under the "8-Mile Cap" Scenario).

Lower Eight Miles of the Lower Passaic River

Figure 5-4b

2014

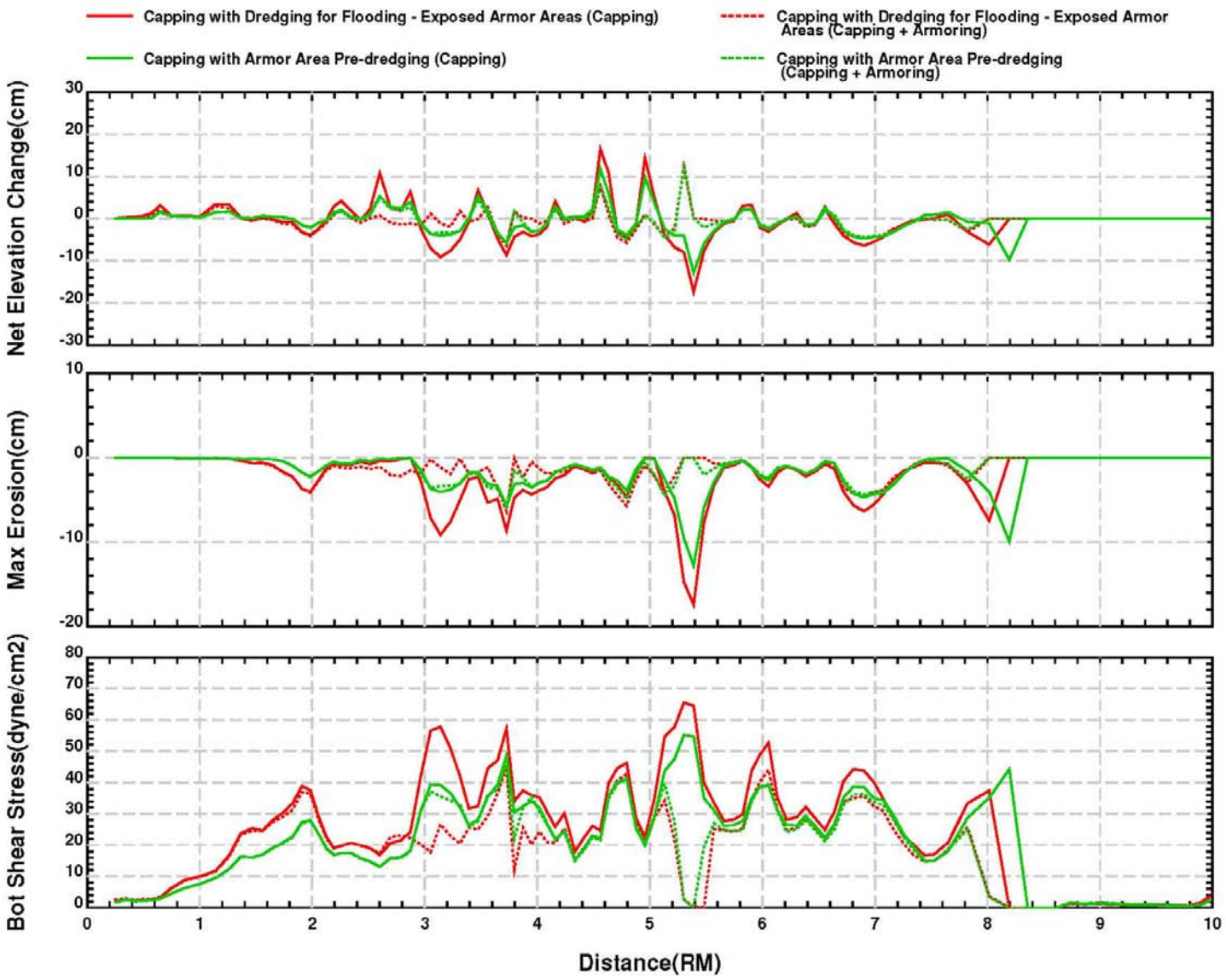

Comparisons of cross-river average net bed elevation change, the maximum erosion, and bottom shear stress along the river under the different depth conditions and the different capping/armoring scenarios. The 100-year return flow was used for these simulations, and upland borrow sand used as the capping material.

Lower Eight Miles of the Lower Passaic River

Figure 5-5

2014

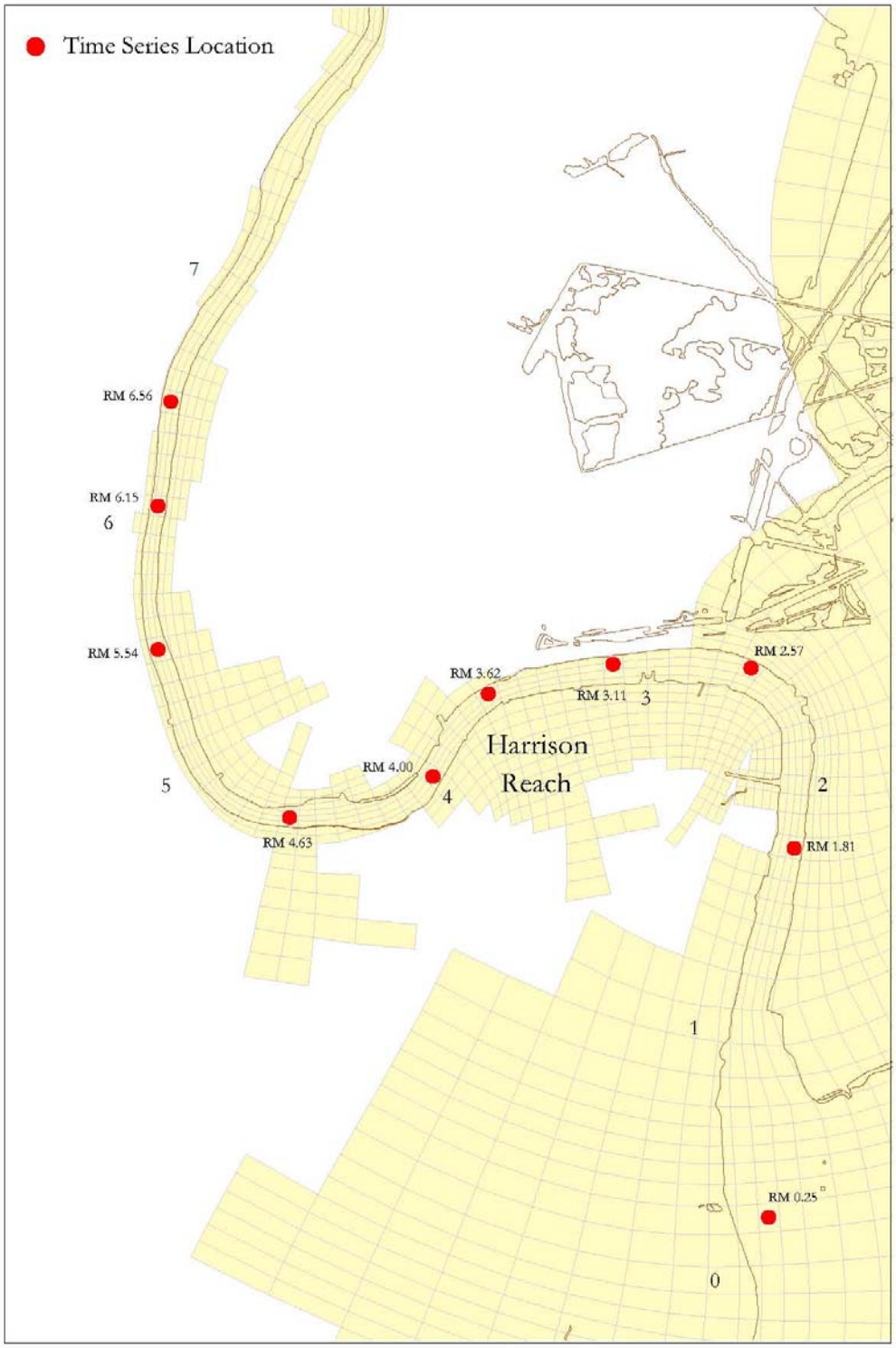

Map showing 10 selected locations along the river, where time-series results are presented under the "Capping with Armor Area Pre-Dredging" and "Capping with Dredging for Flooding - Exposed Armor Areas" Scenarios.

Lower Eight Miles of the Lower Passaic River

Figure 5-6

2014

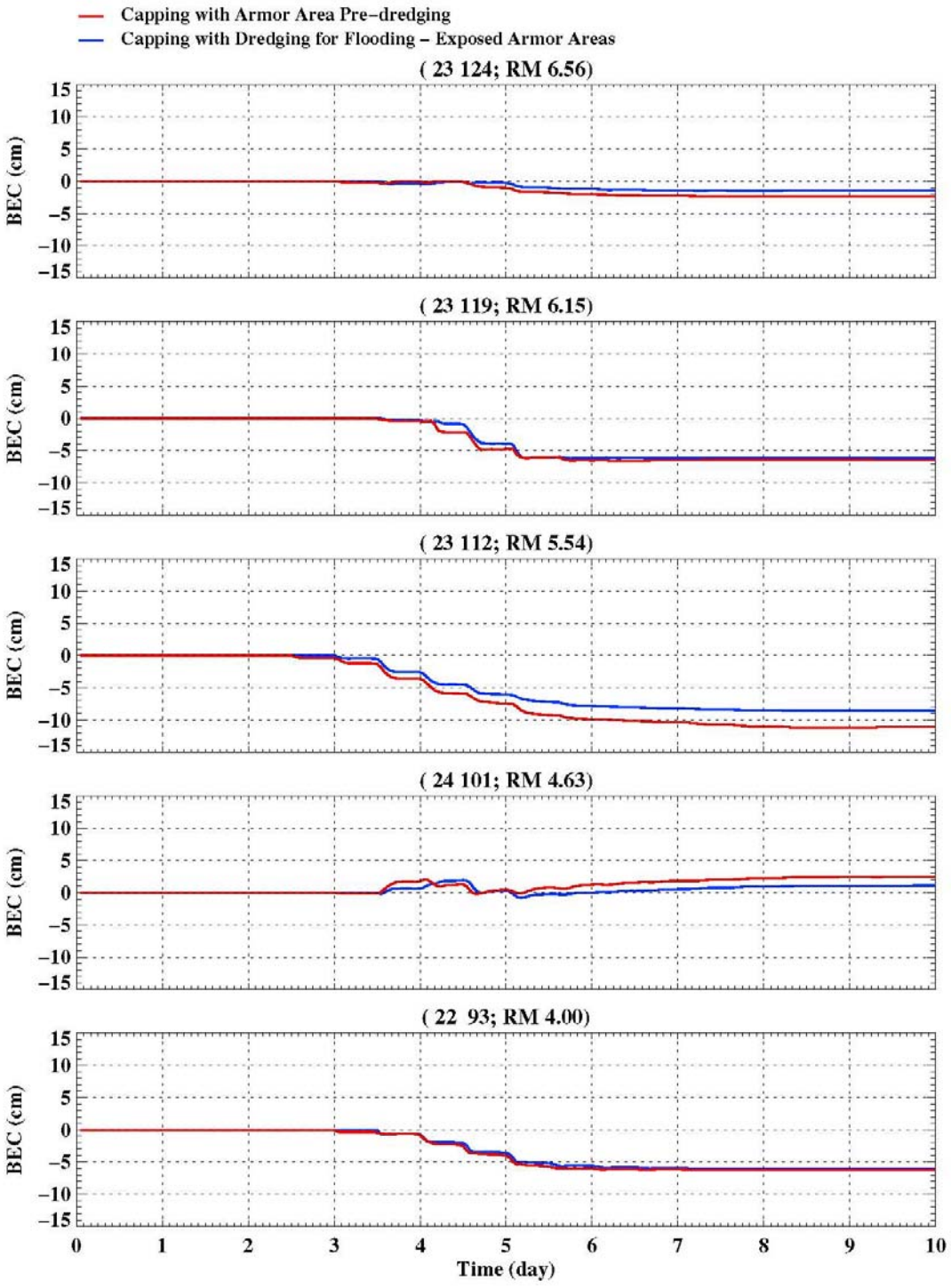

Time-series of bed elevation change (BEC) at the 10 selected locations along the river (Upland borrow sand used as the capping material under the "Capping with Armor Area Pre-Dredging" and "Capping with Dredging for Flooding – Exposed Armor Areas" Scenarios). The numbers in parenthesis at the top of each panel denote the cell identification numbers and the river miles for each of the location.

Lower Eight Miles of the Lower Passaic River

Figure 5-7

2014

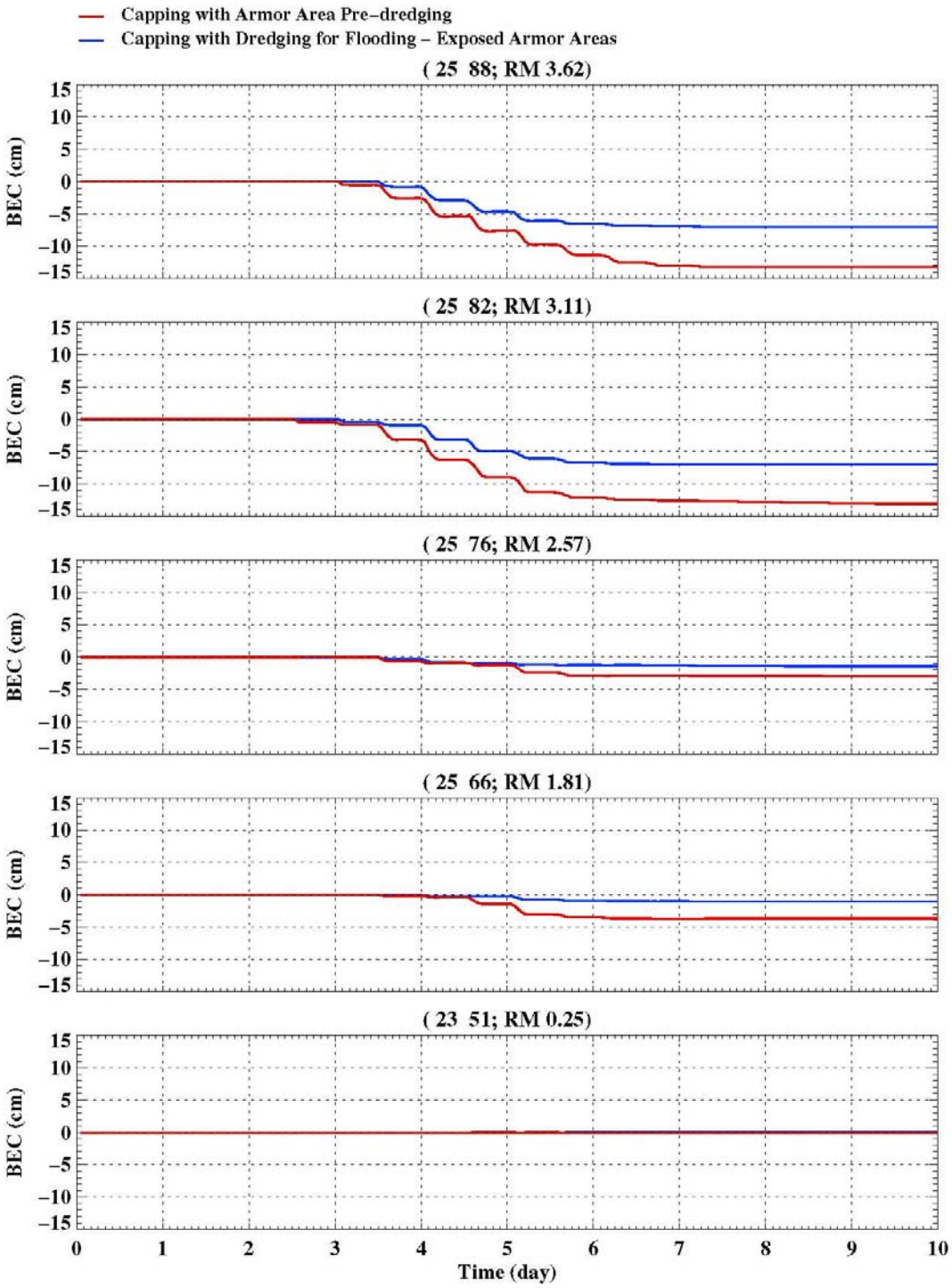

Time-series of bed elevation change (BEC) at the 10 selected locations along the river (Upland borrow sand used as the capping material under the "Capping with Armor Area Pre-Dredging" and "Capping with Dredging for Flooding – Exposed Armor Areas" Scenarios). The numbers in parenthesis at the top of each panel denote the cell identification numbers and the river miles for each of the location.

Lower Eight Miles of the Lower Passaic River

Figure 5-7 Continued

2014

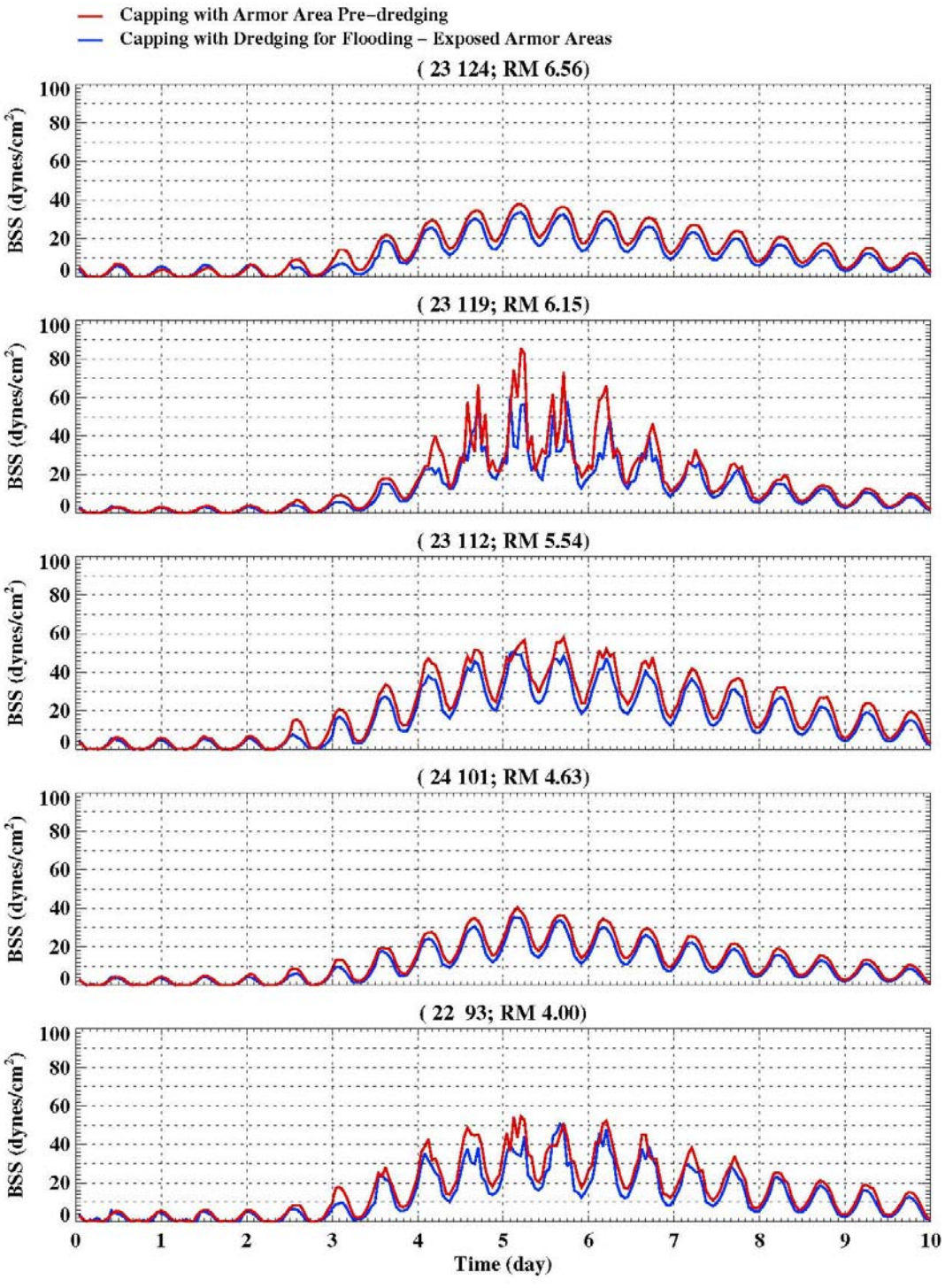

Time-series of bottom shear stress (BSS) at the 10 selected locations along the river (Upland borrow sand used as the capping material under the "Capping with Armor Area Pre-Dredging" and "Capping with Dredging for Flooding – Exposed Armor Areas" Scenarios). The numbers in parenthesis at the top of each panel denote the cell identification numbers and the river miles for each location.

Lower Eight Miles of the Lower Passaic River

Figure 5-8

2014

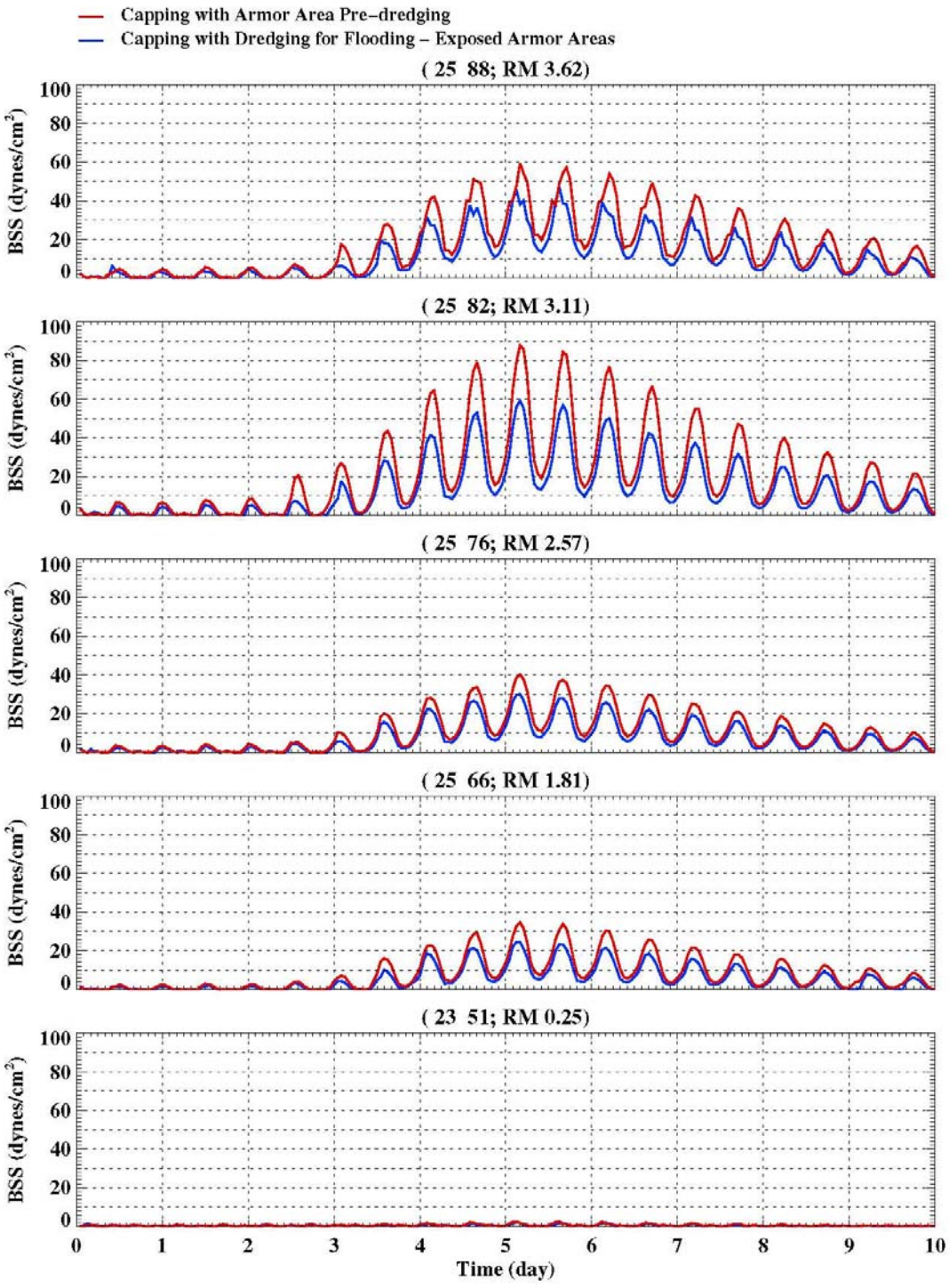

Time-series of bottom shear stress (BSS) at the 10 selected locations along the river (Upland borrow sand used as the capping material under the "Capping with Armor Area Pre-Dredging" and "Capping with Dredging for Flooding – Exposed Armor Areas" Scenarios). The numbers in parenthesis at the top of each panel denote the cell identification numbers and the river miles for each location.

Lower Eight Miles of the Lower Passaic River

Figure 5-8 Continued

2014

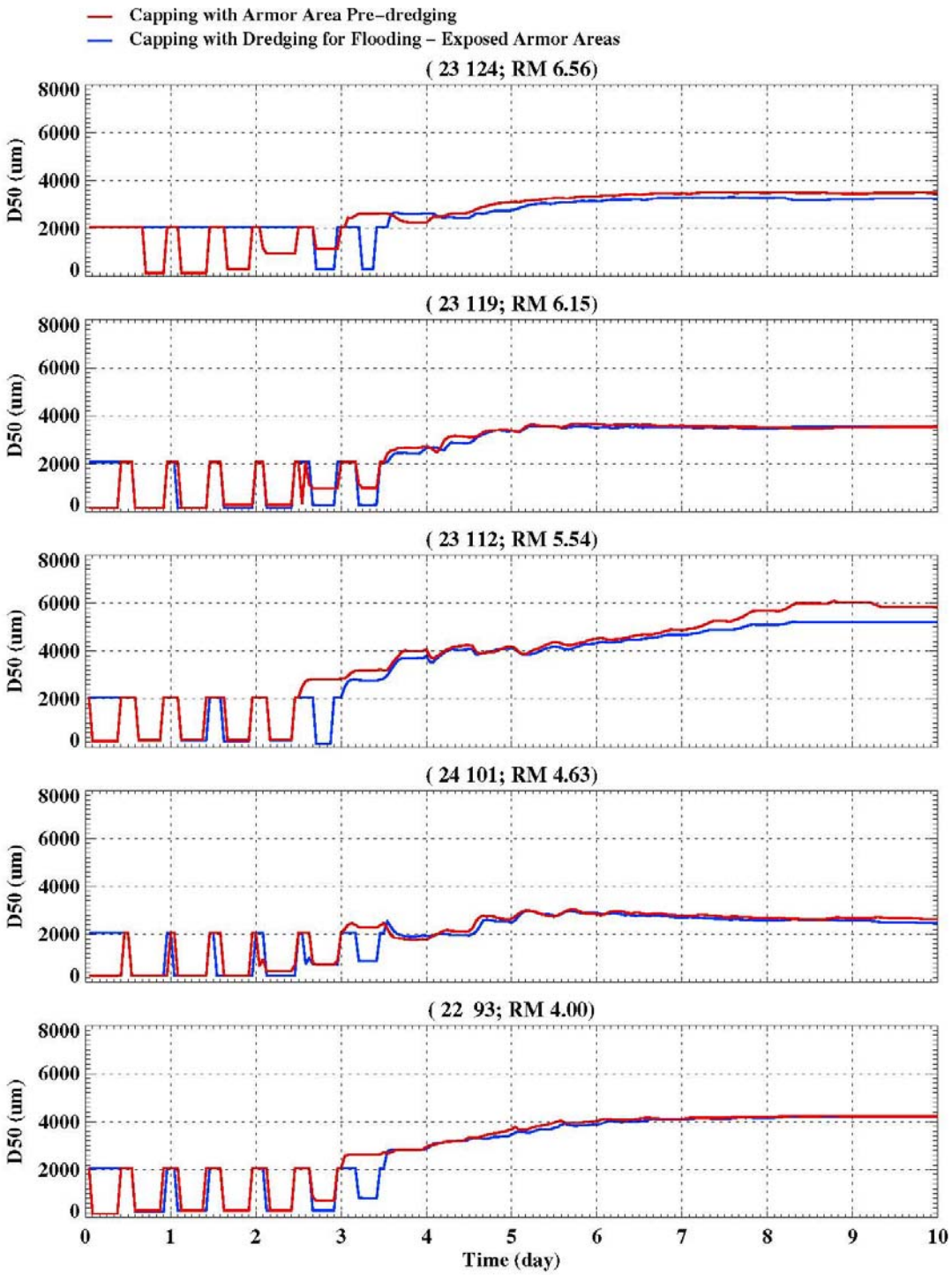

Time-series of median grain size (D_{50}) at the 10 selected locations along the river (Upland borrow sand used as the capping material under the "Capping with Armor Area Pre-Dredging" and "Capping with Dredging for Flooding – Exposed Armor Areas" Scenarios). The numbers in parenthesis at the top of each panel denote the cell identification numbers and the river miles for each location.

Lower Eight Miles of the Lower Passaic River

Figure 5-9

2014

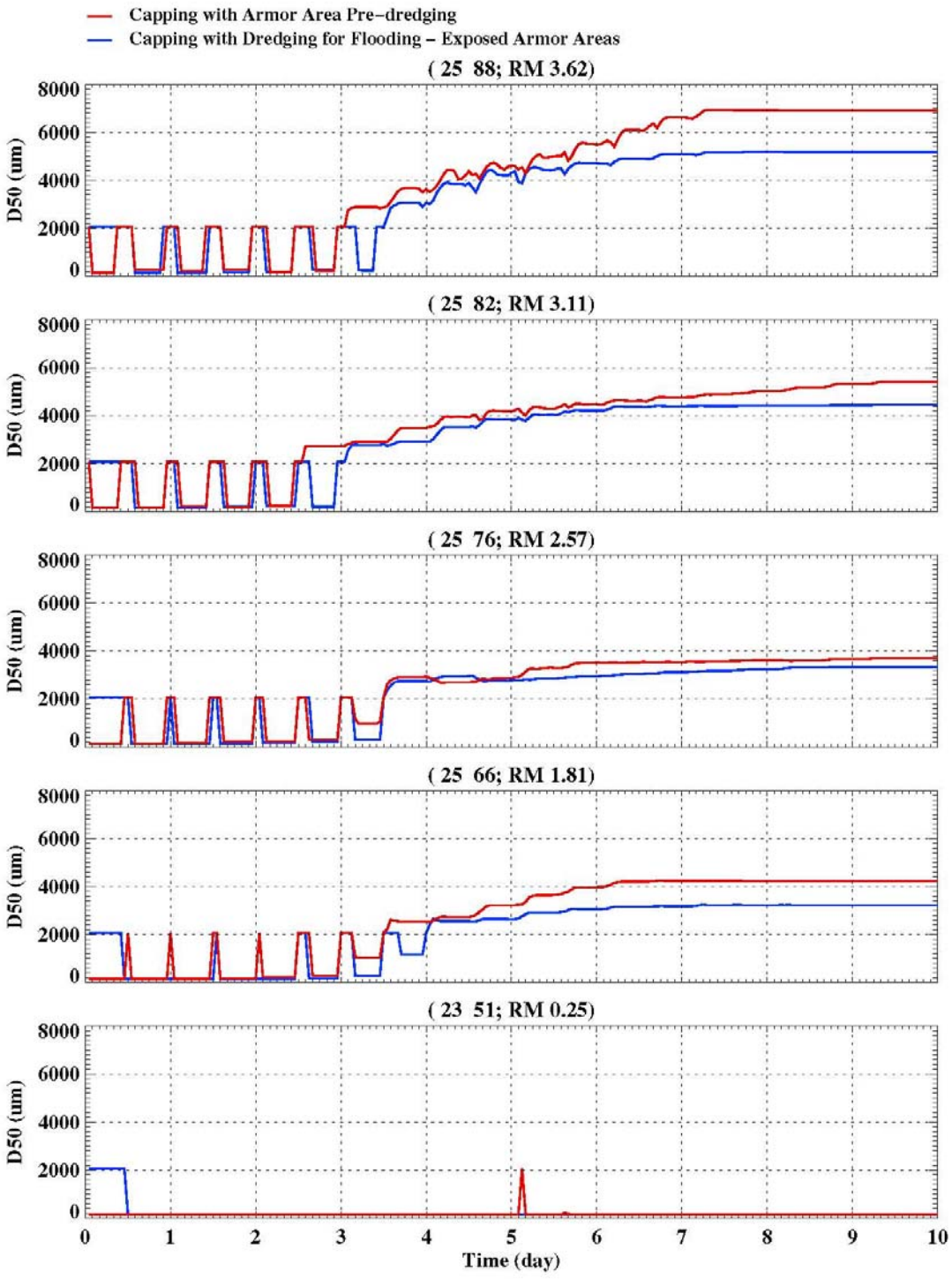

Time-series of median grain size (D_{50}) at the 10 selected locations along the river (Upland borrow sand used as the capping material under the "Capping with Armor Area Pre-Dredging" and "Capping with Dredging for Flooding – Exposed Armor Areas" Scenarios). The numbers in parenthesis at the top of each panel denote the cell identification numbers and the river miles for each location.

Figure 5-9 Continued

Lower Eight Miles of the Lower Passaic River

2014

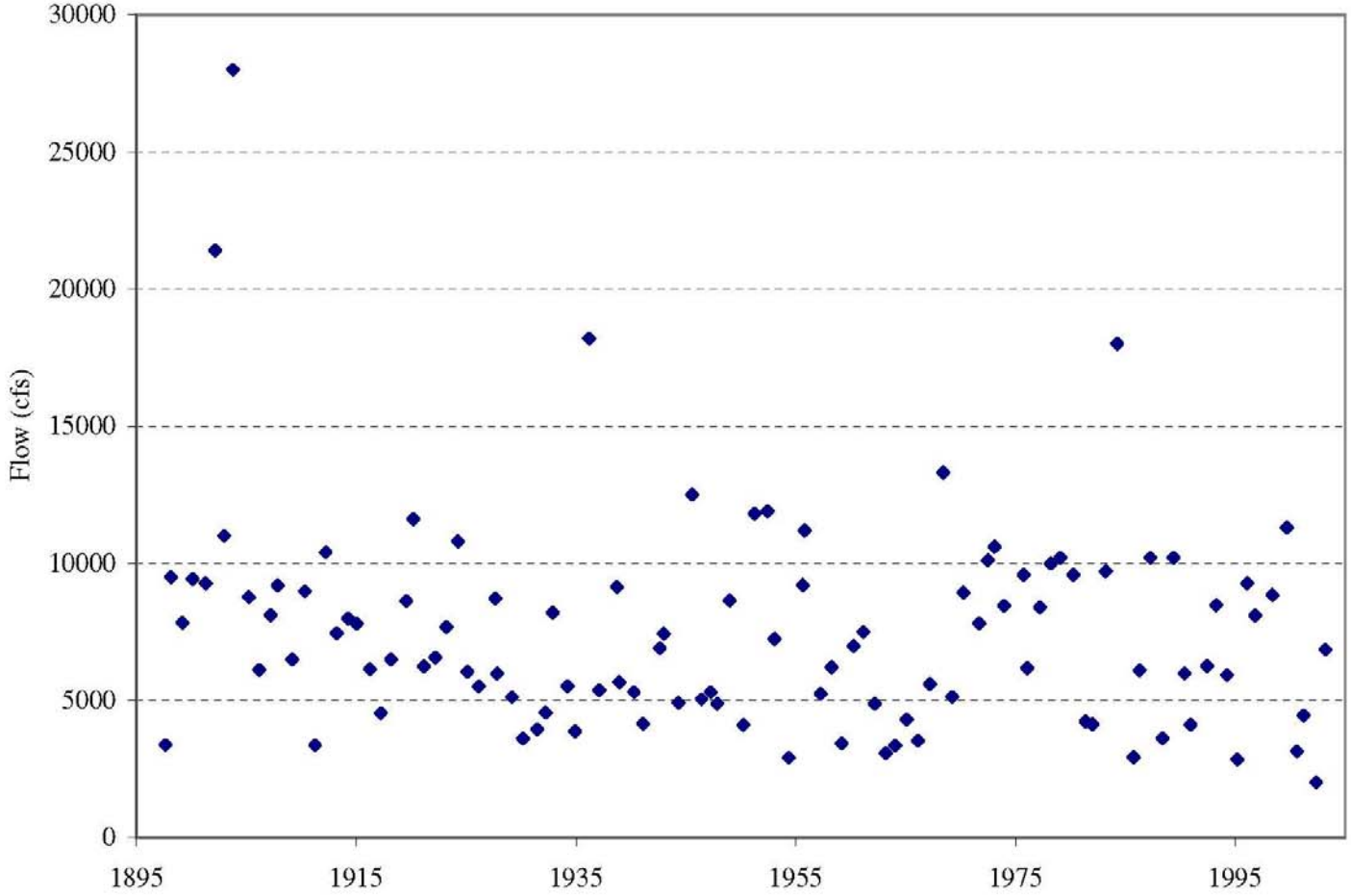

Annual maximum daily flows at Little Falls between 1897 and 2003

Figure 6-1

Lower Eight Miles of the Lower Passaic River

2014

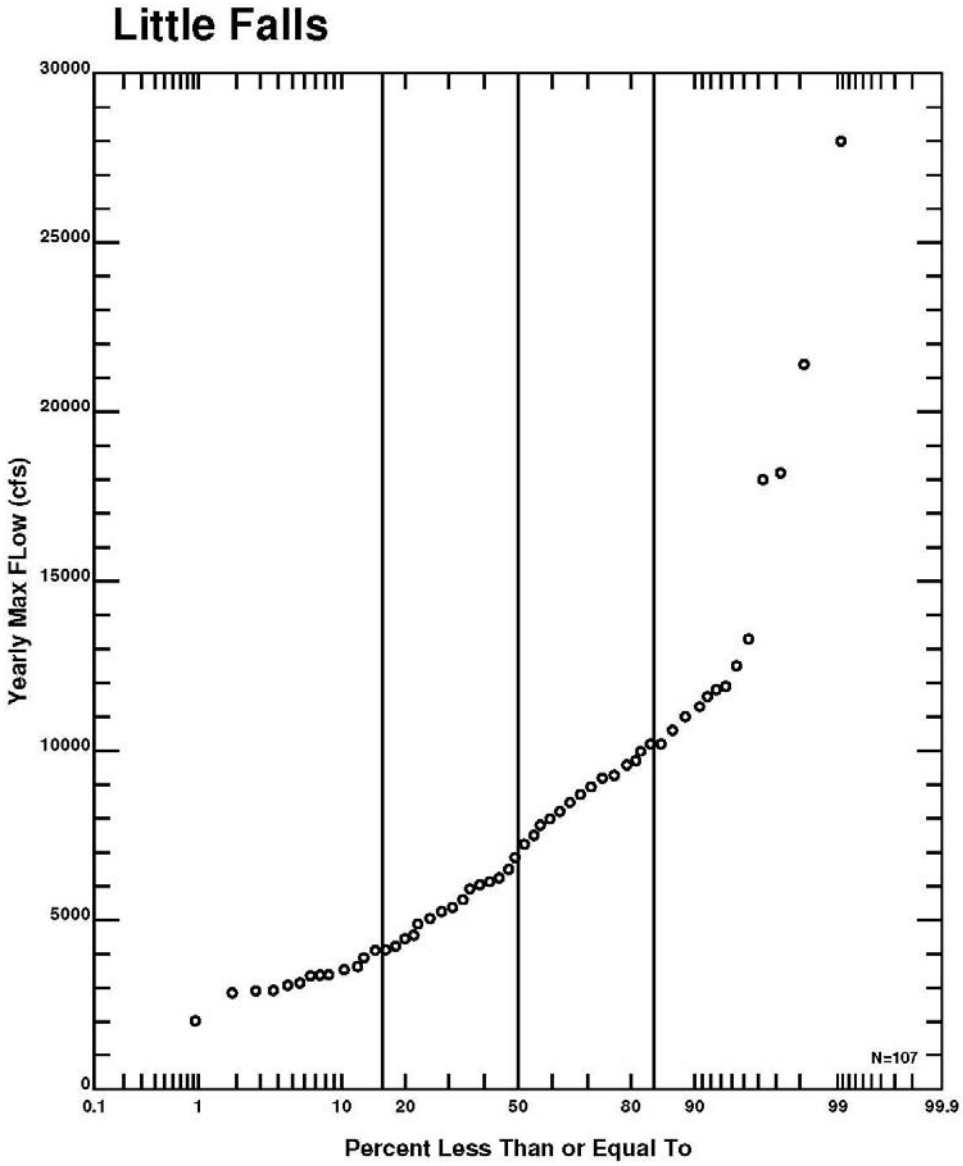

Probability distribution of annual maximum flows observed at the Little Falls	Figure 6-2
Lower Eight Miles of the Lower Passaic River	2014

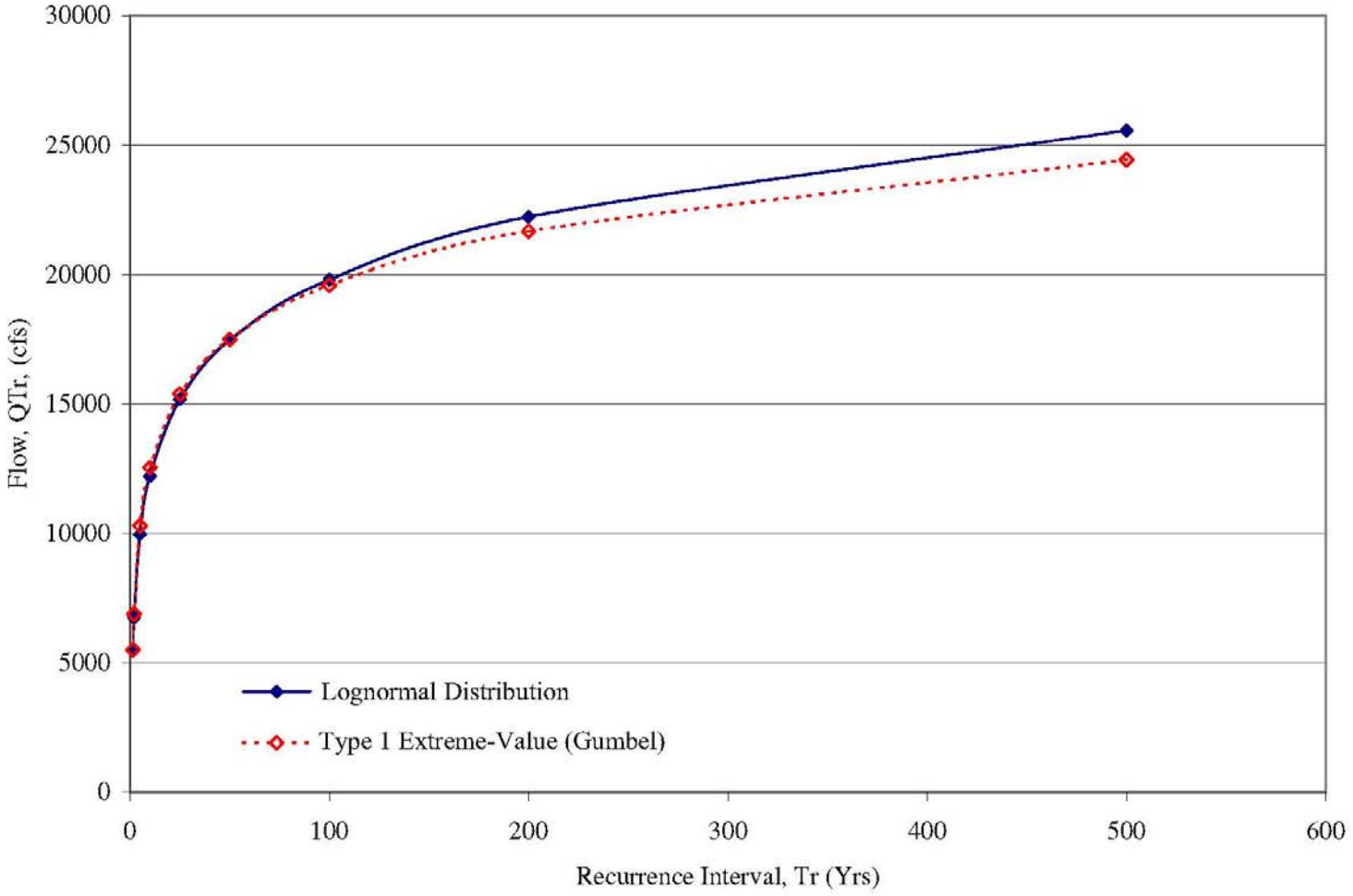

Estimated 100- and 500-year flows using Log-Normal and Type 1 Extreme-Value (Gumbel) methods

Figure 6-3

Lower Eight Miles of the Lower Passaic River

2014

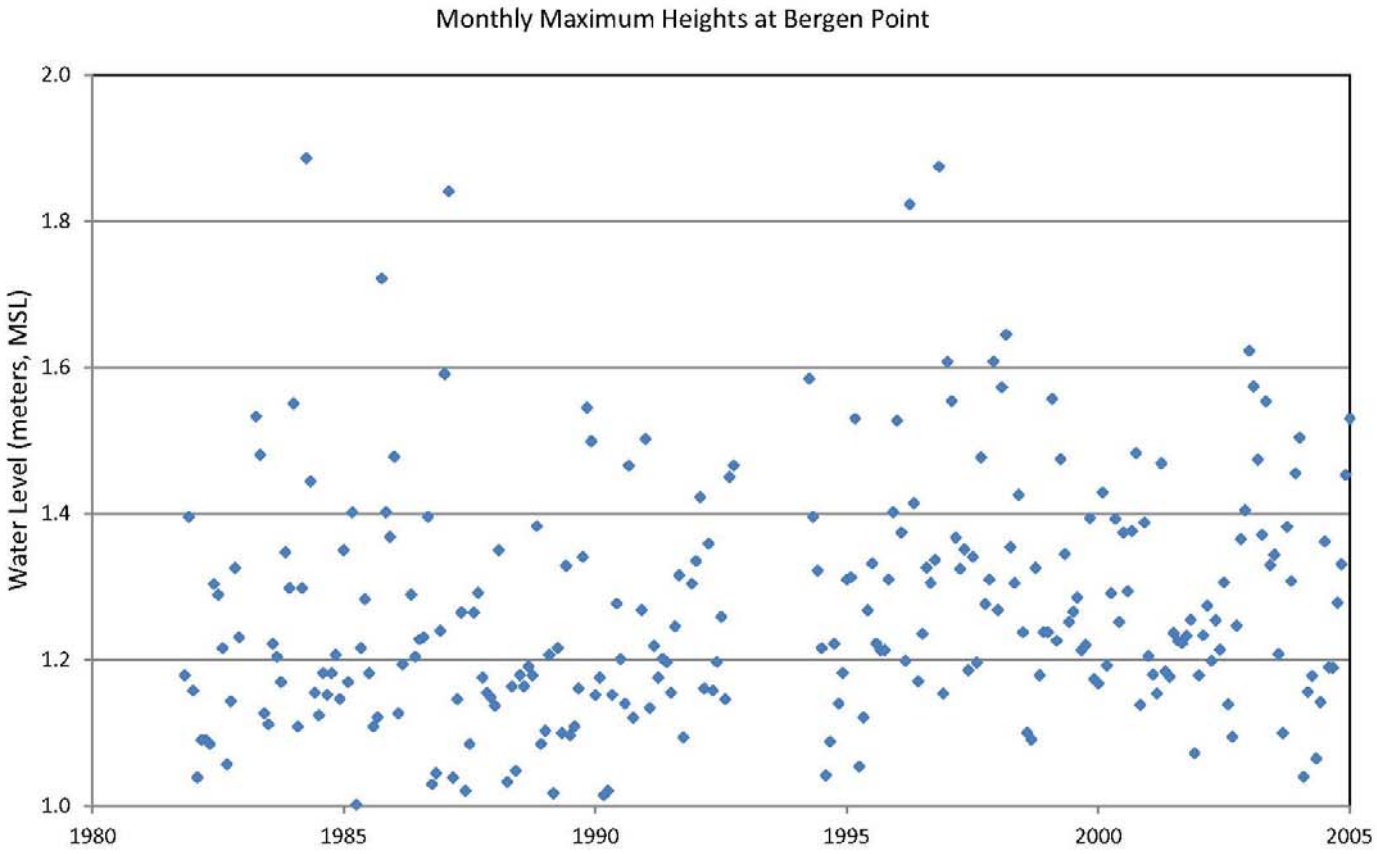

Monthly maximum high water levels at Bergen Point between 1981 and 2004

Figure 6-4

Lower Eight Miles of the Lower Passaic River

2014

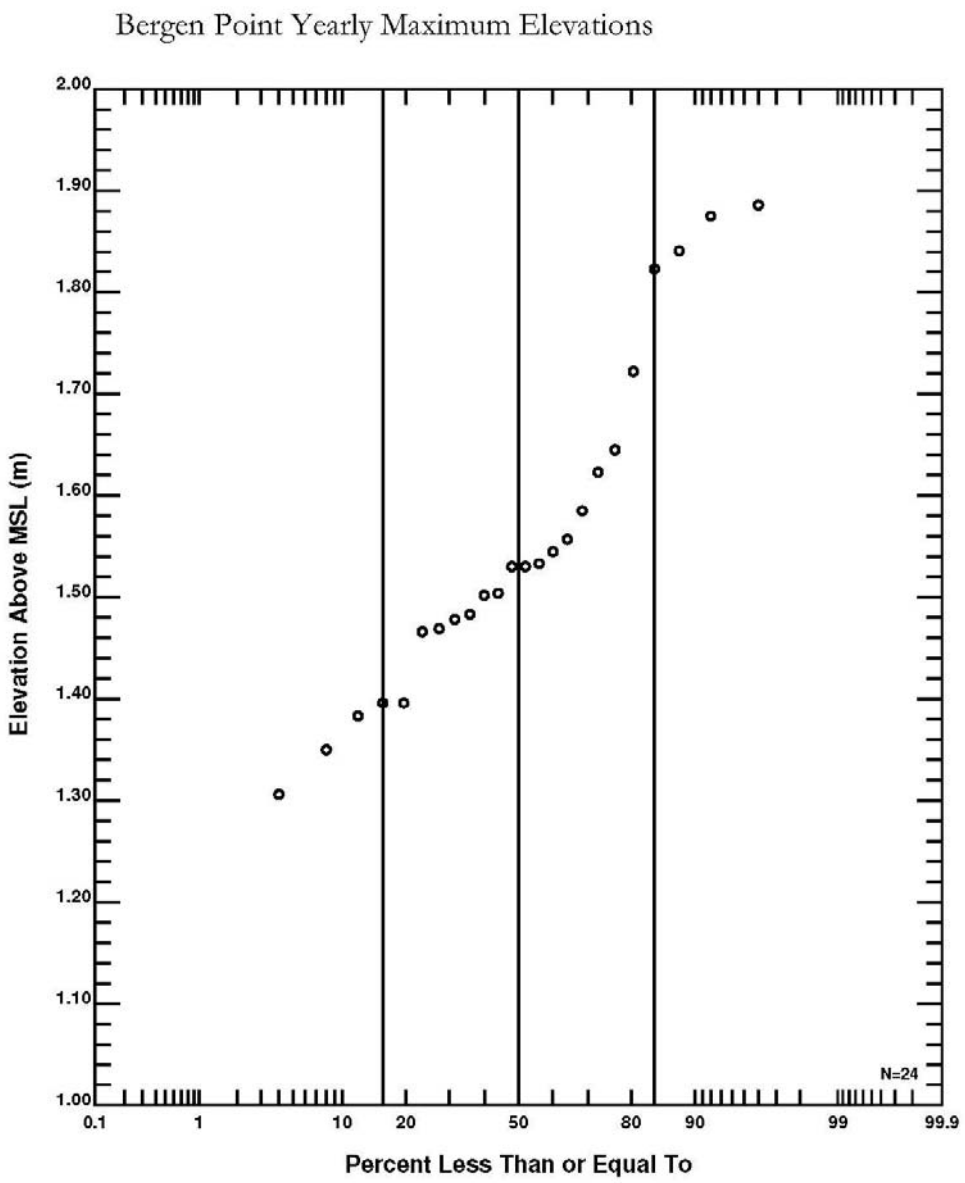

Probability distribution of annual maximum elevations observed at Bergen Point

Figure 6-5

Lower Eight Miles of the Lower Passaic River

2014

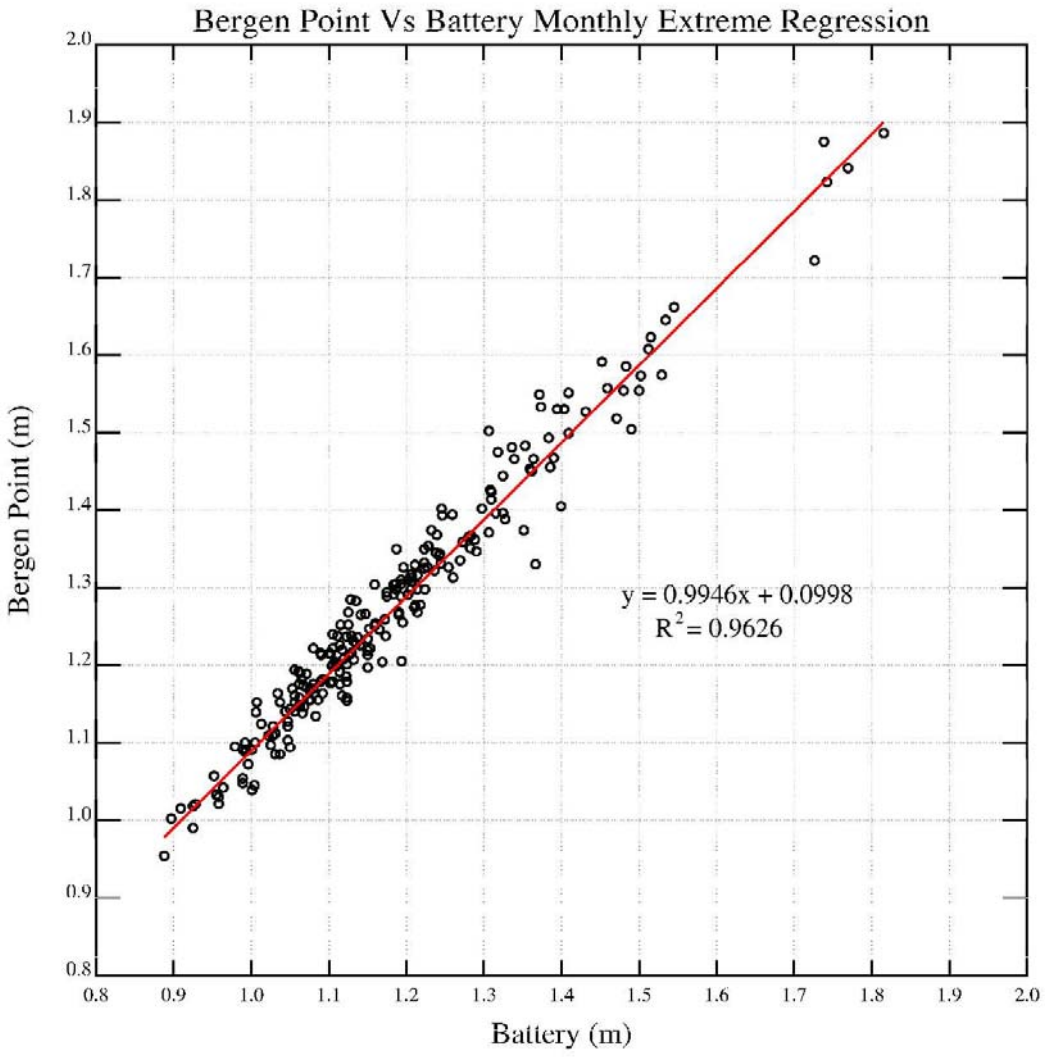

Correlation analysis of the monthly extreme water elevations between Bergen Point and the Battery NOAA stations for the years 1981 through 2004.

Figure 6-6

Lower Eight Miles of the Lower Passaic River

2014

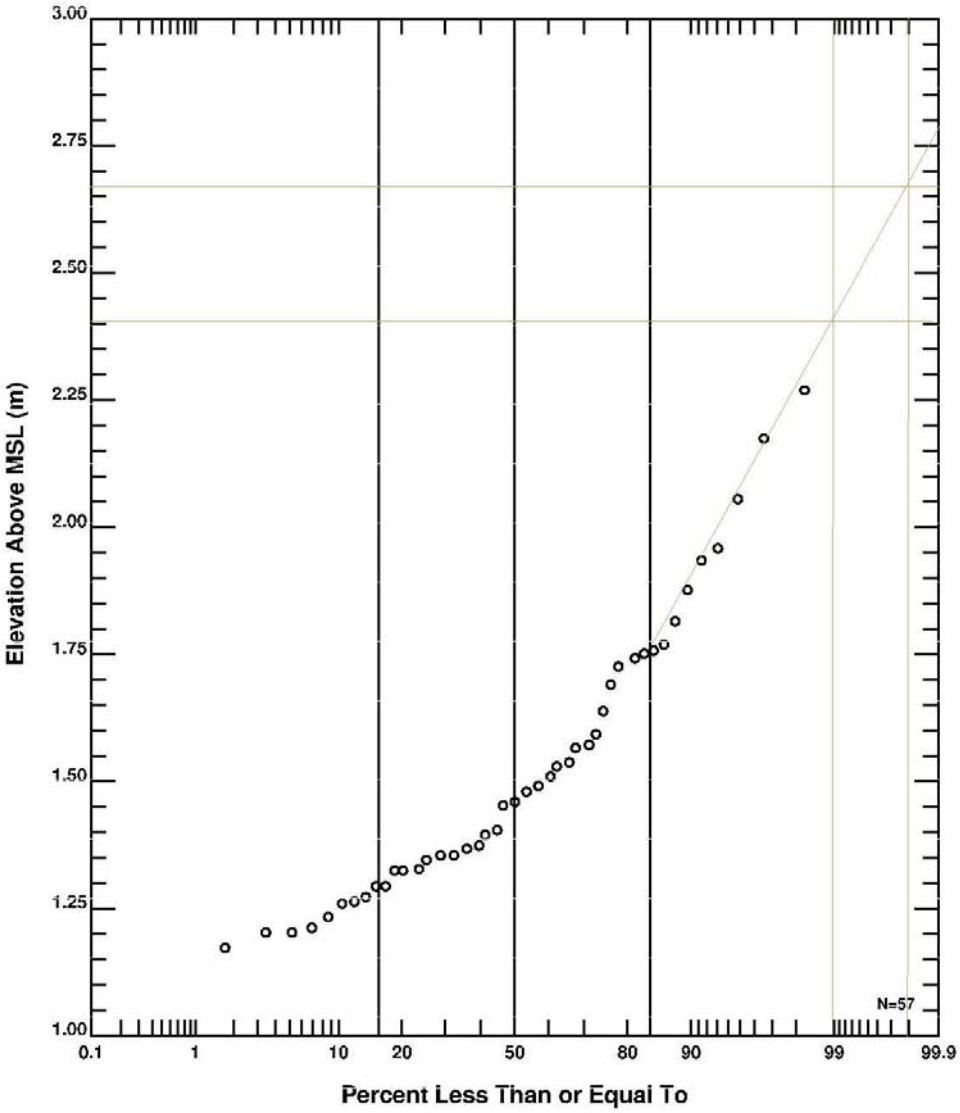

Probability distribution of annual maximum elevations observed at the Battery

Lower Eight Miles of the Lower Passaic River

Figure 6-7

2014

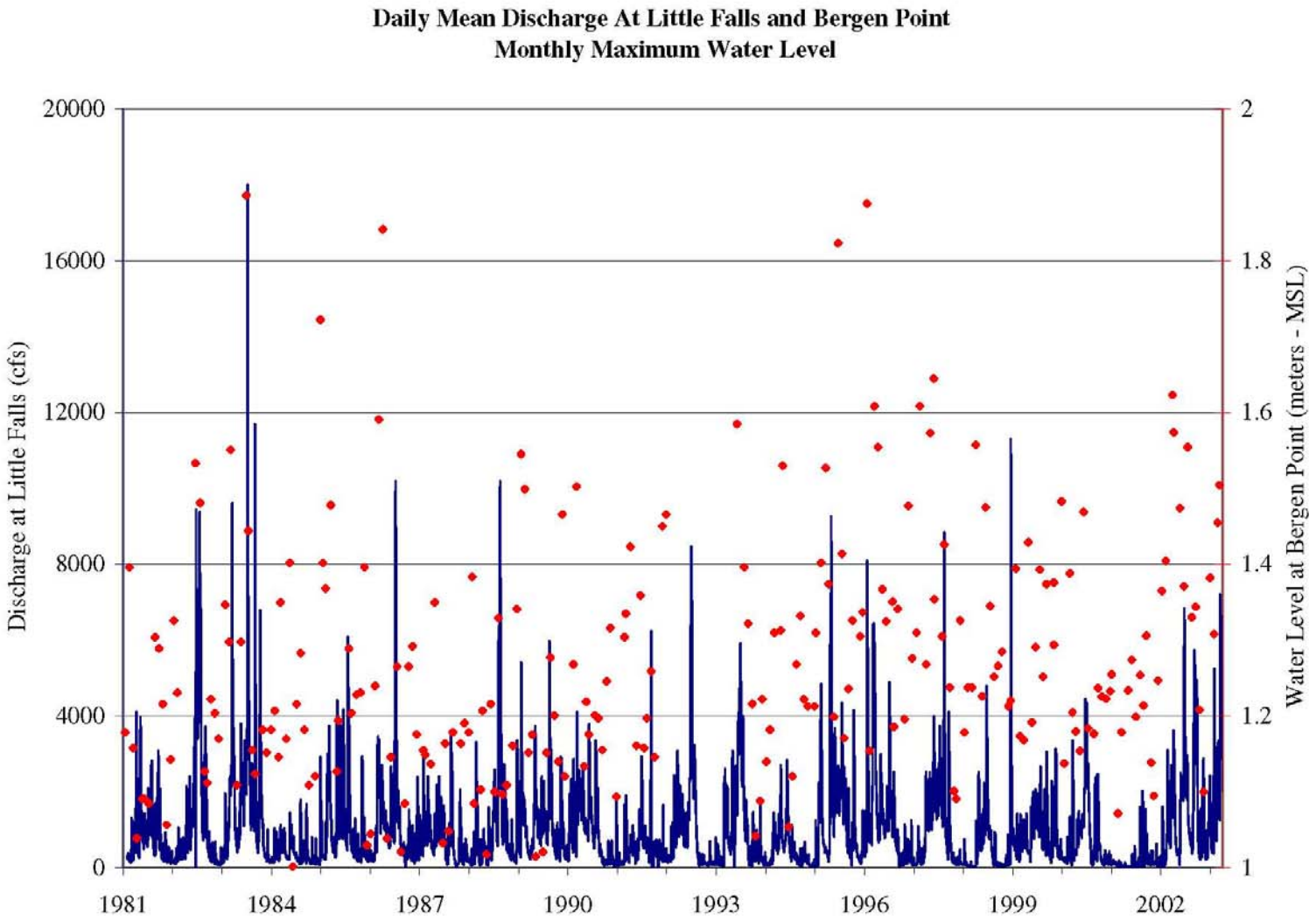

Daily flows measured at Little Falls (shown by blue line) and monthly maximum high water levels at Bergen Point (shown by red dots) between 1981 and 2003

Figure 6-8

Lower Eight Miles of the Lower Passaic River

2014

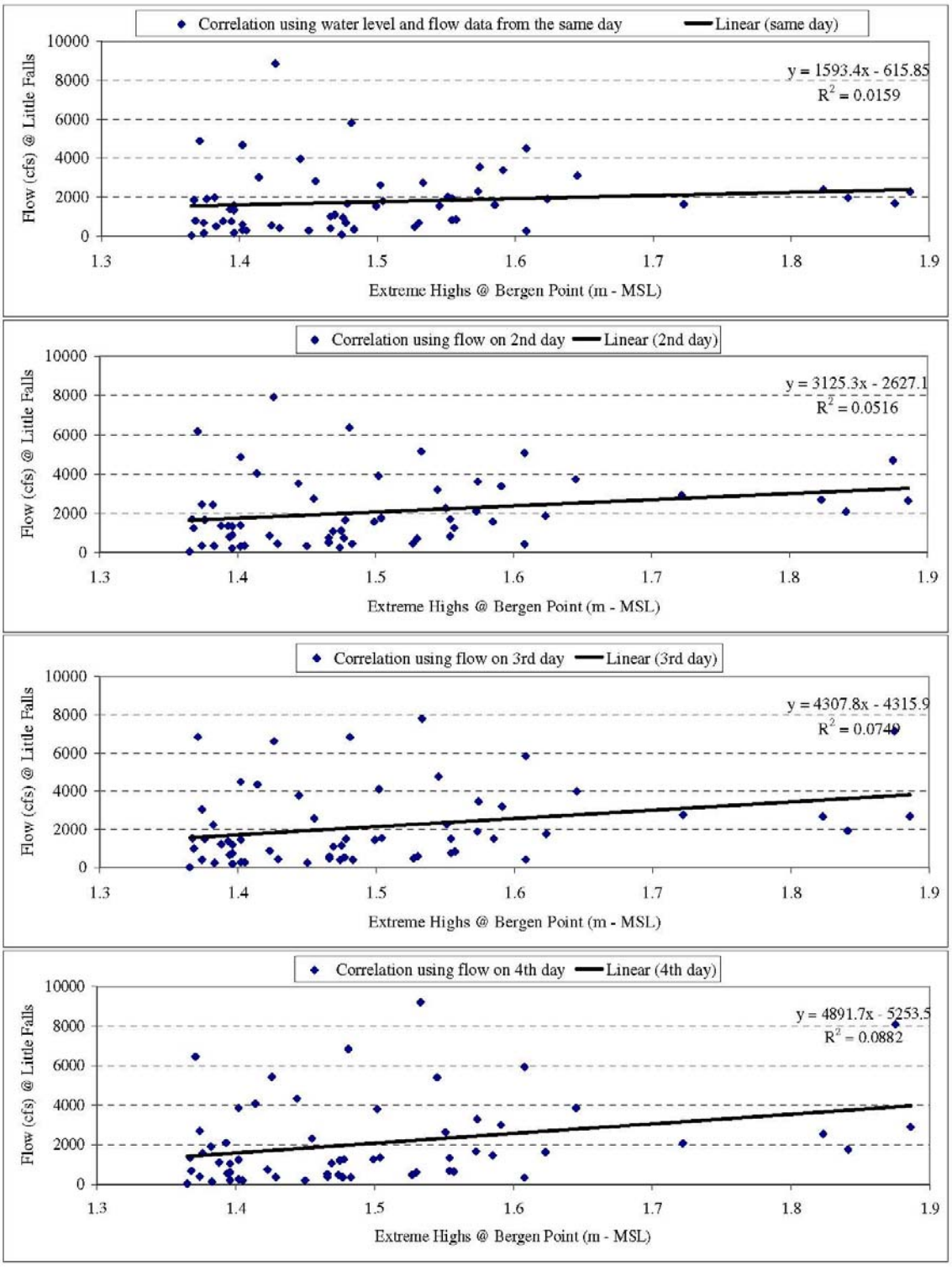

Correlation analysis of maximum water levels and daily flows: correlation of same day events (top panel); water level vs. flow of second day (2nd panel); water level vs. flow of third day (3rd panel); water level vs. flow of 4th day (bottom panel)

Lower Eight Miles of the Lower Passaic River

Figure 6-9

2014

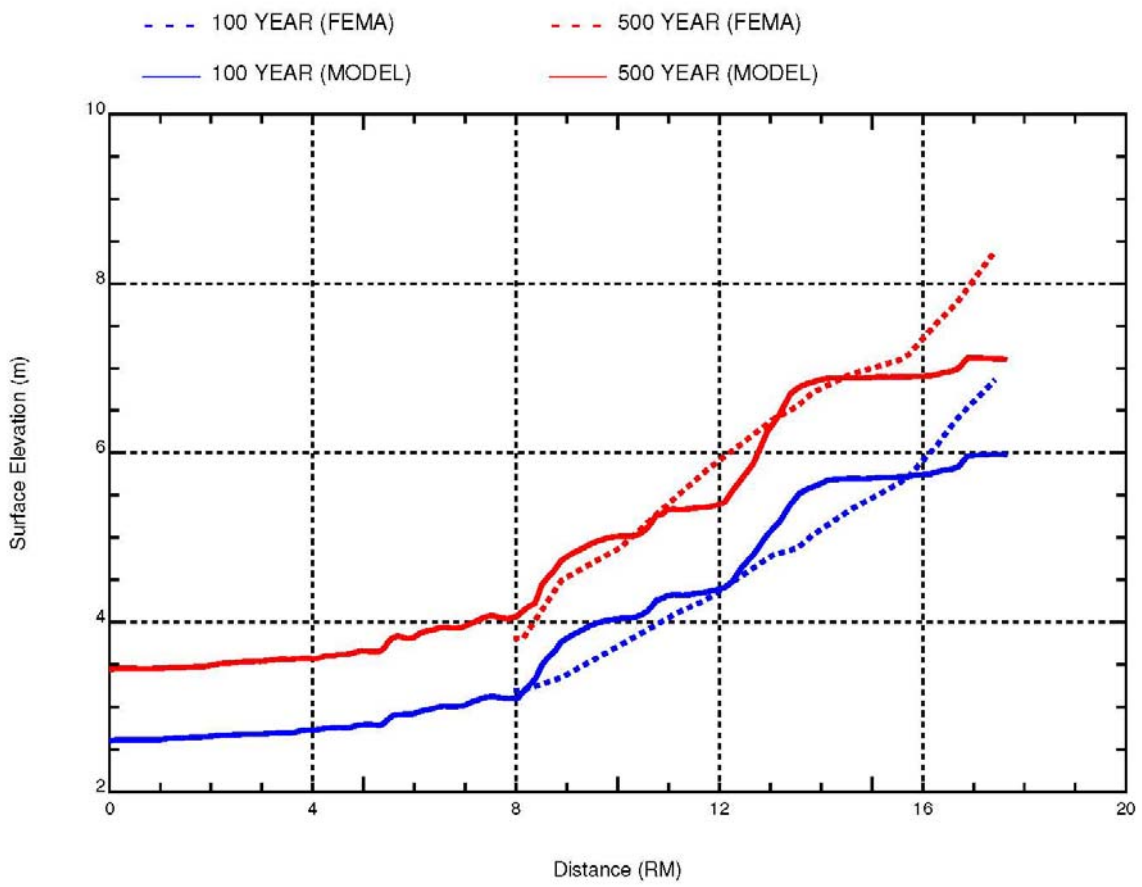

Maximum water elevation computed along the Lower Passaic River during the FEMA flood events

Lower Eight Miles of the Lower Passaic River

Figure 6-10

2014

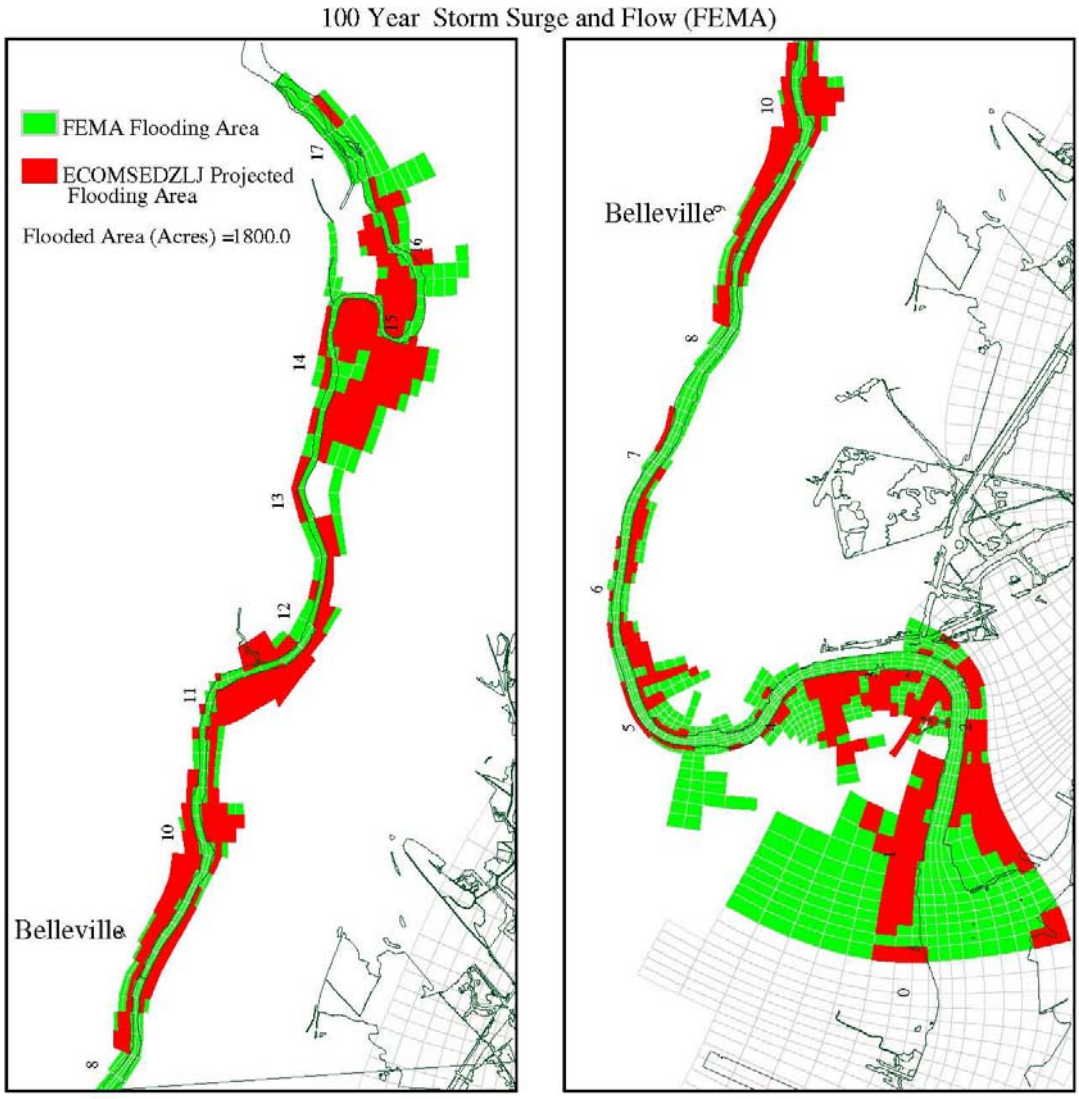

Projected flood area during the FEMA 100-year event	Figure 6-11
Lower Eight Miles of the Lower Passaic River	2014

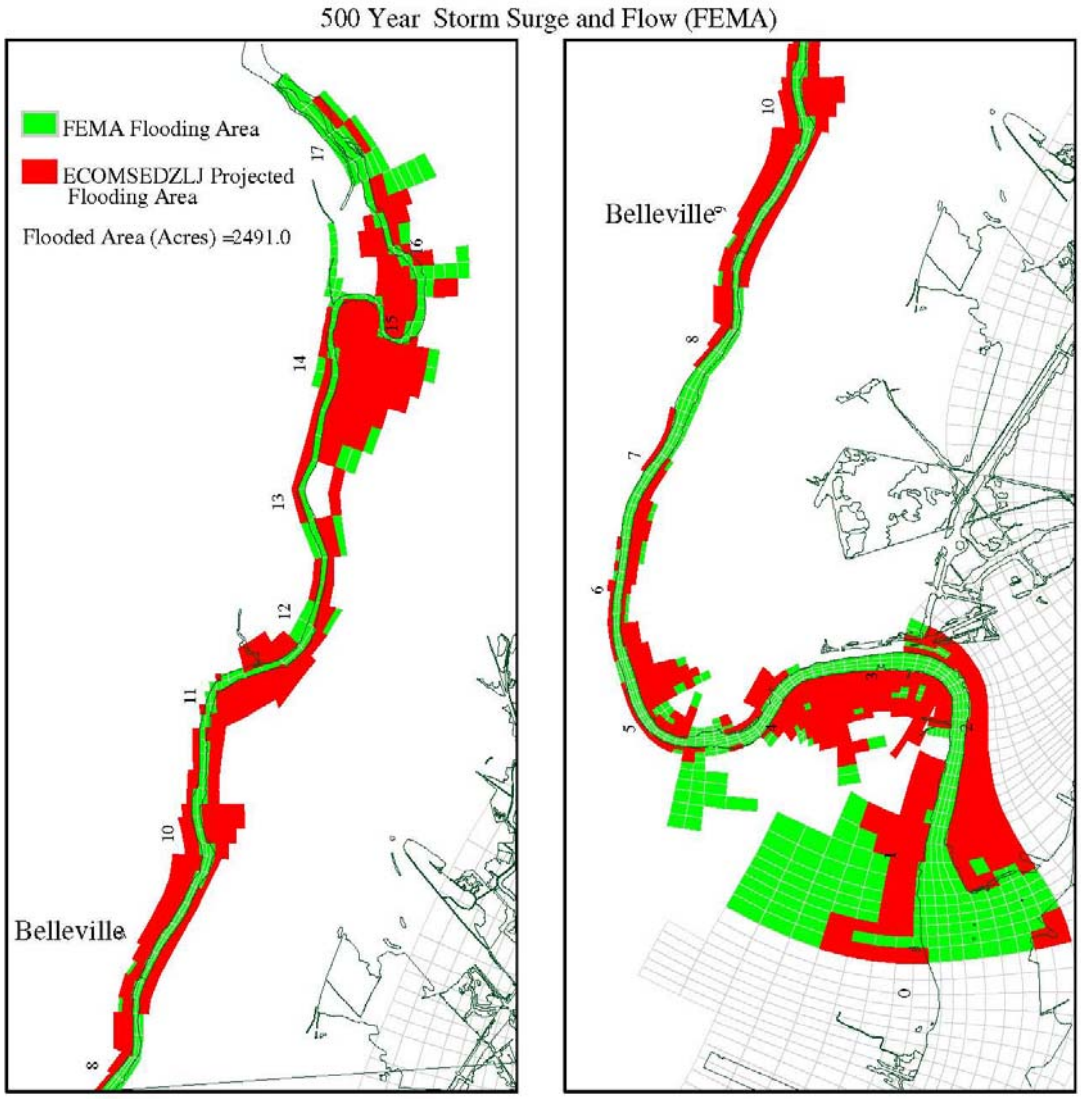

Projected flood area during the FEMA 500-year event

Figure 6-12

Lower Eight Miles of the Lower Passaic River

2014

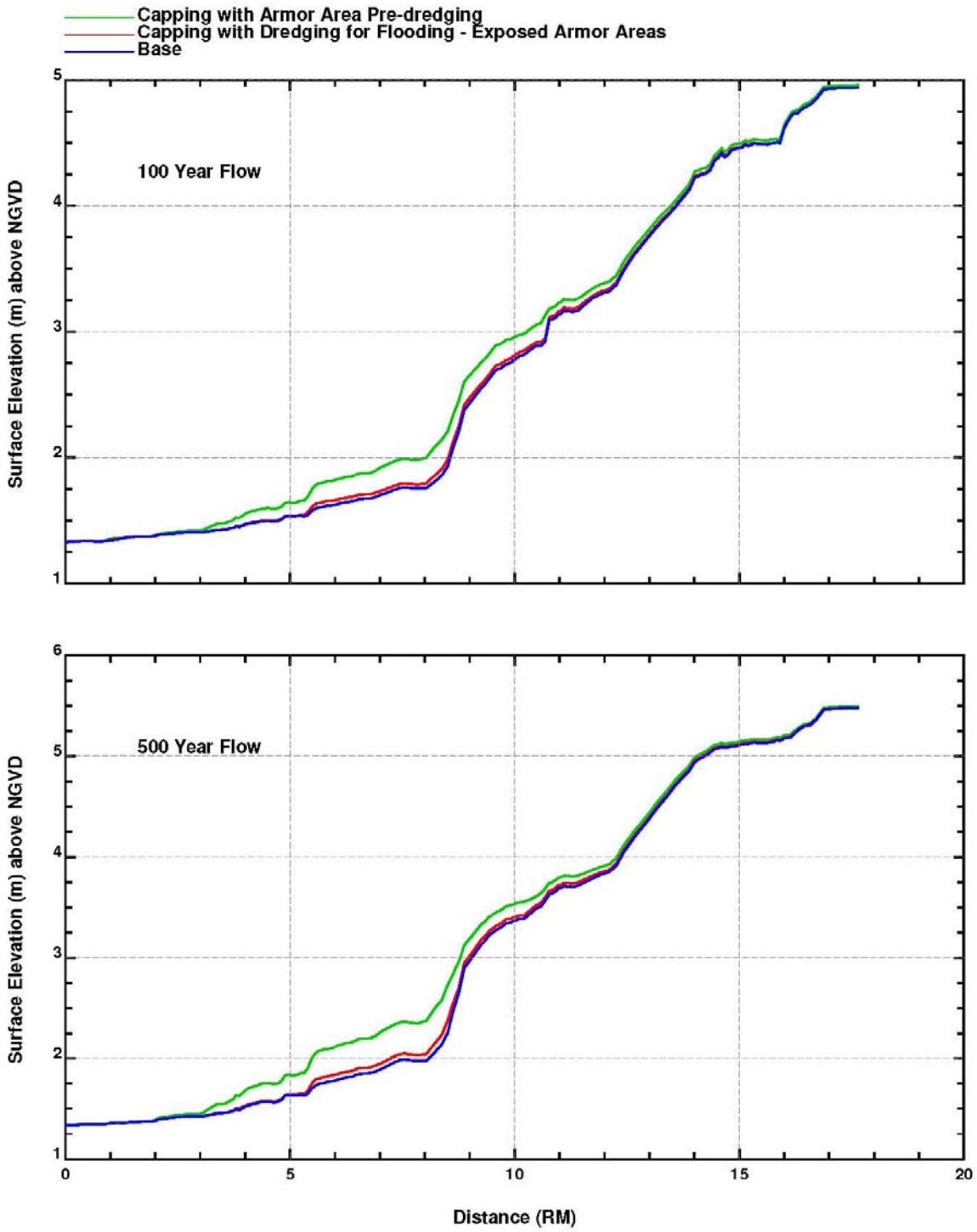

Maximum water surface elevations under different simulation scenarios along the Passaic River during 100- and 500-year flows.

Lower Eight Miles of the Lower Passaic River

Figure 6-13a

2014

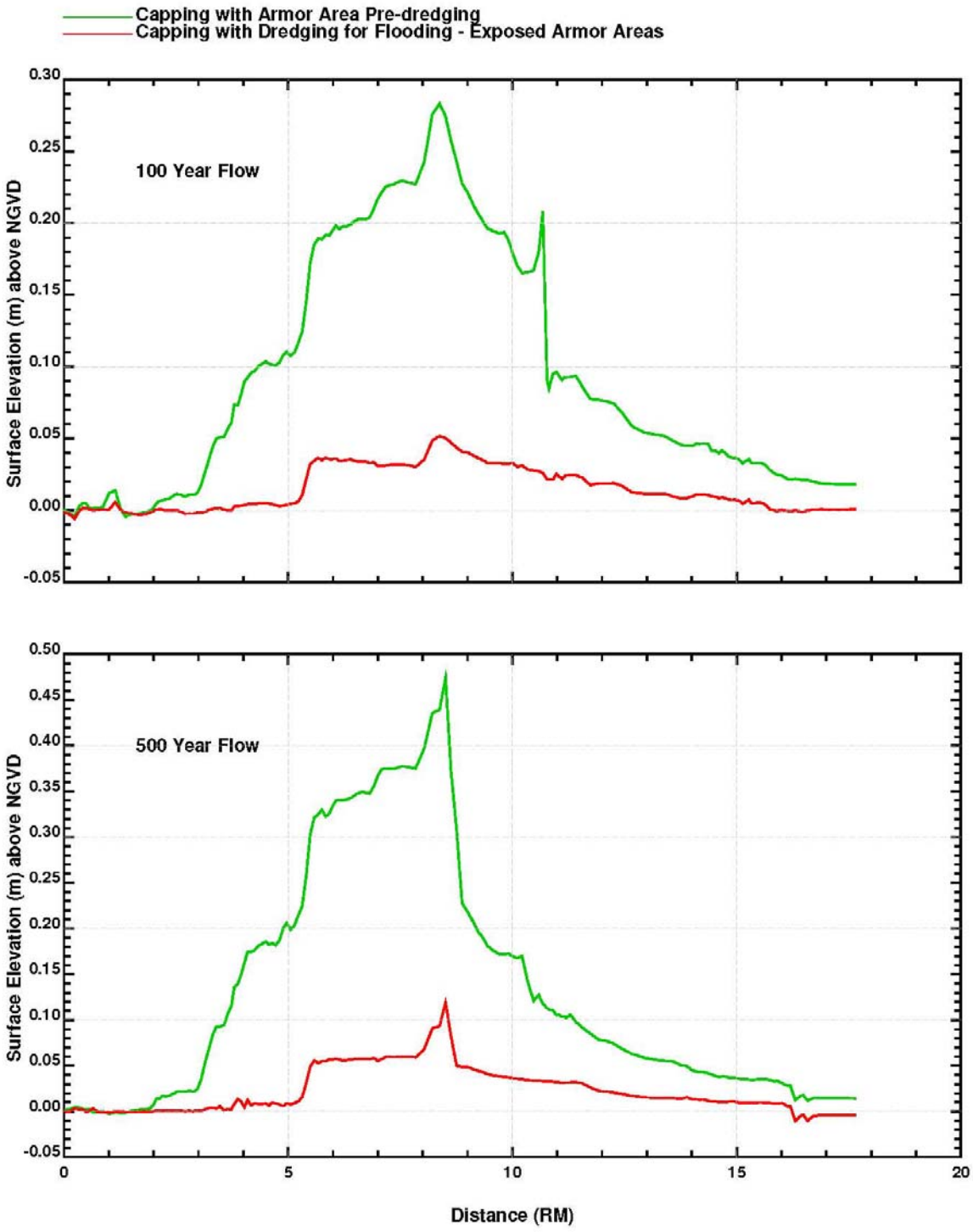

Net changes in water surface elevation under different simulation scenarios along the Passaic River compared to the "Base Case" scenario during 100- and 500-year flows.

Figure 6-13b

Lower Eight Miles of the Lower Passaic River

2014

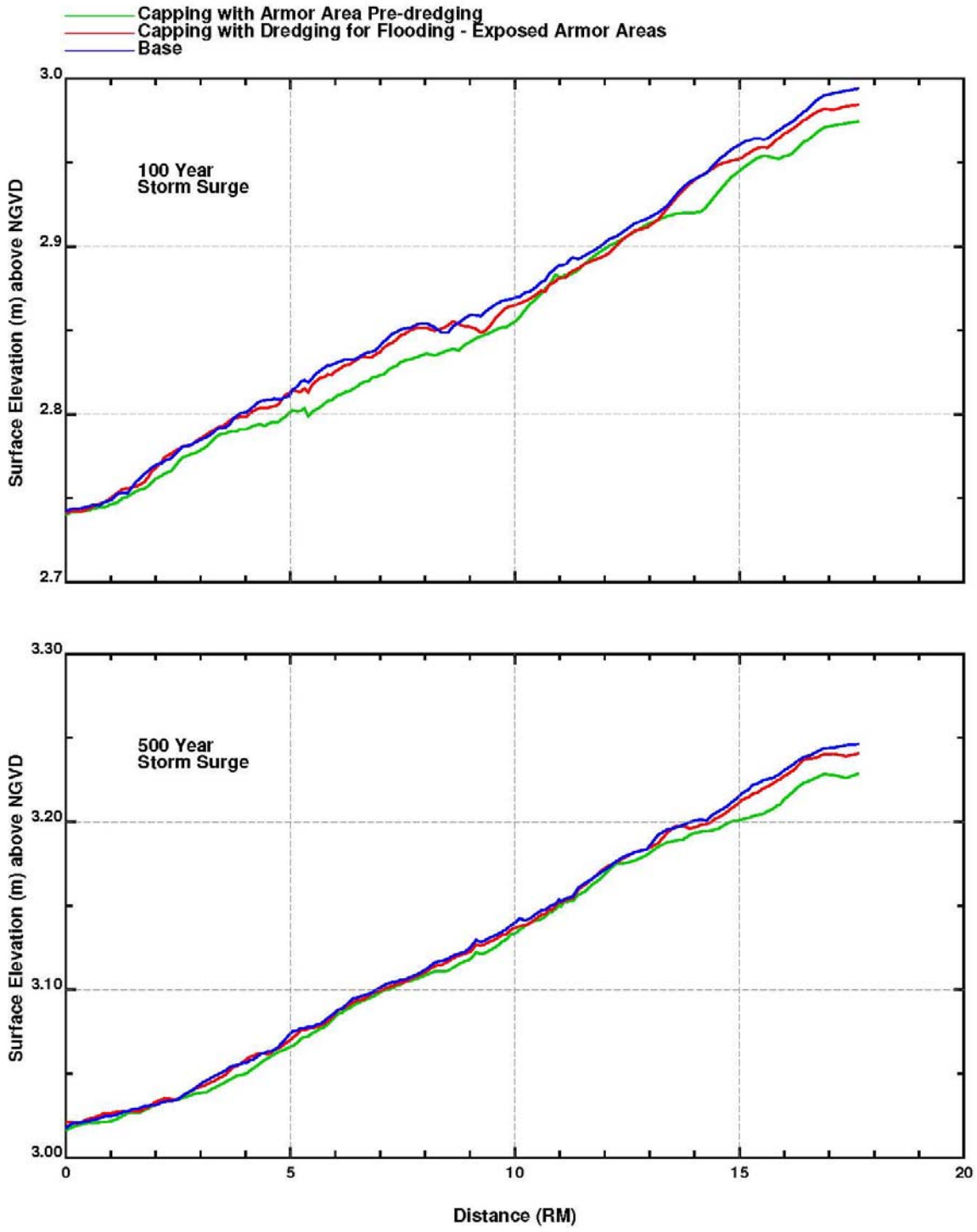

Maximum water surface elevations under different simulation scenarios along the Passaic River during 100- and 500-year storm surges.

Lower Eight Miles of the Lower Passaic River

Figure 6-14a

2014

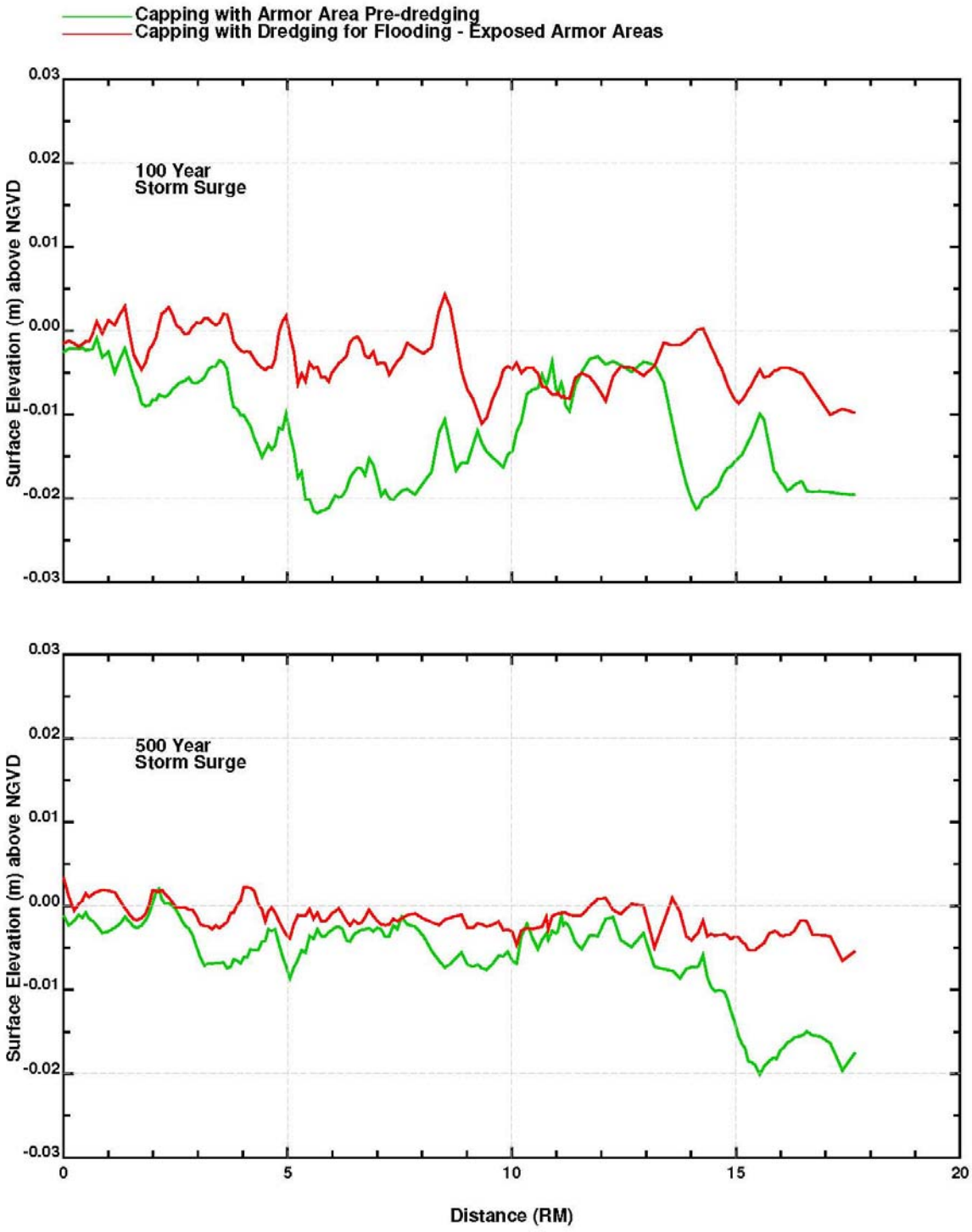

Net changes in water surface elevation under different simulation scenarios along the Passaic River compared to the "Base Case" scenario during 100- and 500-year storm surges.

Lower Eight Miles of the Lower Passaic River

Figure 6-14b

2014

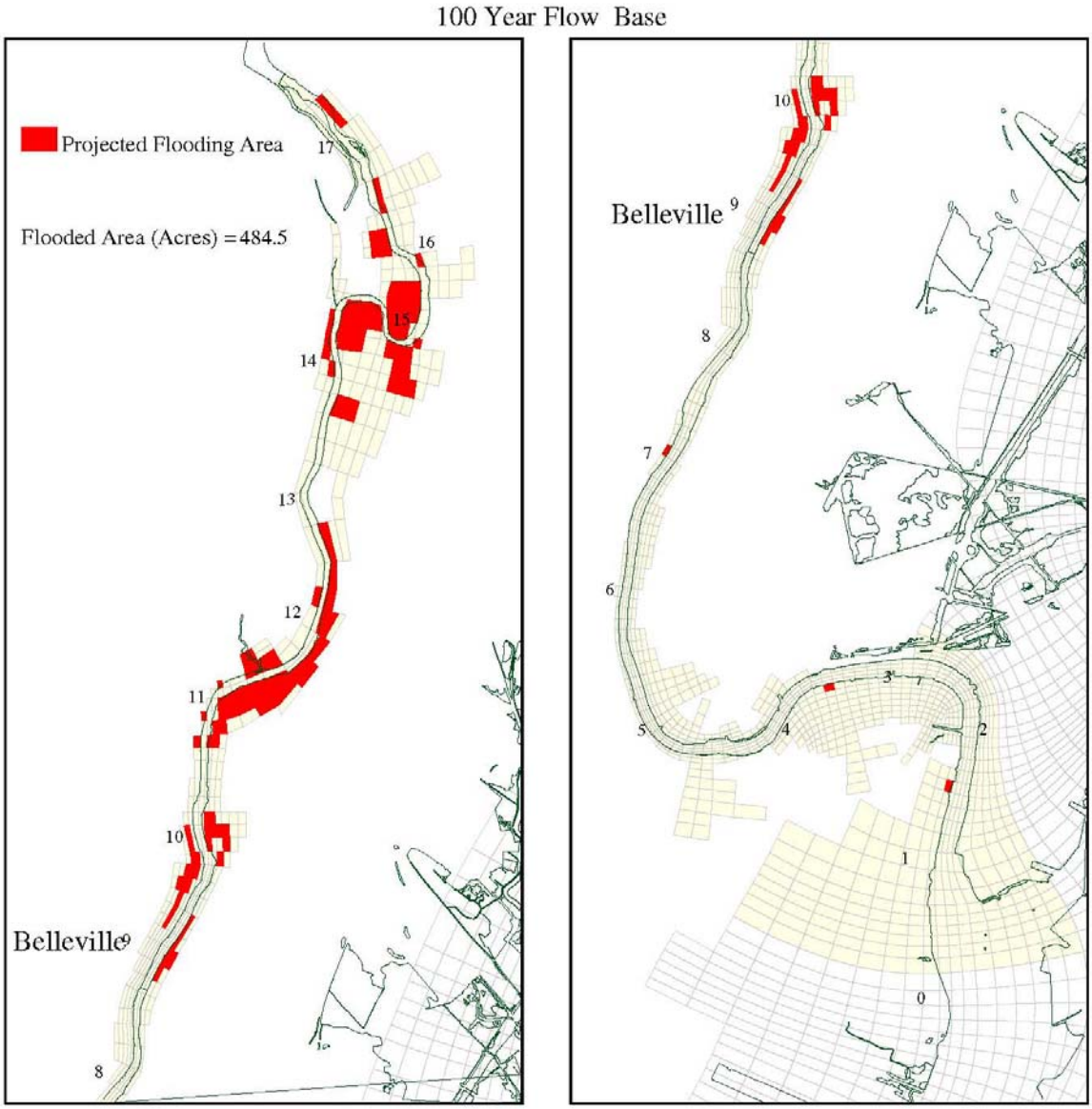

Projected flood area under the "Base Case" scenario during the 100-year flow.

Lower Eight Miles of the Lower Passaic River

Figure 6-15

2014

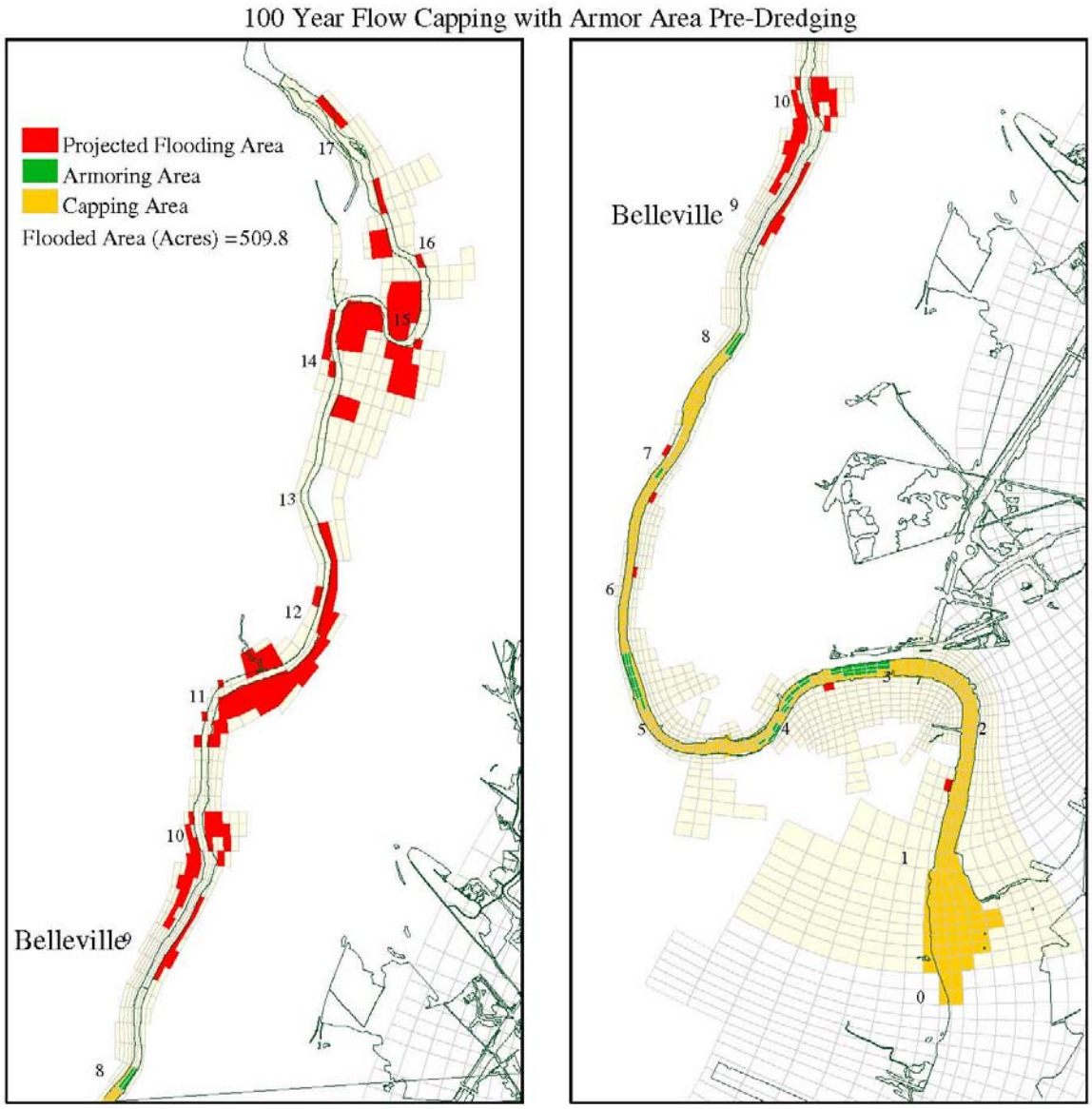

Projected flood area under the "Capping with Armor Area Pre-Dredging" scenario during the 100-year flow.

Lower Eight Miles of the Lower Passaic River

Figure 6-16

2014

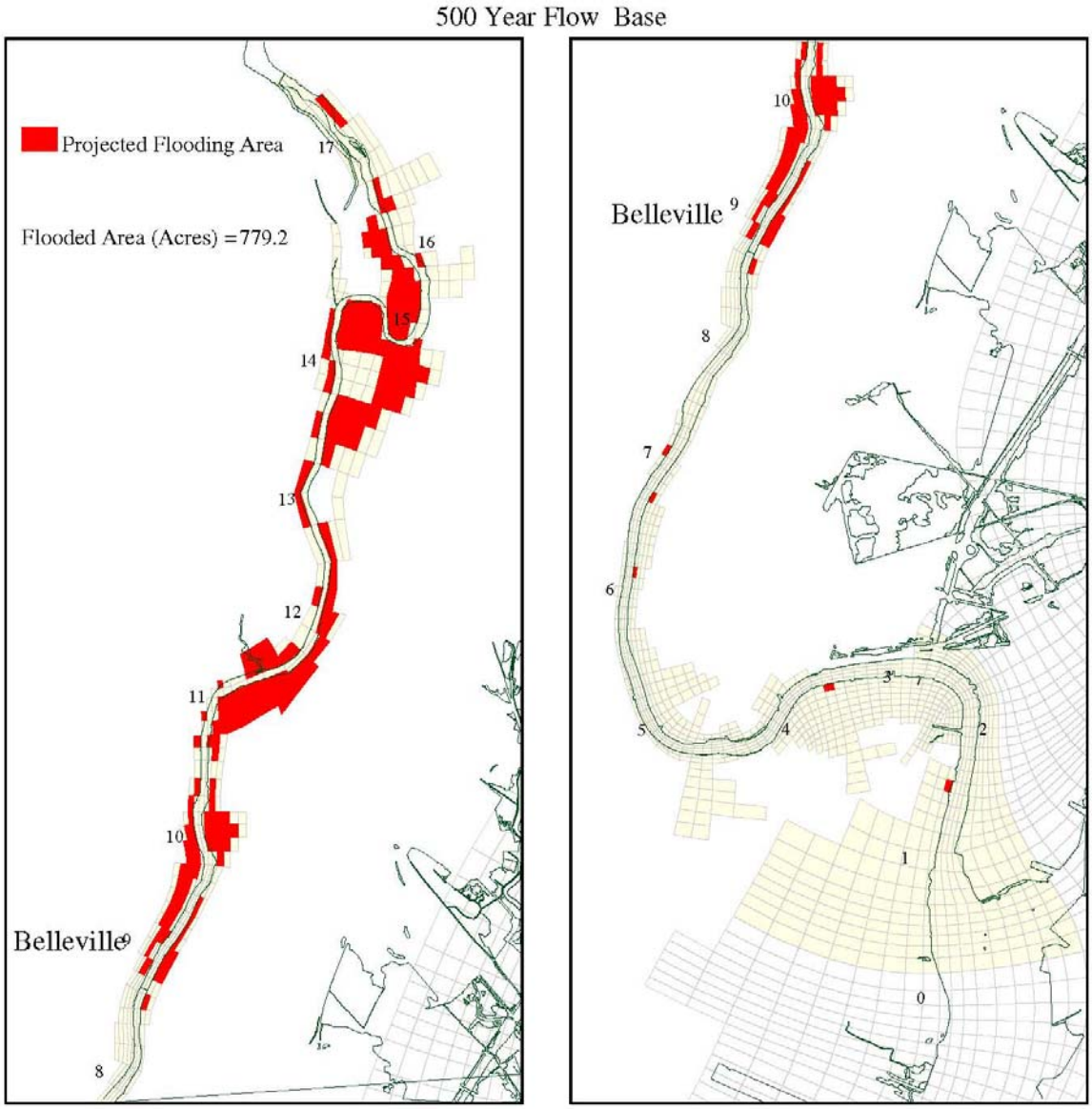

Projected flood area under the "Base Case" scenario during the 500-year flow

Figure 6-17

Lower Eight Miles of the Lower Passaic River

2014

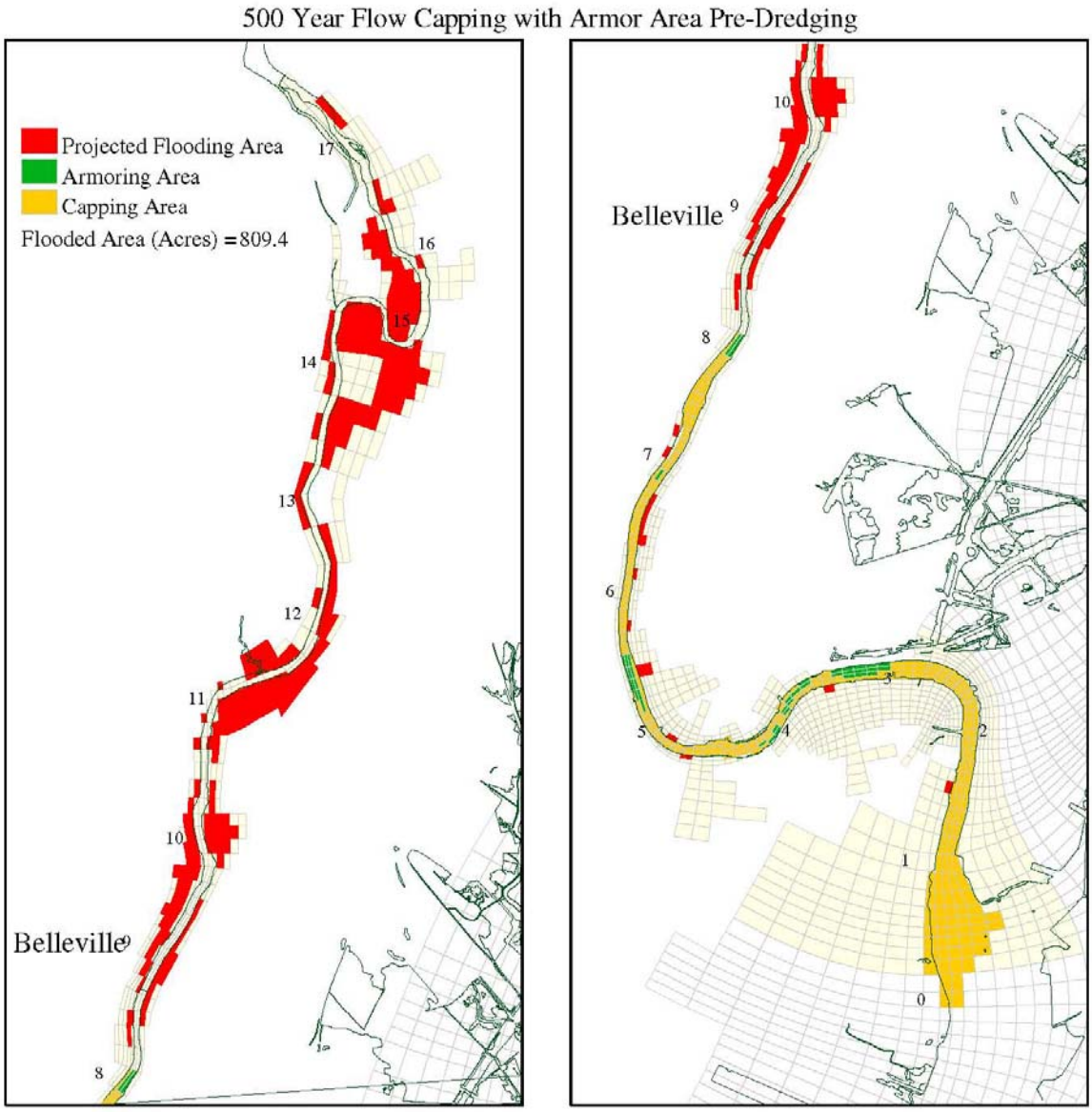

Projected flood area under the "Capping with Armor Area Pre-Dredging" scenario during the 500-year flow

Lower Eight Miles of the Lower Passaic River

Figure 6-18

2014

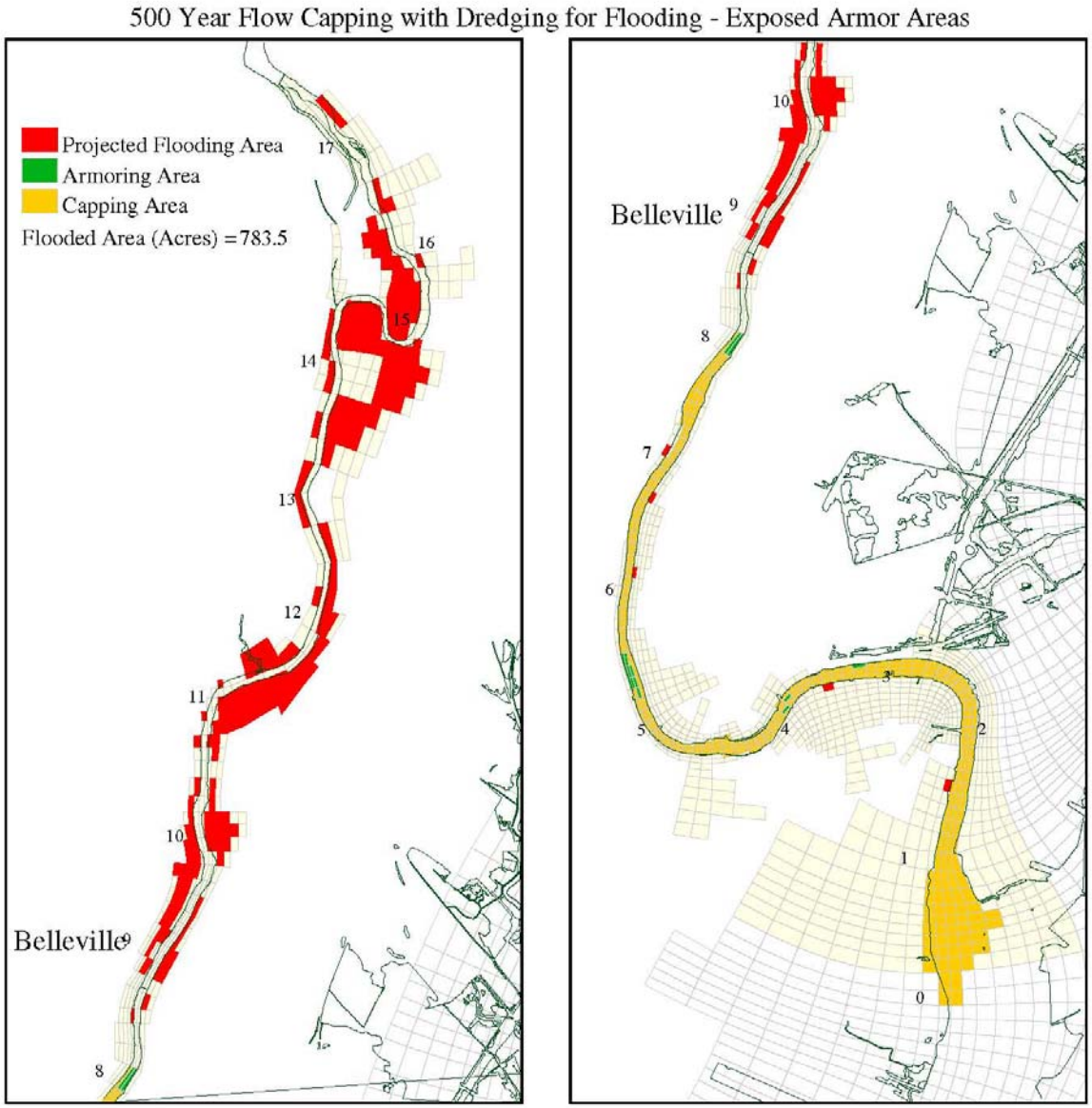

Projected flood area under the "Capping with Dredging for Flooding - Exposed Armor Areas" scenario during the 500-year flow

Lower Eight Miles of the Lower Passaic River

Figure 6-19

2014

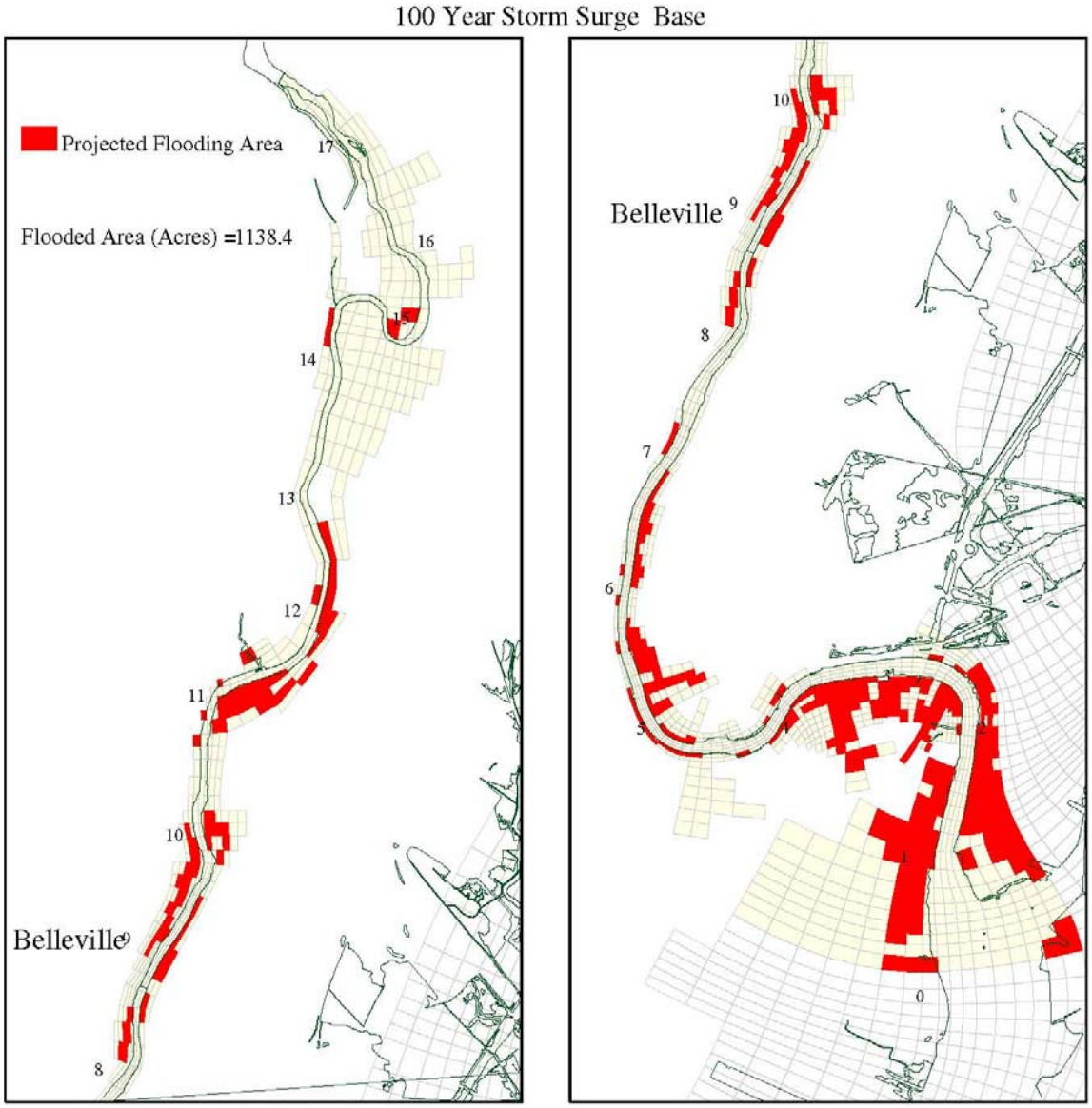

Projected flood area under the "Base Case" scenario during the 100-year storm surge

Lower Eight Miles of the Lower Passaic River

Figure 6-20

2014

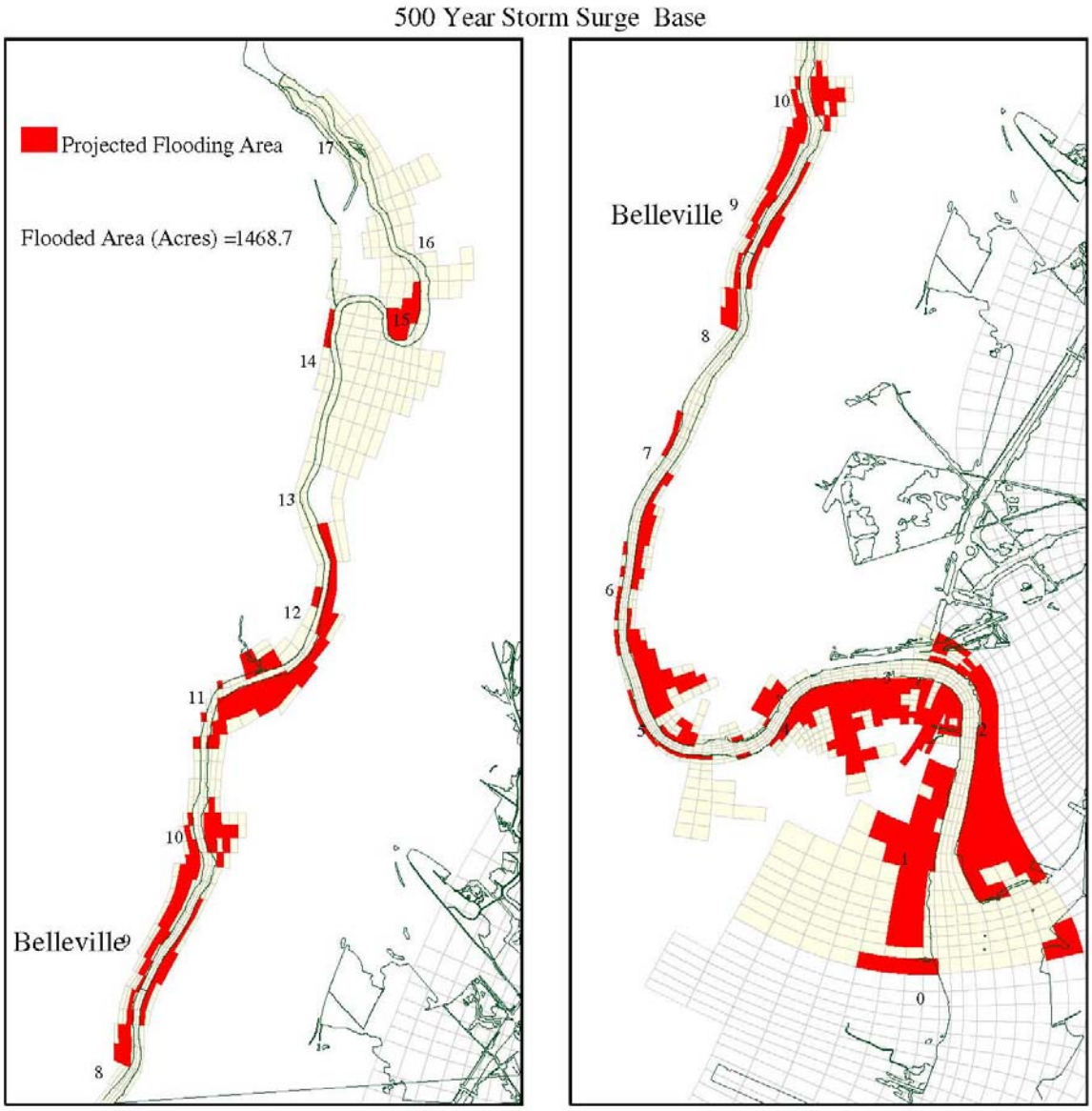

Projected flood area under the "Base Case" scenario during the 500-year storm surge

Lower Eight Miles of the Lower Passaic River

Figure 6-21

2014

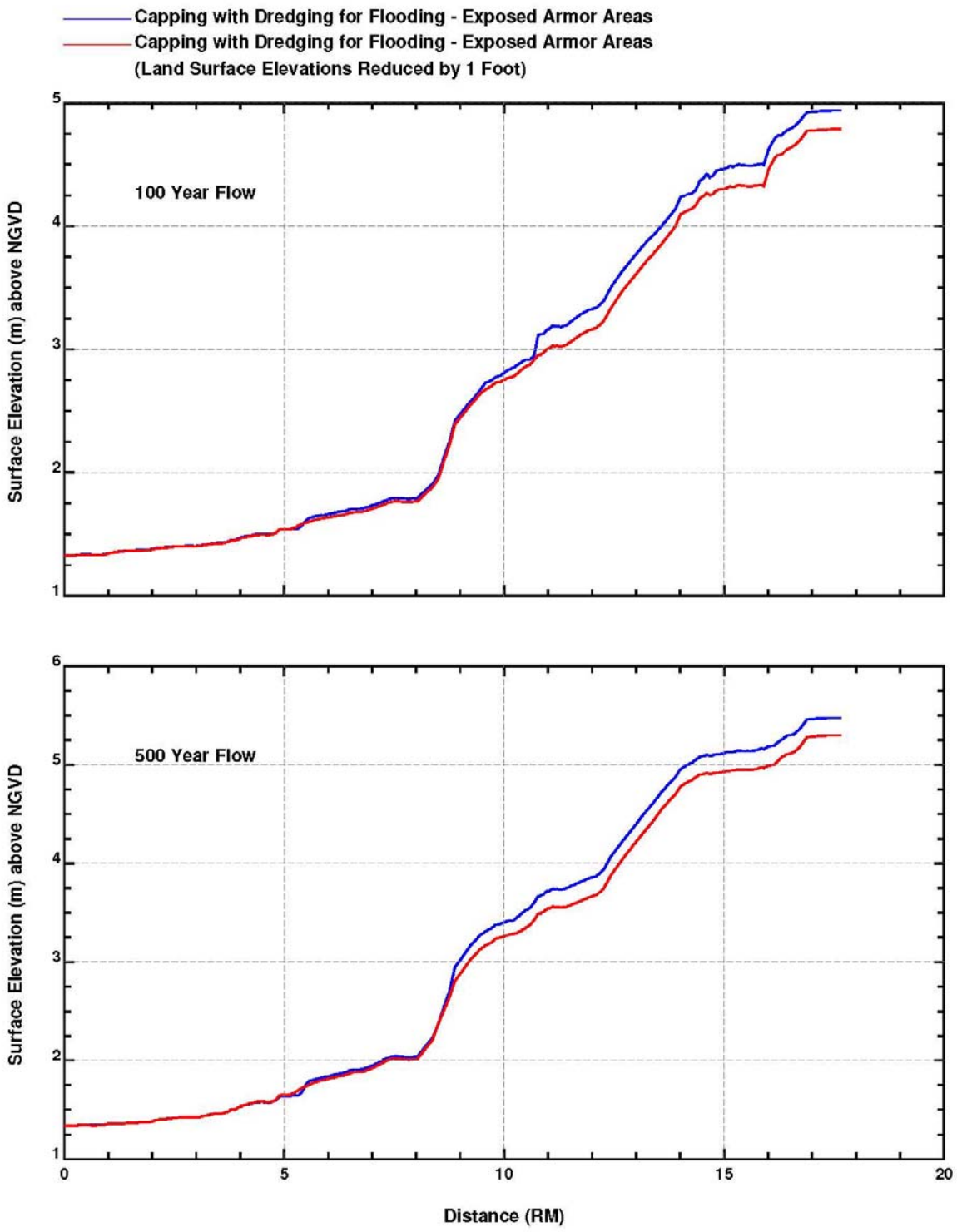

Comparison of water surface elevations for land elevation sensitivity runs for the 100-year flow (upper frame) and the 500-year flow (lower frame).

Lower Eight Miles of the Lower Passaic River

Figure 6-22

2014

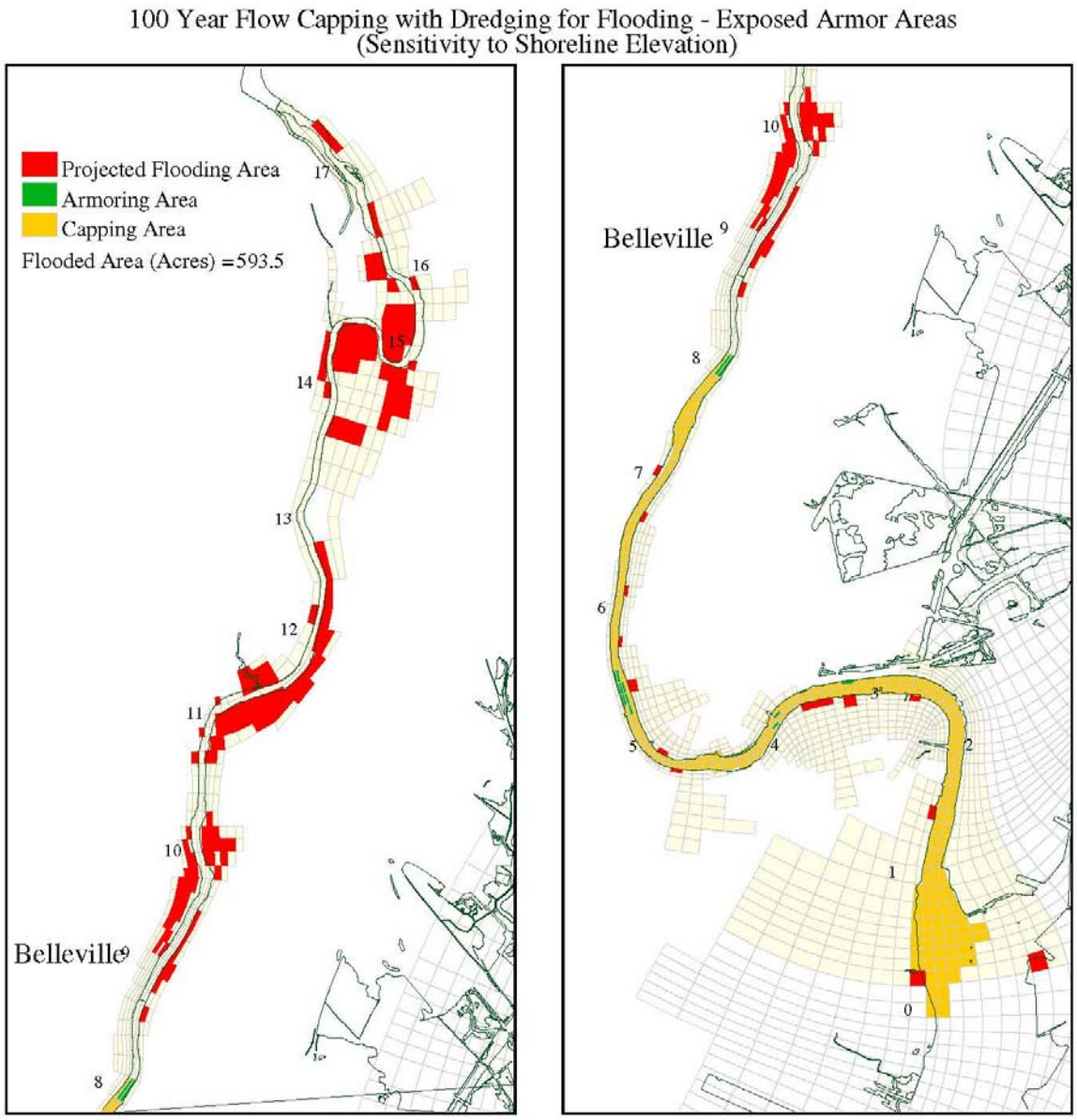

Projected flood area with 1 ft lowered land elevation under the "Capping with Dredging for Flooding - Exposed Armor Areas" scenario during the 100-year flow

Lower Eight Miles of the Lower Passaic River

Figure 6-23

2014

500 Year Flow Capping with Dredging for Flooding - Exposed Armor Areas
(Sensitivity to Shoreline Elevation)

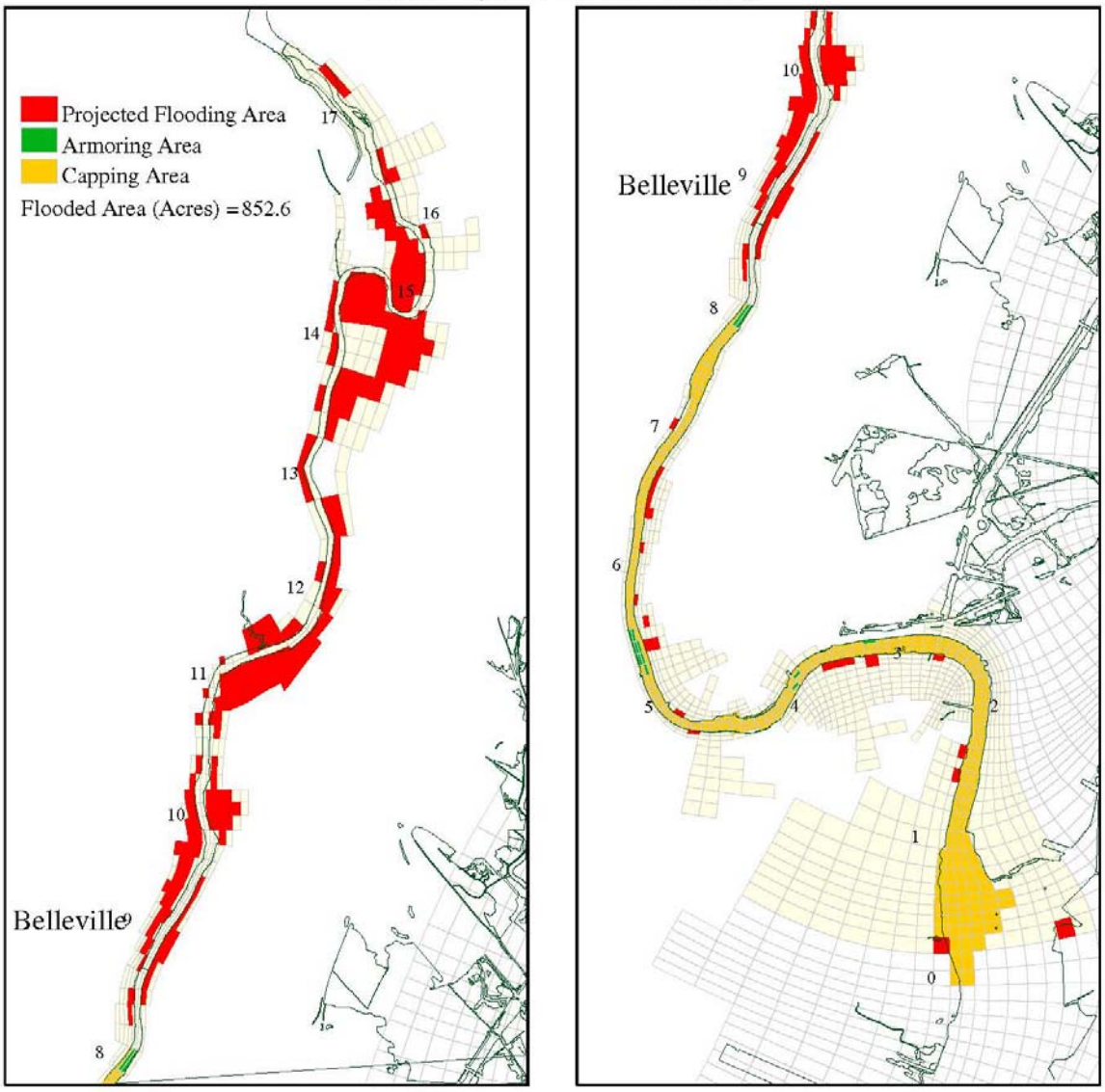

Projected flood area with 1 ft lowered land elevation under the "Capping with Dredging for Flooding - Exposed Armor Areas" scenario during the 500-year flow

Lower Eight Miles of the Lower Passaic River

Figure 6-24

2014

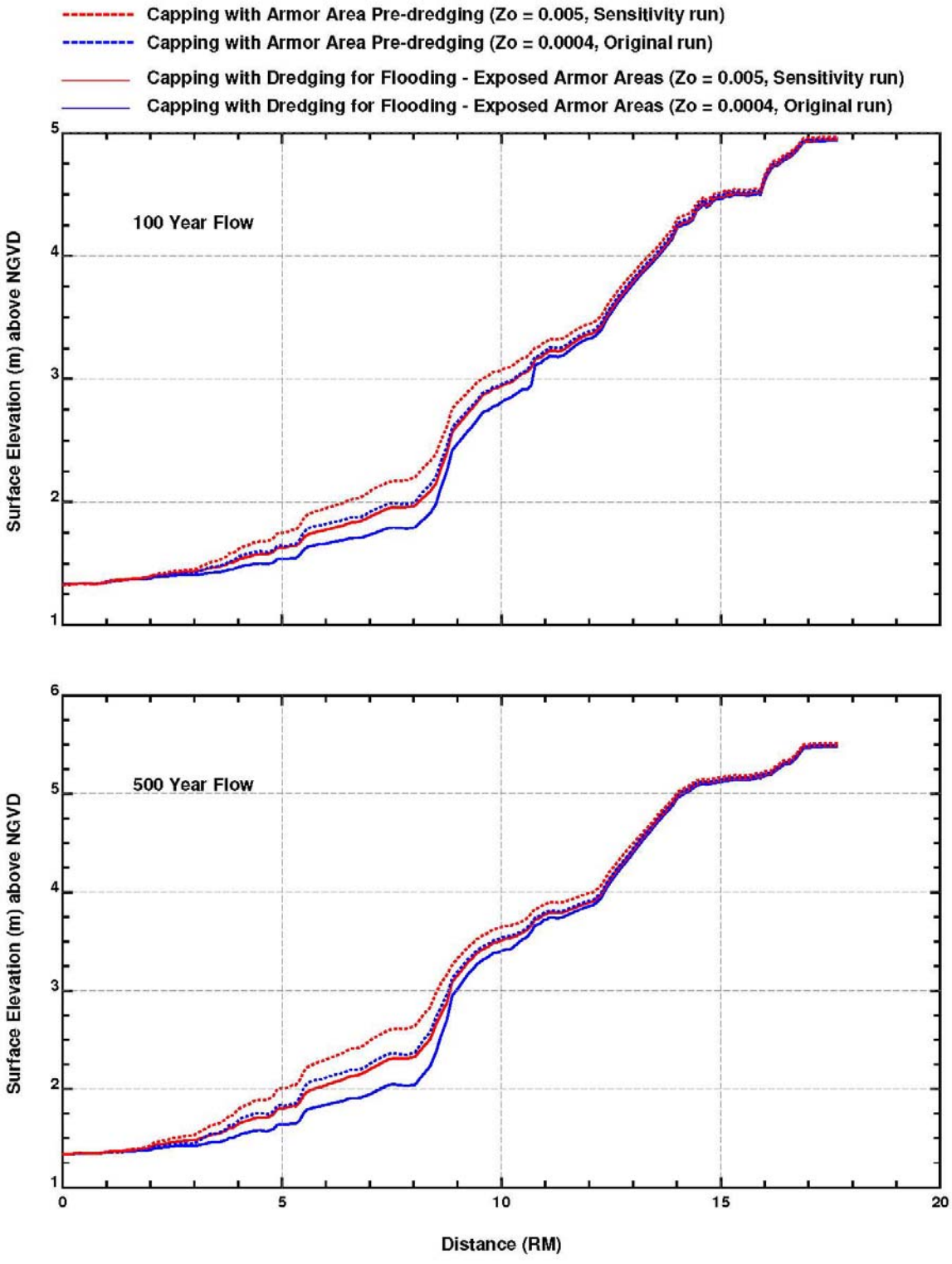

Sensitivity to bottom roughness length (Zo) to maximum water surface elevations along the Lower Passaic River

Lower Eight Miles of the Lower Passaic River

Figure 6-25

2014

100 Year Flow Capping with Armor-Area Pre-Dredging
(Sensitivity to Bottom Roughness Length)

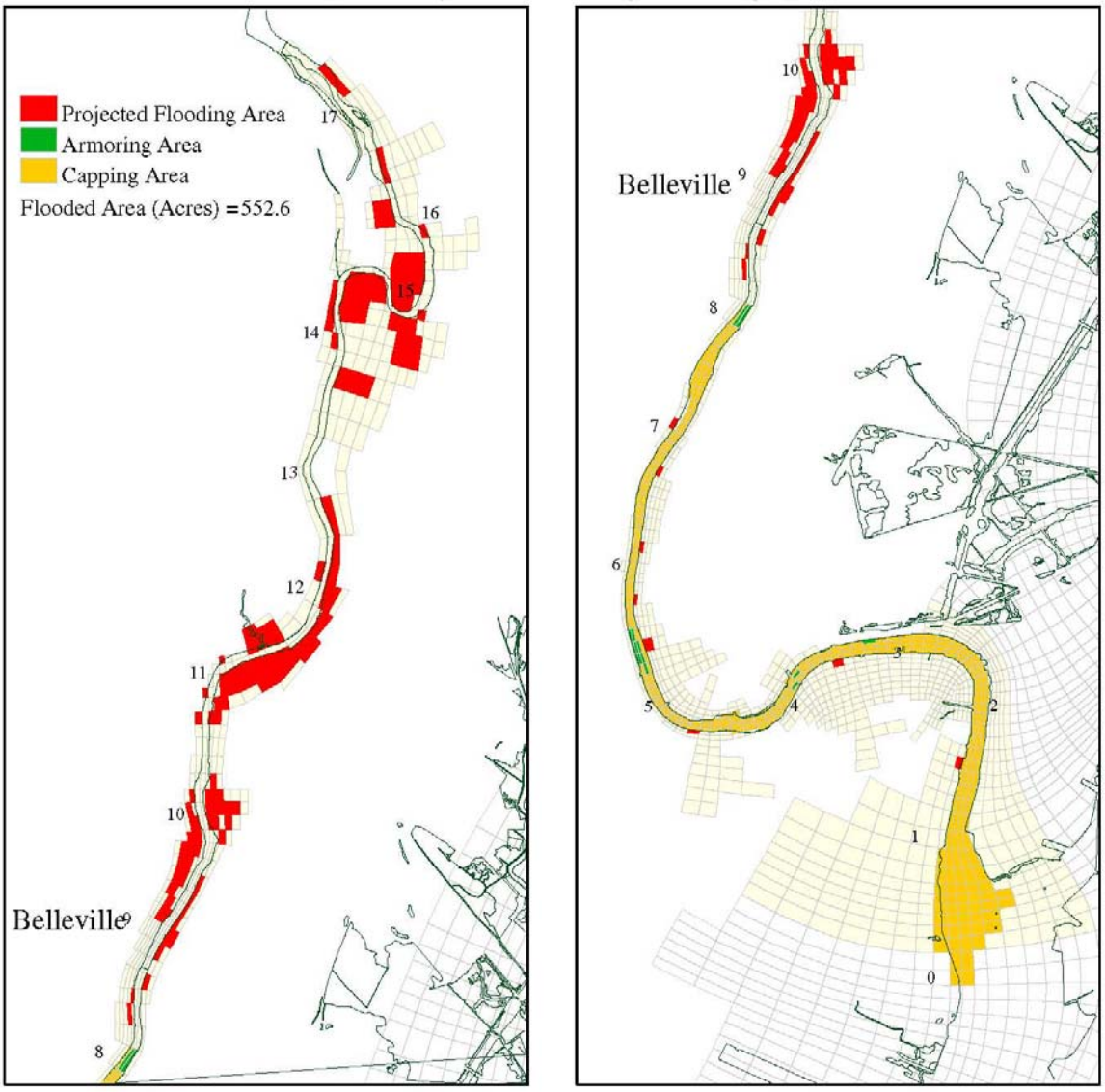

Projected flood area with Zo=0.005 for capping areas under the "Capping with Armor Area Pre-Dredging" scenario during the 100-year flow.

Figure 6-26

Lower Eight Miles of the Lower Passaic River

2014

100 Year Flow Capping with Dredging for Flooding - Exposed Armor Areas
(Sensitivity to Bottom Roughness Length)

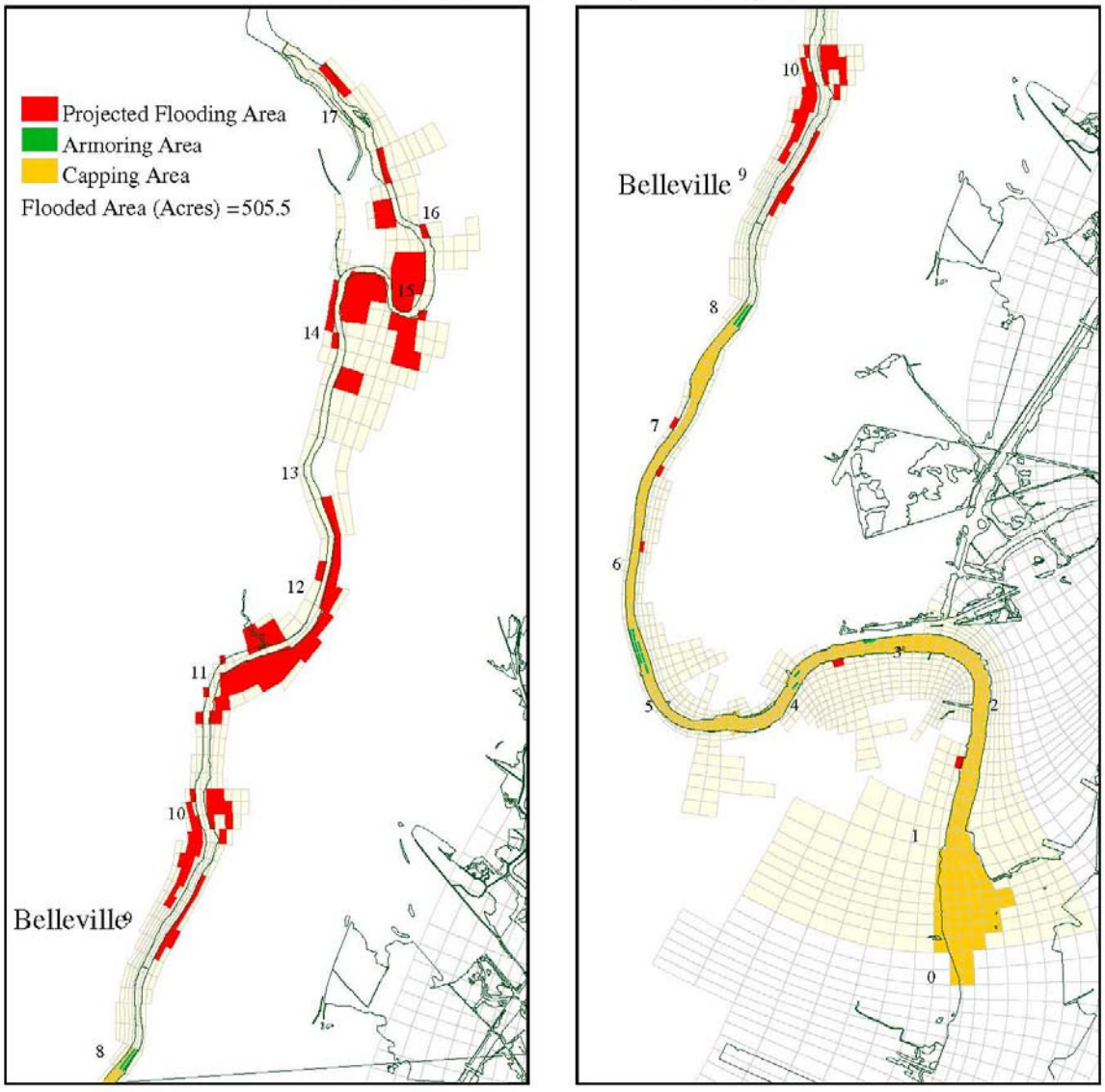

Projected flood area with Zo=0.005 for capping areas under the "Capping with Dredging for Flooding - Exposed Armor Areas" scenario during the 100-year flow

Figure 6-27

Lower Eight Miles of the Lower Passaic River

2014

500 Year Flow Capping with Armor-Area Pre-Dredging
(Sensitivity to Bottom Roughness Length)

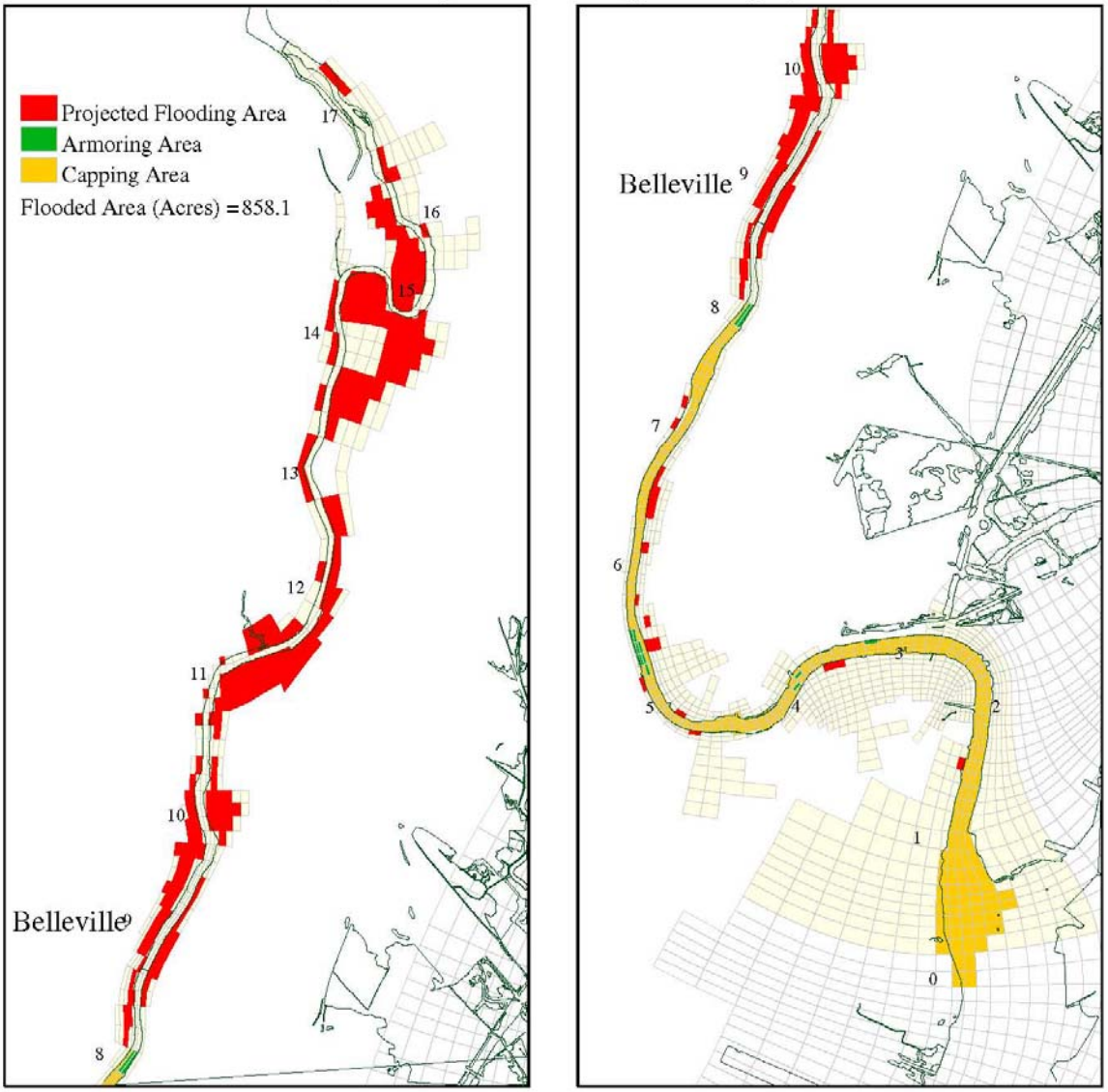

Projected flood area with Zo=0.005 for capping areas under the "Capping with Armor Area Pre-Dredging" scenario during the 500-year flow

Lower Eight Miles of the Lower Passaic River

Figure 6-28

2014

500 Year Flow Capping with Dredging for Flooding - Exposed Armor Areas
(Sensitivity to Bottom Roughness Length)

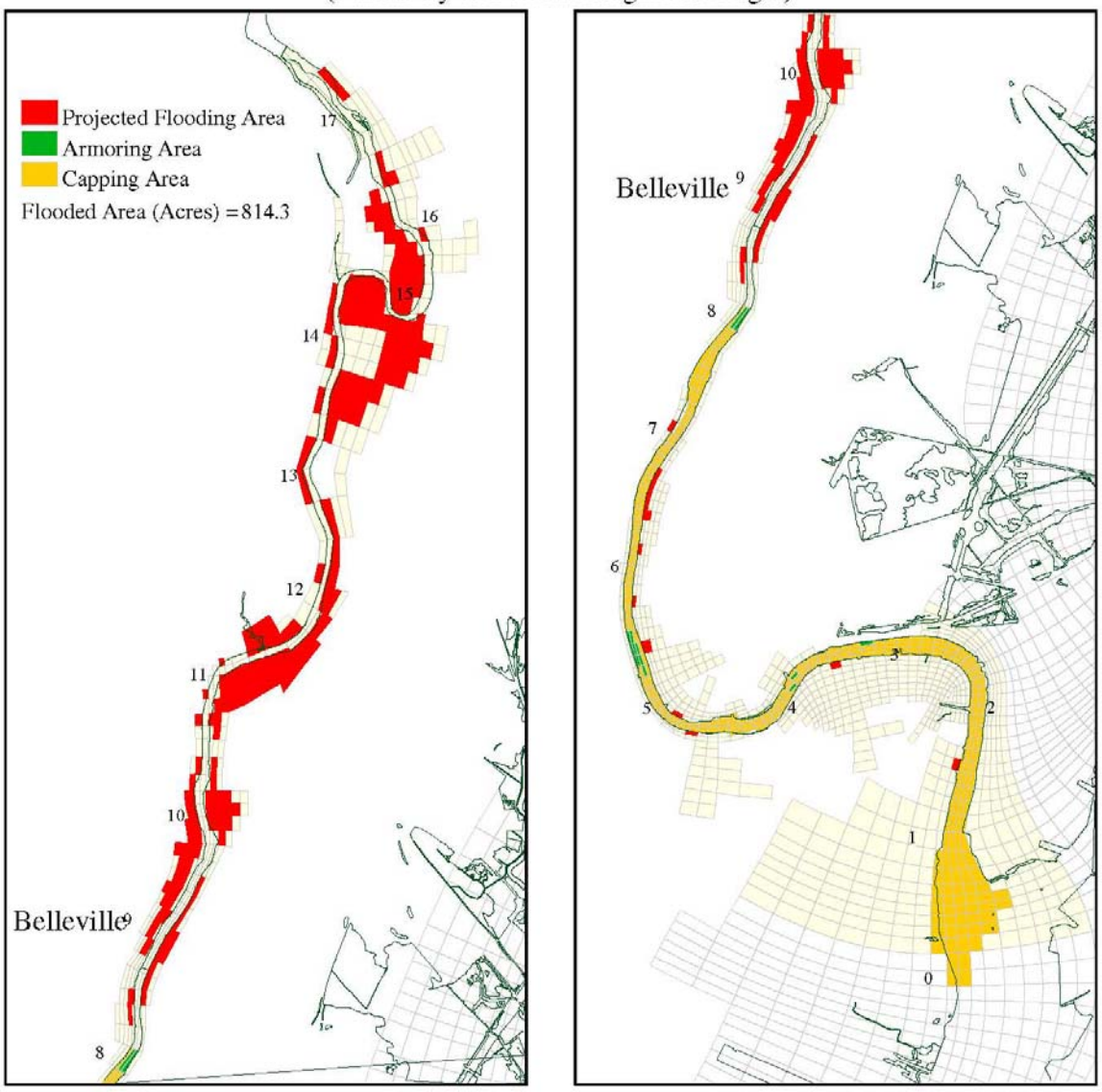

Projected flood area with Zo=0.005 for capping areas under the "Capping with Dredging for Flooding - Exposed Armor Areas" scenario during the 500-year flow

Figure 6-29

Lower Eight Miles of the Lower Passaic River

2014

Attachment A

SEDZLJ Incorporation into ECOM-SEDZLJS

ECOM-SEDZLJ
Model Implementation and Input File Structure

Prepared by:
Sea Engineering, Inc.
200 Washington Street, Suite 210
Santa Cruz, CA 95060
Tel: (831) 421-0871
Fax: (831) 421-0875

Table of Contents

Introduction

As part of the Lower Passaic River Restoration Project, HydroQual and the Technical Advisory Committee (TAC) decided to implement a pre-existing, peer-reviewed (Jones and Lick, 2001) sediment transport model into HydroQual's hydrodynamic model, ECOM. SEDZLJ uses measured sediment erosion data as the basis for modeling sediment transport in a system. Rather than attempt to reconstruct a computer code equivalent to SEDZLJ, it was determined to be more expedient and cost-effective for Sea Engineering, Inc. (SEI) to incorporate SEDZLJ into ECOM.

This document outlines the implementation of the existing version of SEDZLJ into ECOM. The implementation is referred to as ECOM-SEDZLJ As part of the implementation process, SEI verified that the SEDZLJ code has been properly implemented within ECOM by simulating and reproducing the laboratory data set generated by Little and Mayer (1972). This document additionally describes the input file structure of ECOM-SEDZLJ and presents the development and results of an example case.

Model Code Integration

The SEDZLJ code was integrated into the ECOM model to accomplish two goals. The first goal is to calculate the net flux of sediments (g/cm2/s) at the sediment/water interface due to erosion and deposition. The second goal is to calculate bedload transport of sand sized sediments on the computational grid. Water column transport of sediments is unchanged from the current ECOM implementation with the exception of allowing any user selected number of size classes.

The integration was accomplished through the inclusion of multiple subroutines to handle the input and calculation of the above processes. Figure 1 is a flowchart illustrating the main features of the model integration. Point "A" calls the SEDZLJ input routines, point "B" calls the water column transport routines from ECOM to transport all size classes of sediment utilized, and point "C" calls the routines to calculate the sediment flux and the bedload transport. The implementation of this structure allows for easy integration while preserving the main structure of ECOM. The model structure indicated has been verified to fit into the ECOM structure and operate with no variable conflicts or input conflicts. Full variable definitions will be provided upon finalization of SEDZLJ implementation.

In addition to minor modifications to the ECOM source code, the following subroutines were added:

- **SJ_SEDIC** – Reads all input files for SEDZLJ and initializes all required arrays
- **SJ_SEDFLX** – Calculates erosion and deposition fluxes at the sediment water interface and tracks sediment bed structure
- **SJ_BEDLOAD** – Calculates transport of bedload material
- **SJ_TECOUT** – Outputs hydrodynamic and sediment transport data in an ASCII Tecplot format in sedtec1d.dat, sedtec2d.dat, and sedtec3d.dat.

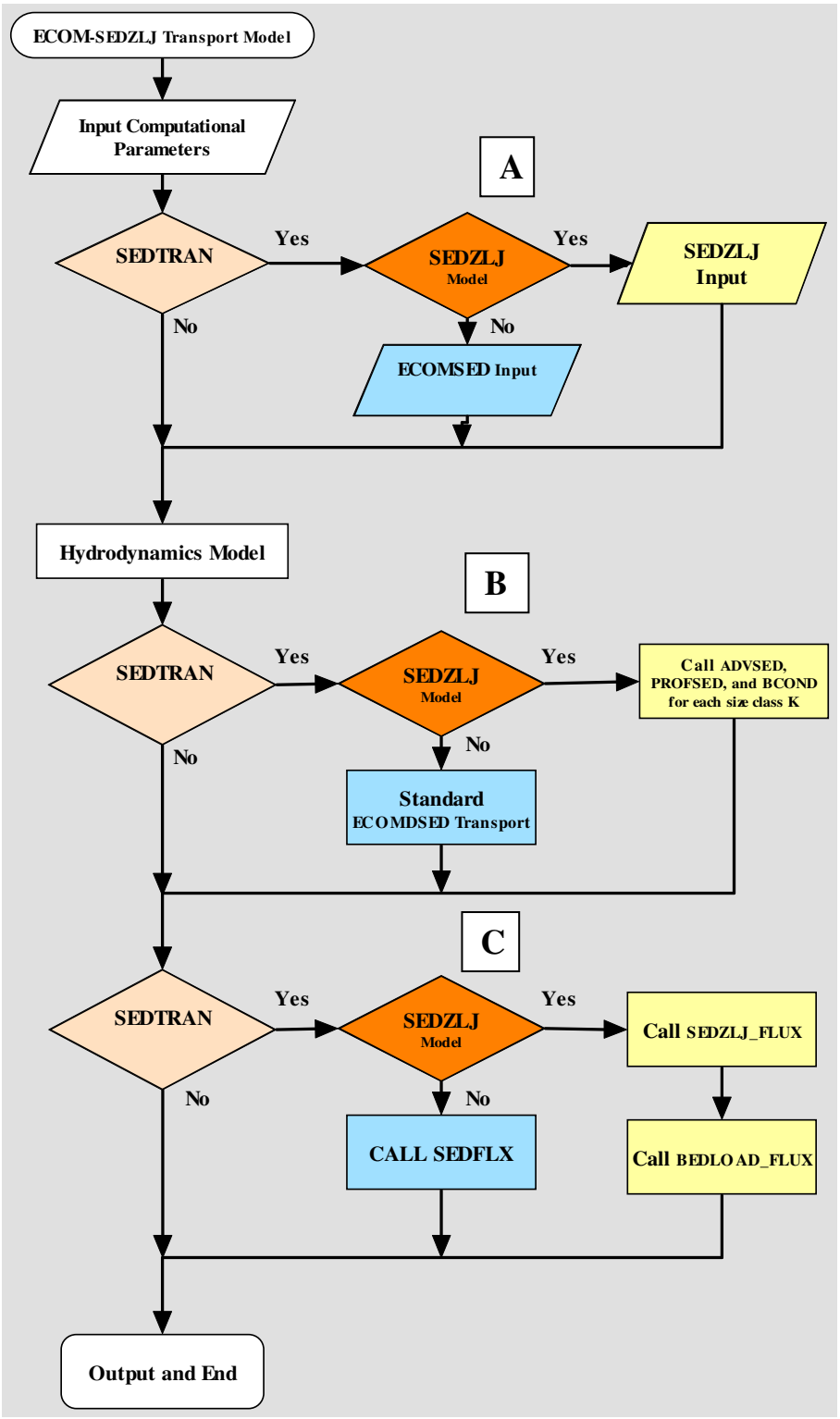

Figure 1. Flow chart of main points of SEDZLJ Integration into ECOM

Model Code Verification

The evaluation and validation of the SEDZLJ implementation required verification with a set of well-documented physical experiments. Little and Mayer (1972), hereafter referred to as LM, conducted detailed measurements of non-cohesive bed-armoring and transport in a straight flume. This case was utilized as a verification here because the bed-armoring and transport measurements over time utilize critical algorithms to the sediment transport process. Additionally, no detailed cohesive data sets for model verification exist at this time.

In their experiment, a flume 12.2 m long and 0.6 m wide was filled with a distribution of sand and gravel sediments. Clear water was then run over the sediment bed at a flow rate of 0.016 m^3/s. The eroded sediment was collected at the outlet of the flume, and the sediment transport rate was determined from this. When the sediment transport rate had decreased to 1 percent of the beginning transport rate, the bed was assumed to be fully armored and the experiment was ended. The full armoring of the sediment bed occurred in 75.5 hours. The final armored bed particle size distribution of the sediment surface was then measured by means of a wax cast.

This experiment was approximated with ECOM-SEDZLJ. Fourteen elements with a downstream dimension of 100 cm and cross-stream dimension of 60 cm were used to discretize the domain. The sediment bed comprised 9 size classes selected to accurately represent the sediment bed in the experiment. Table 7 shows the 9 size classes used in the model and their corresponding properties of settling speed, w_s, critical shear stress for erosion, τ_{ce}, and critical shear stress for suspension, τ_{cs}. These nine size classes were selected to most closely correspond to the size distribution reported by LM. Data from the Roberts et al. (1998) Sedflume studies on quartz were used to define the erosion rates and critical shear stresses for sediments in the model. The coefficient of friction was manually set such that the measured shear stress of 1.0 N/m^2 was reproduced in the model. The active layer was held at a constant thickness of 0.5 cm.

Model Results

The model was run for 75.5 hr with a time step of 0.1 s. The model shows good agreement with the experimental data. In the first few hours, there is a rapid increase in the average particle size from 1,600 to 2,500 μm; this is followed by a much slower rate of increase to a little above 2,500 μm by the end of the experiment. Associated with this increase, is a four order-of-magnitude decrease in erosion rate. The reason for this decrease is that the finer particle sizes are eroded from the sediment bed while the coarser particles are left behind, thereby increasing the average particle size of the bed and decreasing the erosion rates. This is responsible for the drop in the net transport rate of sediments from the channel, and is consistent with bed coarsening as discussed earlier. The bedload and suspended load components of the total transport are shown in Figure 8. Initially the transport is almost equally bedload and suspended load, but as the bed

coarsens the transport rate becomes almost exclusively bedload. This armoring process is expected since coarse particles, incapable of suspension at this shear stress, are mostly present in the bed.

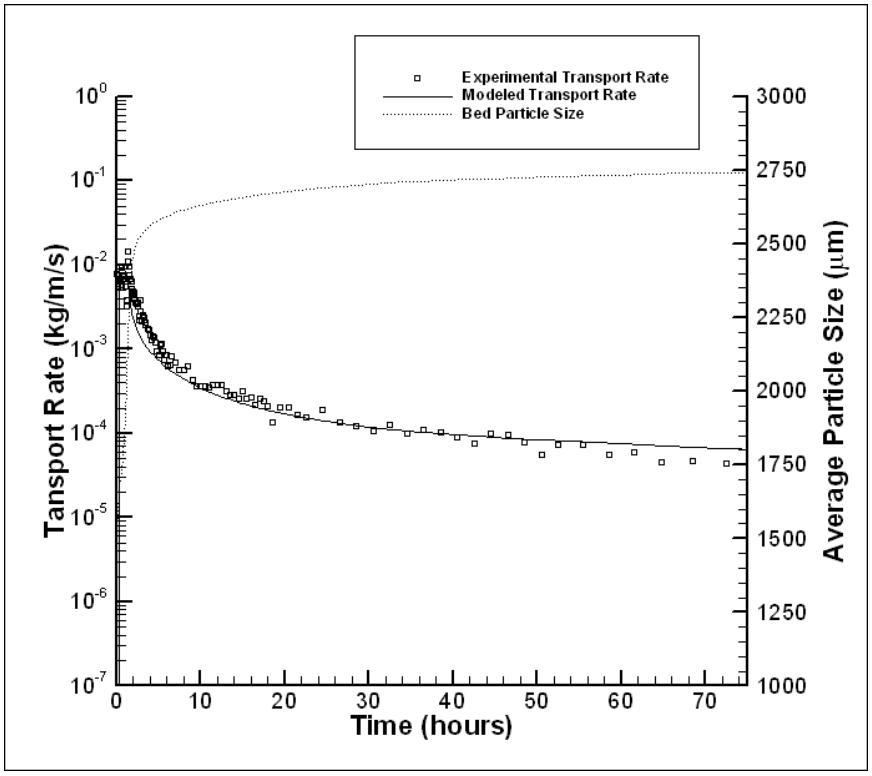

Figure 2. Modeled vs. measured transport rates and average particle size as a function of time.

A comparison is also made between the final particle size distribution in the active layer of the model and the particle size distribution of the surface of the bed in the experiment. Discrepancies between the two distributions are most evident at smaller particle sizes. Qualitatively both model and experiment show a significant amount of coarsening from the initial sediment bed. The final d_{50} was 2,750 μm in the model and 3,200 μm in the experiment yielding a difference of 14 percent.

The results from this model show good overall agreement with the data and trends observed in the LM experiments. Such agreement indicates that the model accurately estimates the erosion, transport, and subsequent coarsening of a sediment bed.

Input File Structure

Four input files control the sediment transport model parameters, sediment bed structure, and boundary conditions. The four input files are:

- *bed.sdf* – controls primary functionality of the sediment transport model
- *erate.sdf* – defines wet bulk density, critical shear stress, particle size, and erosion rates for the sediment bed
- *core_field.sdf* – defines spatial distribution of data in erate.sdf
- *coh_sed.inp* – water column sediment boundary conditions

To activate the SEDZLJ sediment transport model within EFDC, the SEDTRAN switch in *run_data* must be set to 'INCLUDE' and the SEDTYPE switch must be set to 'SEDZLJ'. Please refer to the ECOMSED manual for more information on the *run_data* file.

The following section details the four sediment transport input files required for the SEDZLJ sediment transport model. The FORTRAN 77 code used to read each line of input is presented with a description of the variables being read. Unless specified otherwise, the input is kept unformatted on each line for simplicity. Each line or type of input is separated by a STR_LINE input which allows for comments to be included into the input files.

bed.sdf Input File

```
READ (407,'(A80)') STR_LINE
READ (407,*) NSEDBEG,NSBED,Z0BCOH,CFMIN
```

NSEDBEG – Timestep at which the sediment transport calculations begin.
NSBED – The number of hydrodynamic timesteps between each sediment transport timestep.
Z0BCOH - The z_o of the sediment bed.
CFMIN – The minimum coefficient of friction for the shear stress calculation.

```
READ (407,'(A80)') STR_LINE
READ (407,*) VAR_BED,NCALC_BL,CONTAU
```

VAR_BED – Switch for turning on variable sediment bed. If it equals 1 then core_field.sdf is called so that spatial variation in bed properties can be defined.
NCLAC_BL – Switch for turning on bedload calculations. If it equals 1 then bedload transport is calculated, otherwise all material is assumed to transport as suspended load.
CONTAU – If CONTTAU is greater than zero, then the number is specified as a constant shear stress throughout the domain. This is a useful tool for testing.

```
READ (407,'(A80)') STR_LINE
READ (407,*) (D50(K),K=1,KSED)
```

Reads in the average particle size, D50, of each size class (μm) where KSED is the number of size classes.

```
READ (407,'(A80)') STR_LINE
READ (407,*) (TCRDPS(K),K=1,KSED)
```

Reads in the critical shear stress for suspension, TCRDPS, of each size class in dynes/cm^2.

```
READ (407,'(A80)') STR_LINE
READ(407,*) (TAUCRS(K),K=1,KSED)
```

Reads in the critical shear stress for erosion, TAUCRS, of each size class in dynes/cm^2.

```
READ (407,'(A80)') STR_LINE
READ (407,*)  (SCLOC(SC),SC=1,SCMAX)
```

This is the start of input data for sediments in the active layer. After the formation of an active layer due to deposition and coarsening, the average particle size of the active layer or deposited layer is determined. Then from that particle size the appropriate erosion rate is used. SCLOC represents the average particle sizes of the active for which data are available. Above 200 μm, the Roberts et al. (1998) quartz data can be used. Below that, the data is gathered from field sediments brought back to the laboratory to determine their erosion rates. This model will be modified in the future to include bed consolidation and variable bulk densities. As the active layer particle size changes, SEDZLJ interpolates between these values.

This line reads in the size classes for which active layer erosion rates are available.

```
READ (407,'(A80)') STR_LINE
READ (407,*)  (TAUCRITE(SC),SC=1,SCMAX)
```

The critical shear stress for erosion of active layer bed at each SCLOC particle size. As the active layer particle size changes, SEDZLJ interpolates between these values to determine the critical shear stress of the active layer.

```
READ (407,'(A80)') STR_LINE
DO SC=1,SCMAX
    READ(407,*) (ENRATE(SC,M),M=1,ITBM)
CONTINUE
```

Erosion rates (cm/s) at each predetermined shear stress (same shear stresses entered in erate.sdf file) for each particular particle size SCLOC. SEDZLJ interpolates between these values as the active layer particle size changes.

***erate.sdf* Input File**

This file inputs all of the bed properties. Due to current model structure the first two layers are initially dummy layers and the actual sediment bed starts with layer 3. The input file still reads in data for the first two layers. It is recommended that the data for layers 1, 2, and 3 are all set equal to the initial surface interval data.

```
READ (408,'(A80)') STR_LINE
READ (408,*) (TAUTMP(1,LL),LL=1,LAYMAX)
```

Reads in the critical shear stress, TAUTMP, for erosion for each layer in core in dynes/cm^2. LAYMAX is specified as a parameter in *comdeck*.

```
READ (408,'(A80)') STR_LINE
READ(408,*) (BLKTMP(LL),LL=1,LAYMAX)
```

Reads in the wet bulk density for each layer in the sediment bed in g/cm^3.

```
READ (408,'(A80)') STR_LINE
DO LL=1,LAYMAX
    READ (408,*) (PNEW(1,LL,K),K=1,KSED)
CONTINUE
```

Reads in the mass percentage of each size class in each layer of core. Read as a percentage not as a fraction (i.e. 100.0 = 100% of that size class).

```
READ (408,'(A80)') STR_LINE
 DO M=1,ITBM
    READ (408,*)  TAULOC(M)
    READ(408,*) (E0RATE(1,LL,M),LL=1,LAYMAX)
CONTINUE
```

Reads in the basic shear stresses for which data are available, TAULOC, in dynes/cm^2. Note that this is the same for all cores as well as the intervals used in the erosion rate inputs in *bed.sdf*. They are indexed by ITBM, which is the number of shear stress intervals defined in *comdeck*.

The next line is the measured erosion rates (cm/s) for each shear stress at each layer in the core. This value is the specified erosion rate at the top of each layer.

```
READ (408,'(A80)') STR_LINE
READ(408,*) (TSED0S(LL),LL=1,LAYMAX)
```

Reads in the thickness of each layer, TSED0S, in cm.

For multiple cores, each core is repeated and defined as above and core locations are read in through *core_field.sdf*.

***core_field.sdf* Input File**

```
READ(94,*)  INCORE
DO  J=JM-1,1,-1
      READ(94,2000) (CORENO(I,J),I=2,IM-1)
CONTINUE
 2000   FORMAT (20I3)
```

This reads in the number of cores used (INCORE) and reads in the appropriate core number (CORENO) for each location in the format shown.

***coh_sed.inp* Input File**

When SEDZLJ is activated this file is read in differently than its default ECOM format. The format is:

```
READ(IUT402,11)  (COM(I),I=1,80)
READ (IUT402,*)KSED
```

Reads in the number of sediment size classes, KSED.

```
READ(IUT402,11)  (COM(I),I=1,80)
READ (IUT402,*)NUMEBCSE
READ(IUT402,77,ERR=6201) TIME
DO N=1,NUMEBCSE
    READ(IUT402,*) II,JJ,IIC,JJC
    DO KK=1,KSED
        READ(IUT402,*) (CBDRYSL(KK,N,K),K=1,KSL)
     ENDDO
ENDDO
```

This reads in the number of sediment concentration boundary specifications. This is the same as that outlined in the ECOMSED manual except for the inclusion of multiple size classes in the CBDRYSL loop. Note that TIME is the only formatted read and that TIME is continuously looped as in the original version.

```
READ(IUT402,11)  (COM(I),I=1,80)
READ (IUT402,*)NUMQBCSE
DO N=1,NUMQBCSE
    READ (IUT402,179)ISEQD(N),JSEQD(N),ISEQC(N),JSEQC(N)
CONTINUE
READ(IUT402,77,ERR=6593) TIME
DO KK=1,KSED
    READ(IUT402,*)  (CDIS(KK,N),N=1,NUMQBCSE)
ENDDO
```

This reads in the number of sediment discharge specifications. This is the same as that outlined in the ECOMSED manual except for the inclusion of multiple size classes in the CDIS loop. Note that TIME is the only formatted read and that TIME is continuously looped as in the original version.

Example Case

An example case is outlined here which approximates a simplified model of the Little and Mayer (1972) experiment. The model uses the same flume dimensions but with only 3 size classes specified and a lower shear stress applied constantly throughout the model. This case allows for an illustration of the setup of a constant sediment bed with multiple size classes. Also, the results include suspended and bed load transport as well as a dynamically armoring sediment bed. Output can be viewed in the ASCII Tecplot format in sedtec1d.dat, sedtec2d.dat, and sedtec3d.dat. Variable names are contained in the header of each file.

The *bed.sdf* file is used to setup the initial model parameters. Notes are included here in the following example files.

```
# NSEDBEG  NSBED  Z0BCOH [m] CFMIN #
   1000     1     0.001     0.002
# VariSedBed Bedload  Const Shear [dynes/cm2] #
       0        1        4.5
# D50 of Size Class D50(K) [um] #
18.  125.  1020.
# Critical Shear for Deposition TCRDPS(K) [dynes/cm2] #
0.5   1.6   16.8
# Critical Shear for Erosion TAUCRS(K) [dynes/cm2] #
0.5   1.6   4.25
# Sediment Bed Size (um) Tables #
  5.00 222.00 432.00 1020.00 2400.00 2600.00 3360.00 6000.00
# Critical Shear for Erosion of Bed Surface [dynes/cm^2]  #
  1.50   2.40   3.30   4.25   8.28   9.50  9.80  25.00
#  Erosion rates for active and deposited Layers [cm/s] #
 0.00000001 0.00097900 0.00486000 0.02410000 0.11900000 0.59200000 ! 18 Micron
 0.00000001 0.00000001 0.00059700 0.00596000 0.05950000 0.59400000 !222 Micron
 0.00000001 0.00000001 0.00216000 0.01270000 0.07490000 0.44200000 !432 Micron
 0.00000001 0.00000001 0.00114000 0.00651000 0.03710000 0.21100000 !1020 Micron
 0.00000001 0.00000001 0.00000001 0.00062800 0.00470000 0.03510000 !2400 Micron
 0.00000001 0.00000001 0.00000001 0.00045500 0.00340000 0.02610000 !2600 Micron
 0.00000001 0.00000001 0.00000001 0.00001310 0.00104000 0.00817000 !3360 Micron
 0.00000001 0.00000001 0.00000001 0.00000001 0.00000001 0.00010700 !6000 Micron
```

The model is set to begin after 1000 timesteps with a bottom Z0 of 0.001 m. Bedload is activated and a constant shear stress of 4.5 dynes/cm^2 is applied uniformly to the bottom. Three size classes of 18, 125, and 1020 µm diameter are used for the model. The critical shear stresses for deposition and erosion are determined from van Rijn (1993). The sediment bed size lookup table for the active layer as well as its critical shear stress and erosion rates are all determined from the Roberts et al. (1998) quartz experiments. These are the same values utilized in the Little and Mayer (1972) test cases.

The *erate.sdf* file is used to setup the initial sediment bed. Since the variable sediment bed switch is set to zero, only one core is specified for the entire bed.

```
#  Critical Shear Stress (dynes/cm^2)  #
4.1 4.1 4.1 4.1 4.1
#  Bulk Denity (g/cm^3)              #
1.85  1.85  1.85  1.85  1.85
#  Particle Size Distribution        #
88. 10. 02.
88. 10. 02.
88. 10. 02.
88. 10. 02.
88. 10. 02.
#  Initial Bed Erosion Rates         #
   0.
 1.000E-09 1.000E-09 1.000E-09 1.000E-09 1.000E-09
    2.00000
 1.000E-09 1.000E-09 1.000E-09 1.000E-09 1.000E-09
    4.00000
 1.000E-09 1.000E-09 1.000E-09 1.000E-09 1.000E-09
    8.00000
 3.970E-04 3.970E-04 3.970E-04 3.970E-04 3.970E-04
    16.0000
 1.860E-03 1.860E-03 1.860E-03 1.860E-03 1.860E-03
    32.0000
 8.730E-03 8.730E-03 8.730E-03 8.730E-03 8.730E-03
#  Layer Thicknesses                 #
 0.0    0.00  5000.00  5000.00  5000.00
```

As noted previously, the first 3 layers are all set to be equal as only the 3rd layer represents the initial surface. The values are all obtained from the Roberts et al. (1998) data for a uniform quartz sediment bed with a distribution at 48 µm and a bulk density of 1.85 g/cm^3. The first two layer thicknesses are always set to zero. The next three layers define an approximately infinitely deep bed of uniform properties.

Since the sediment bed is uniform spatially, *core_field.sdf* is not required. The file *coh_sed.sdf* is needed to define the sediment boundary conditions.

```
#  Number of Size Classes (KSED) #
   3
#  Input specified concentration boundary conditions CBDRYSL #
   1
     0.0
  14    2   13    2
  0.0  0.0  0.0  0.0  0.0
  0.0  0.0  0.0  0.0  0.0
  0.0  0.0  0.0  0.0  0.0
   9999.000
  14    2   13    2
  0.0  0.0  0.0  0.0  0.0
  0.0  0.0  0.0  0.0  0.0
  0.0  0.0  0.0  0.0  0.0
#  Input specified discharge boundary conditions CDIS  #
   1
   2    2    1    2
   0.0000
   0.0000
   0.0000
   0.0000
 9999.0000
   0.0000
   0.0000
   0.0000
#  End file #
```

The boundary and discharge conditions are set to clear water with zero sediment concentrations. The # End file# line is required here.

Results

The results are similar to the Little and Mayer case. The total sediment flux measured at the end of the channel decreases rapidly over the 10 hours of the model run due to bed coarsening. Bed coarsening can be readily seen as the particle size increases. Figure 3 illustrates the flux and surface particle size as a function of time at a point at the end of the channel. Figure 4 shows a similar plot with the surface erosion and deposition rates as a function of time. The erosion rate rapidly decreases as the bed coarsens. The deposition rate increases towards the erosion rate as the channel approaches equilibrium. Figure 5 shows a cross section of suspended sediment concentrations in the channel after 10 hours.

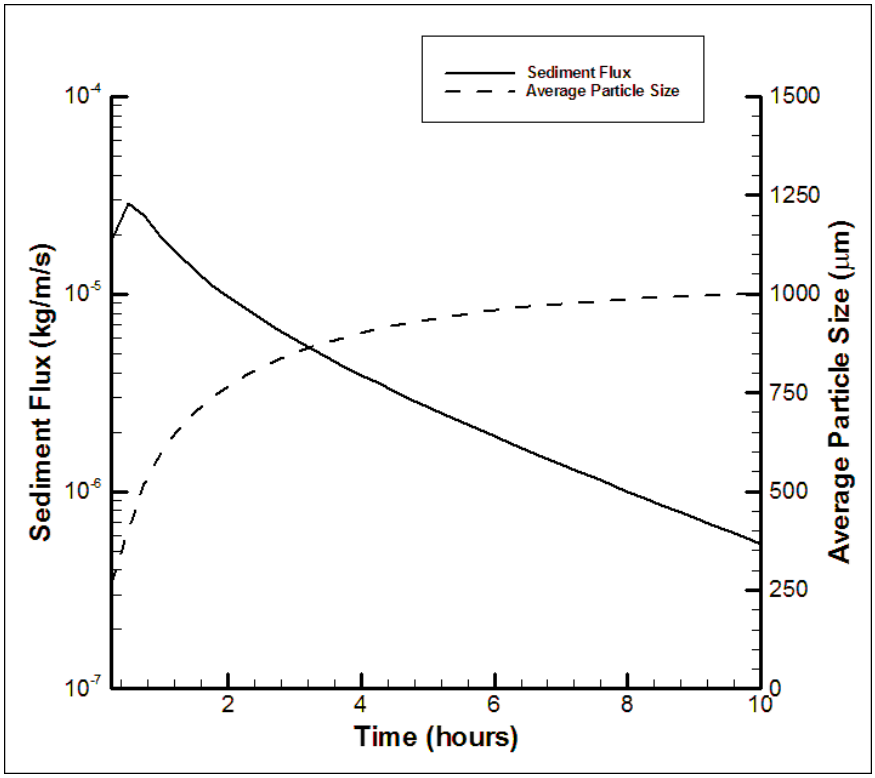

Figure 3. Plot of sediment flux and average particle size as a function of time for the example case.

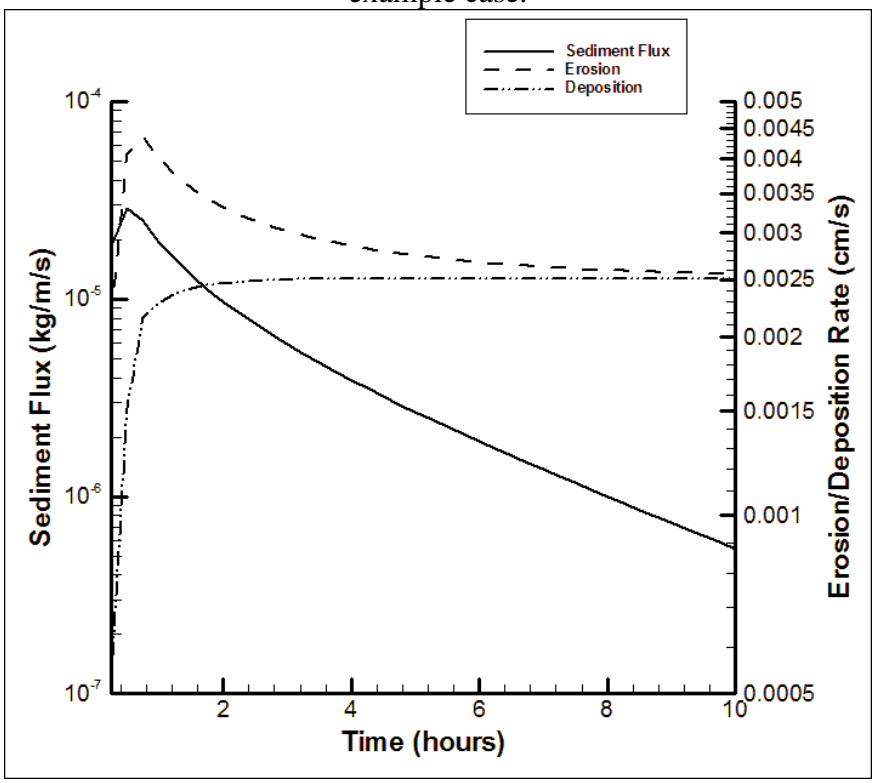

Figure 4. Plot of sediment flux and erosion and deposition rate as a function of time for the example case.

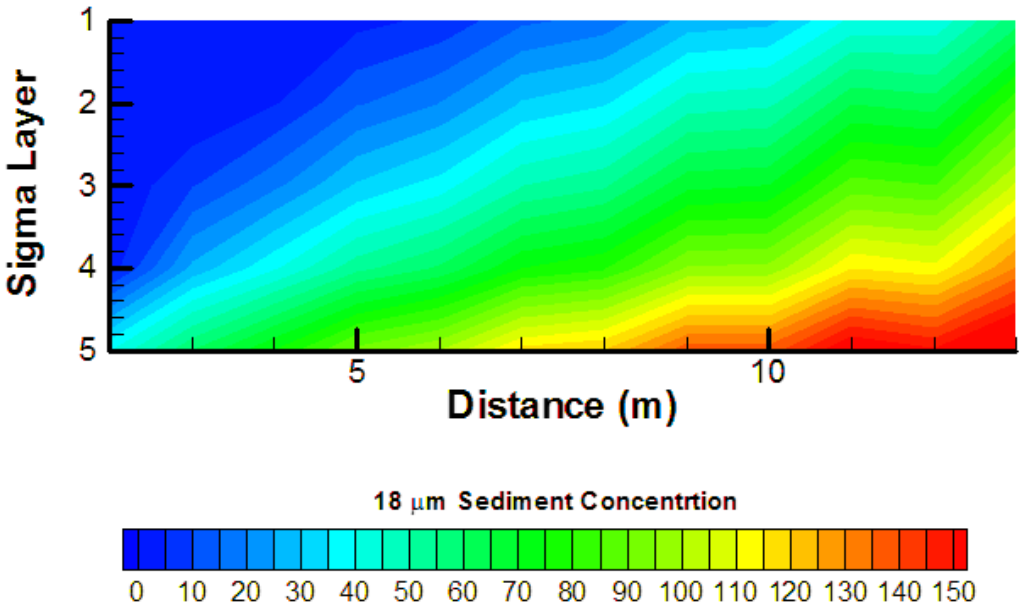

Figure 4. 2-D slice of 18 µm suspended sediment concentration after 10 hours.

Sediment Transport Variable Definitions

SJ_SEDIC

INCORE	Number of Sedflume cores used to describe sediment bed.
CORENO	Identification number of each Sedflume core.
LAYMAX	Maximum number of layers.
BLKTMP	Temporary wet bulk density for entire domain. (g/cm^3)
TAUTMP	Critical shear for erosion for layer. ($dynes/cm^2$)
PNEW	Mass percentage of each size class in layer.
TAULOC	Shear stress associated with erosion data. ($dynes/cm^2$)
E0RATE	Initial erosion rate for each layer. (cm/s)
TAUCOR	Critical shear for erosion for layer. ($dynes/cm^2$)
ERATE	Erosion rate for each layer. (cm/s)
P	Mass percentage of each size class in layer.
BULKDEN	Spatially defined wet bulk density throughout domain. (g/cm^3)
TSED0S	Initial thickness of each layer. (g/cm^2)
TSED	Current thickness of each layer. (g/cm^2)
TSED0	Initial thickness of each layer. (g/cm^2)
LAYER	0 or 1 for layer presence at location.
KSED	Number of particle size classes.
D50	Particle diameter for each size class. (um)
DSTARR	Non-dimensional particle diameter for each size class.
BETA	Settling speed for each size class. (cm/s)
SCLOC	Particle size for new deposited bed erosion data. (um)
TAUCRITE	Critical shear stress for erosion for new deposited bed. ($dynes/cm^2$)
ENRATE	Erosion rate for new deposited bed. (cm/s)
TCRDPS	Critical shear stress for suspension for each size class. ($dynes/cm^2$)
TAUCRS	Critical shear stress for erosion for each size class. ($dynes/cm^2$)

SJ_SEDFLX

TTEMP	Temporary mass in layer. (g/cm^3)
CTB	Concentration at sediment bed. (g/cm^3)
PROB	Probability of suspended load deposition.
DDD	Deposition from suspended load. (g/cm^2)
BLFLAG	0 or 1 for bedload presence at that location and size class.
CSEDVR	Van Rijn's equilibrium bedload concentration. (g/cm^3)
TRANS	Transport parameter for bedload calculations.
PROBVR	Probability of deposition from bedload.
CBL	Bedload concentration. (g/cm^3)
DBL	Deposition from bedload. (g/cm^2)
DEPP	Total deposition rate. (global)
LLN	Next layer under active layer.
D50AVG	Average particle size of surface layer. (um)
TAUCRIT	Critical shear stress for erosion of surface. ($dynes/cm^2$)
TACT	Active layer thickness. (cm)
ACTLAYT	Flag for active layer formation.
ERATEMOD	Erosion rate for layer. ($g/cm^2/s$)
EB	Erosion for layer. (g/cm^2)
EE	Total erosion of size class k. (g/cm^2)
ETOTO	Total erosion of all size classes. (g/cm^2)
ELAY	Erosion of size class k from layer. (g/cm^2)
ESED	Total erosion from layer. (g/cm^2)
QBSED	Net flux into bedload. (g/cm^2)
ESUS	Erosion into suspended load. (g/cm^2)
EBL	Erosion into bed load. (g/cm^2)

SJ_BEDLOAD

USW	Shear velocity. (cm/s)
PSUS	Percentage of total erosion into suspended load.
BLVEL, UBL, and VBL	Bedload velocities. (cm/s)
DZBL	Bedload height. (cm)
XBLFLUX YBLFLUX	Horizontal bedload fluxes. (g/cm^2) X and Y are transformed into computational space for curvilinear calculations.

References

Jones, C. and W. Lick, 2001. Contaminant flux due to sediment erosion, *Proceedings of the 7th International Conference: Estuarine and Coastal Modeling*, 280–293.

Roberts, J., Jepsen, R., Gotthard, D., and Lick, W., 1998, Effects of particle size and bulk density on erosion of quartz particles, *J. Hydr. Engrg.*, 124(12):1261-1267.

Little, W.C. and Mayer, P.G. 1972. The role of sediment gradation on channel armoring. Publication No. ERC-0672, School of Civil Engineering in Cooperation with Environmental Research Center, Georgia Institute of Technology, Atlanta, GA. 1-104.

Van Rijn, L. 1993. *Principles of Sediment Transport in Rivers, Estuaries, and Coastal Seas*. Aqua Publications, Amsterdam, The Netherlands.

Attachment B

Bed Elevation Changes, Maximum Erosion and Bottom Shear Stresses for Ambrose Sand Cap

Figure B-1a. Plan view of the net elevation change under the 1-year return flow conditions
(Ambrose sand used as the capping material under the “8-Mile Cap” scenario).

Figure B-1b. Plan view of the maximum erosion under the 1-year return flow conditions
(Ambrose sand used as the capping material under the “8-Mile Cap” scenario).

Figure B-1c. Plan view of the bottom shear stress under the 1-year return flow conditions
(Ambrose sand used as the capping material under the “8-Mile Cap” scenario).

Figure B-2a. Plan view of the net elevation change under the 25-year return flow conditions
(Ambrose sand used as the capping material under the “8-Mile Cap” scenario).

Figure B-2b. Plan view of the maximum erosion under the 25-year return flow conditions
(Ambrose sand used as the capping material under the “8-Mile Cap” scenario).

Figure B-2c. Plan view of the bottom shear stress under the 25-year return flow conditions
(Ambrose sand used as the capping material under the “8-Mile Cap” scenario).

Figure B-3a. Plan view of the net elevation change under the 100-year return flow conditions
(Ambrose sand used as the capping material under the “8-Mile Cap” scenario).

Figure B-3b. Plan view of the maximum erosion under the 100-year return flow conditions
(Ambrose sand used as the capping material under the “8-Mile Cap” scenario).

Figure B-3c. Plan view of the bottom shear stress under the 100-year return flow conditions
(Ambrose sand used as the capping material under the “8-Mile Cap” scenario).

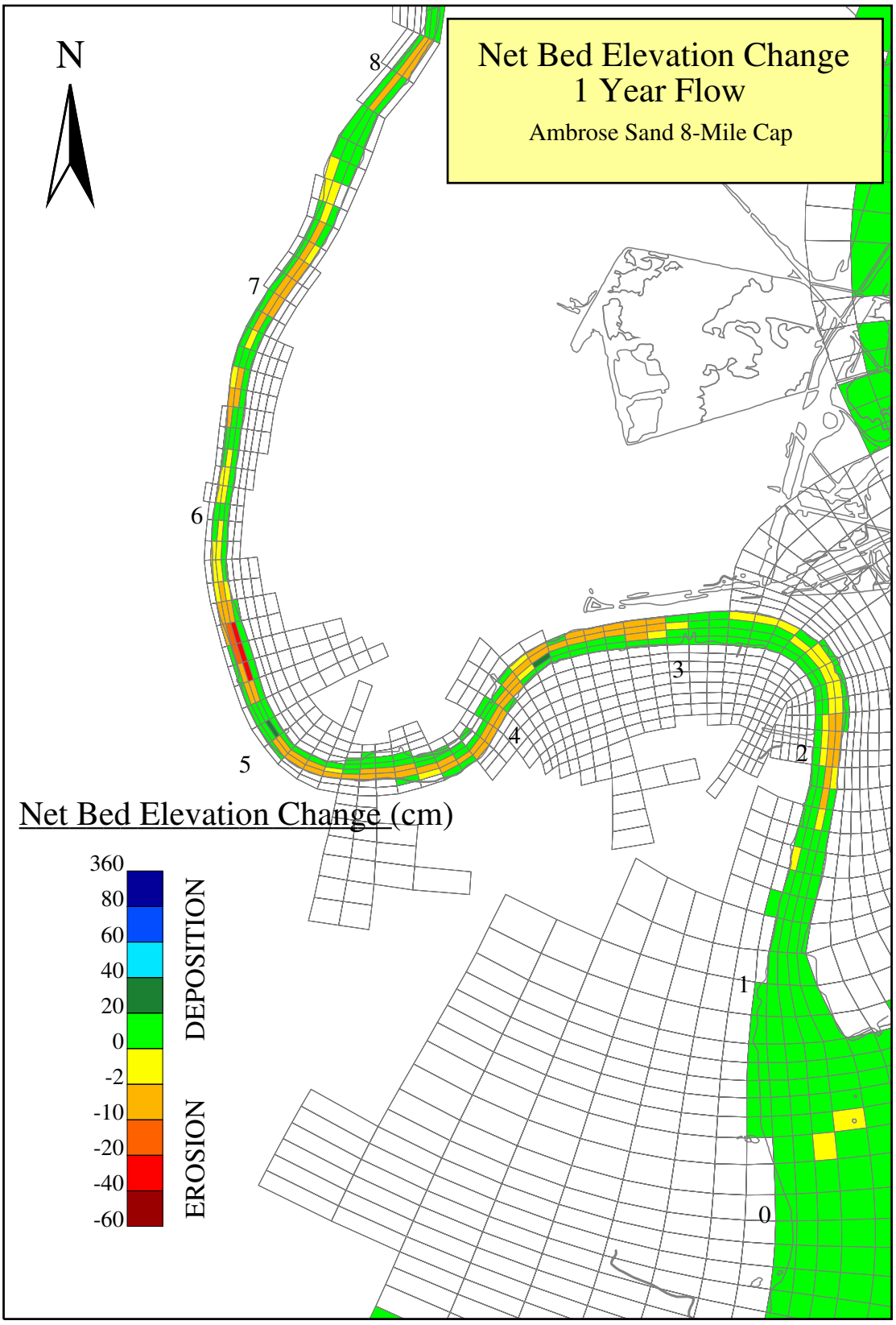

Figure B-1a. Plan view of the net elevation change under the 1-year return flow conditions (Ambrose sand used as the capping material).

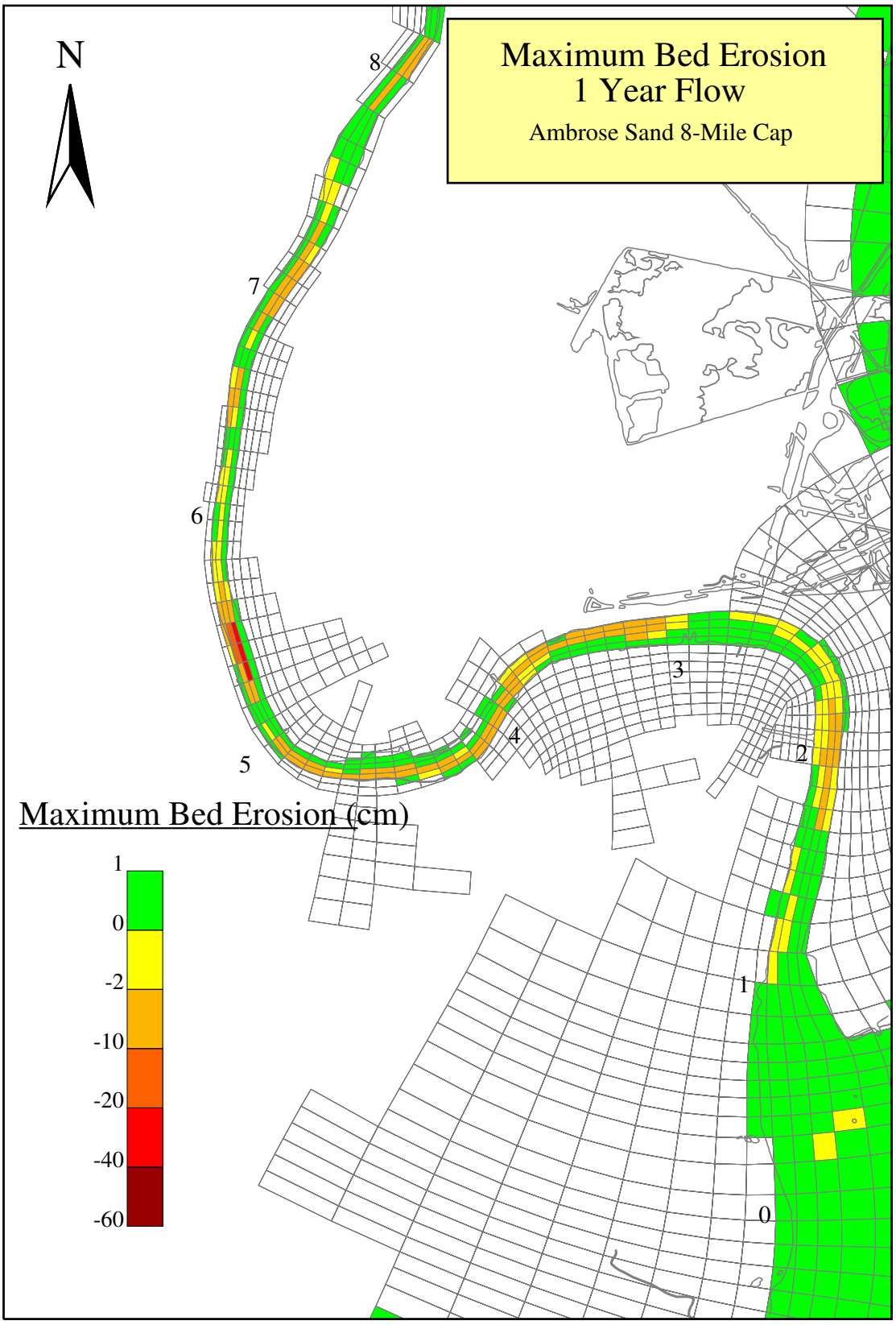

Figure B-1b. Plan view of the maximum erosion under the 1-year return flow conditions (Ambrose sand used as the capping material).

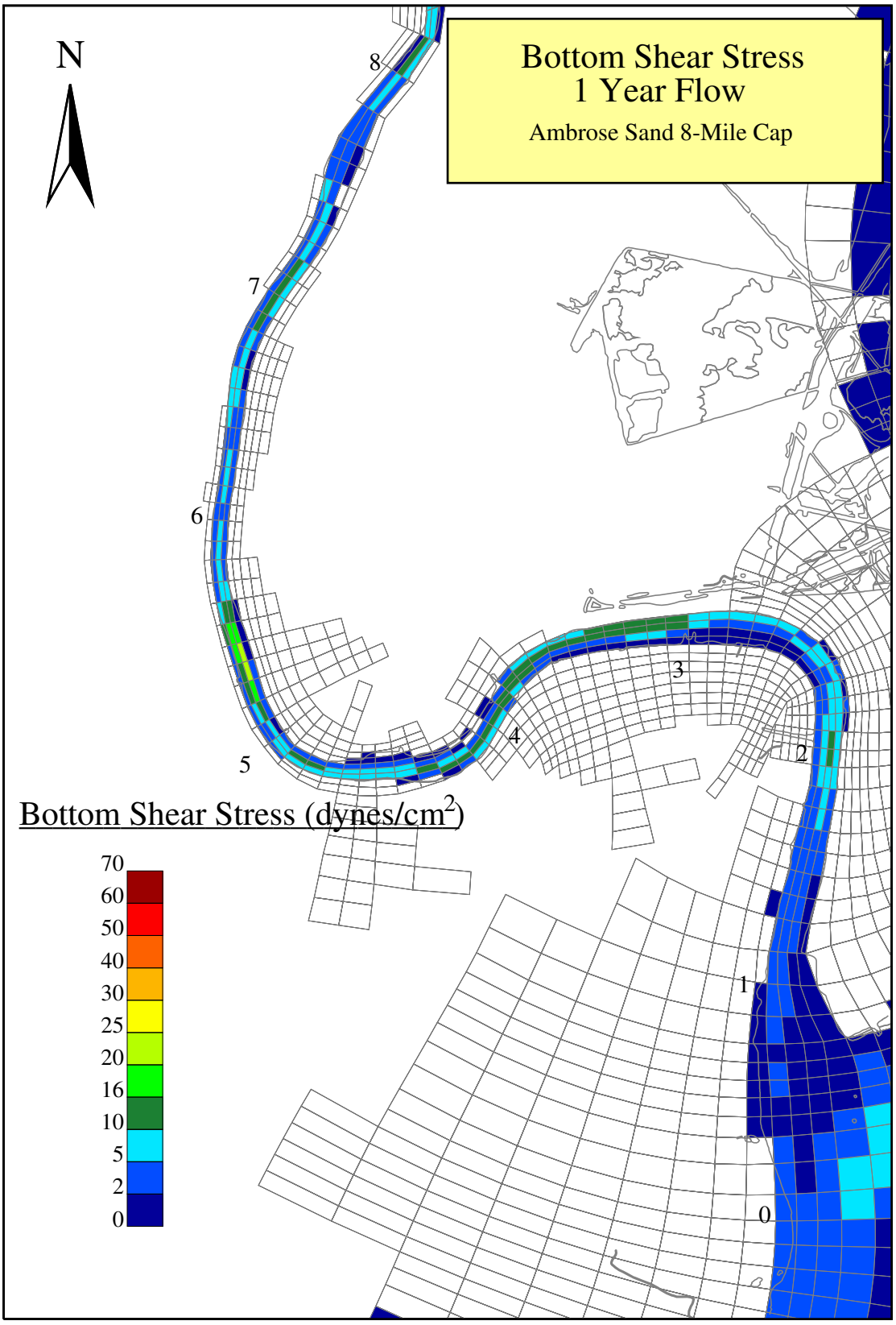

Figure B-1c. Plan view of the bottom shear stress under the 1-year return flow conditions (Ambrose sand used as the capping material).

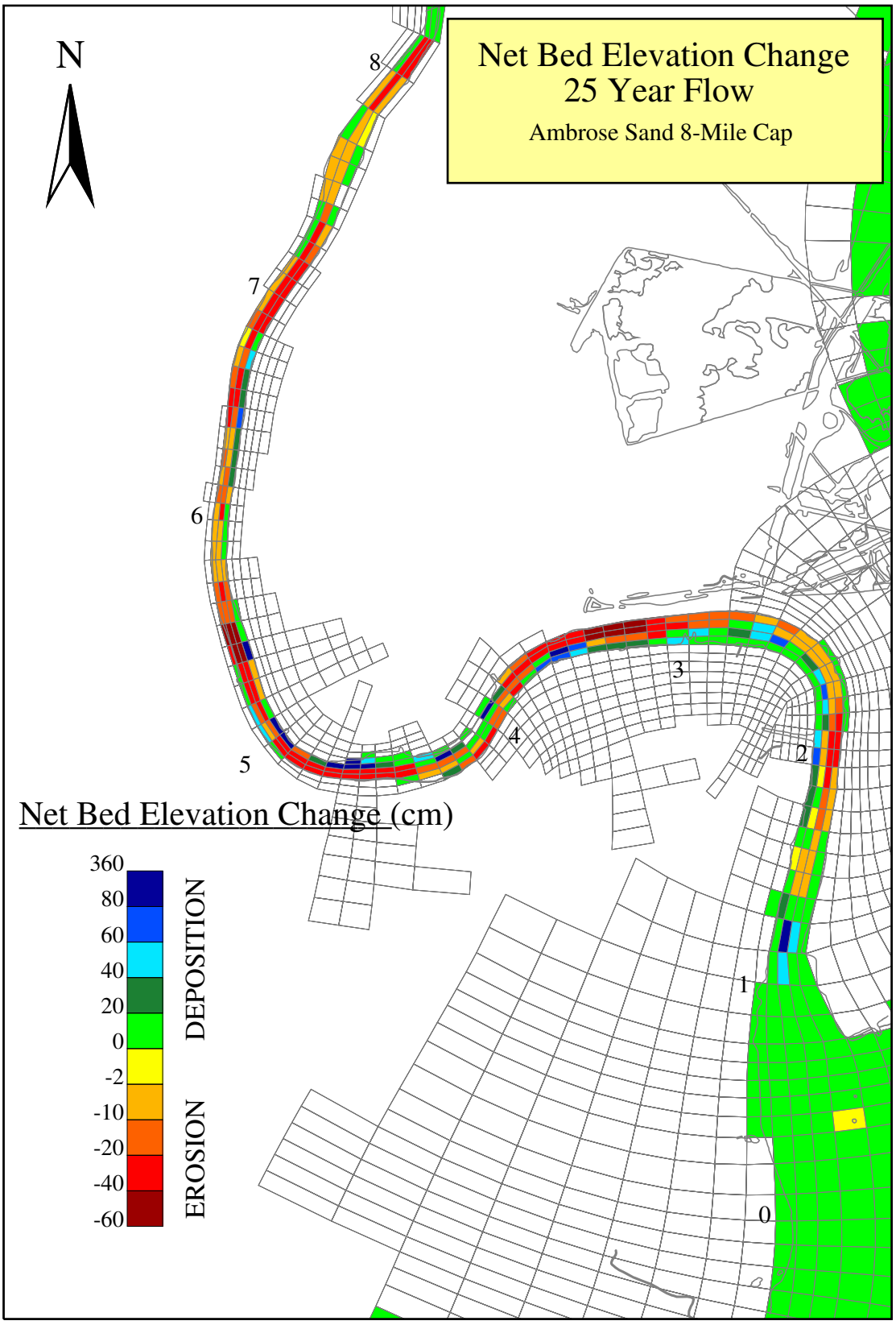

Figure B-2a. Plan view of the net elevation change under the 25-year return flow conditions (Ambrose sand used as the capping material).

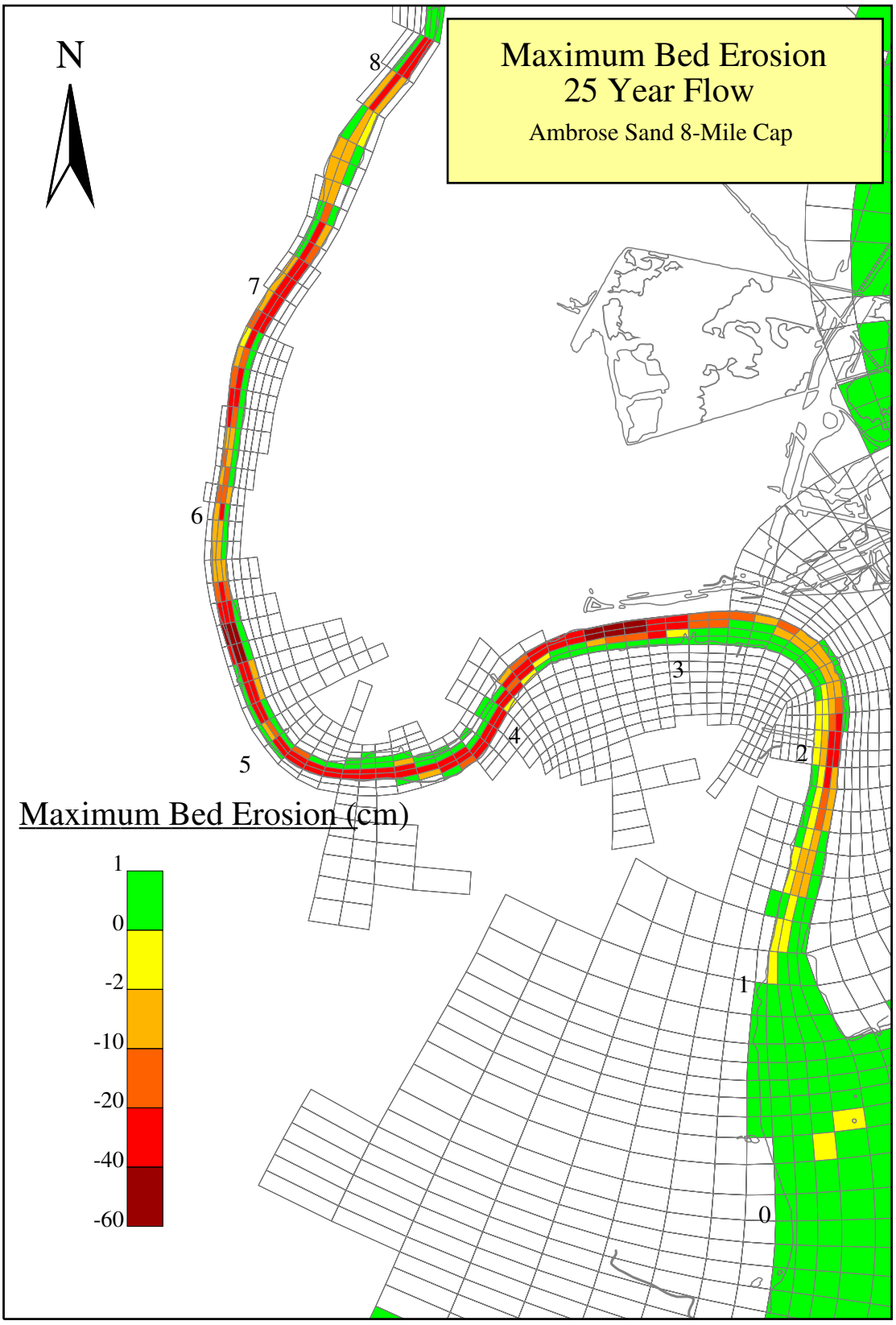

Figure B-2b. Plan view of the maximum erosion under the 25-year return flow conditions (Ambrose sand used as the capping material).

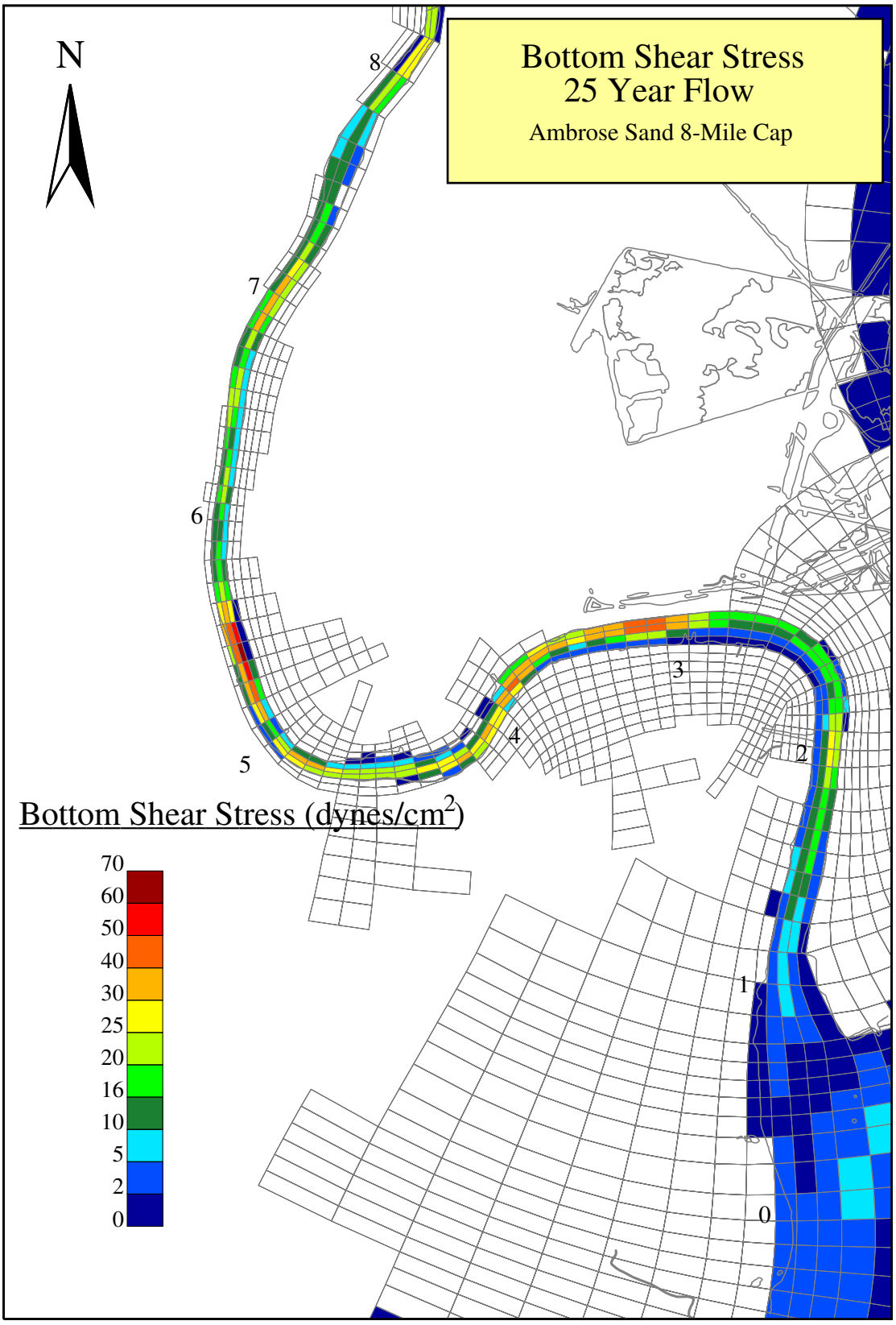

Figure B-2c. Plan view of the bottom shear stress under the 25-year return flow conditions (Ambrose sand used as the capping material).

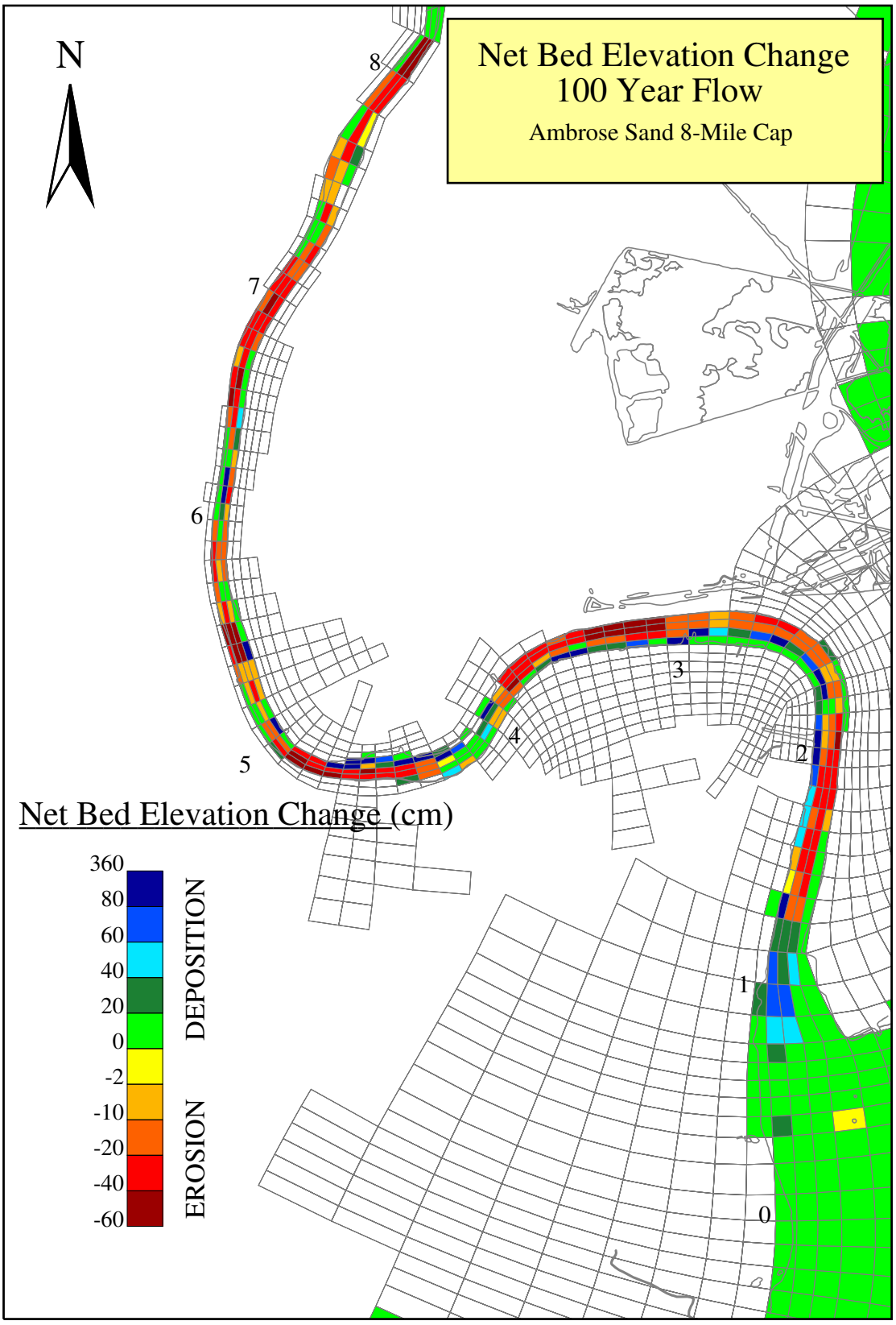

Figure B-3a. Plan view of the net elevation change under the 100-year return flow conditions (Ambrose sand used as the capping material).

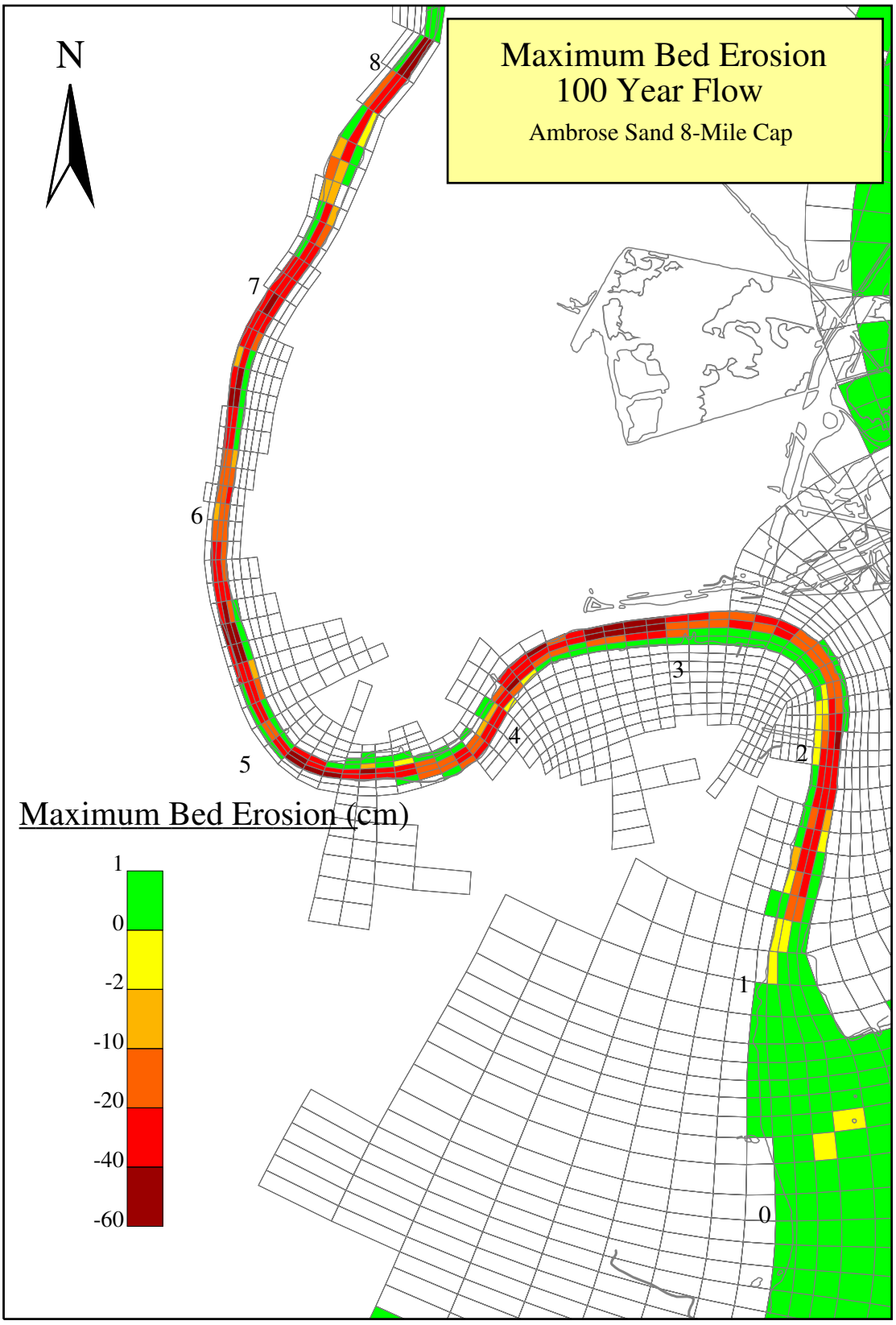

Figure B-3b. Plan view of the maximum erosion under the 100-year return flow conditions (Ambrose sand used as the capping material).

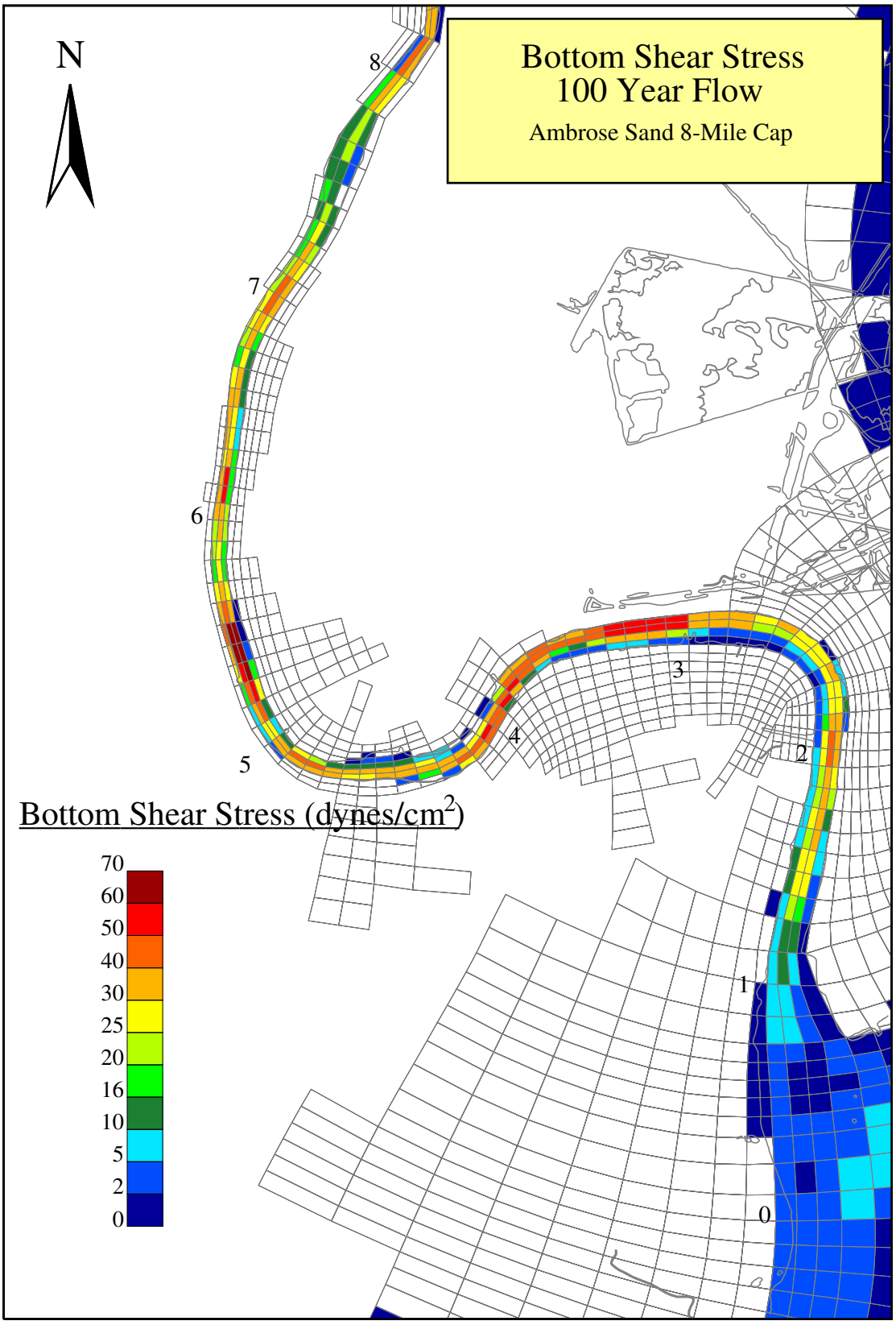

Figure B-3c. Plan view of the bottom shear stress under the 100-year return flow conditions (Ambrose sand used as the capping material).

Attachment C

Bed Elevation Changes, Maximum Erosion and Bottom Shear Stresses under Different Depths and Capping/Armoring Scenarios

Figure C-1a. Plan view of the net elevation change under the “Capping with Armor Area Pre-Dredging” (Capping only) scenario (Upland Borrow Sand used as the capping material).

Figure C-1b. Plan view of the maximum erosion under the “Capping with Armor Area Pre-Dredging” (Capping only) scenario (Upland Borrow Sand used as the capping material).

Figure C-1c. Plan view of the bottom shear stress under the “Capping with Armor Area Pre-Dredging” (Capping only) scenario (Upland Borrow Sand used as the capping material).

Figure C-2a. Plan view of the net elevation change under the “Capping with Armor Area Pre-Dredging” (Capping and Armoring) scenario (Upland Borrow Sand used as the capping material).

Figure C-2b. Plan view of the maximum erosion under the “Capping with Armor Area Pre-Dredging” (Capping and Armoring) scenario (Upland Borrow Sand used as the capping material).

Figure C-2c. Plan view of the bottom shear stress under the “Capping with Armor Area Pre-Dredging” (Capping and Armoring) scenario (Upland Borrow Sand used as the capping material).

Figure C-3a. Plan view of the net elevation change under the “Capping with Pre-Dredging for Flooding - Exposed Armor Areas” (Capping only) scenario (Upland Borrow Sand used as the capping material).

Figure C-3b. Plan view of the maximum erosion under the “Capping with Pre-Dredging for Flooding - Exposed Armor Areas” (Capping only) scenario (Upland Borrow Sand used as the capping material).

Figure C-3c. Plan view of the bottom shear stress under the “Capping with Pre-Dredging for Flooding - Exposed Armor Areas” (Capping only) scenario (Upland Borrow Sand used as the capping material).

Figure C-4a. Plan view of the net elevation change under the “Capping with Pre-Dredging for Flooding - Exposed Armor Areas” (Capping and Armoring) scenario (Upland Borrow Sand used as the capping material).

Figure C-4b. Plan view of the maximum erosion under the “Capping with Pre-Dredging for Flooding - Exposed Armor Areas” (Capping and Armoring) scenario (Upland Borrow Sand used as the capping material).

Figure C-4c. Plan view of the bottom shear stress under the “Capping with Pre-Dredging for Flooding - Exposed Armor Areas” (Capping and Armoring) scenario (Upland Borrow Sand used as the capping material).

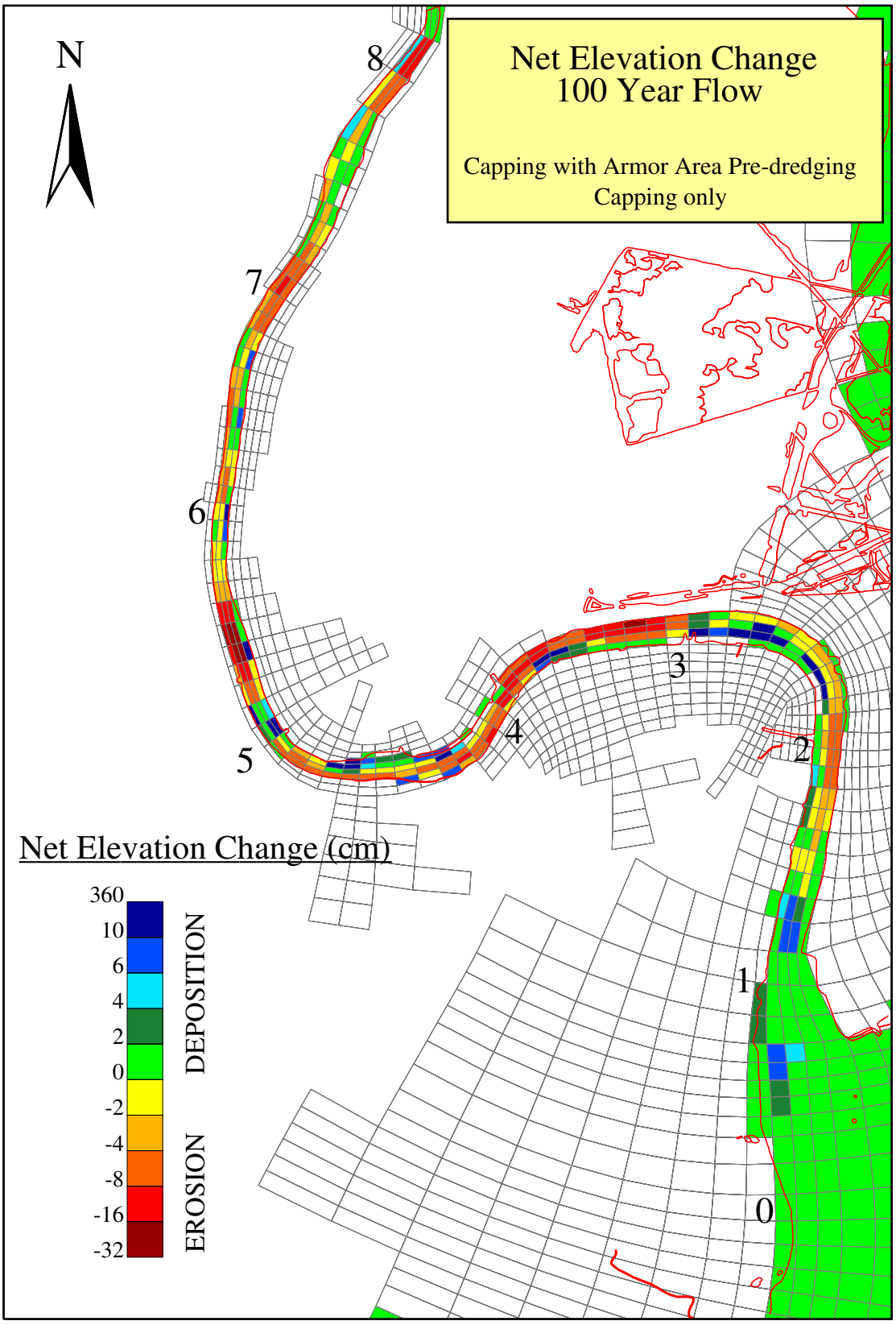

Figure C-1a. Plan view of the net elevation change under the "Capping with Armor Area Pre-Dredging" (Capping only) Scenario (Upland Borrow Sand used as the capping material).

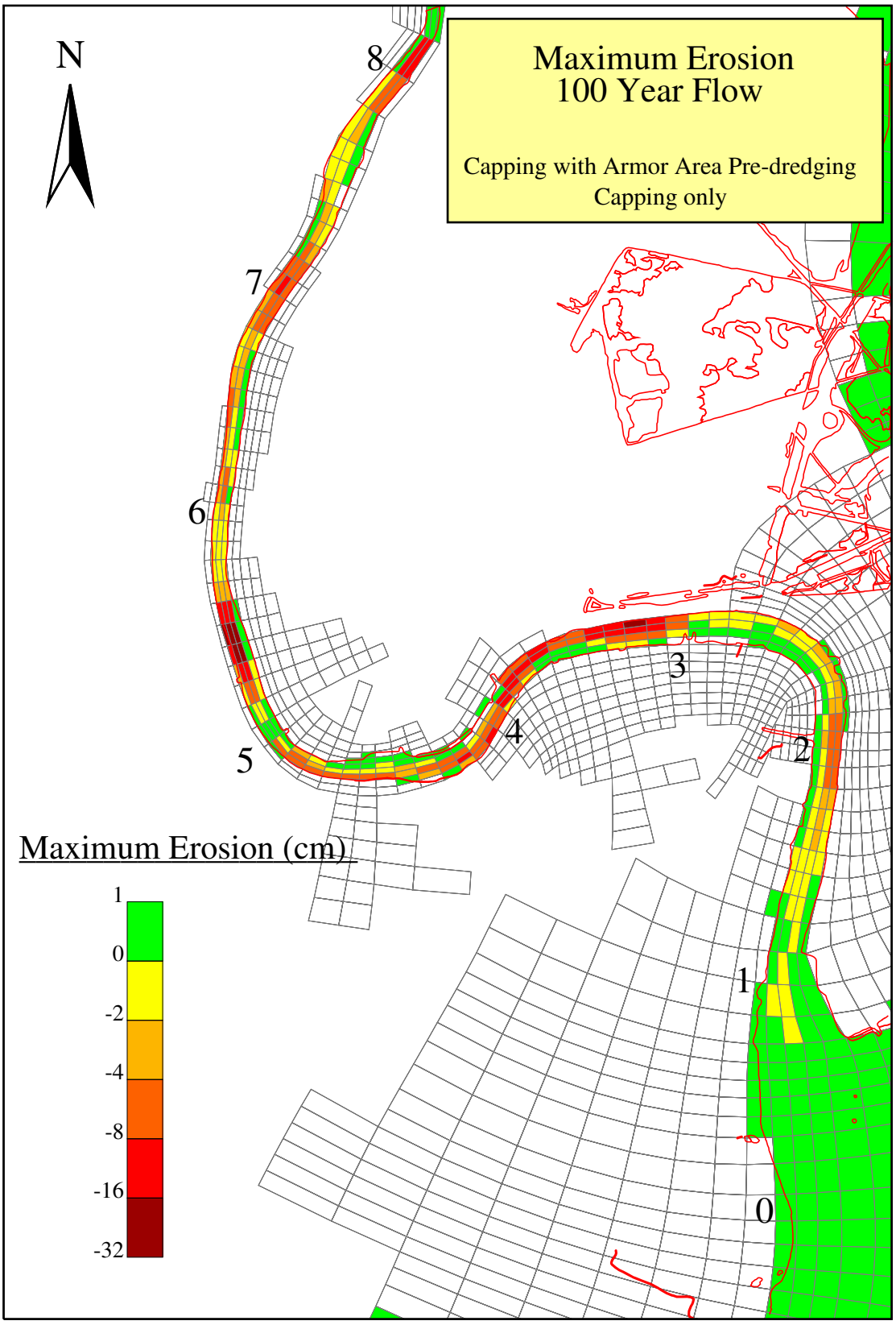

Figure C-1b. Plan view of the maximum erosion under the "Capping with Armor Area Pre-Dredging" (Capping only) Scenario (Upland Borrow Sand used as the capping material).

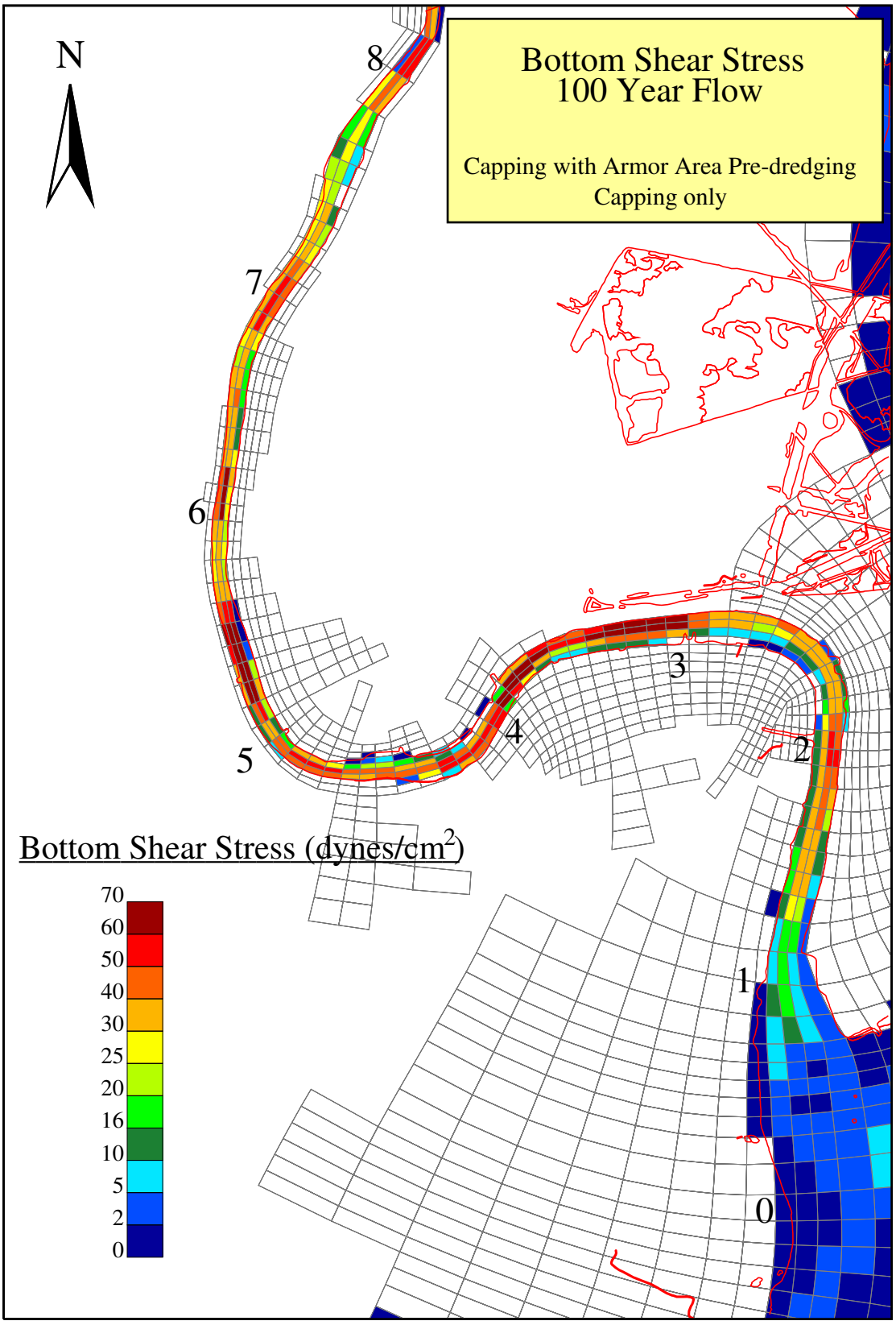

Figure C-1c. Plan view of the bottom shear stress under the "Capping with Armor Area Pre-Dredging" (Capping only) Scenario (Upland Borrow Sand used as the capping material).

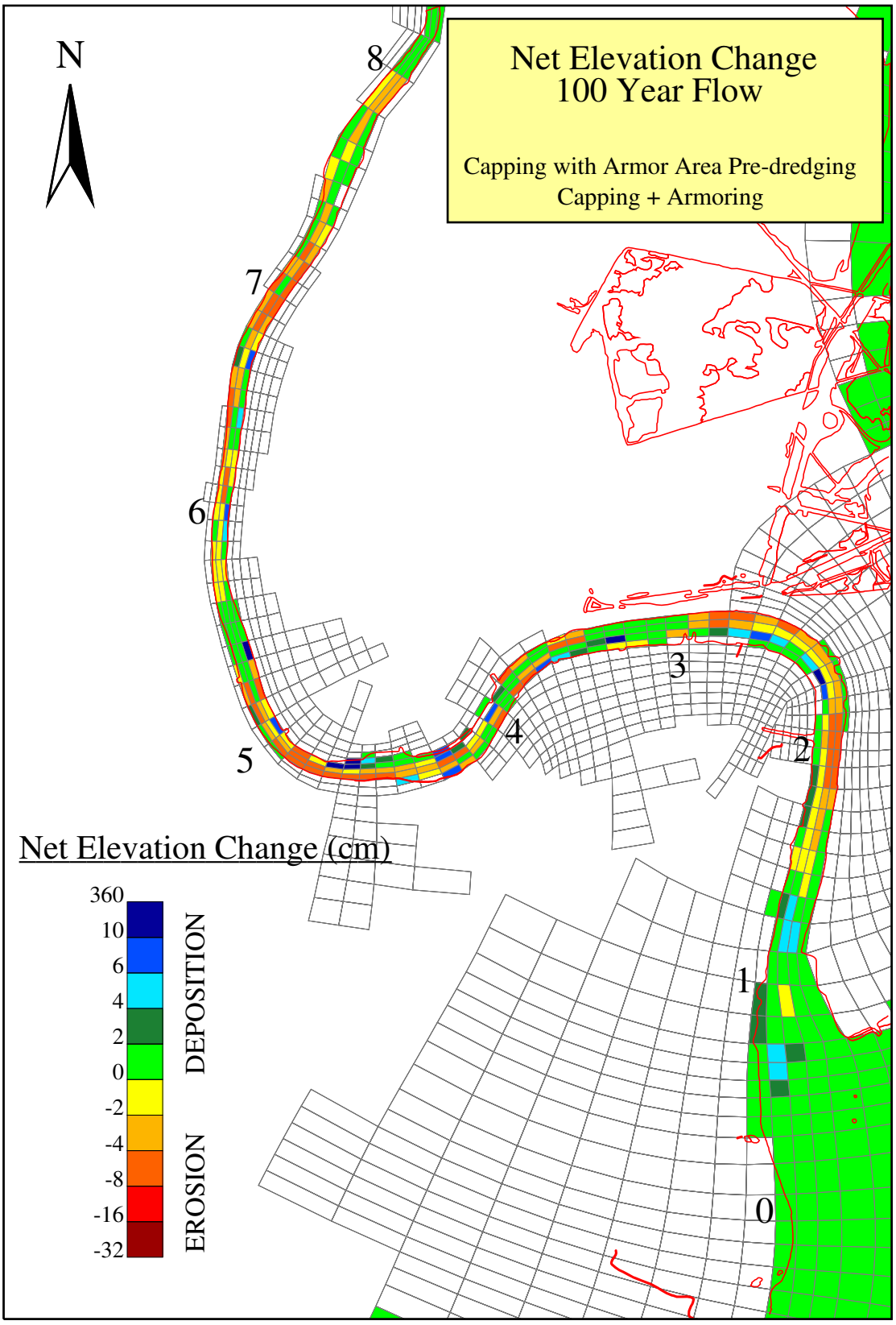

Figure C-2a. Plan view of the net elevation change under the "Capping with Armor Area Pre-Dredging" (Capping and Armoring) Scenario (Upland Borrow Sand used as the capping material).

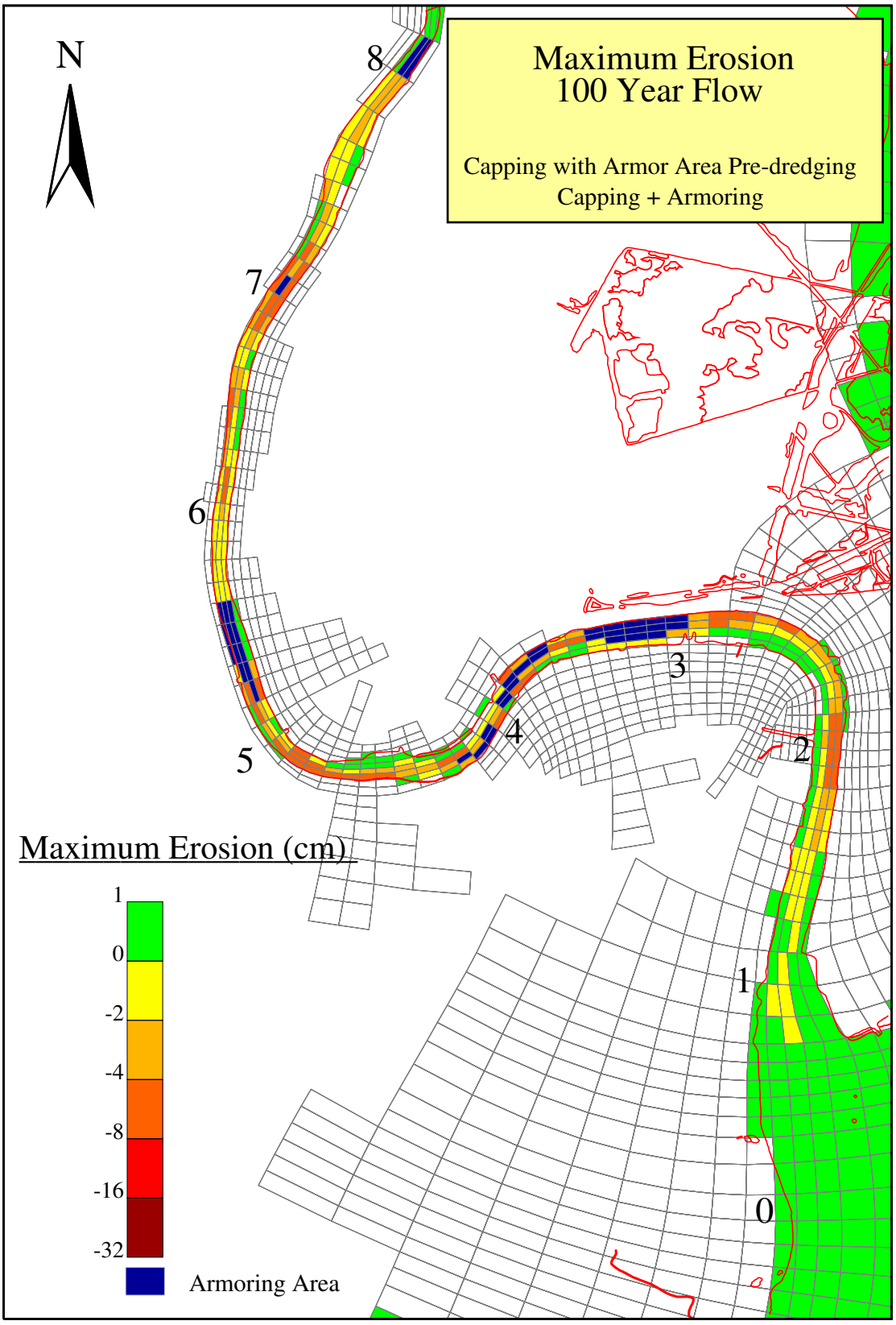

Figure C-2b. Plan view of the maximum erosion under the "Capping with Armor Area Pre-Dredging" (Capping and Armoring) Scenario (Upland Borrow Sand used as the capping material).

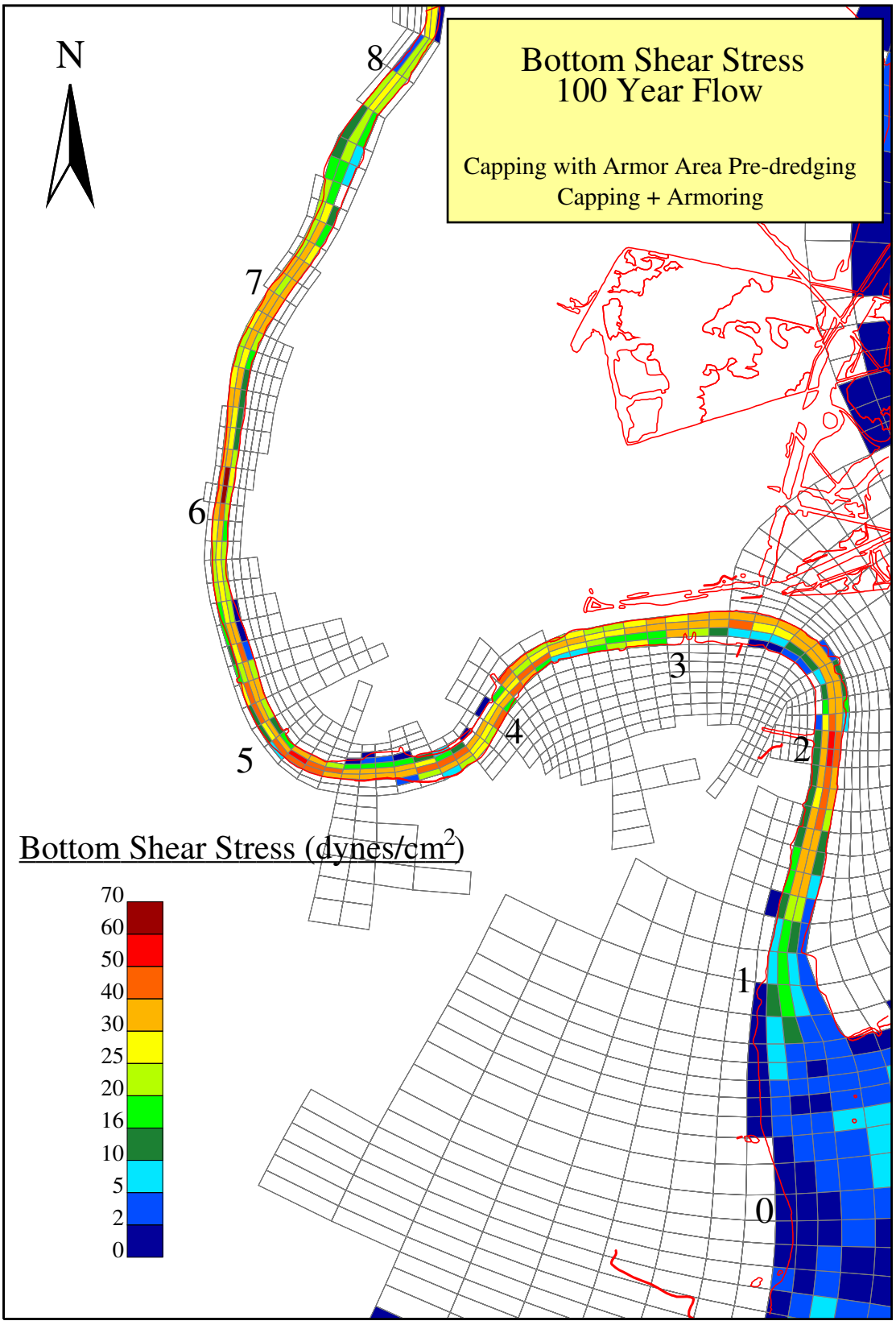

Figure C-2c. Plan view of the bottom shear stress under the "Capping with Armor Area Pre-Dredging" (Capping and Armoring) Scenario (Upland Borrow Sand used as the capping material).

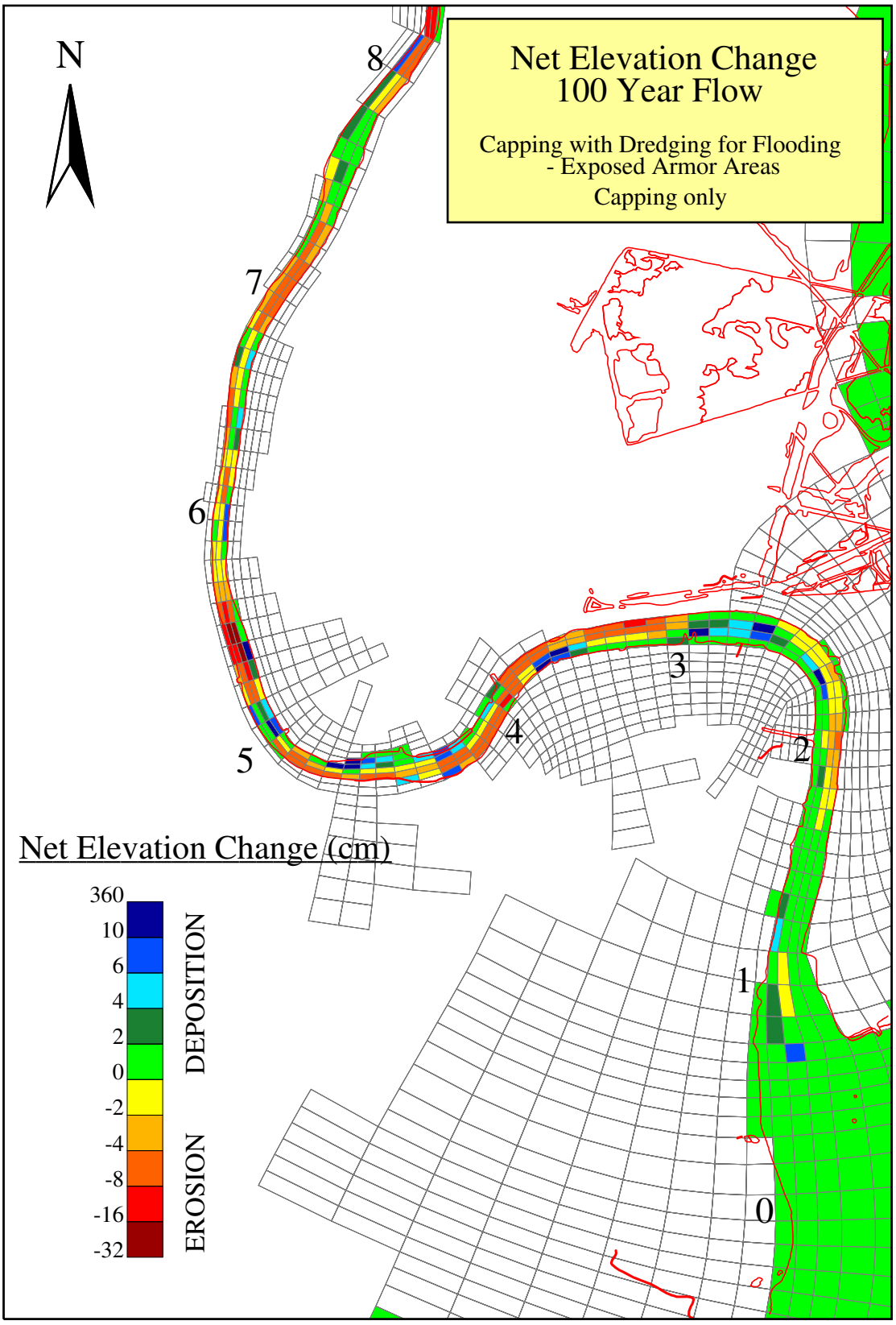

Figure C-3a. Plan view of the net elevation change under the "Capping with Pre-Dredging for Flooding - Exposed Armor Areas" (Capping only) Scenario (Upland Borrow Sand used as the capping material).

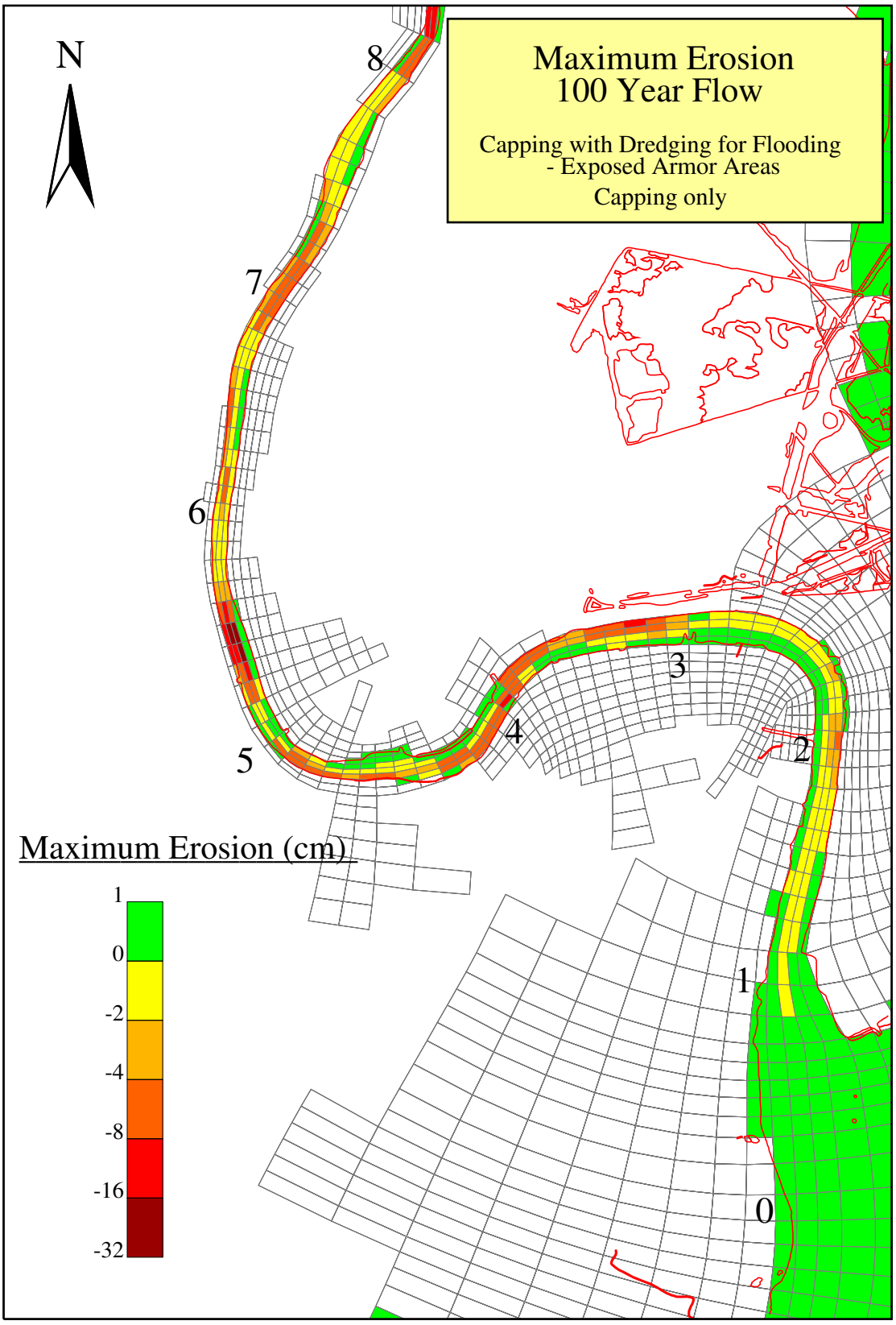

Figure C-3b. Plan view of the maximum erosion under the "Capping with Pre-Dredging for Flooding - Exposed Armor Areas" (Capping only) Scenario (Upland Borrow Sand used as the capping material).

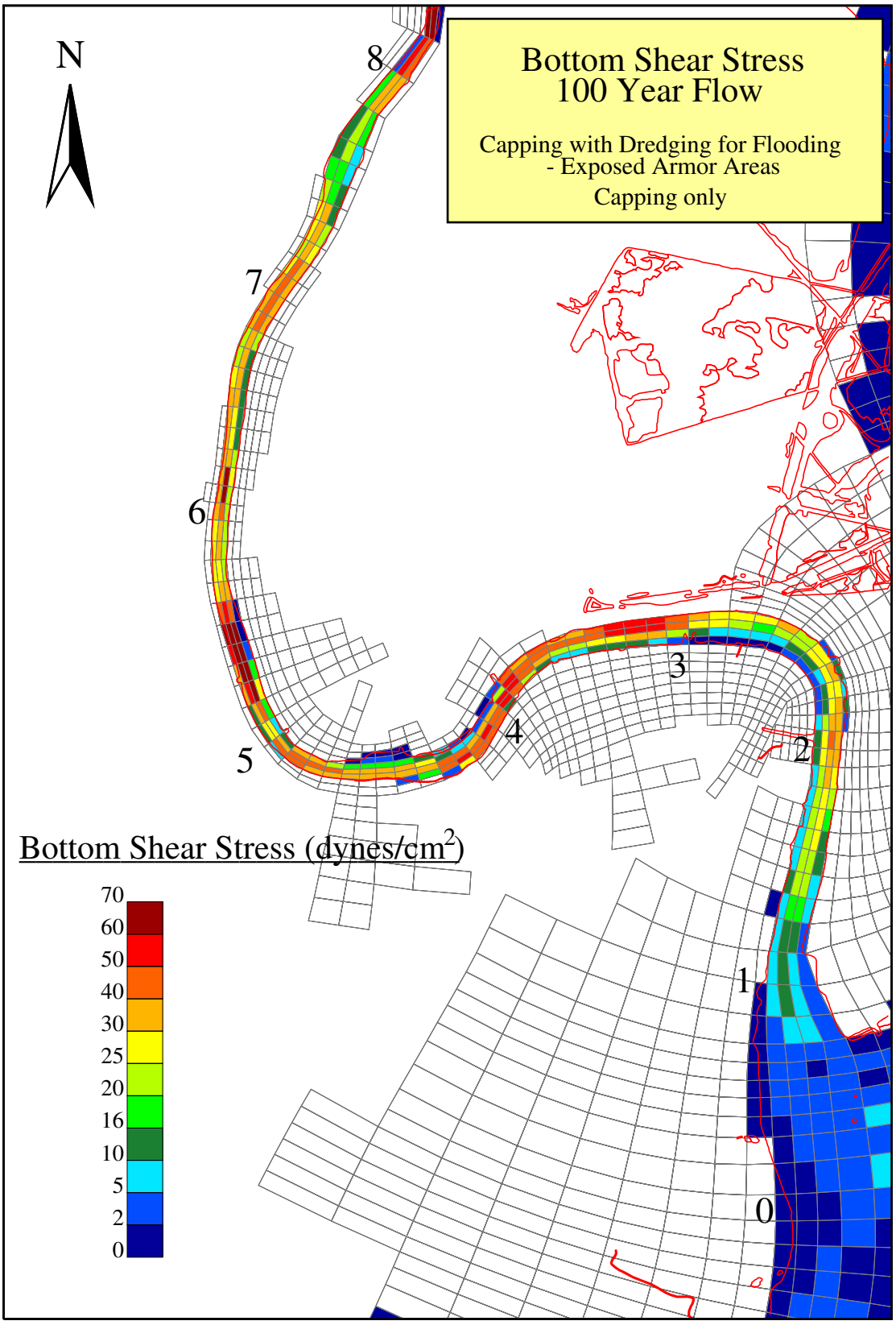

Figure C-3c. Plan view of the bottom shear stress under the "Capping with Pre-Dredging for Flooding - Exposed Armor Areas" (Capping only) Scenario (Upland Borrow Sand used as the capping material).

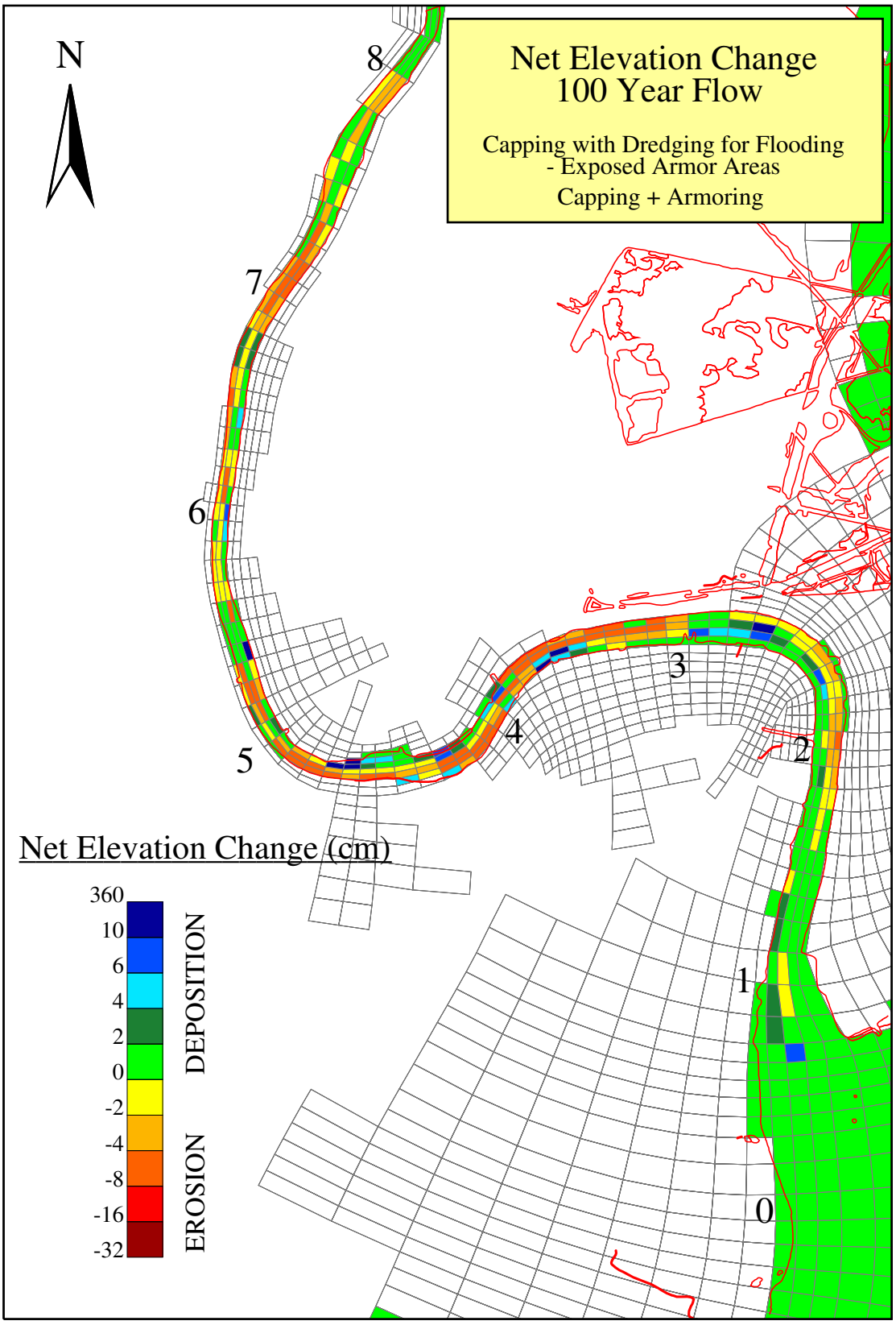

Figure C-4a. Plan view of the net elevation change under the "Capping with Pre-Dredging for Flooding - Exposed Armor Areas" (Capping and Armoring) Scenario (Upland Borrow Sand used as the capping material).

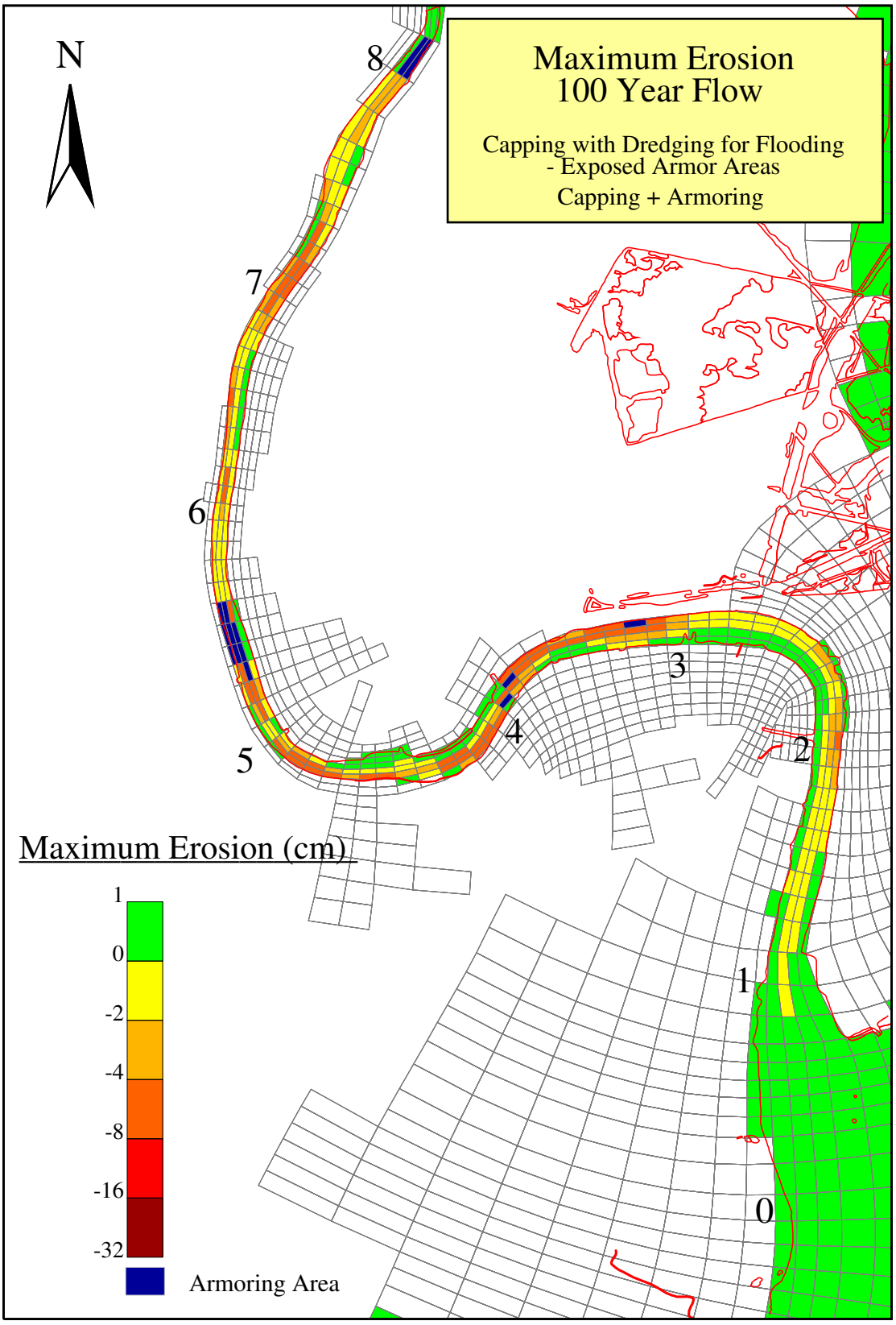

Figure C-4b. Plan view of the maximum erosion under the "Capping with Pre-Dredging for Flooding - Exposed Armor Areas" (Capping and Armoring) Scenario (Upland Borrow Sand used as the capping material).

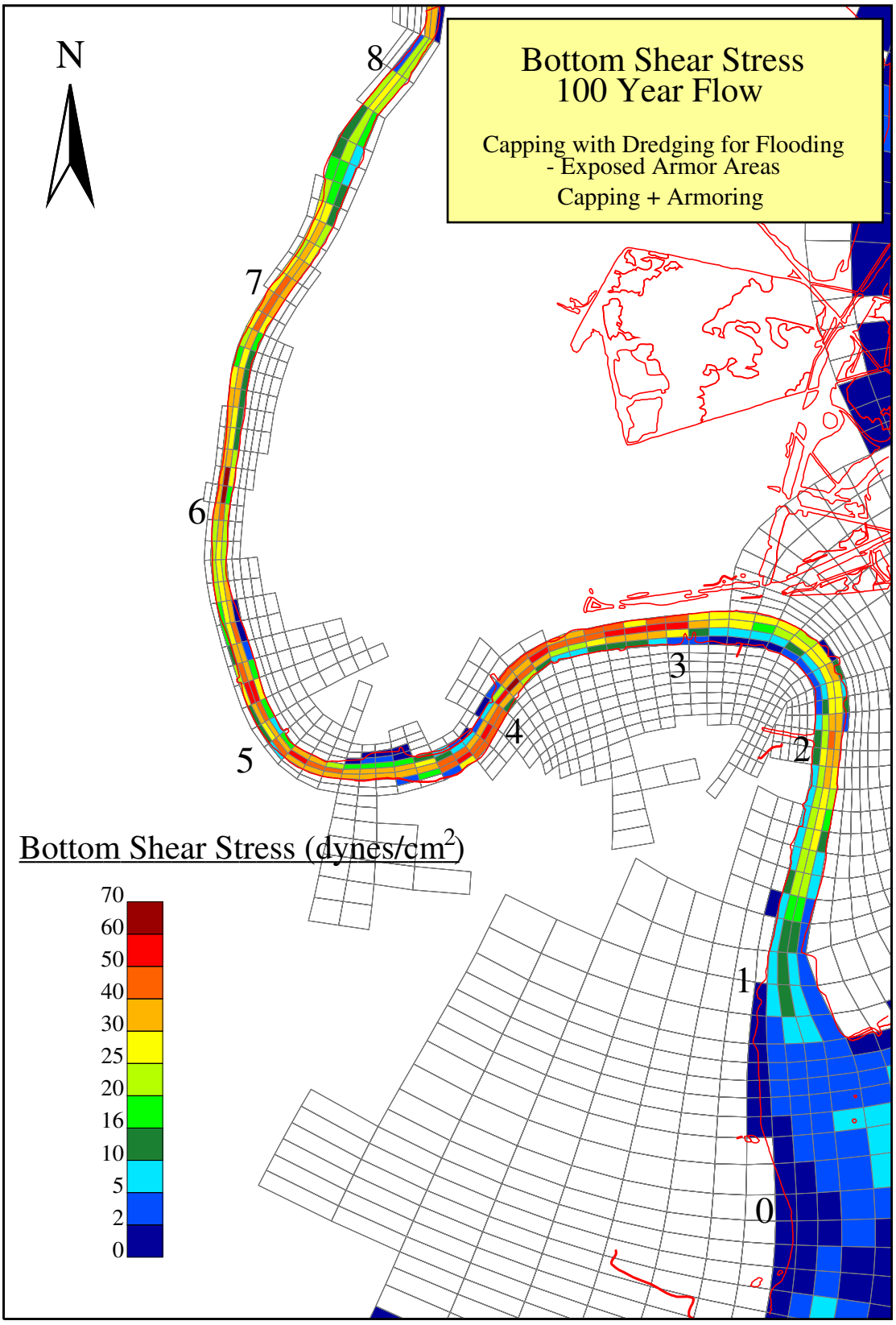

Figure C-4c. Plan view of the bottom shear stress under the "Capping with Pre-Dredging for Flooding - Exposed Armor Areas" (Capping and Armoring) Scenario (Upland Borrow Sand used as the capping material).